Title
Earthquake Gates and Off-fault Deformation

Author
Rodriguez Padilla, Alba Mar

Publication Date
2023

Peer reviewed|Thesis/dissertation

Earthquake Gates and Off-fault Deformation

By

ALBA MAR RODRÍGUEZ PADILLA
DISSERTATION

Submitted in partial satisfaction of the requirements for the degree of

DOCTOR OF PHILOSOPHY

in

Earth and Planetary Sciences

in the

OFFICE OF GRADUATE STUDIES

of the

UNIVERSITY OF CALIFORNIA

DAVIS

Approved:

Michael E. Oskin, Chair

Magali I. Billen

Emily E. Brodsky

Committee in Charge

2023

Abstract

Plate tectonics drives the slip budget available for deformation across a plate boundary. Within the upper crust, tectonic deformation is accommodated through a combination of frictional slip on faults and distributed deformation in the surrounding rock volume. Large earthquakes accommodate the majority of the slip budget. However, because faults are non-planar and have finite lengths, ruptures must breach zones of geometrical complexity along faults, or the spacing between neighboring faults, to continue growing. Geometrical complexity forces slip on the fault to taper and trade off with the surrounding volume, through a combination of elastic and permanent deformation. How these modes of deformation -localized frictional slip and distributed deformation of the bulk- operate together plays a fundamental role in the distribution of earthquake magnitude and locations across a fault system and the evolution of the physical properties of the crustal volume. This dissertation explores the mechanics of slip transfer through zones of geometrical complexity and the generation of permanent off-fault deformation over multiple earthquake cycles.

Chapters 1 and 2 in this dissertation are concerned with earthquake gates. Zones of geometrical complexity, or earthquake gates, can act as barriers to rupture propagation conditional on the fault geometry, rupture directivity effects, crustal properties, and prior stress history. In the first chapter, I focus on the geometrical aspect of the earthquake gate problem. I map step-overs, bends, gaps, splays, and strands from the surface ruptures of 31 strike-slip earthquakes at 1:50,000 scale, classifying each population into breached and unbreached groups. Based on these classifications, I calculate passing probability as a function of geometry for each group. Step-overs, gaps, and single bends halt ruptures more effectively than double bends, and <20% of the ruptures stopped on straight segments. Based on the modeled probabilities, I estimate event likelihood as the joint passing probabilities of breached gates and straight segments along an event's rupture length. Event likelihood decreases with magnitude, where the size and spacing of earthquake gates along ruptures support a barrier model for controlling earthquake magnitude. Through a simple mechanical model rooted in linear elastic fracture mechanics, I find that ruptures seldom renucleate on receiver faults across step-overs with Coulomb stress change below a critical threshold of 20% of the stress drop.

Complex stress distributions resulting from an integrated history of continuing and halting ruptures, as well as rheological heterogeneity, also act as earthquake gates, but their influence in the passing probability of a barrier are much harder to quantify observationally. By looking at the integrated history of events at an earthquake gate, comparing the number of events that halted versus those that made it past, it is possible to implicitly account for the effects of these harder to observe variables. In the second chapter of this dissertation, I combine a paleoseismic investigation with finite element modeling of secondary slip on a minor fault to determine the frequency and mechanics of earthquakes that co-rupture the San Andreas and

the San Jacinto faults in southern California, with rupture transfer across the Cajon Pass releasing step-over. I find evidence that multi-fault events through Cajon Pass have occurred 3 times in the past 2000 years, where 20-23% of the events on the San Andreas and the San Jacinto faults are co-ruptures.

Chapters 3, 4, and 5 of this dissertation are concerned with how distributed deformation around faults is created and evolves over multiple earthquake cycles. Some of the distributed deformation around faults exceeds the yield stress the rock mass can support, resulting in the creation of permanent deformation that is accommodated by a suite of dissipative mechanisms, including fracture, granular flow, warping, and block rotations. In chapter 3, I combine fracture, aftershock, and strain maps from the 2019 Ridgecrest earthquakes to quantify the distribution of inelastic deformation in the surrounding volume of the rupturing faults. I find the decay of inelastic deformation with distance from the fault is well described by an inverse power law, consistent across datasets, and continuous without breaks in scaling, suggesting that a single mechanism dominates yielding.

Widespread distributed fracturing, such as that characterized in chapter 3, threatens infrastructure and lifelines. In chapter 4, I use high-resolution rupture maps from the five major surface-rupturing strike-slip earthquakes in southern California and northern Mexico since 1992 to incorporate the displacements produced by distributed ruptures into a probabilistic displacement hazard analysis framework. Through analysis of the spatial distribution of mapped ruptures and displacements for each of these events, I develop a magnitude-dependent expression for the probability per unit area of finding a distributed rupture that accommodates a displacement that exceeds a user-defined threshold at a given distance from the principal fault.

In chapter 5, I shift focus to the question of how permanent deformation accumulates over multiple earthquake cycles. Using lidar and field observations, I measure coseismic and cumulative folding from five locales in western North America. The observations link coseismic to cumulative deformation and show that folding amplitude accumulates over multiple slip cycles, scaling as the square root of fault throw. The distribution of folding strains is well described by the decay of elastic stress surrounding a crack tip, though the strains exceed the elastic limit of rock by over an order of magnitude. The field observations suggest that pre-existing fabrics in the rock mass help accommodate the large folding strains while maintaining the elastically created shape. The lidar and field observations can be explained by a simple model where the rock mass deforms linearly with stress, though the shear modulus that defines the rate of change in deformation decreases once the yield stress of the rock mass is reached.

Through the use of high-resolution topography, aerial imagery, earthquake catalogs and field observations, this dissertation contributes to the increasingly detailed picture of how tectonic strain is transferred and accommodated across the upper crust over different spatiotemporal scales. This work also contributes

outstanding questions to this growing understanding: How much of the complexity and damage mapped at the surface persists at depth? Why do step-overs appear to require very high (∼20% of the stress drop) Coulomb stress changes for rupture to renucleate yet widespread fracturing and aftershocks are easily triggered and populate a very large crustal volume following earthquakes? Fracturing and folding contribute to large reductions in the compliance around faults, even coseismically, how much of this reduction is recovered post- or interseismically through healing mechanisms? These questions will guide future data collection and modeling efforts addressing the mechanics of strain accumulation and release in the crust.

Contents

Acknowledgments

This dissertation would not be possible without the guidance and support of my advisor, Mike Oskin. With his incredibly broad expertise and sharpness, Mike has supported every research direction I have wanted to pursue during my PhD. I have learned a lot from working with together and I look forward to the many years of collaboration to come.

Magali Billen and Emily Brodsky taught two of the courses that I benefited from the most in graduate school and, as committee members, have challenged me and supported me in developing the science in this thesis. I am grateful to Max Rudolph and Sarah Roeske for serving as members of my qualifying exam committee. Despite spending little time in Davis past my first year, I am incredible grateful for the friendships of Becky Fildes and Dylan Vasey, which have transcended distance. I am indebted to fellow members of the Oskin lab, present and past, for their mentorship and just for generally being a fun bunch to hang out with, including Veronica Prush, Alex Morelan, Yiran Wang, Elaine Young, Yvonne Leon, Austin Elliott, Eitan Shelef, Scott Bennett, and Kim Blisniuk. I look forward to many years of AGU and SCEC catch-up beers.

Spending time at the UCSC Seismo lab empowered me to venture into projects that I never thought possible given my limited math and physics background. I am grateful to faculty members Thorne Lay, Susan Schwartz, Emily Brodsky, and Heather Savage for sharing their endless wisdom, and for their continued support after I left Santa Cruz. I am thankful that Travis Alongi decided to embark in researching damage zones at the same time I did. It has been fun to have a companion in this process. Over my years as an intruder in the seismo lab, I was lucky to spend time with Heather Crume, Kristina Okamoto, Ricky Garza Giron, Huiyun Guo, Em Schnorr, Litong Huang, Will Steindhart, Valere Lambert, and Julia Krog. One of my favorite memories is the two weekends we spent camping during the pandemic.

I am grateful to Roland Burgmann for welcoming me to the Active Tectonics group at UC Berkeley, where I have learned a lot over the past year. Thanks to Dani Lindsey (thanks for always getting coffee with me!), Curtis Baden, Isis Lemus, Yuankun Xu, and Yuaxin Li for the shared wisdom during group meetings.

I am incredibly lucky to have spent 2020-2022 as a resident of 214 Segre Pl, Santa Cruz. I am grateful to Colleen Murphy, Coby Abrahams, Calvin Munson, Zach Kauffmann, and Araceli Serrano for their friendship and company during the lock-down period. I am especially indebted to the ones that put up with Qualba for months, I am forever sorry y'all. Beyond Segre Pl, I am grateful for the incredible community of friends I made in Santa Cruz, and all the shared bike rides, bonfires, hikes, and bar adventures.

Gaby Noriega gave me an incredible opportunity when she allowed me to serve as a SCEC SOURCES mentor during the summer of 2021. With her trust and guidance, I have been lucky to mentor undergraduates

for the past three summers through the program. I am thankful to Mercedes Quintana, Vanessa Herrera, Sophia White, Ruth Prado, Tom Shea, Michael Hernandez, and Brian Castillo for their patience as I grew as a mentor. I have thoroughly enjoyed seeing them grow their ideas into research projects through our time together. I have also enjoyed working with UC Davis undergraduates Sofia Marino, Lupita Bravo, Kimberly Bowman, Leslie Garcia, and Karen Castañeda, through thesis and quarter-long research projects.

I have been lucky to do my PhD in a community that has openly shared code, data, and advice with me. The following is a (definitely non-exhaustive) list of people who have shared either one or several of those things with me over the years: Tom Rockwell, Irina Delusina, Drake Singleton, Ned Field, Kevin Milner, Ruth Harris, Chris Milliner, Glenn Biasi, Andreas Plesch, So Ozawa, Ramon Arrowsmith, Chelsea Scott, Rui Chen, Mark Petersen, Solene Antoine, George Hilley, Curtis Baden, Kang Wang, Xiaohua Xu, Craig Nicholson, Ed Nissen, Ryan Gold, Yehuda Ben-Zion, Jeremy Rimando, Vashan Wright, Sue Hough, Camilla Cattania, Rowena Lohman, Koji Okumura, Eileen Evans, Luca Malatesta, Jean-Arthur Olive, Michele Cooke, Bill Barnhart, Josie Nevitt, and John Naliboff.

The parts of this dissertation that are already published or in review have greatly benefited from comments from Julian Lozos, Kate Scharer, Robert Zinke, Chris Scholz, Alessandro Valentini, Steve Thompson, and at least three additional anonymous reviewers.

Research is powered by funding. I am grateful to the Southern California Earthquake Center for two years of financial support and five years of learning in an incredible intellectual and social community. Receiving a NASA FINESST fellowship allowed me to focus the last two years of my PhD solely on research. PG&E supported two quarters of my research and allowed me to venture into the world of hazard modeling. A UC Davis award for engineering a computer science funded one of my summers.

I am forever indebted to my parents, who have offered endless support to my career and life ambitions. Since very early on, they fed my curiosity for science and the outdoors with books, hikes, and trips. They have listened to endless practice talks in a language they do not understand, and picked up geology as a hobby to keep up with what I do. My grandpa Pepe did not receive a formal education past the age of 12 but continued to study alone at night for decades. His love of books and learning remain a big source of inspiration.

Last, but not least, I am indebted to Kelian Dascher-Cousineau, my partner in life and science. There are a lot less bugs in this thesis because of you. I think we make a pretty good team.

Acknowledgements for use of Copyrighted Materials

The text of this dissertation includes reprints of the following previously published material. The co-authors listed in these publications directed and supervised the research which forms the basis for the dissertation.

Chapter 2: Rodriguez Padilla, A. M., Oskin, M. E., Rockwell, T. K., Delusina, I., & Singleton, D. M. (2022). Joint earthquake ruptures of the San Andreas and San Jacinto faults, California, USA. Geology, 50(4), 387-391.

Chapter 3: Rodriguez Padilla, A. M., Oskin, M. E., Milliner, C. W., & Plesch, A. (2022). Accrual of widespread rock damage from the 2019 Ridgecrest earthquakes. Nature Geoscience, 15(3), 222-226.

Introduction

Plate tectonics sets the deformation budget that must be accommodated at plate boundaries. Rheology (the relationship of stress to permanent deformation or flow) controls the transfer of tectonically generated stress to faults. Below the seismogenic zone, crustal faults deform by distributed plastic flow in shear zones. Within the seismogenic zone, deformation occurs both by frictional slip on faults, and by distributed deformation of the surrounding rock volume. How these modes of deformation operate together constitutes a fundamental piece of the mechanics of deformation transfer and accommodation in the Earth's crust.

Earthquakes account for the majority of the stress release on fault systems by a combination of frictional slip on the fault, some energy dissipation in the form of heat and rock damage, and the radiation of seismic waves. Because faults are non-planar features with finite length, ruptures must often overcome zones of geometrical complexity along a fault, or even bridge the space between neighboring faults, for a sufficiently large area to slip for earthquakes to grow into moderate to large magnitude events (M_W>6). These zones of geometrical complexity are termed "Earthquake Gates". The effectiveness of an earthquake gate to allow ruptures to propagate through conditions the distribution of large events, and the related accommodation of stress, across a fault system.

Geometrical complexity on faults also forces slip gradients that result in deformation trade-offs with the surrounding volume driving a portion of the strain budget to be accommodated off-fault. Some of the deformation distributed off-fault is elastic and recoverable. However, a portion of the distributed deformation exceeds the yield stress of the rock mass, resulting in the creation of permanent deformation accommodated by a suite of mechanisms, including fracture, granular flow, warping, and block rotations. This inelastic deformation acts as a strain energy sink, increases compliance in the crustal volume around faults, locally amplifies seismic shaking in future earthquakes, and facilitates the creation of fluid pathways in the crust. Advances in geodesy have enabled detailed characterization of the partitioning of deformation between on and off-fault components during earthquakes, as well as establishing what portion of the coseismic deformation is permanent. In this introduction, I review recent advances in the understanding of the accommodation of strain in the upper crust, and outline the outstanding questions that drive the research in this dissertation.

Earthquake gates

Earthquake gates are regions of complexity on faults that can act as barriers to rupture propagation conditional on the fault geometry, rupture directivity effects, crustal properties, and prior stress history (e.g. Oskin et al., 2015; Prush, 2020). Zones of geometrical complexity along the surface traces of faults have long been recognized as earthquake gates from field observations (e.g. Segall and Pollard, 1980; Sibson, 1985; King

and Nabelek, 1985, Wesnousky, 2006; Biasi and Wesnousky, 2016; Biasi and Wesnousky, 2017)(Figure 1). Increasing resolution in geodetic and seismological observations has highlighted the importance of directivity effects and fault geometry at depth in rupture propagation and arrest (e.g. Cesca et al., 2017; Bao et al., 2019). These observations have informed dynamic rupture models, which enable testing the effects of crustal properties and different stress histories on earthquake gates over multiple earthquake cycles (e.g. Harris and Day, 1993; Oglesby, 2005; Duan and Oglesby, 2006; Ampuero and Ben-Zion, 2008; Lozos et al., 2011; Erickson and Day, 2016; Liu et al., 2022). Earthquake simulators sacrifice some of the complexity of dynamic rupture models to create large-scale spatial and temporal forecasts of events across a fault system to inform hazard assessment (e.g. Field, 2009; Richards-Dinger and Dieterich, 2012; Milner et al., 2022). The rapidly growing literature on earthquake gates largely follows two themes: pursuing a mechanistic understanding of rupture propagation through barriers and constraining the frequency of barrier-breaching events. In this section, I review fundamental and recent advances along both lines and highlight the outstanding questions that motivate chapters 1 and 2 of this dissertation.

Empirical constraints on earthquake gate behavior from surface rupture maps and displacements

The Borrego 1968 earthquake in California motivated the onset of exhaustive mapping of surface ruptures immediately after events to record perishable data. These observations, paired with a body of work in fault mechanics, reinforced the notion that zones of geometrical complexity on faults play a key role in modulating the extent of earthquake rupture (e.g. Sibson, 1985; King and Nabelek, 1985; Wesnousky, 1988). Pioneered by Wesnousky (2006), studies began to compile surface ruptures to systematically map step-overs, gaps, and bends along faults to estimate the frequency at which each of these earthquake gates are breached given their geometry (Figure 1).

From a compilation of 22 surface ruptures on strike-slip faults, Wesnousky (2006) found that $\sim$2/3 of the events ended at step-overs, and step-overs wider than 4 km were never observed to be breached. This result was verified with 15 additional rupture maps in Wesnousky (2008). A later survey considering 76 events of all faulting styles found that 90% of the rupture termini occurred at mapped discontinuities (Biasi and Wesnousky, 2016), and that dip-slip earthquakes could breach larger step-overs (up to 12 km) than strike-slip events (5 km). Within this dataset, step-overs wider than 4 km were breached only $<$8% of the time. Wesnousky (2006) noted that larger step-overs could be breached in releasing configurations while cautioning that the observational data to support this was biased by the much larger number of releasing features mapped.

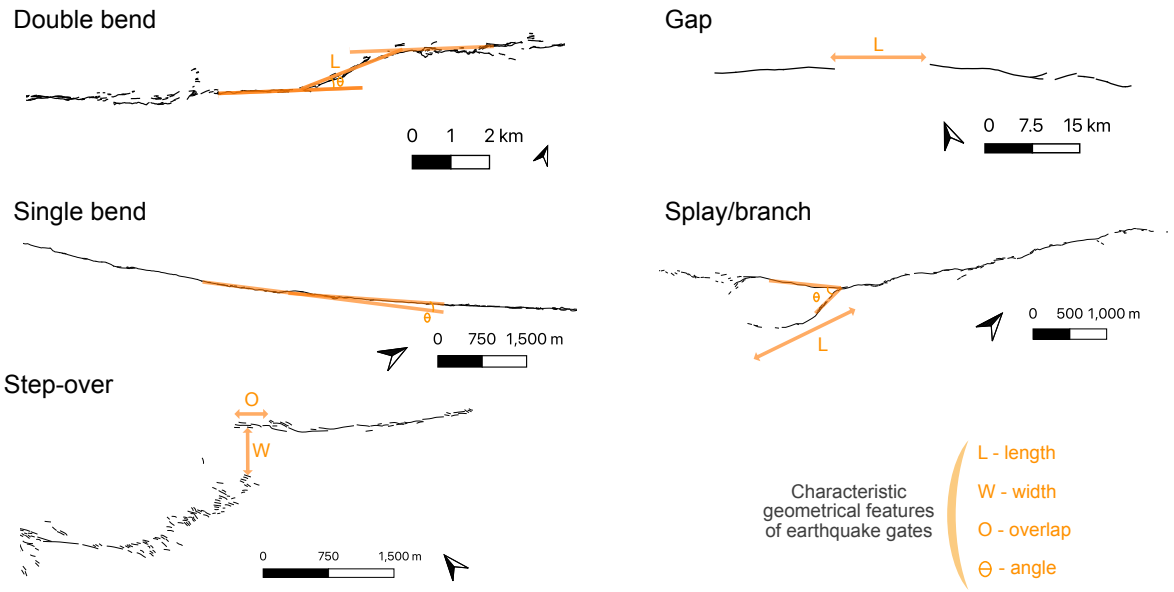

Figure 1: Types of earthquake gates and geometrical features characterized for each of them. Examples of breached earthquake gates from the FDHI surface rupture database (Sarmiento et al., 2021). The single and double bends are from the 2013 Balochistan earthquake in Pakistan. The gap is from the 2010 Yushu earthquake in China, the splay is from the 1995 Kobe event in Japan, and the step-over is from the 1968 Borrego earthquake in California.

Investigations of the frequency at which earthquake gates are breached given their geometry have been supplemented by empirical work tackling the mechanics of rupture propagation through step-overs from field observations. Elliott et al. (2009) found that ruptures that breached step-overs had steeper slip tapers as they approached the earthquake gate than those that did not propagate past the step-over. They asserted that rupture dynamics exert the first-order control on whether a step-over is breached, as rapidly halting (losing slip) ruptures generate strong seismic waves propagating ahead of the rupture front and assist in rupture re-nucleation on the adjacent segment.

King and Nabelek (1985) used surface rupture maps from eight events to show that earthquake ruptures were often confined to straight segments limited by large fault bends, positing that the bends acted as barriers to rupture propagation. Biasi and Wesnousky (2017) mapped bends from 67 historical rupture maps and found that the probability of breaching a bend >25° was less than half. They also noted that, for strike-slip faults, bends on rupture termini were larger than interior bends along the rupture, while on dip slip faults these are of similar size. Extending their empirical work to gain a mechanical understanding of bends, they asserted that the interior angles breached could be explained by changes in the frictional resistance within the bend under the assumption of a constant regional stress field.

Since the publication of the most recent empirically estimated passing probabilities (Biasi and Wesnousky, 2016; Biasi and Wesnousky, 2017; applied to hazard model development in Biasi and Wesnousky, 2021), there have been additional surface rupturing earthquakes involving several faults and rupture through earthquake gates (e.g. Huang and Huang, 2018; Ross et al., 2019; Chen et al., 2022). Concurrently, there has been an ongoing effort to compile and standardize past surface rupture maps and displacement measurements in public databases (e.g. Sarmiento et al., 2021; Nurminen et al., 2022). These efforts homogenize past data and contribute new information to update the passing probabilities of earthquake gates and revisit whether there is a limiting earthquake gate size for rupture propagation. This exercise is part of the foci of Chapter 1 of this dissertation.

Empirical constraints from paleoseismology and geochronology

Knowledge of the long-term behavior of a particular earthquake gate from the geologic record requires constraints on the frequency and characteristics of confined and multi-fault events across an earthquake gate. Two approaches have been followed, and both require a strong chronological record across the target earthquake gate. The first method is to estimate fault slip rates at different locations on each side of the earthquake gate, where decreases in slip rate are interpreted as a lower frequency of events, indicative of a conditional barrier (e.g. Yule et al., 2009; Elliott et al., 2018; Shao et al., 2018; Prush, 2020). The second approach is to compare the timing of discrete events, and their frequencies, from paleoseismic sites across an earthquake gate (e.g. Yuan et al., 2018; Scharer and Yule, 2020; Howarth et al., 2021).

Because both methods require extensive chronological records, they are currently limited to a few continental fault systems, including the San Andreas and the San Jacinto faults in southern California (San Gorgonio and Cajon Pass)(Yule et al., 2014; Onderdonk et al., 2018; Scharer and Yule, 2020; Blisniuk et al., 2021), the Altyn Tagh (e.g. Elliott et all., 2015; Eliott et al., 2018; Shao et al., 2018; Yuan et al., 2018; Prush, 2020) and the Kunlun (Kirby et al., 2007; Gold and Cowgill, 2011) faults in the Tibetan Plateau, the North Anatolian Fault in Turkey (Fraser et al., 2010; Uavsar et al., 2014), the Wasatch Fault in Utah (DuRoss et al., 2016; Bennett et al., 2018), the Fucino Fault System in the Apennines (Galli et al., 2019; Cinti et al., 2021), and the Alpine Fault in New Zealand (Howarth et al., 2021).

After success in improving the understanding of the frequency and mechanics of multi-fault events in the Ventura Basin and rupture propagation past the San Gorgonio structural knot, the Cajon Pass releasing step-over became the next target earthquake gate for study in southern California. This focus was motivated by the hazard San Andreas-San Jacinto joint ruptures pose to major infrastructure and lives in the densely populated LA Basin. The Mojave and San Bernadino strands of the San Andreas fault have well-established event chronologies from several paleoseismic sites (Seitz et al., 1997; Biasi et al., 2002; McGill et al., 2002;

Fumal et al., 2002; Scharer et al., 2010). The paleoseismic record for the northern San Jacinto fault is limited, though an excellent chronology exists for the Mystic Lake site (Onderdonk et al., 2013; Onderdonk et al., 2018). Nevertheless, there have been efforts to compare chronologies across the step-over and consider the frequency of multi-fault events (Onderdonk et al., 2018; Scharer and Yule, 2020).

Dynamic rupture models show that multi-fault earthquakes through Cajon Pass are possible (Anderson et al., 2003; Lozos, 2016; Liu et al., 2022), where Lozos (2016) proposed that the 1812 historical earthquake is the most recent multi-fault event to have breached this earthquake gate. Yet, direct geologic evidence of the 1812 event at Cajon Pass, or any past earthquakes, was lacking due to the geomorphic setting of the northern San Jacinto fault, which precludes paleoseismic trenches from being dug across the fault, so the closest trench to Cajon Pass is the Colton site (Kendrick and Fumal, 2005), 30 kilometers south of the Pass.

In chapter 2 of this dissertation, I establish a frequency of joint San Andreas-San Jacinto fault ruptures through Cajon Pass by developing a chronology of events on the Lytle Creek Ridge Fault, a "passenger fault" sitting in the San Gabriel Mountains, inside Cajon Pass, which we hypothesize slips in response to simultaneous large slip on the San Andreas and the San Jacinto faults. I supplement this chronology by comparing finite element models of triggered slip on the Lytle Creek Ridge Fault to paleoseismic measurements of slip from the trench. This work sheds light on the frequency of shared events between the San Andreas and the San Jacinto faults, including the most recent multi-fault event, as well as the mechanics of gate-breaching earthquakes through this barrier.

Multi-fault events in large-scale earthquake simulators

Because multi-fault earthquakes produce larger magnitude events than those confined to a single fault, leading to longer surface rupture and more sustained ground motions, they have long been a focus area for probabilistic seismic hazard assessment. Large-scale earthquake simulators prescribe a set of physics to a fault system to generate long-term forecasts of the timing and extent of ruptures across the system (e.g. Field et al., 2009; Richards-Dinger and Dieterich, 2012; Field et al., 2014; Page, 2021; Milner et al., 2022). In these simulators, faults are allowed to interact and host multi-fault events when certain rules are met. Some of these simulators rely on a combination of empirical data and dynamic rupture models to inform the physics of multi-fault events (e.g. Field et al., 2014), whereas others rely only on physics-based modeling to determine fault interactions (e.g. Richards-Dinger and Dieterich, 2012; Milner et al., 2022). To first order, these simulators produce event frequencies comparable to those in the paleoseismic record for the few earthquake gates where a long-term paleoseismic history has been established (Scharer and Yule, 2020; Howarth et al., 2021).

Insights from empirically-informed models of specific earthquakes

Increasingly denser and higher-resolution geodetic and seismological observations have revealed that most moderate-sized ($> M_w$ 6) events in continental settings involve more than one fault segment (e.g. Allen et al., 1968; Hudnut et al., 1989; Sieh et al., 1993; Oskin et al., 2012; Hamling et al., 2017; Ross et al., 2019; Okuwaki et al., 2023). This rapidly growing observational record, concurrent with increasingly sophisticated numerical models enabled by computational advances, has led to detailed investigations on the mechanical conditions that allowed specific earthquake gates within those events to be breached (e.g. Fletcher et al., 2016; Hemling et al., 2016; Ross et al., 2019; Taufiqurrahman et al., 2023) or not (Klinger et al., 2006). This line of inquiry typically focuses on explaining the peculiarities of rupture propagation during the target event: for example, rupture transfer from the Denali to the Totschunda fault in the 2004 event (Bhat et al., 2004), large rupture jumps and cascading kinematics of the 2016 Kaikoura earthquake (Lamb et al., 2018; Shi et al., 2019), the triggering of cross-faults during the Ridgecrest mainshock-foreshock pair (Barnhart et al., 2019, Taufiqurrahman et al., 2023), or the rupture initiation dynamics on a keystone fault during the El Mayor-Cucapah earthquake (Fletcher et al., 2016). Because of the focus on individual earthquake gates and events, these models often employ complex fault representations, rheologies, and stress states.

Insights from parametric dynamic rupture models

Dynamic rupture models offer the opportunity to examine the role of different earthquake gates in the physics of rupture propagation and arrest. The magnitude and distribution of stress on a fault system before an earthquake have long been recognized to exert a first-order control on the behavior of the incoming rupture as it propagates on the fault system (Day, 1982; Harris, 2004; Lambert et al., 2021). Minor changes in the regional stress orientation can cause fundamental changes in the behavior of ruptures across barriers (e.g. Kame et al., 2003; Lozos et al., 2011). Over multiple earthquake cycles, stress can accumulate at barriers as consecutive ruptures fail to breach the earthquake gate, promoting throughgoing rupture in subsequent events (e.g. Duan and Oglesby, 2006; Liu et al., 2022)(Figure 2).

Dynamic rupture models consistently find that step-overs wider than a few kilometers cannot be breached (Segall and Pollard, 1980; Harris et al., 1991; Harris and Day, 1999; Kase and Kuge, 2001; Harris et al., 2002; Hu et al., 2016). Harris and Day (1993) found that dynamic rupture was possible through restraining and releasing step-overs a few kilometers wide, where wider releasing step-overs could be breached, a result validated by subsequent studies. Oglesby (2008) investigated the effect of slip tapers on whether a step-over was breached or not during dynamic rupture, finding that steeper tapers foster breaching by the resulting static stress field and the creation of strong stopping phases from the deceleration of the rupture through

the taper.

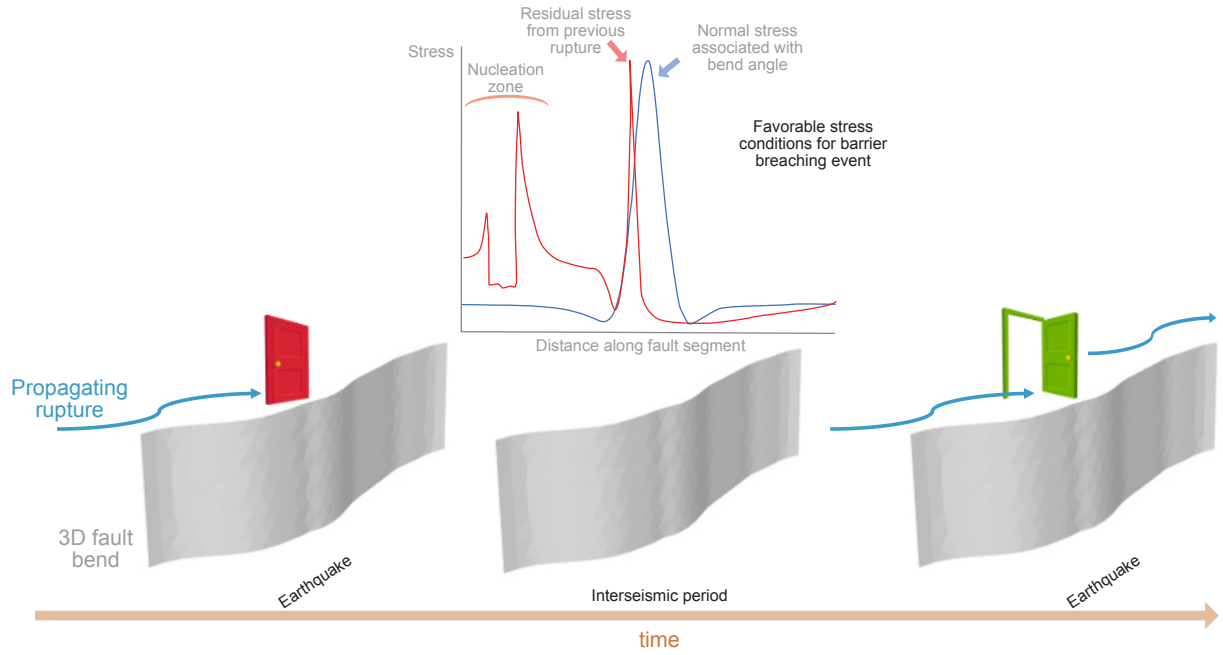

Figure 2: Cartoon illustrating the effect of residual stresses in promoting rupture propagation in subsequent events at earthquake gates. The stress plots are based on Figure 7 in Ozawa et al. (2023).

Magistrale and Day (1999) and Oglesby (2005) showed that step-overs hard-linked by dip-slip faults were more easily breached than those step-overs that were not, a result Lozos et al. (2011) validated for step-overs hard-linked by strike-slip faults (i.e., double bends). Lozos et al. (2011) found that releasing double bends were more easily breached than restraining double bends, where bends with angles $<18°$ and $<34°$ were always breached for restraining and releasing bends respectively. However, small rotations ($10°$) in the homogeneous regional stress field prescribed in the model could cause this result to flip. Lozos et al. (2011) also showed that bends with lengths (length of the segment with a different strike) of 500 meters were always breached, regardless of angle, though only angles up to $45°$ were tested. For lengths exceeding 1 km, whether a bend was breached was conditioned by a trade off between bend length and angle, with smaller lengths allowing steeper angles to be breached.

Kame et al. (2003), following up on the work of Poliakov et al. (2002), found that infinite, extensional branches (i.e., splay faults) were preferred over compressional ones in dynamic rupture simulations, though this behavior flipped as the angle between the maximum compressive regional stress and the strike of the fault decreased. They also found that activation of both branches past a junction was favored for wide splay angles but hindered by stress interactions between the branches when the splay angle is small, an effect that can be overcome by fast propagating rupture speeds. Bhat et al. (2007) revisited the case of

dynamic rupture past a fault splay for a finite branch, finding that the branch length was also an important parameter in determining whether a splay would be breached, though not deterministic without knowledge of the kinematics of the splay and dynamic rupture effects. Lozos (2022) tested the case of orthogonal splays for faults with opposite senses of motion, inspired by the Ridgecrest 2019 earthquakes. He found that, when both cross faults had uniform initial tractions, the slip distribution on the first fault had to cause a normal stress reduction on the second fault for it to rupture. The cross fault could also be triggered if the first fault ends at the junction, promoted by a stopping phase in the rupture dynamics.

Dynamic rupture models also enable testing the effects of the host material on rupture propagation past earthquake gates. Finzi and Langer (2012) tested the effect of bulk inelasticity in step-over breaching, finding the presence of off-fault damage in the step-over helped promote rupture propagation past the barrier. A problem that has gathered a lot of attention is the effect of bimaterial interfaces across mature strike-slip faults, which juxtapose different lithologies as they accumulate displacement. Most work suggests that these lithological contrasts, translated into differences in elastic properties across the fault, can play a fundamental role in the direction of rupture propagation, fostering propagation in the direction of slip of the more compliant side of the fault (Ampuero and Ben-Zion, 2008; Dor et al., 2008; Langer et al., 2015; Share and Ben-Zion, 2018), though other work finds no strong direction predictability in the presence of a bimaterial interface (Harris and Day, 2005).

Off-fault deformation

Off-fault deformation (the deformation distributed in the surrounding medium of a fault rather than localized on the fault plane) is a ubiquitous feature of crustal deformation, recognized in numerous faulting regimes, for example, fault-bend folding above thrust faults, warping of markers adjacent to strike-slip faults, and flexural bending of the footwall of normal faults (e.g. Figure 3). The realization that off-fault deformation accounts for a portion of the deformation during earthquakes and contributes to the long-term build up of topography dates back to the early 20^{th} century from field observations. Since that time, our view of off-fault deformation has been revolutionized with the advent of radar and high-resolution satellite imagery and topography.

Advances in the resolution and availability of geodetic data and the capabilities of numerical models have propelled investigations of off-fault deformation spanning a wide range of spatial and temporal scales. These studies have revealed a wide spectrum of deformation styles and processes contributing to off-fault deformation, and how these relate to lithology, fault slip magnitude and variability, rupture depth, and rupture propagation velocity. This emerging body of work has helped clarify some long-standing questions in

earthquake science, such as the persisting discrepancies between geologic and geodetic slip rates, the origin of the shallow slip deficit, or the partitioning of strain between elastic and inelastic processes during earthquakes. In this section, I review the origins and significance of off-fault deformation, discuss measurements of the amount and style of off-fault deformation compiled across different spatial and temporal scales, and consider the different mechanisms involved in the creation and evolution of distributed deformation adjacent to faults. I conclude by outlining some of the outstanding challenges that motivate chapters 3, 4, and 5 of this dissertation.

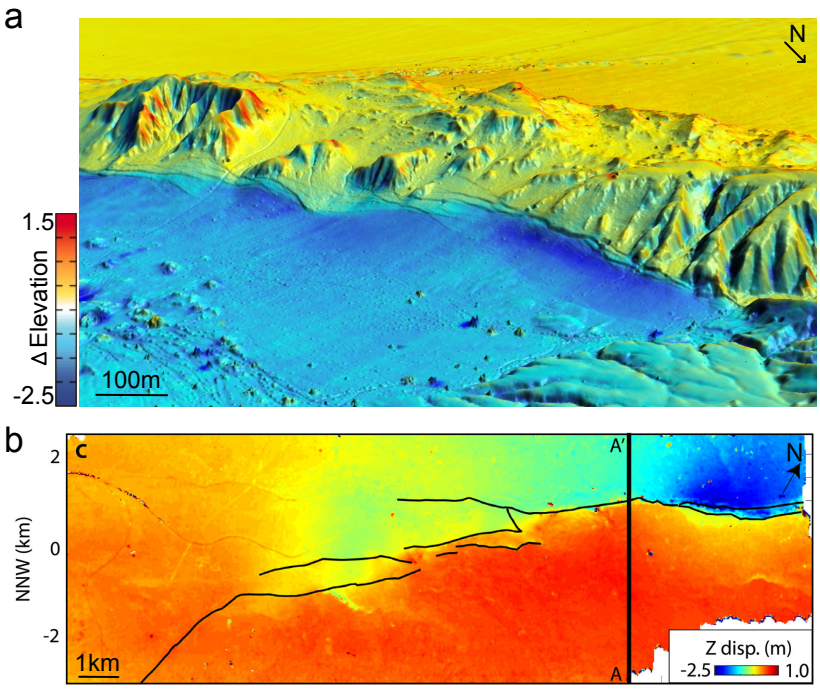

Figure 3: a) Vertical coseismic displacements from differential lidar topography of the El Paso Superior Normal Fault that ruptured in the El Mayor Cucapah earthquake. b) Vertical coseismic displacements from differential lidar topography of the strike-slip Kumamoto earthquake (after Scott et al. (2018), refer to paper for cross-section).

Observations of off-fault deformation along strike-slip faults: damage zones

Deformation across a fault zone is typically distributed as a combination of slip along discrete fault planes and off-fault deformation resulting from a variety of processes. The majority of the off-fault deformation adjacent to faults is accommodated within damage zones, which can be approximated as tabular volumes of fractured and warped rock that extend ~100 m to 1 km perpendicular to the main fault trace (Chester and Logan, 1986; Kim et al., 2004). Within the damage zone, fracture and aftershock density decay with distance away from the fault plane until they reach a background level (Chester et al., 2005; Mitchell and Faulkner,

2009; Savage and Brodsky, 2011; Powers and Jordan, 2010; Perrin et al., 2021; Alongi et al., 2022). Damage zones are also geodetically measurable as zones of reduced shear rigidity inferred from stress-change-induced displacements (Fialko et al., 2002; Fialko, 2004; Xu et al., 2020; Xu et al., 2023), and from decreases in shear wave velocities (Li et al., 1998; Cochran et al., 2009; Ben-Zion et al., 2015; Qiu et al., 2021). More recently, for directly imaged earthquakes, damage zones have been characterized as the area where shear or volumetric strains exceed the elastic strength of the material (Scott et al., 2018; Barnhart et al., 2020; Milliner et al., 2021).

Fault damage zones are characterized by lower elastic moduli and seismic velocities compared to the host lithology (Li et al., 2004). These different material properties reflect the cumulative effect of past large earthquakes (Dor et al., 2006; Ben-Zion and Ampuero, 2009), and influence rupture propagation (Harris and Day, 1997; Huang et al., 2014), ground shaking amplification (Wu et al., 2009; Kurzon et al., 2014), and seismic wave attenuation in subsequent events. The low-velocity structure associated with the damage zone can be readily measured through waves excited by seismicity or explosions (Ben-Zion, 1998; Mooney and Ginzburg, 1986; Li and Leary, 1990). These low-velocity zones can act as a waveguide, resulting in waves getting trapped by the constructive interference of reflected phases (Ben-Zion and Aki, 1990). These trap zones can span a small portion of the wider low-velocity zone or constitute the bulk of it (e.g. Qiu et al., 2021). Determination of the extent of low-velocity zones is sensitive to the aperture of the measuring seismic array (Yang et al., 2014) and timing within the earthquake cycle (Cochran et al., 2009; Lu and Ben-Zion, 2021).

Beyond the imaging of a localized damage zones, studies have shown that earthquakes can be followed by subtle ($\sim$1-5%) regional drops in seismic velocities up to distances >100 km away from the causative faults (Peng and Ben-Zion, 2006; Nakata and Snieder, 2012; Lu and Ben-Zion, 2021). These velocity drops are interpreted to represent changes in the properties of the shallow crust (0-3 km depth) caused by fracture opening/closing or fluid mobilization in response to the passage of seismic waves from the earthquake. These regional drops are largely recovered in the days following the earthquake, suggesting rapid postseismic healing (Lu and Ben-Zion, 2021).

Geodetically, damage zones have been characterized as areas of reduced shear rigidity inferred from SAR displacements and phase gradient maps (Fialko et al., 2002; Fialko, 2004; Cochran et al., 2009; Xu et al., 2020). These zones have been mapped as areas that experience distributed motion due to strain localization on a compliant fault zone after an increase or decrease in stress following an earthquake (Fialko et al., 2002; Fialko, 2004; Xu et al., 2020; Xu et al., 2023). This strain localization is the result of the contrast between the lower rigidity of the compliant zone and the higher rigidity of the host rock. The width of these compliant zones is variable, ranging from a few hundred meters to less than 3 kilometers (Fialko et al., 2002; Fialko,

2004; Xu et al., 2020; Xu et al., 2023). Measurements of the shear modulus contrast between the compliant zone and the host rock vary, with some compliant zones having as little as a few percent decreased rigidity and others being up to 90% less rigid than the surrounding rock (Fialko et al., 2002; Xu et al., 2020; Xu et al., 2023). Typically, moduli reductions measured seismologically do not exceed ∼30% whereas geodetically estimated values, more sensitive to shallow depths, can greatly exceed that threshold (up to 90% reductions, Xu et al., 2020, 2023).

For directly imaged earthquake ruptures from differential topography and cross-correlated satellite imagery, studies characterize the damage zone as the zone surrounding the fault where strains exceed the elastic limit of rock. This strain threshold was measured by Michel and Avouac (2006) to be $\sim 3 \text{x} 10^{-3}$ based on deformation features from the Landers earthquake. This type of characterization typically reveals a much narrower damage zone than low velocity zones, with inelastic deformation extending only 30-250 meters from the fault hosting the mainshock (Scott et al., 2018; Barnhart et al., 2020; Milliner et al., 2021). Approaches to quantifying near-field distributed strain differ by study, with workers choosing to focus on different strain components (shear and normal), and the use of infinitesimal versus finite strain. Differences in the methodology used to measure strain for an individual event result in small variations in the extent of inelastic deformation mapped but, nevertheless, these studies tend to estimate the extent of the coseismic inelastic deformation zone within 10s of meters of each other's estimates and never extending beyond 300 m from the fault.

Deformation within the damage zone occurs on a range of scales from micro-fracturing and grain comminution of the rock mass to macroscopic fracture networks, secondary faulting, veins, deformation bands, and folds. At the mesoscale, damage zones have been extensively described from field observations (Chester and Logan, 1986; Chester et al., 1993; Caine et al., 1996; Cello et al., 2001; Faulkner et al., 2003; Flodin and Aydin, 2004; Chester et al., 2005; Mitchell and Faulkner, 2009; Savage and Brodsky, 2011). Typically, field studies report a high-strain fault core, or network of anastomosing fault cores centered at the principal slip surface, surrounded by a halo of lower-intensity, distributed damage (e.g., Faulkner et al., 2003).

Numerous studies have quantitatively described the decay in damage intensity with distance away from the fault. Chester et al. (2005) proposed a logarithmic fit to the decay in fracture and microfracture density with distance away from the Punchbowl fault in California. Mitchell and Faulkner (2009) fit an exponential function to the decay of micro and macro fracture density with distance away from faults in the Atacama Desert, a functional form supported by later work (e.g. Alongi et al., 2022). Other workers instead favor a power-law decay in fracture density with distance away from the fault (Savage and Brodsky, 2011; Johri et al., 2014; Ostermeijer et al, 2020). In general, these studies agree that damage zones are characterized by a relatively sharp fall-off of damage intensity in the near-field of the fault.

Aftershocks represent a subset of the fracture population within the damage zone (i.e., shear fracture) at depth. As a result, fault damage zones appear as zones of enhanced seismicity between the fault core and the host rock. Several studies have used earthquake catalogs to determine the size and characteristics of fault damage zones, based on the decay in seismicity with distance from a fault (Powers and Jordan, 2010; Hauksson, 2010; Perrin et al., 2021). In these studies, the decay of seismicity with distance away from the fault is characterized by a plateau of constant earthquake density, followed by a zone where earthquake density decreases as an inverse power law, ending in a zone where the decay meets the background seismicity of the region. Powers and Jordan (2010) argued that the width of the plateau is a function of the number and density of fault cores present (e.g. Faulkner et al., 2003). Perrin et al. (2021) argued that the plateau in earthquake density is representative of a dilatant damage zone and the zone with power law decay represents a shear deformation zone, where volumetric and shear strains dominate respectively. In chapter 3, I combine rupture maps, aftershock catalogs, and geodetic maps from the Ridgecrest 2019 earthquakes in southern California. The combination of datasets allows characterization of the damage zone in detail and across different spatial scales and to assess sensitivity to fault slip, lithology and data resolution. As part of this exercise, I revisit the hypotheses of Perrin et al. (2021) and Powers and Jordan (2010) regarding the inner damage zone.

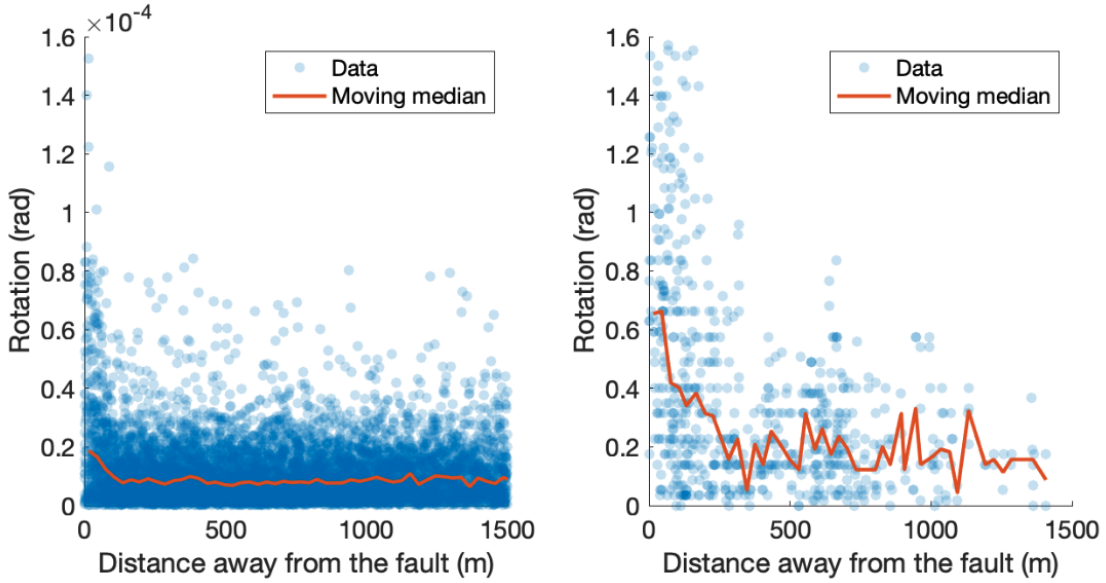

Figure 4: Infinitesimal and cumulative rotations with distance away from the fault. Left: Infinitesimal rotations from the Ridgecrest earthquakes (Milliner et al., 2016). Right: Cumulative rotations along the Harper Lake fault in the Eastern California Shear Zone (Shelef and Oskin, 2010). The moving window spans thirty points.

Rigid block rotations account for a component of the off-fault strain associated with faulting. Nissen et

al. (2012) measured infinitesimal rotations associated with the Idosawa earthquake using differential lidar. Using optical image-correlation, Milliner et al. (2021) measured finite rotations from vorticity (rigid-body rotation) within the damage zone of the Ridgecrest earthquake surface rupture. Both studies show that large rotations are typically confined to <30 m away from the fault, with rotations becoming too small to discern from noise at ∼100 m away from the fault. In the long-term, large rotational strains are accommodated via brittle deformation, where one rotational component may be directly measured when offset markers or paleomagnetic data are available (Shelef and Oskin, 2010; Titus et al., 2011; Titus et al., 2018). These finite rotations are sufficiently large to be measured up to kilometers away from the fault (Shelef and Oskin, 2010). While rotations are sensitive to lithology and transitions in fault frictional behavior (Titus et al., 2011), in general, the magnitude of rotations systematically decreases with distance from the fault. Coseismic and finite rotations exhibit very similar spatial distributions (Figure 4).

Observations of off-fault deformation along normal faults: folding

Folding, the dominant observable form of off-fault deformation in extensional settings, occurs in association with normal faults over a large range of spatial scales (e.g. Schilsche, 1995; Janecke et al., 1998; Sharp et al., 2000; Grasemann et al., 2005; Okamura et al., 2007; Kane et al., 2010; Ferrill et al., 2012; Brandes and Tanner, 2014). Generally, folding adjacent to normal faults forms and evolves in response to three fundamental features: slip on the fault plane (Wheeler, 1939; Hambling, 1965; Harding, 1984), the growth and propagation of the fault (Gawthorpe et al., 1997; Sharp et al., 2000; Willsey et al., 2002; Ferrill et al., 2007; Kane et al., 2010; Coleman et al., 2019), and displacement variability along strike, often related to fault segmentation (Janecke et al., 1998; Ferrill and Morris, 2008). Thus, folds are temporally and geometrically tied to faulting.

Folds in extensional settings have received ample attention because of their ability to trap hydrocarbons of economic importance (e.g. Ferrill et al., 2007; Tavani et al., 2018), prompting the collection of field and 3D seismic observations to study them. Most of these observations come from locations with dense normal faulting from rifting (Withjack et al., 1988; Gawthorpe et al., 1997; Sharp et al., 2000; Peacock and Parfitt, 2002; Khalil and McClay, 2017) and they reveal fault-propagation folding occurs over a wide range of wavelengths from meters to tens of kilometers (e.g. John, 1987; Coleman et al., 2019). Fault propagation folds, sometimes referred to as drag folds, form as the result of distributed warping of the surrounding volume ahead of a propagating fault tip (e.g. Withjack et al., 1990; Gawthorpe et al., 1997; Sharp et al., 2000; Cornfield and Sharp, 2002; Grant and Kattenhorn, 2004; White and Crider, 2006; Khalil et al., 2020). Folds develop ahead of blind fault tips both vertically and laterally (White and Crider, 2006; Kaven and Martel, 2006; Kaven and Martel, 2007; Villemin and Bergerat, 2013)(Figure 5).

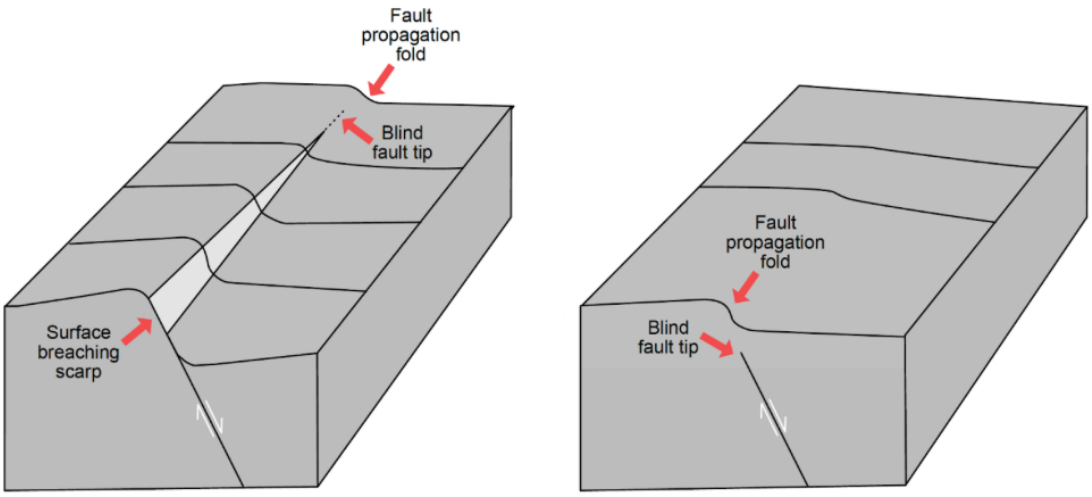

Figure 5: Fault propagation folds in extensional settings. Left: Folding ahead of the laterally-propagating fault. Right: Folding ahead of the vertically propagating fault. Modified after White and Crider (2006).

As slip accumulates on the propagating fault, the geometry and size of the folds evolve in response. Fault throw is the primary control on folding amplitude, where amplitude scales with increasing throw (e.g. Cornfield and Sharp, 2000; Coleman et al., 2019). Wavelength also scales with fault throw (Cornfield and Sharp, 2000; Conneally et al., 2017). Where propagating fault tips are buried by sediment, the thickness of the cover exerts the predominant control on folding wavelength, where thicker cover promotes longer wavelength folding (Coleman et al., 2019). Cover rheology appears to exert a secondary control in determining fold shape and size, where softer covers foster the development of folding (higher amplitude and wavelength) as they inhibit fault propagation (Hardy and Finch, 2007; Cardozo et al., 2011; Coleman et al., 2019). Fault dip exerts a primary role in determining folding wavelength, where gentler dips promote longer-wavelength folds (e.g. Withjack et al., 1990). Fault dip also influences the degree of asymmetry of the fold, where hanging wall subsidence decreases with increasing dip (White and Crider, 2006). In addition, the distribution of slip, and the degree to which the fault is blind also influence the overall folding shape (White and Crider, 2006; Kaven and Martel, 2006). For faults in bedrock, the elastic properties of the material play a large role in folding shape, though different elastic properties and geometry combinations can lead to the same folding shapes, so these controls are non-unique (e.g. White and Crider, 2006).

Folding along normal faults is recognized both as a coseismic deformation feature and a long-term deformation feature. Oskin et al. (2012) showed from differential lidar of the El Mayor-Cucapah earthquake that even within a single event, the folding strains at fault tips approach the elastic failure limit. To understand the evolution of finite folding with fault propagation (incremental slip), Kaven and Martel (2007) compared an elastic model of normal fault propagation to observed faults on the flanks of Kilauea volcano, Hawaii. In

their elastic model, a monocline develops until the fault breaches the surface and generates a scarp. After surfacing, the deformation accommodated by the monocline is recovered. However, the authors noted in their field measurements that, unlike in the models, the monoclines remained as permanent deformation after surface breaching. Their study did not incorporate a failure criterion, and therefore the modeled folding strains were much larger than can be sustained by rocks. White and Crider (2006) used elastic modeling to reproduce fold geometries at propagating normal-fault tips within the Modoc Plateau of northeast California. They hypothesize that elastically generated folding becomes permanent by slip on joint planes and other fractures within the rock mass. How coseismic strain near the elastic limit such as that observed in Oskin et al. (2012) is accrued in the landscape constitutes the focus of chapter 5 in this dissertation, where we test White and Crider (2006)'s hypothesis.

Folding can promote inelastic deformation in response to bending strains. In particular, the relationship between folding and secondary fracturing has long been a focus of study because of its importance in groundwater and hydrocarbon flow through reservoirs (e.g. Odling et al., 1999; Bergbauer and Pollard, 2004; Cipolla et al., 2008). Stearns (1968) developed a classification of five kinds of fold-related fracture comprising eleven joint orientations. Within each of these five subgroups, there are two conjugate shear sets and one tensile, so that each group includes three joint orientations. While fractures are often found in orientation and mode in agreement with the Stearns (1968) classification, many workers have also reported disagreements with this model, including a random distribution of joints throughout a folded region (McQuillan, 1973), or evidence of fracture that both pre- and postdates folding (Twiss and Moores, 1992). When tectonic fractures predate the folding, these joints may accommodate much of the folding strain, minimizing or even completely inhibiting the nucleation of joints contemporary with folding (e.g Bergbauer and Pollard, 2004; Ferrill et al., 2016). Joint orientations will also change as a fold propagates, where beds that fracture early in the fold history can preserve joint patterns that are inconsistent with the maximum bending stress from the modern geometry of the fold (Savage et al., 2010).

Controls on slip partitioning between on and off-fault components

The advent of topographic and image differencing in the past decade have enabled detailed characterization of the amount of distributed deformation of surface rupturing events, and established the factors that control the partitioning of strain between the strain localized on the fault and the strain distributed in the volume.

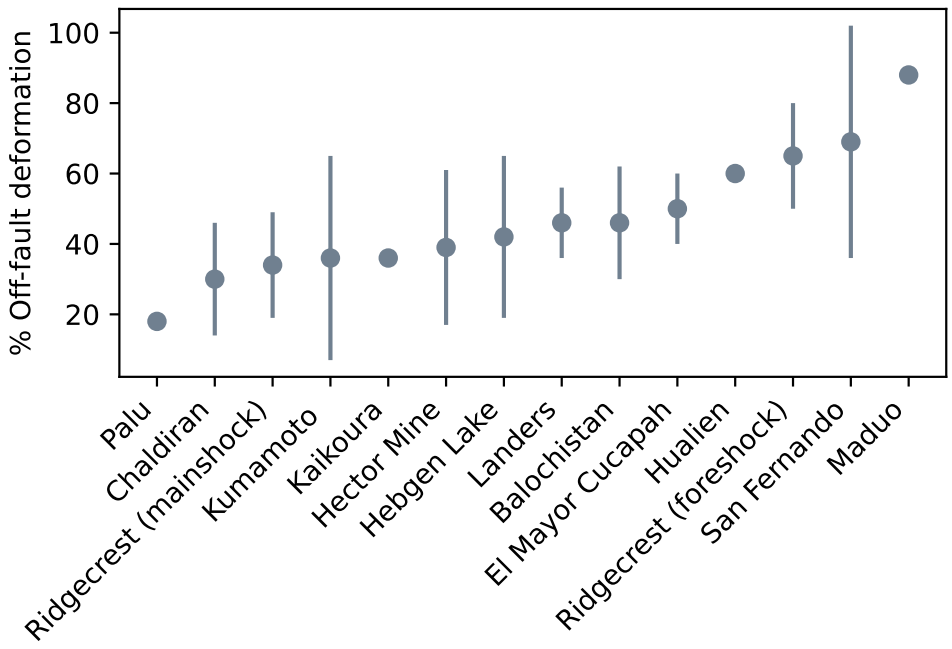

Figure 6: Percentage of surficial, coseismic off-fault deformation calculated from image correlation and field data. The references for each event are available in Table 1. Error bars represent the varibility in the preferred off-fault deformation value as reported by the original studies.

The total amount of coseismic off-fault deformation is sensitive to natural variability related to rupture segmentation (Milliner et al., 2015; Milliner et al., 2016) and mechanical properties (Zinke et al., 2014; Milliner et al., 2016; Scott et al., 2018; Soquet et al., 2019). Method aperture and differences in the definition of off-fault deformation also influence the portion of off-fault deformation measured (Zinke et al., 2019; Scott et al., 2018; Soquet et al., 2019). Thus, different sectors of the same surface rupture are likely to exhibit variability in the amount and style of off-fault deformation as these controlling parameters vary (e.g. Soquet et al., 2019). Nevertheless, off-fault deformation takes up, on average, over 30% of the total surface deformation for most events imaged, with along-rupture variability for a single event standing between 5-40% (Figure 6). Field measurements of off-fault deformation precede their geodetic counterparts by decades (Reid, 1910) but are seldom continuous. With off-fault deformation extending kilometers away from the fault (e.g. Xu et al., 2020; Antoine et al., 2021), complete mapping of off-fault deformation in the field becomes a labor-intensive task. Nevertheless, Zinke et al. (2019) found that field measurements within 100 m in aperture captured nearly ∼90% of the total surface deformation for the Kaikoura earthquake, despite ∼36% of it being distributed off-fault. They did so by comparing measurements from the field with geodetic constraints on the extent of on versus off-fault deformation.

Table 1: Percentage of surficial, coseismic off-fault deformation calculated from image correlation and field data.

Year	Event	Off-fault deformation (%)	Variability (± %)	Reference
2018	Kumamoto	36	29.0	Scott et al., 2018
1992	Landers	46	10.0	Milliner et al., 2016
1999	Hector Mine	39	22.0	Milliner et al., 2016
2013	Balochistan	46	16.0	Zinke et al., 2014
2016	Kaikoura	36	-	Zinke et al., 2019
2019	Ridgecrest (foreshock)	65	15.0	Milliner et al., 2021
2019	Ridgecrest (mainshock)	34	15.0	Milliner et al., 2021
2018	Palu	18	-	Soquet et al., 2019
2010	El Mayor Cucapah	50	10.0	Teran et a., 2015
2020	Maduo	88	-	Li et al., 2022
1971	San Fernando	69	33.0	Gaudreau et al. 2023
2018	Hualien	60	-	Kuo et al. 2019
1959	Hebgen Lake	42	23.0	Andreuttiova et al., 2023
1976	Chaldiran	30	16.0	Lu and Zhou, 2023

The effect of lithology in modulating the distribution and style of off-fault deformation has been subject to extended debate, with some workers arguing for primary controls of lithology in off-fault deformation patterns while others finding no correlation. Milliner et al. (2016) investigated the relationship between off-fault deformation percentage and lithology for the Landers and Hector Mine earthquakes. They found that distributed deformation was larger for areas in sediment and where the rupture was more geometrically complex. Zinke et al. (2014) found significantly more off-fault deformation in thicker and younger sediments along the Balochistan surface rupture than in bedrock. Titus et al. (2011) found that weak lithologies (e.g., serpentine) adjacent to the creeping central San Andreas fault were more heavily deformed and accommodate more off-fault deformation than stronger lithologies in the same area. Similar patterns have been noted along other faults, where rupture localization and distribution exhibits a strong lithological dependence, drastically changing when crossing contacts between units (e.g. Aben et al., 2017; Livio et al., 2020).

Observations suggesting off-fault deformation is insensitive to lithology exist as well. Barnhart et al. (2020) argued that changes in the amount and width of off-fault deformation in the Ridgecrest earthquakes were predominantly related to changes in rupture speed and independent of lithology. Cheng and Barnhart (2021) found that inelastic deformation in the Balochistan earthquake was independent of lithology or off-fault deformation width. Two of the chapters in this dissertation continue to address the dependence (or lack thereof) of off-fault deformation with lithology. In chapter 3, I explore whether the decay of fracture density in the surrounding volume of the Ridgecrest faults is sensitive to lithology. In chapter 5, I explore how pre-existing fabrics in the undeformed host rock affect how finite, off-fault deformation is accommodated.

As faults accumulate displacement, strain localizes into a principal slip surface that hosts most of the deformation, in a process typically referred to as maturation (Chester and Chester, 1998; Crider and Peacock,

2004; Chester et al., 2004; Zinke et al., 2015). This behavior has been widely observed in natural faults and also emerges in analog experiments of fault zone evolution (e.g. Hatem et al., 2017). As a result of this process, the ratio of on-fault to off-fault deformation is expected to decrease over time as the fault accumulates displacement (Dolan and Haravitch, 2014).

Dolan and Haravitch (2014) investigated the relationship between the amount of off-fault deformation and on-fault slip versus fault maturity for six large strike-slip earthquakes. They found that earthquakes on immature (∼25 km or less total displacement) faults localize ∼50-60% of the total deformation on the fault trace, whereas 85-95% of the total surface deformation is localized on the trace for earthquakes on mature faults (>>25km total displacement). Later studies found these relationships to hold consistent for earthquakes in the Eastern California Shear Zone (Milliner et al., 2016), the Balochistan earthquake in Pakistan (Zinke et al., 2014), the Kumamoto earthquake in Japan (Scott et al., 2018), the Kaikoura earthquake in New Zealand (Zinke et al., 2016), and the Ridgecrest foreshock and mainshock (Milliner et al., 2021).

Zinke et al. (2015) compared surface faulting patterns for the Wairau (>100 km total slip) and Awatere (13-20 km total slip) faults in New Zealand, and found that the width of topographically expressed off-fault deformation exceeded hundreds of meters for the less mature Awatere fault with little to no distributed deformation adjacent to the Wairau fault, in agreement with the prediction of Dolan and Haravitch (2014). Shelef and Oskin (2010) found amounts of off-fault deformation of 23% and 31% for the Calico and Harper Lake faults in southern California respectively. These faults are structurally immature but localize much more of the total deformation than the relationship in Dolan and Haravitch (2014) would predict. Scott et al. (2020) found that the amount of off-fault deformation for the mature, creeping San Andreas varies along strike (from meters to kilometers wide zones) with an average of 90±30% of the deformation accommodated over 3-4 meters, and in many locations exceeding the 85-95% localization predicted by Dolan and Haravitch (2014). A lot of the work exploring fault maturity has focused on strike-slip faults. In chapter 5, we explore how maturation influences the partitioning of slip between on and off-fault for normal faults.

The shallow slip deficit

Per elastic rebound theory, the total slip on a fault over multiple earthquake cycles should be uniform with depth. Inversions of coseismic slip from moderate and large earthquakes (M_W 6+) systematically reveal a 15-60% reduction in coseismic slip in the uppermost (∼1-5 km) portion of the fault, termed the "shallow slip deficit" (Fialko et al., 2005). Over the past two decades, studies based on geodetic inversions and numerical models have focused on understanding the physical basis of the shallow slip deficit and clarifying whether its emergence is model-dependent (Fialko et al., 2005; Hussain et al., 2016; Xu et al., 2016; Milliner et al.,

2020).

Several physical mechanisms have been proposed to explain the shallow slip deficit. Some of these mechanisms are credited for inhibiting rupture propagation through the shallow crust, including rupture passage through unconsolidated sediment or other velocity-strengthening materials due to low confining pressures (Marone et al., 1998; Kaneko and Fialko, 2011; Brooks et al., 2017), and compliant deformation in fault damage zones (Barbot et al,. 2008). Other work has instead proposed that the shallow-slip deficit may be compensated interseismically by shallow creep or continuous distributed failure (Fialko et al., 2005; Lindsey et al., 2014).

There have been several attempts to refine coseismic measurements of the shallow slip deficit in an effort to determine model and data dependence. Xu et al. (2016) revisited the coseismic slip inversions for the Landers, Hector Mine, and El Mayor Cucapah earthquakes to include the near-field deformation, refine the processing of the inSAR data, include better-constrained fault geometries, and incorporate GPS data. The refined inversions from these improvements resulted in much smaller shallow slip deficits of 3-19%, suggesting that the previously observed shallow slip deficit was at least in part the result of incomplete data coverage. Milliner et al. (2020) incorporated several geodetic datasets into their slip inversion for the Kumamoto earthquake and found no coseismic slip deficit. Marchandon et al. (2021) showed that the lack of near-field coverage, neglecting variability in elastic properties in slip inversions, and correlated noise artificially contribute to the shallow slip deficit. Improvements in near-field data coverage and inclusion of material variability in inversions should aid in further refining the extent to which coseismic slip is inhibited in the shallow crust.

Postseismic and interseismic deformation

Postseismic transients characterized from inSAR and GPS surveys show shallow, time-dependent deformation related to dilatancy recovery, afterslip, and poroelastic rebound (Jonsson et al., 2003; Fielding et al., 2009). Poroelastic rebound was first inferred following the Landers 1992 earthquake (Peltzer et al., 1998) and later directly confirmed from surface deformation and water level changes following a sequence of earthquakes in Iceland in 2000 (Johnsson et al., 2003). Since, poroelastic rebound has been observed following numerous earthquakes (e.g Fielding et al., 2006; Hu et al., 2014; Gonzalez-Ortega et al., 2014; Panuntun et al., 2018; Wang et al., 2020). Typically, surface displacements and water level changes showing pore pressure recovery during the postseismic period mimic the coseismic change in pore pressure and coseismic displacements but are reversed in sign (e.g. coseismic uplift becomes postseismic subsidence).

Fielding et al. (2009) observed postseismic fault-zone dilatancy and its recovery geodetically following the 2003 Bam earthquake. Fault-zone dilatancy is hypothesized to be caused by the opening of coseismic

fractures that results in an increase in volume and porosity of the shallow fault zone (Scholz, 1974; Ben-Zion and Sammis, 2003). Fielding et al. (2009) found that zones of prominent volumetric compaction were located directly above the patch of highest coseismic slip and in areas of geometrical complexity along strike of the fault (e.g. restraining bends). The recovery of fault zone dilatancy was logarithmic with time and localized within meters of the fault. Barnhart and Lohman (2013) observed that, for blind thrust earthquakes in the Zagros Mountains, about half of the total moment release occurred in the form of continuous, distributed deformation in the weeks to months following the events.

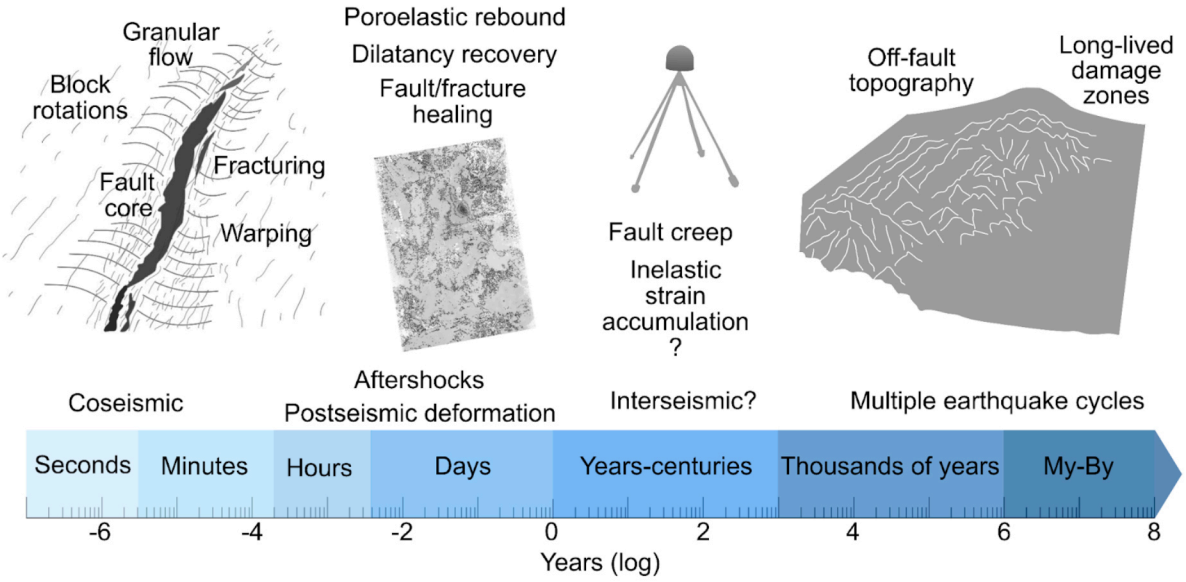

Figure 7: Contributions to off-fault deformation over the earthquake cycle. Figure inspired by Burgmann et al. (2000).

The accumulation of interseismic elastic strain has been geodetically measured for numerous fault systems worldwide (e.g. Pandey et al 1995; Bevis et al., 2001; Wright et al., 2001; Argus et al., 2005; Fialko, 2006; Szeliga et al., 2012). In general, these measurements show the accumulation of elastic strain occurs steadily over time and occupies a large volume around the fault. Scott et al. (2020a) combined topographic differencing, inSAR, and measurements of surficial fracturing to image deformation at the Dry Lake Paleoseismic site along the creeping central San Andreas fault. From these datasets spanning different spatiotemporal scales, they estimated that ∼90% of the deformation is localized by the 3-4 meter-wide trace of the San Andreas fault, with surface fractures accommodating over 80% of the deformation in the two-year time period over which they formed. Scott et al. (2020b) used differential lidar topography spanning 11-13 years to measure the surface deformation field along a 150 km section of the San Andreas and Calaveras faults. From these observations, they noted that creep is often localized along discrete fault traces but distributed in areas of

geometrical complexity.

The energy budget of inelastic deformation

Earthquakes can be described as the release of stress on a fault surface. During this stress drop, the potential energy of the system, which includes both strain and gravitational terms, drops. A portion of this energy is dynamically radiated as seismic waves, while the remaining, considering a slip-weakening model, is dissipated in the form of fracture energy and frictional heat (Kanamori and Brodsky, 2004). Dissipative processes within the fault zone are part of the fracture energy component of the earthquake energy budget, and they are seismologically indistinguishable from frictional heat or dissipative processes on the fault.

Off-fault deformation spans a suite of dissipative processes, including grain crushing (Chester et al., 2005), folding, fracturing, coseismic melting along principal or secondary slip surfaces (Di Toro et al., 2005), granular flow, and rigid block rotations (e.g. Shelef and Oskin, 2010) that constitute a sink of strain energy. These processes operate coseismically (e.g. Milliner et al., 2016) and may remain active at lower strain rates during the postseismic and interseismic period (Fialko et al., 2005; Fielding et al., 2006; Oskin et al., 2012). Over longer timescales, fluid flow facilitated by fractures throughout the damage zone (Sibson, 2001), subcritical crack growth (Swanson, 1984), and mineral alterations also consume energy (Evans and Chester, 1995), operating throughout the earthquake cycle (Figure 7).

When evaluating the energy budget for the 2011 Tohoku earthquake, Brodsky et al. (2020) found that most solutions to the energy balance required off-fault deformation to account for stress dissipation during the rupture. This requirement was consistent with the widely observed coseismic damage and the presence of permanent folding in the area (Keren and Kirkpatrick, 2016). Shipton et al. (2006) noted that the width of crushed gouge surrounding the principal slip surface remains relatively thin as faults grow, though the surrounding damage zone grows in complexity with fault length. As the damage zone grows with increasing fault slip but the total energy available for a given earthquake is limited, the principal slip zone remains thin and increasingly more energy is dissipated off-fault versus on fault.

Wilson et al. (2005) measured the characteristics of gouge zones along the mature San Andreas faults ($\sim$160 km of slip) and immature faults in a South African mine ($\sim$0.4 m of slip). Based on their measurements, they proposed that generation of the gouge surrounding the principal slip surface is responsible for 50% of the earthquake energy budget in the immature faults. Laboratory experiments of shear fracture also yield large values of dissipated energy via fracturing in comparison to the energy expenditure of frictional sliding. Chester et al. (2005) considered the free-surface energy of fractures produced within the fault core and the surrounding damage zone of the Punchbowl fault in California. In contrast with the results of Wilson et al. (2005), Chester et al. (2005) attributed a much smaller portion of the earthquake energy

budget devoted to dissipation by fracture generation (<1%). A potential explanation for these differences is that damage may be unevenly created over the lifespan of a fault (Chester et al., 2005). If fractures are re-activated in subsequent events instead of newly generated, the energy dissipated by fracture will decrease over time, as fracture generation requires more energy than frictional sliding on a pre-existing crack.

The presence of widely distributed off-fault deformation violates the assumption of linear elastic fracture mechanics that all inelastic deformation is confined to a small region surrounding the fault tip. A work minimization approach, which considers a global energy budget for a much larger volume than the local crack tip, serves as an alternative (Cooke and Madden, 2014). The work minimization approach is rooted in the assumption that deformation of the crust occurs so that the tectonic work exerted is minimized. Under this framework, permanent off-fault deformation is considered as part of an internal work term (the integral of strain energy density over the volume), and a gravitational work term to account for vertical deformation (Cooke and Murphy, 2004). This approach relaxes the assumption of linear elasticity and enables consideration of widely distributed inelastic deformation, though it still requires knowledge of the stress-strain relationship for the individual mechanisms contributing to internal work through off-fault deformation (Cooke and Murphy, 2004).

References

1. Aben, F. M., Doan, M. L., Gratier, J. P., & Renard, F. (2017). High strain rate deformation of porous sandstone and the asymmetry of earthquake damage in shallow fault zones. Earth and Planetary Science Letters, 463, 81-91.

2. Alongi, T., Brodsky, E. E., Kluesner, J., & Brothers, D. (2022). Using active source seismology to image the Palos Verdes Fault damage zone as a function of distance, depth, and geology. Earth and Planetary Science Letters, 600, 117871.

3. Ampuero, J. P., & Ben-Zion, Y. (2008). Cracks, pulses and macroscopic asymmetry of dynamic rupture on a bimaterial interface with velocity-weakening friction. Geophysical Journal International, 173(2), 674-692.

4. Anderson, G., Aagaard, B., & Hudnut, K. (2003). Fault interactions and large complex earthquakes in the Los Angeles area. Science, 302(5652), 1946-1949.

5. Andreuttiova, L., Hollingsworth, J., Vermeesch, P., & Mitchell, T. (2023). Assessing distribution and pattern of the earthquake-related deformation caused by large continental normal earthquakes using optical image correlation (No. EGU23-16199). Copernicus Meetings.

6. Antoine, S. L., Klinger, Y., Delorme, A., Wang, K., Bürgmann, R., & Gold, R. D. (2021). Diffuse deformation and surface faulting distribution from submetric image correlation along the 2019 Ridgecrest, California, ruptures. Bulletin of the Seismological Society of America, 111(5), 2275-2302.

7. Argus, D. F., Heflin, M. B., Peltzer, G., Crampé, F., & Webb, F. H. (2005). Interseismic strain accumulation and anthropogenic motion in metropolitan Los Angeles. Journal of Geophysical Research: Solid Earth, 110(B4).

8. Avsar, U., Hubert-Ferrari, A., Batist, M. D., & Fagel, N. (2014). A 3400 year lacustrine paleoseismic record from the North Anatolian Fault, Turkey: Implications for bimodal recurrence behavior. Geophysical Research Letters, 41(2), 377-384.

9. Bao, H., Ampuero, J. P., Meng, L., Fielding, E. J., Liang, C., Milliner, C. W., ... & Huang, H. (2019). Early and persistent supershear rupture of the 2018 magnitude 7.5 Palu earthquake. Nature Geoscience, 12(3), 200-205.

10. Barbot, S., Fialko, Y., & Sandwell, D. (2008). Effect of a compliant fault zone on the inferred earthquake slip distribution. Journal of Geophysical Research: Solid Earth, 113(B6).

11. Barnhart, W. D., & Lohman, R. B. (2013). Phantom earthquakes and triggered aseismic creep: Vertical partitioning of strain during earthquake sequences in Iran. Geophysical Research Letters, 40(5), 819-823.

12. Barnhart, W. D., Hayes, G. P., & Gold, R. D. (2019). The July 2019 Ridgecrest, California, earthquake sequence: Kinematics of slip and stressing in cross-fault ruptures. Geophysical Research Letters, 46(21), 11859-11867.

13. Barnhart, W. D., Gold, R. D., & Hollingsworth, J. (2020). Localized fault-zone dilatancy and surface inelasticity of the 2019 Ridgecrest earthquakes. Nature Geoscience, 13(10), 699-704.

14. Bennett, S. E., DuRoss, C. B., Gold, R. D., Briggs, R. W., Personius, S. F., Reitman, N. G., ... & Odum, J. K. (2018). Paleoseismic Results from the Alpine Site, Wasatch Fault Zone: Timing and Displacement Data for Six Holocene Earthquakes at the Salt Lake City–Provo Segment Boundary Paleoseismic Results from the Alpine Site, Wasatch Fault Zone. Bulletin of the Seismological Society of America, 108(6), 3202-3224.

15. Ben-Zion, Y. (1998). Properties of seismic fault zone waves and their utility for imaging low-velocity structures. Journal of Geophysical Research: Solid Earth, 103(B6), 12567-12585.

16. Ben-Zion, Y., & Sammis, C. G. (2003). Characterization of fault zones. Pure and applied geophysics, 160, 677-715.

17. Ben-Zion, Y., & Ampuero, J. P. (2009). Seismic radiation from regions sustaining material damage. Geophysical Journal International, 178(3), 1351-1356.

18. Ben-Zion, Y., & Aki, K. (1990). Seismic radiation from an SH line source in a laterally heterogeneous planar fault zone. Bulletin of the Seismological Society of America, 80(4), 971-994.

19. Ben-Zion, Y., Vernon, F. L., Ozakin, Y., Zigone, D., Ross, Z. E., Meng, H., ... & Barklage, M. (2015). Basic data features and results from a spatially dense seismic array on the San Jacinto fault zone. Geophysical Journal International, 202(1), 370-380.

20. Bergbauer, S., & Pollard, D. D. (2004). A new conceptual fold-fracture model including prefolding joints, based on the Emigrant Gap anticline, Wyoming. Geological Society of America Bulletin, 116(3-4), 294-307.

21. Bevis, M., Kendrick, E., Smalley Jr, R., Brooks, B., Allmendinger, R., & Isacks, B. (2001). On the strength of interplate coupling and the rate of back arc convergence in the central Andes: An analysis of the interseismic velocity field. Geochemistry, Geophysics, Geosystems, 2(11).

22. Bhat, H. S., Dmowska, R., Rice, J. R., & Kame, N. (2004). Dynamic slip transfer from the Denali to Totschunda faults, Alaska: Testing theory for fault branching. Bulletin of the Seismological Society of America, 94(6B), S202-S213.

23. Bhat, H. S., Olives, M., Dmowska, R., & Rice, J. R. (2007). Role of fault branches in earthquake rupture dynamics. Journal of Geophysical Research: Solid Earth, 112(B11).

24. Biasi, G. P., Weldon, R. J., Fumal, T. E., & Seitz, G. G. (2002). Paleoseismic event dating and the conditional probability of large earthquakes on the southern San Andreas fault, California. Bulletin of the Seismological Society of America, 92(7), 2761-2781.

25. Biasi, G. P., & Wesnousky, S. G. (2016). Steps and gaps in ground ruptures: Empirical bounds on rupture propagation. Bulletin of the Seismological Society of America, 106(3), 1110-1124.

26. Biasi, G. P., & Wesnousky, S. G. (2017). Bends and ends of surface RupturesBends and ends of surface ruptures. Bulletin of the Seismological Society of America, 107(6), 2543-2560.

27. Biasi, G. P., & Wesnousky, S. G. (2021). Rupture passing probabilities at fault bends and steps, with application to rupture length probabilities for earthquake early warning. Bulletin of the Seismological Society of America, 111(4), 2235-2247.

28. Blisniuk, K., Scharer, K., Sharp, W. D., Burgmann, R., Amos, C., & Rymer, M. (2021). A revised position for the primary strand of the Pleistocene-Holocene San Andreas fault in southern California. Science advances, 7(13), eaaz5691.

29. Brandes, C., & Tanner, D. C. (2014). Fault-related folding: A review of kinematic models and their application. Earth-Science Reviews, 138, 352-370.

30. Brooks, B. A., Minson, S. E., Glennie, C. L., Nevitt, J. M., Dawson, T., Rubin, R., ... & Zaccone, D. (2017). Buried shallow fault slip from the South Napa earthquake revealed by near-field geodesy. Science Advances, 3(7), e1700525.

31. Cardozo, N., Jackson, C. A. L., & Whipp, P. S. (2011). Determining the uniqueness of best-fit trishear models. Journal of Structural Geology, 33(6), 1063-1078.

32. Caine, J. S., Evans, J. P., & Forster, C. B. (1996). Fault zone architecture and permeability structure. Geology, 24(11), 1025-1028.

33. Cello, G., Tondi, E., Micarelli, L., & Invernizzi, C. (2001). Fault zone fabrics and geofluid properties as indicators of rock deformation modes. Journal of Geodynamics, 32(4-5), 543-565.

34. Cesca, S., Zhang, Y., Mouslopoulou, V., Wang, R., Saul, J., Savage, M., ... & Dahm, T. (2017). Complex rupture process of the Mw 7.8, 2016, Kaikoura earthquake, New Zealand, and its aftershock sequence. Earth and Planetary Science Letters, 478, 110-120.

35. Chen, K., Avouac, J. P., Geng, J., Liang, C., Zhang, Z., Li, Z., & Zhang, S. (2022). The 2021 Mw 7.4 Madoi earthquake: An archetype bilateral slip-pulse rupture arrested at a splay fault. Geophysical Research Letters, 49(2), e2021GL095243.

36. Cheng, G., & Barnhart, W. D. (2021). Permanent co-seismic deformation of the 2013 Mw7. 7 Baluchistan, Pakistan earthquake from high-resolution surface strain analysis. Journal of Geophysical Research: Solid Earth, 126(3), e2020JB020622.

37. Chester, F. M., & Chester, J. S. (1998). Ultracataclasite structure and friction processes of the Punchbowl fault, San Andreas system, California. Tectonophysics, 295(1-2), 199-221.

38. Chester, F. M., & Logan, J. M. (1986). Implications for mechanical properties of brittle faults from observations of the Punchbowl fault zone, California. Pure and applied geophysics, 124, 79-106.

39. Chester, F. M., Chester, J. S., Kirschner, D. L., Schulz, S. E., & Evans, J. P. (2004). Structure of large-displacement, strike-slip fault zones in the brittle continental crust. In Rheology and Deformation of the Lithosphere at continental Margins (pp. 223-260). Columbia University Press.

40. Chester, J. S., Chester, F. M., & Kronenberg, A. K. (2005). Fracture surface energy of the Punchbowl fault, San Andreas system. Nature, 437(7055), 133-136.

41. Chester, F. M., Evans, J. P., & Biegel, R. L. (1993). Internal structure and weakening mechanisms of the San Andreas fault. Journal of Geophysical Research: Solid Earth, 98(B1), 771-786.

42. Cipolla, C. L., Warpinski, N. R., Mayerhofer, M. J., Lolon, E. P., & Vincent, M. C. (2008, September). The relationship between fracture complexity, reservoir properties, and fracture treatment design. In SPE Annual Technical Conference and Exhibition? (pp. SPE-115769). SPE.

43. Cinti, F. R., Pantosti, D., Lombardi, A. M., & Civico, R. (2021). Modeling of earthquake chronology from paleoseismic data: Insights for regional earthquake recurrence and earthquake storms in the Central Apennines. Tectonophysics, 816, 229016.

44. Cochran, E. S., Li, Y. G., Shearer, P. M., Barbot, S., Fialko, Y., & Vidale, J. E. (2009). Seismic and geodetic evidence for extensive, long-lived fault damage zones. Geology, 37(4), 315-318.

45. Coleman, A. J., Duffy, O. B., & Jackson, C. A. L. (2019). Growth folds above propagating normal faults. Earth-Science Reviews, 196, 102885.

46. Conneally, J., Childs, C., & Nicol, A. (2017). Monocline formation during growth of segmented faults in the Taranaki Basin, offshore New Zealand. Tectonophysics, 721, 310-321.

47. Cooke, M. L., & Madden, E. H. (2014). Is the Earth lazy? A review of work minimization in fault evolution. Journal of Structural Geology, 66, 334-346.

48. Cooke, M. L., & Murphy, S. (2004). Assessing the work budget and efficiency of fault systems using mechanical models. Journal of Geophysical Research: Solid Earth, 109(B10).

49. Crider, J. G., & Peacock, D. C. (2004). Initiation of brittle faults in the upper crust: a review of field observations. Journal of Structural Geology, 26(4), 691-707.

50. Day, S. M. (1982). Three-dimensional simulation of spontaneous rupture: the effect of nonuniform prestress. Bulletin of the Seismological Society of America, 72(6A), 1881-1902.

51. Di Toro, G., Nielsen, S., & Pennacchioni, G. (2005). Earthquake rupture dynamics frozen in exhumed ancient faults. Nature, 436(7053), 1009-1012.

52. Dolan, J. F., & Haravitch, B. D. (2014). How well do surface slip measurements track slip at depth in large strike-slip earthquakes? The importance of fault structural maturity in controlling on-fault slip versus off-fault surface deformation. Earth and Planetary Science Letters, 388, 38-47.

53. Dor, O., Ben-Zion, Y., Rockwell, T. K., & Brune, J. (2006). Pulverized rocks in the Mojave section of the San Andreas Fault Zone. Earth and Planetary Science Letters, 245(3-4), 642-654.

54. Dor, O., Yildirim, C., Rockwell, T. K., Ben-Zion, Y., Emre, O., Sisk, M., & Duman, T. Y. (2008). Geological and geomorphologic asymmetry across the rupture zones of the 1943 and 1944 earthquakes on the North Anatolian Fault: possible signals for preferred earthquake propagation direction. Geophysical Journal International, 173(2), 483-504.

55. Duan, B., & Oglesby, D. D. (2006). Heterogeneous fault stresses from previous earthquakes and the effect on dynamics of parallel strike-slip faults. Journal of Geophysical Research: Solid Earth, 111(B5).

56. DuRoss, C. B., Personius, S. F., Crone, A. J., Olig, S. S., Hylland, M. D., Lund, W. R., & Schwartz, D. P. (2016). Fault segmentation: New concepts from the Wasatch fault zone, Utah, USA. Journal of Geophysical Research: Solid Earth, 121(2), 1131-1157.

57. Elliott, A. J., Oskin, M. E., Liu-Zeng, J., & Shao, Y. (2015). Rupture termination at restraining bends: The last great earthquake on the Altyn Tagh Fault. Geophysical Research Letters, 42(7), 2164-2170.

58. Elliott, A. J., Dolan, J. F., & Oglesby, D. D. (2009). Evidence from coseismic slip gradients for dynamic control on rupture propagation and arrest through stepovers. Journal of Geophysical Research: Solid Earth, 114(B2).

59. Elliott, A. J., Oskin, M. E., Liu-Zeng, J., & Shao, Y. X. (2018). Persistent rupture terminations at a restraining bend from slip rates on the eastern Altyn Tagh fault. Tectonophysics, 733, 57-72.

60. Erickson, B. A., & Day, S. M. (2016). Bimaterial effects in an earthquake cycle model using rate-and-state friction. Journal of Geophysical Research: Solid Earth, 121(4), 2480-2506.

61. Evans, J. P., & Chester, F. M. (1995). Fluid-rock interaction in faults of the San Andreas system: Inferences from San Gabriel fault rock geochemistry and microstructures. Journal of Geophysical Research: Solid Earth, 100(B7), 13007-13020.

62. Faulkner, D. R., Lewis, A. C., & Rutter, E. H. (2003). On the internal structure and mechanics of large strike-slip fault zones: field observations of the Carboneras fault in southeastern Spain. Tectonophysics, 367(3-4), 235-251.

63. Faulkner, D. R., Mitchell, T. M., Healy, D., & Heap, M. J. (2006). Slip on'weak'faults by the rotation of regional stress in the fracture damage zone. Nature, 444(7121), 922-925.

64. Ferrill, D. A., & Morris, A. P. (2008). Fault zone deformation controlled by carbonate mechanical stratigraphy, Balcones fault system, Texas. AAPG bulletin, 92(3), 359-380.

65. Fialko, Y., Sandwell, D., Agnew, D., Simons, M., Shearer, P., & Minster, B. (2002). Deformation on nearby faults induced by the 1999 Hector Mine earthquake. Science, 297(5588), 1858-1862.

66. Fialko, Y. (2004). Probing the mechanical properties of seismically active crust with space geodesy: Study of the coseismic deformation due to the 1992 Mw7. 3 Landers (southern California) earthquake. Journal of Geophysical Research: Solid Earth, 109(B3).

67. Fialko, Y. (2006). Interseismic strain accumulation and the earthquake potential on the southern San Andreas fault system. Nature, 441(7096), 968-971.

68. Fialko, Y., Sandwell, D., Simons, M., & Rosen, P. (2005). Three-dimensional deformation caused by the Bam, Iran, earthquake and the origin of shallow slip deficit. Nature, 435(7040), 295-299.

69. Field, E. H., Dawson, T. E., Felzer, K. R., Frankel, A. D., Gupta, V., Jordan, T. H., ... & Wills, C. J. (2009). Uniform California earthquake rupture forecast, version 2 (UCERF 2). Bulletin of the Seismological Society of America, 99(4), 2053-2107.

70. Field, E. H., Arrowsmith, R. J., Biasi, G. P., Bird, P., Dawson, T. E., Felzer, K. R., ... & Zeng, Y. (2014). Uniform California earthquake rupture forecast, version 3 (UCERF3)—The time-independent model. Bulletin of the Seismological Society of America, 104(3), 1122-1180.

71. Fielding, E. J., Lundgren, P. R., Bürgmann, R., & Funning, G. J. (2009). Shallow fault-zone dilatancy recovery after the 2003 Bam earthquake in Iran. Nature, 458(7234), 64-68.

72. Finzi, Y., & Langer, S. (2012). Damage in step-overs may enable large cascading earthquakes. Geophysical Research Letters, 39(16).

73. Fletcher, J. M., Oskin, M. E., & Teran, O. J. (2016). The role of a keystone fault in triggering the complex El Mayor–Cucapah earthquake rupture. Nature Geoscience, 9(4), 303-307.

74. Flodin, E. A., & Aydin, A. (2004). Evolution of a strike-slip fault network, Valley of Fire State Park, southern Nevada. Geological Society of America Bulletin, 116(1-2), 42-59.

75. Fossen, H., Soliva, R., Ballas, G., Trzaskos, B., Cavalcante, C., & Schultz, R. A. (2018). A review of deformation bands in reservoir sandstones: geometries, mechanisms and distribution. Geological Society, London, Special Publications, 459(1), 9-33.

76. Fraser, J., Vanneste, K., & Hubert-Ferrari, A. (2010). Recent behavior of the North Anatolian Fault: Insights from an integrated paleoseismological data set. Journal of Geophysical Research: Solid Earth, 115(B9).

77. Ferrill, D. A., Morris, A. P., McGinnis, R. N., Smart, K. J., Watson-Morris, M. J., & Wigginton, S. S. (2016). Observations on normal-fault scarp morphology and fault system evolution of the Bishop Tuff in the Volcanic Tableland, Owens Valley, California, USA. Lithosphere, 8(3), 238-253.

78. Ferrill, D. A., Morris, A. P., & Smart, K. J. (2007). Stratigraphic control on extensional fault propagation folding: Big Brushy Canyon monocline, Sierra del Carmen, Texas. Geological Society, London, Special Publications, 292(1), 203-217.

79. Ferrill, D. A., Morris, A. P., & McGinnis, R. N. (2012). Extensional fault-propagation folding in mechanically layered rocks: The case against the frictional drag mechanism. Tectonophysics, 576, 78-85.

80. Fielding, E. J., Lundgren, P. R., Bürgmann, R., & Funning, G. J. (2009). Shallow fault-zone dilatancy recovery after the 2003 Bam earthquake in Iran. Nature, 458(7234), 64-68.

81. Fumal, T. E., Weldon, R. J., Biasi, G. P., Dawson, T. E., Seitz, G. G., Frost, W. T., & Schwartz, D. P. (2002). Evidence for large earthquakes on the San Andreas fault at the Wrightwood, California, paleoseismic site: AD 500 to present. Bulletin of the Seismological Society of America, 92(7), 2726-2760.

82. Galli, P., Galderisi, A., Peronace, E., Giaccio, B., Hajdas, I., Messina, P., ... & Polpetta, F. (2019). The awakening of the dormant Mount Vettore fault (2016 central Italy earthquake, Mw 6.6): Paleoseismic clues on its millennial silences. Tectonics, 38(2), 687-705.

83. Grant, J. V., & Kattenhorn, S. A. (2004). Evolution of vertical faults at an extensional plate boundary, southwest Iceland. Journal of Structural Geology, 26(3), 537-557.

84. Grasemann, B., Martel, S., & Passchier, C. (2005). Reverse and normal drag along a fault. Journal of Structural Geology, 27(6), 999-1010.

85. Gaudreau, E., Hollingsworth, J., Nissen, E., & Funning, G. J. (2023). Complex 3-D Surface Deformation in the 1971 San Fernando, California Earthquake Reveals Static and Dynamic Controls on Off-Fault Deformation. Journal of Geophysical Research: Solid Earth, 128(3), e2022JB024985.

86. Gawthorpe, R. L., Sharp, I., Underhill, J. R., & Gupta, S. (1997). Linked sequence stratigraphic and structural evolution of propagating normal faults. Geology, 25(9), 795-798.

87. Gold, R. D., & Cowgill, E. (2011). Deriving fault-slip histories to test for secular variation in slip, with examples from the Kunlun and Awatere faults. Earth and Planetary Science Letters, 301(1-2), 52-64.

88. Gonzalez-Ortega, A., Fialko, Y., Sandwell, D., Alejandro Nava-Pichardo, F., Fletcher, J., Gonzalez-Garcia, J., ... & Funning, G. (2014). El Mayor-Cucapah (Mw 7.2) earthquake: Early near-field postseismic deformation from InSAR and GPS observations. Journal of Geophysical Research: Solid Earth, 119(2), 1482-1497.

89. Griffith, W. A., Nielsen, S., Di Toro, G., & Smith, S. A. (2010). Rough faults, distributed weakening, and off-fault deformation. Journal of Geophysical Research: Solid Earth, 115(B8).

90. Hamling, I. J., Hreinsdóttir, S., Clark, K., Elliott, J., Liang, C., Fielding, E., ... & Stirling, M. (2017). Complex multifault rupture during the 2016 M w 7.8 Kaikōura earthquake, New Zealand. Science, 356(6334), eaam7194.

91. Hardy, S., & Finch, E. (2007). Mechanical stratigraphy and the transition from trishear to kink-band fault-propagation fold forms above blind basement thrust faults: a discrete-element study. Marine and Petroleum Geology, 24(2), 75-90.

92. Harris, R. A., Archuleta, R. J., & Day, S. M. (1991). Fault steps and the dynamic rupture process: 2-D numerical simulations of a spontaneously propagating shear fracture. Geophysical Research Letters, 18(5), 893-896.

93. Harris, R. A., & Day, S. M. (1993). Dynamics of fault interaction: Parallel strike-slip faults. Journal of Geophysical Research: Solid Earth, 98(B3), 4461-4472.

94. Harris, R. A., & Day, S. M. (1997). Effects of a low-velocity zone on a dynamic rupture. Bulletin of the Seismological Society of America, 87(5), 1267-1280.

95. Harris, R. A., & Day, S. M. (1999). Dynamic 3D simulations of earthquakes on en echelon faults. Geophysical Research Letters, 26(14), 2089-2092.

96. Harris, R. A., Dolan, J. F., Hartleb, R., & Day, S. M. (2002). The 1999 Izmit, Turkey, earthquake: A 3D dynamic stress transfer model of intraearthquake triggering. Bulletin of the Seismological Society of America, 92(1), 245-255.

97. Harris, R. A. (2004). Numerical simulations of large earthquakes: Dynamic rupture propagation on heterogeneous faults. Computational earthquake science part II, 2171-2181.

98. Harris, R. A., & Day, S. M. (2005). Material contrast does not predict earthquake rupture propagation direction. Geophysical research letters, 32(23).

99. Harding, T. P. (1984). Graben hydrocarbon occurrences and structural style. AAPG bulletin, 68(3), 333-362.

100. Hatem, A. E., Cooke, M. L., & Toeneboehn, K. (2017). Strain localization and evolving kinematic efficiency of initiating strike-slip faults within wet kaolin experiments. Journal of Structural Geology, 101, 96-108.

101. Hauksson, E. (2010). Spatial separation of large earthquakes, aftershocks, and background seismicity: Analysis of interseismic and coseismic seismicity patterns in southern California. Seismogenesis and earthquake forecasting: The frank evison volume II, 125-143.

102. Hamblin, W. K. (1965). Origin of "reverse drag" on the downthrown side of normal faults. Geological society of America bulletin, 76(10), 1145-1164.

103. Herbert, J. W., Cooke, M. L., Oskin, M., & Difo, O. (2014). How much can off-fault deformation contribute to the slip rate discrepancy within the eastern California shear zone?. Geology, 42(1), 71-75.

104. Howarth, J. D., Barth, N. C., Fitzsimons, S. J., Richards-Dinger, K., Clark, K. J., Biasi, G. P., ... & Sutherland, R. (2021). Spatiotemporal clustering of great earthquakes on a transform fault controlled by geometry. Nature Geoscience, 14(5), 314-320.

105. Hu, Y., Bürgmann, R., Freymueller, J. T., Banerjee, P., & Wang, K. (2014). Contributions of poroelastic rebound and a weak volcanic arc to the postseismic deformation of the 2011 Tohoku earthquake. Earth, Planets and Space, 66, 1-10.

106. Hu, F., Zhang, Z., & Chen, X. (2016). Investigation of earthquake jump distance for strike-slip step overs based on 3-D dynamic rupture simulations in an elastic half-space. Journal of Geophysical Research: Solid Earth, 121(2), 994-1006.

107. Huang, Y., Ampuero, J. P., & Helmberger, D. V. (2014). Earthquake ruptures modulated by waves in damaged fault zones. Journal of Geophysical Research: Solid Earth, 119(4), 3133-3154.

108. Huang, M. H., & Huang, H. H. (2018). The complexity of the 2018 Mw 6.4 Hualien earthquake in east Taiwan. Geophysical Research Letters, 45(24), 13-249.

109. Hudnut, K. W., Seeber, L., & Pacheco, J. (1989). Cross-fault triggering in the November 1987 Superstition Hills earthquake sequence, southern California. Geophysical Research Letters, 16(2), 199-202.

110. Hussain, E., Wright, T. J., Walters, R. J., Bekaert, D., Hooper, A., & Houseman, G. A. (2016). Geodetic observations of postseismic creep in the decade after the 1999 Izmit earthquake, Turkey: Implications for a shallow slip deficit. Journal of Geophysical Research: Solid Earth, 121(4), 2980-3001.

111. Janecke, S. U., Vandenburg, C. J., & Blankenau, J. J. (1998). Geometry, mechanisms and significance of extensional folds from examples in the Rocky Mountain Basin and Range province, USA. Journal of Structural Geology, 20(7), 841-856.

112. John, B. E. (1987). Geometry and evolution of a mid-crustal extensional fault system: Chemehuevi Mountains, southeastern California. Geological Society, London, Special Publications, 28(1), 313-335.

113. Johri, M., Dunham, E. M., Zoback, M. D., & Fang, Z. (2014). Predicting fault damage zones by modeling dynamic rupture propagation and comparison with field observations. Journal of Geophysical Research: Solid Earth, 119(2), 1251-1272.

114. Jonsson, S., Segall, P., Pedersen, R., & Björnsson, G. (2003). Post-earthquake ground movements correlated to pore-pressure transients. Nature, 424(6945), 179-183.

115. Kame, N., Rice, J. R., & Dmowska, R. (2003). Effects of prestress state and rupture velocity on dynamic fault branching. Journal of Geophysical Research: Solid Earth, 108(B5).

116. Kane, K. E., Jackson, C. A. L., & Larsen, E. (2010). Normal fault growth and fault-related folding in a salt-influenced rift basin: South Viking Graben, offshore Norway. Journal of Structural Geology, 32(4), 490-506.

117. Kase, Y., & Kuge, K. (2001). Rupture propagation beyond fault discontinuities: Significance of fault strike and location. Geophysical Journal International, 147(2), 330-342.

118. Kanamori, H., & Brodsky, E. E. (2004). The physics of earthquakes. Reports on progress in physics, 67(8), 1429.

119. Kaneko, Y., & Fialko, Y. (2011). Shallow slip deficit due to large strike-slip earthquakes in dynamic rupture simulations with elasto-plastic off-fault response. Geophysical Journal International, 186(3), 1389-1403.

120. Martel, S. J., & Langley, J. S. (2006). Propagation of normal faults to the surface in basalt, Koae fault system, Hawaii. Journal of Structural Geology, 28(12), 2123-2143.

121. Kaven, J. O., & Martel, S. J. (2007). Growth of surface-breaching normal faults as a three-dimensional fracturing process. Journal of Structural Geology, 29(9), 1463-1476.

122. Kendrick, K. J., & Fumal, T. (2005, October). Paleoseismicity of the northern San Jacinto fault, Colton and San Bernardino, southern California; preliminary results. In Geological Society of America Abstracts with Programs (Vol. 37, No. 7, p. 559).

123. Keren, T. T., & Kirkpatrick, J. D. (2016). Data report: Tectonic and induced structures in the JFAST core. In Proc. IODP— Volume (Vol. 343, No. 343T, p. 343T).

124. Khalil, S. M., & McClay, K. R. (2017). 3D geometry and kinematic evolution of extensional fault-related folds, NW Red Sea, Egypt. Geological Society, London, Special Publications, 439(1), 109-130.

125. King, G., & Nabelek, J. (1985). Role of fault bends in the initiation and termination of earthquake rupture. Science, 228(4702), 984-987.

126. Kim, Y. S., Peacock, D. C., & Sanderson, D. J. (2004). Fault damage zones. Journal of structural geology, 26(3), 503-517.

127. Kirby, E., Harkins, N., Wang, E., Shi, X., Fan, C., & Burbank, D. (2007). Slip rate gradients along the eastern Kunlun fault. Tectonics, 26(2).

128. Klinger, Y., Michel, R., & King, G. C. (2006). Evidence for an earthquake barrier model from Mw$\sim$ 7.8 Kokoxili (Tibet) earthquake slip-distribution. Earth and Planetary Science Letters, 242(3-4), 354-364.

129. Kuo, Y. T., Wang, Y., Hollingsworth, J., Huang, S. Y., Chuang, R. Y., Lu, C. H., ... & Chang, C. P. (2019). Shallow fault rupture of the Milun fault in the 2018 Mw 6.4 Hualien earthquake: A

high-resolution approach from optical correlation of Pléiades satellite imagery. Seismological Research Letters, 90(1), 97-107.

130. Kurzon, I., Vernon, F. L., Ben-Zion, Y., & Atkinson, G. (2014). Ground motion prediction equations in the San Jacinto fault zone: Significant effects of rupture directivity and fault zone amplification. Pure and Applied Geophysics, 171, 3045-3081.

131. Lamb, S., Arnold, R., & Moore, J. D. (2018). Locking on a megathrust as a cause of distributed faulting and fault-jumping earthquakes. Nature Geoscience, 11(11), 871-875.

132. Lambert, V., Lapusta, N., & Perry, S. (2021). Propagation of large earthquakes as self-healing pulses or mild cracks. Nature, 591(7849), 252-258.

133. Langer, S., Finzi, Y., & Olsen-Kettle, L. M. (2015). Dynamic triggering of earthquakes is promoted by crustal heterogeneities and bimaterial faults. Physics of the Earth and Planetary Interiors, 238, 34-41.

134. Li, Y. G., & Leary, P. C. (1990). Fault zone trapped seismic waves. Bulletin of the Seismological Society of America, 80(5), 1245-1271.

135. Li, Y. G., Vidale, J. E., & Cochran, E. S. (2004). Low-velocity damaged structure of the San Andreas Fault at Parkfield from fault zone trapped waves. Geophysical Research Letters, 31(12).

136. Lindsey, E. O., Fialko, Y., Bock, Y., Sandwell, D. T., & Bilham, R. (2014). Localized and distributed creep along the southern San Andreas Fault. Journal of Geophysical Research: Solid Earth, 119(10), 7909-7922.

137. Li, C., Li, T., Shan, X., & Zhang, G. (2023). Extremely Large Off-Fault Deformation during the 2021 M w 7.4 Maduo, Tibetan Plateau, Earthquake. Seismological Society of America, 94(1), 39-51.

138. Liu, D., Duan, B., Scharer, K., & Yule, D. (2022). Observation-Constrained Multicycle Dynamic Models of the Southern San Andreas and the Northern San Jacinto faults: Addressing Complexity in Paleoearthquake Extent and Recurrence With Realistic 2D Fault Geometry. Journal of Geophysical Research: Solid Earth, 127(2), e2021JB023420.

139. Liu, C., Lay, T., Pollitz, F. F., Xu, J., & Xiong, X. (2021). Seismic and geodetic analysis of Rupture characteristics of the 2020 M w 6.5 Monte Cristo range, Nevada, earthquake. Bulletin of the Seismological Society of America, 111(6), 3226-3236.

140. Livio, F. A., Ferrario, M. F., Frigerio, C., Zerboni, A., & Michetti, A. M. (2020). Variable fault tip propagation rates affected by near-surface lithology and implications for fault displacement hazard assessment. Journal of Structural Geology, 130, 103914.

141. Lozos, J. C., Oglesby, D. D., Duan, B., & Wesnousky, S. G. (2011). The effects of double fault bends on rupture propagation: A geometrical parameter study. Bulletin of the Seismological Society of America, 101(1), 385-398.

142. Lozos, J. C. (2016). A case for historic joint rupture of the San Andreas and San Jacinto faults. Science advances, 2(3), e1500621.

143. Lozos, J. C. (2022). Dynamic Rupture Modeling of Coseismic Interactions on Orthogonal Strike-Slip Faults. Geophysical Research Letters, 49(5), e2021GL097585.

144. Lu, Y., & Ben-Zion, Y. (2022). Regional seismic velocity changes following the 2019 M w 7.1 Ridgecrest, California earthquake from autocorrelations and P/S converted waves.

145. Lu, L., & Zhou, Y. (2023). Coseismic deformation of the 1976 Ms 7.3 Chaldiran earthquake in eastern Turkey measured by satellite imagery, in comparison with field measurements. Geophysical Journal International, 234(2), 1342-1354. Geophysical Journal International, 228(1), 620-630.

146. Magistrale, H., & Day, S. (1999). 3D simulations of multi-segment thrust fault rupture. Geophysical Research Letters, 26(14), 2093-2096.

147. Marchandon, M., Hollingsworth, J., & Radiguet, M. (2021). Origin of the shallow slip deficit on a strike slip fault: Influence of elastic structure, topography, data coverage, and noise. Earth and Planetary Science Letters, 554, 116696.

148. Marone, C. (1998). Laboratory-derived friction laws and their application to seismic faulting. Annual Review of Earth and Planetary Sciences, 26(1), 643-696.

149. McGill, S., Dergham, S., Barton, K., Berney-Ficklin, T., Grant, D., Hartling, C., ... & Williams, J. (2002). Paleoseismology of the San Andreas fault at Plunge Creek, near San Bernardino, southern California. Bulletin of the Seismological Society of America, 92(7), 2803-2840.

150. McQuillan, H. (1973). Small-scale fracture density in Asmari Formation of southwest Iran and its relation to bed thickness and structural setting. AAPG Bulletin, 57(12), 2367-2385.

151. Michel, R., & Avouac, J. P. (2006). Coseismic surface deformation from air photos: The Kickapoo step over in the 1992 Landers rupture. Journal of Geophysical Research: Solid Earth, 111(B3).

152. Milliner, C. W., Dolan, J. F., Hollingsworth, J., Leprince, S., Ayoub, F., & Sammis, C. G. (2015). Quantifying near-field and off-fault deformation patterns of the 1992 Mw 7.3 L anders earthquake. Geochemistry, Geophysics, Geosystems, 16(5), 1577-1598.

153. Milliner, C. W. D., Dolan, J. F., Hollingsworth, J., Leprince, S., & Ayoub, F. (2016). Comparison of coseismic near-field and off-fault surface deformation patterns of the 1992 Mw 7.3 Landers and 1999 Mw 7.1 Hector Mine earthquakes: Implications for controls on the distribution of surface strain. Geophysical Research Letters, 43(19), 10-115.

154. Milliner, C., Bürgmann, R., Inbal, A., Wang, T., & Liang, C. (2020). Resolving the kinematics and moment release of early afterslip within the first hours following the 2016 Mw 7.1 Kumamoto earthquake: Implications for the shallow slip deficit and frictional behavior of aseismic creep. Journal of Geophysical Research: Solid Earth, 125(9), e2019JB018928.

155. Milliner, C., Donnellan, A., Aati, S., Avouac, J. P., Zinke, R., Dolan, J. F., ... & Bürgmann, R. (2021). Bookshelf kinematics and the effect of dilatation on fault zone inelastic deformation: Examples from optical image correlation measurements of the 2019 Ridgecrest earthquake sequence. Journal of Geophysical Research: Solid Earth, 126(3), e2020JB020551.

156. Milner, K. R., Shaw, B. E., & Field, E. H. (2022). Enumerating plausible multifault ruptures in complex fault systems with physical constraints. Bulletin of the Seismological Society of America, 112(4), 1806-1824.

157. Mitchell, T. M., & Faulkner, D. R. (2009). The nature and origin of off-fault damage surrounding strike-slip fault zones with a wide range of displacements: A field study from the Atacama fault system, northern Chile. Journal of Structural Geology, 31(8), 802-816.

158. Mooney, W. D., & Ginzburg, A. (1986). Seismic measurements of the internal properties of fault zones. Pure and Applied Geophysics, 124, 141-157.

159. Nevitt, J. M., Brooks, B. A., Catchings, R. D., Goldman, M. R., Ericksen, T. L., & Glennie, C. L. (2020). Mechanics of near-field deformation during co-and post-seismic shallow fault slip. Scientific Reports, 10(1), 5031.

160. Nissen, E., Maruyama, T., Arrowsmith, J. R., Elliott, J. R., Krishnan, A. K., Oskin, M. E., & Saripalli, S. (2014). Coseismic fault zone deformation revealed with differential lidar: Examples from Japanese Mw$\sim$ 7 intraplate earthquakes. Earth and Planetary Science Letters, 405, 244-256.

161. Nurminen, F., Baize, S., Boncio, P., Blumetti, A. M., Cinti, F. R., Civico, R., & Guerrieri, L. (2022). SURE 2.0–New release of the worldwide database of surface ruptures for fault displacement hazard analyses. Scientific Data, 9(1), 729.

162. Odling, N. E., Gillespie, P., Bourgine, B., Castaing, C., Chiles, J. P., Christensen, N. P., ... & Watterson, J. (1999). Variations in fracture system geometry and their implications for fluid flow in fractures hydrocarbon reservoirs. Petroleum Geoscience, 5(4), 373-384.

163. Oglesby, D. D. (2005). The dynamics of strike-slip step-overs with linking dip-slip faults. Bulletin of the Seismological Society of America, 95(5), 1604-1622.

164. Oglesby, D. (2008). Rupture termination and jump on parallel offset faults. Bulletin of the Seismological Society of America, 98(1), 440-447.

165. Okamura, Y., Ishiyama, T., & Yanagisawa, Y. (2007). Fault-related folds above the source fault of the 2004 mid-Niigata Prefecture earthquake, in a fold-and-thrust belt caused by basin inversion along the eastern margin of the Japan Sea. Journal of Geophysical Research: Solid Earth, 112(B3).

166. Okuwaki, R., Yuji, Y., Taymaz, T., & Hicks, S. P. (2023). Multi-scale rupture growth with alternating directions in a complex fault network during the 2023 south-eastern Türkiye and Syria earthquake doublet.

167. Onderdonk, N. W., Rockwell, T. K., McGill, S. F., & Marliyani, G. I. (2013). Evidence for seven surface ruptures in the past 1600 years on the Claremont fault at Mystic Lake, northern San Jacinto fault zone, California. Bulletin of the Seismological Society of America, 103(1), 519-541.

168. Onderdonk, N., McGill, S., & Rockwell, T. (2018). A 3700 yr paleoseismic record from the northern San Jacinto fault and implications for joint rupture of the San Jacinto and San Andreas faults. Geosphere, 14(6), 2447-2468.

169. Oskin, M., Perg, L., Blumentritt, D., Mukhopadhyay, S., & Iriondo, A. (2007). Slip rate of the Calico fault: Implications for geologic versus geodetic rate discrepancy in the Eastern California Shear Zone. Journal of Geophysical Research: Solid Earth, 112(B3).

170. Oskin, M. E., Arrowsmith, J. R., Corona, A. H., Elliott, A. J., Fletcher, J. M., Fielding, E. J., ... & Teran, O. J. (2012). Near-field deformation from the El Mayor–Cucapah earthquake revealed by differential LIDAR. Science, 335(6069), 702-705.

171. Oskin, M., Elliot, A., Duan, B., Liu-Zeng, J., Liu, Z., Shao, Y., ... & Elizondo, D. (2015, November). Earthquake gates: Linking rupture length to geologically constrained dynamics of fault complexity, with examples from the Altyn Tagh and San Andreas faults. In Geological Society of America Abstracts with Programs (Vol. 47, No. 7, p. 35).

172. Ostermeijer, G. A., Mitchell, T. M., Aben, F. M., Dorsey, M. T., Browning, J., Rockwell, T. K., ... & Ostermeijer, F. (2020). Damage zone heterogeneity on seismogenic faults in crystalline rock; a field study of the Borrego Fault, Baja California. Journal of Structural Geology, 137, 104016.

173. Page, M. T. (2021). More fault connectivity is needed in seismic hazard analysis. Bulletin of the Seismological Society of America, 111(1), 391-397.

174. Pandey, M. R., Tandukar, R. P., Avouac, J. P., Lave, J., & Massot, J. P. (1995). Interseismic strain accumulation on the Himalayan crustal ramp (Nepal). Geophysical Research Letters, 22(7), 751-754.

175. Panuntun, H., Miyazaki, S. I., Fukuda, Y., & Orihara, Y. (2018). Probing the Poisson's ratio of poroelastic rebound following the 2011 M w 9.0 Tohoku earthquake. Geophysical Journal International, 215(3), 2206-2221.

176. Peacock, D. C. P., & Parfitt, E. A. (2002). Active relay ramps and normal fault propagation on Kilauea Volcano, Hawaii. Journal of structural geology, 24(4), 729-742.

177. Perrin, C., Waldhauser, F., & Scholz, C. H. (2021). The shear deformation zone and the smoothing of faults with displacement. Journal of Geophysical Research: Solid Earth, 126(5), e2020JB020447.

178. Poliakov, A. N., Dmowska, R., & Rice, J. R. (2002). Dynamic shear rupture interactions with fault bends and off-axis secondary faulting. Journal of Geophysical Research: Solid Earth, 107(B11), ESE-6.

179. Powers, P. M., & Jordan, T. H. (2010). Distribution of seismicity across strike-slip faults in California. Journal of Geophysical Research: Solid Earth, 115(B5).

180. Prush, V. B. (2020). Fault Activity and Mechanical Conditions for Rupture of the Akatengneng Shan Earthquake Gate Along the Altyn Tagh Fault, Northwest China (Doctoral dissertation, University of California, Davis).

181. Qiu, H., Ben-Zion, Y., Catchings, R., Goldman, M. R., Allam, A. A., & Steidl, J. (2021). Seismic imaging of the Mw 7.1 Ridgecrest earthquake rupture zone from data recorded by dense linear arrays. Journal of Geophysical Research: Solid Earth, 126(7), e2021JB022043.

182. Reid, H.F., 1910. The mechanics of the earthquake. In: The California earthquake of April 18, 1906. Rept. State Earthquake Invest. Comm.,Carnegie Inst., Washington, D.C., 192 pp.

183. Richards-Dinger, K., & Dieterich, J. H. (2012). RSQSim earthquake simulator. Seismological Research Letters, 83(6), 983-990.

184. Ross, Z. E., Idini, B., Jia, Z., Stephenson, O. L., Zhong, M., Wang, X., ... & Jung, J. (2019). Hierarchical interlocked orthogonal faulting in the 2019 Ridgecrest earthquake sequence. Science, 366(6463), 346-351.

185. Sarmiento, A., Madugo, D., Bozorgnia, Y., Shen, A., Mazzoni, S., Lavrentiadis, G., Dawson, T., Madugo, C., Kottke, A., Thompson, S., Baize, S., Milliner, C., Nurminen, F., Boncio, P., & Visini, F. (2021). Fault Displacement Hazard Initiative Database, UCLA B. John Garrick Institute for the Risk Sciences, Report GIRS-2021-08, doi: 10.34948/N36P48.

186. Savage, H. M., Shackleton, J. R., Cooke, M. L., & Riedel, J. J. (2010). Insights into fold growth using fold-related joint patterns and mechanical stratigraphy. Journal of Structural Geology, 32(10), 1466-1475.

187. Savage, H. M., & Brodsky, E. E. (2011). Collateral damage: Evolution with displacement of fracture distribution and secondary fault strands in fault damage zones. Journal of Geophysical Research: Solid Earth, 116(B3).

188. Scharer, K. M., Biasi, G. P., Weldon, R. J., & Fumal, T. E. (2010). Quasi-periodic recurrence of large earthquakes on the southern San Andreas fault. Geology, 38(6), 555-558.

189. Scharer, K. M., & Yule, D. (2020). A maximum rupture model for the southern San Andreas and San Jacinto faults, California, derived from paleoseismic earthquake ages: Observations and limitations. Geophysical Research Letters, 47(15), e2020GL088532.

190. Schlische, R. W. (1995). Geometry and origin of fault-related folds in extensional settings. AAPG bulletin, 79(11), 1661-1678.

191. Scott, C. P., Arrowsmith, J. R., Nissen, E., Lajoie, L., Maruyama, T., & Chiba, T. (2018). The M7 2016 Kumamoto, Japan, earthquake: 3-D deformation along the fault and within the damage zone constrained from differential lidar topography. Journal of Geophysical Research: Solid Earth, 123(7), 6138-6155.

192. Scott, C. P., DeLong, S. B., & Arrowsmith, J. R. (2020). Distribution of aseismic deformation along the Central San Andreas and Calaveras faults from differencing repeat airborne lidar. Geophysical Research Letters, 47(22), e2020GL090628.

193. Segall, P., & Pollard, D. D. (1980). Mechanics of discontinuous faults. Journal of Geophysical Research: Solid Earth, 85(B8), 4337-4350.

194. Seitz, G., Weldon II, R., & Biasi, G. P. (1997). The Pitman Canyon paleoseismic record: A re-evaluation of southern San Andreas fault segmentation. Journal of Geodynamics, 24(1-4), 129-138.

195. Shao, Y., Liu-Zeng, J., Oskin, M. E., Elliott, A. J., Wang, P., Zhang, J., ... & Li, Z. (2018). Paleoseismic investigation of the Aksay Restraining Double Bend, Altyn Tagh Fault, and its implication for barrier-breaching ruptures. Journal of Geophysical Research: Solid Earth, 123(5), 4307-4330.

196. Share, P. E., & Ben-Zion, Y. (2018). A bimaterial interface along the northern San Jacinto fault through Cajon Pass. Geophysical Research Letters, 45(21), 11-622.

197. Sharp, I. R., Gawthorpe, R. L., Underhill, J. R., & Gupta, S. (2000). Fault-propagation folding in extensional settings: examples of structural style and synrift sedimentary response from the Suez rift, Sinai, Egypt. Geological Society of America Bulletin, 112(12), 1877-1899.

198. Scholz, C. H. (1974). Post-earthquake dilatancy recovery. Geology, 2(11), 551-554.

199. Shelef, E., & Oskin, M. (2010). Deformation processes adjacent to active faults: Examples from eastern California. Journal of Geophysical Research: Solid Earth, 115(B5).

200. Shi, X., Tapponnier, P., Wang, T., Wei, S., Wang, Y., Wang, X., & Jiao, L. (2019). Triple junction kinematics accounts for the 2016 Mw 7.8 Kaikoura earthquake rupture complexity. Proceedings of the National Academy of Sciences, 116(52), 26367-26375.

201. Shipton, Z. K., Evans, J. P., Abercrombie, R. E., & Brodsky, E. E. (2006). The missing sinks: Slip localization in faults, damage zones, and the seismic energy budget.

202. Sibson, R. H. (1985). Stopping of earthquake ruptures at dilational fault jogs. Nature, 316(6025), 248-251.

203. Sibson, R. H. (2001). Seismogenic framework for hydrothermal transport and ore deposition.

204. Sieh, K., Jones, L., Hauksson, E., Hudnut, K., Eberhart-Phillips, D., Heaton, T., ... & Zachariasen, J. (1993). Near-field investigations of the Landers earthquake sequence, April to July 1992. Science, 260(5105), 171-176.

205. Simpson, R. W, M. Barall, J. Langbein, J. R. Murray, & M. J. Rymer (2006). San Andreas fault geometry in the Parkfield, California, re- gion, Bull. Seism. Soc. Am. 96, no. 4B, S28–S37.

206. Socquet, A., Hollingsworth, J., Pathier, E., & Bouchon, M. (2019). Evidence of supershear during the 2018 magnitude 7.5 Palu earthquake from space geodesy. Nature Geoscience, 12(3), 192-199.

207. Stearns, D.W., 1968, Certain aspects of fractures in natu- rally deformed rocks, in Riecker, R.E., ed., Rock mechanics seminar: Bedford, Terrestrial Sciences Laboratory, p. 97–118.

208. Swanson, P. L. (1984). Subcritical crack growth and other time-and environment-dependent behavior in crustal rocks. Journal of Geophysical Research: Solid Earth, 89(B6), 4137-4152.

209. Szeliga, W., Bilham, R., Kakar, D. M., & Lodi, S. H. (2012). Interseismic strain accumulation along the western boundary of the Indian subcontinent. Journal of Geophysical Research: Solid Earth, 117(B8).

210. Taufiqurrahman, T., Gabriel, A. A., Li, D., Ulrich, T., Li, B., Carena, S., ... & Gallovič, F. (2023). Dynamics, interactions and delays of the 2019 Ridgecrest rupture sequence. Nature, 1-8.

211. Tavani, S., Balsamo, F., & Granado, P. (2018). Petroleum system in supra-salt strata of extensional forced-folds: A case-study from the Basque-Cantabrian basin (Spain). Marine and Petroleum Geology, 96, 315-330.

212. Teran, O. J., Fletcher, J. M., Oskin, M. E., Rockwell, T. K., Hudnut, K. W., Spelz, R. M., ... & Morelan, A. E. (2015). Geologic and structural controls on rupture zone fabric: A field-based study of the 2010 Mw 7.2 El Mayor–Cucapah earthquake surface rupture. Geosphere, 11(3), 899-920.

213. Titus, S. J., Crump, S., McGuire, Z., Horsman, E., & Housen, B. (2011). Using vertical axis rotations to characterize off-fault deformation across the San Andreas fault system, central California. Geology, 39(8), 711-714.

214. Titus, S. J., Chapman, W., Horst, A. J., Brown, M., & Davis, J. R. (2018). Distributed deformation in an oceanic transform system: Applying statistical tools to structural and paleomagnetic data near the Húsavík-Flatey fault, northern Iceland. Tectonics, 37(10), 3986-4017.

215. Twiss, R. J., & Moores, E. M. (1992). Structural geology. Macmillan.

216. Villemin, T., & Bergerat, F. (2013). From surface fault traces to a fault growth model: The Vogar Fissure Swarm of the Reykjanes Peninsula, Southwest Iceland. Journal of Structural Geology, 51, 38-51.

217. Wang, K., & Bürgmann, R. (2020). Co-and early postseismic deformation due to the 2019 Ridgecrest earthquake sequence constrained by Sentinel-1 and COSMO-SkyMed SAR data. Seismological Research Letters, 91(4), 1998-2009.

218. Wesnousky, S. G. (1988). Seismological and structural evolution of strike-slip faults. Nature, 335(6188), 340-343.

219. Wesnousky, S. G. (2006). Predicting the endpoints of earthquake ruptures. Nature, 444(7117), 358-360.

220. Wheeler, G. (1939). Triassic fault-line deflections and associated warping. The Journal of Geology, 47(4), 337-370.

221. Willsey, S. P., Umhoefer, P. J., & Hilley, G. E. (2002). Early evolution of an extensional monocline by a propagating normal fault: 3D analysis from combined field study and numerical modeling. Journal of Structural Geology, 24(4), 651-669.

222. White, I. R., & Crider, J. G. (2006). Extensional fault-propagation folds: Mechanical models and observations from the Modoc Plateau, northeastern California. Journal of Structural Geology, 28(7), 1352-1370.

223. Wilson, B., Dewers, T., Reches, Z. E., & Brune, J. (2005). Particle size and energetics of gouge from earthquake rupture zones. Nature, 434(7034), 749-752.

224. Withjack, M. O., Olson, J., & Peterson, E. (1990). Experimental models of extensional forced folds. Aapg Bulletin, 74(7), 1038-1054.

225. Wright, T., Parsons, B., & Fielding, E. (2001). Measurement of interseismic strain accumulation across the North Anatolian Fault by satellite radar interferometry. Geophysical Research Letters, 28(10), 2117-2120.

226. Wu, C., Peng, Z., & Ben-Zion, Y. (2009). Non-linearity and temporal changes of fault zone site response associated with strong ground motion. Geophysical Journal International, 176(1), 265-278.

227. Xu, X., Tong, X., Sandwell, D. T., Milliner, C. W., Dolan, J. F., Hollingsworth, J., ... & Ayoub, F. (2016). Refining the shallow slip deficit. Geophysical Journal International, 204(3), 1867-1886.

228. Xu, X., Sandwell, D. T., Ward, L. A., Milliner, C. W., Smith-Konter, B. R., Fang, P., & Bock, Y. (2020). Surface deformation associated with fractures near the 2019 Ridgecrest earthquake sequence. Science, 370(6516), 605-608.

229. Xu, X., Liu, D., & Lavier, L. (2023). Constraining fault damage zone properties from geodesy: A case study near the 2019 Ridgecrest earthquake sequence. Geophysical Research Letters, 50(5), e2022GL101692.

230. Yang, H., Li, Z., Peng, Z., Ben-Zion, Y., & Vernon, F. (2014). Low-velocity zones along the San Jacinto Fault, Southern California, from body waves recorded in dense linear arrays. Journal of Geophysical Research: Solid Earth, 119(12), 8976-8990.

231. Yuan, Z., Liu-Zeng, J., Wang, W., Weldon II, R. J., Oskin, M. E., Shao, Y., ... & Zhang, J. (2018). A 6000-year-long paleoseismologic record of earthquakes along the Xorkoli section of the Altyn Tagh fault, China. Earth and Planetary Science Letters, 497, 193-203.

232. Yule, D. (2009). The enigmatic San Gorgonio Pass. Geology, 37(2), 191-192.

233. Yule, D., Scharer, K., Sieh, K., Wolff, L., McBurnett, P., Ramzan, S., ... & Desjarlais, I. (2014). Paleoseismology and slip rate of the San Andreas fault system at San Gorgonio Pass. In Geological Society of America abstracts with programs (Vol. 46, No. 5, p. 25). Geological Society of America.

234. Zinke, R., Hollingsworth, J., & Dolan, J. F. (2014). Surface slip and off-fault deformation patterns in the 2013 MW 7.7 B alochistan, P akistan earthquake: Implications for controls on the distribution of near-surface coseismic slip. Geochemistry, Geophysics, Geosystems, 15(12), 5034-5050.

235. Zinke, R., Dolan, J. F., Van Dissen, R., Grenader, J. R., Rhodes, E. J., McGuire, C. P., ... & Hatem, A. E. (2015). Evolution and progressive geomorphic manifestation of surface faulting: A comparison of the Wairau and Awatere faults, South Island, New Zealand. Geology, 43(11), 1019-1022.

236. Zinke, R., Hollingsworth, J., Dolan, J. F., & Van Dissen, R. (2019). Three-dimensional surface deformation in the 2016 MW 7.8 Kaikōura, New Zealand, earthquake from optical image correlation: Implications for strain localization and long-term evolution of the Pacific-Australian plate boundary. Geochemistry, Geophysics, Geosystems, 20(3), 1609-1628.

Chapter 1: The role of earthquake gates in strike-slip events

Abstract

Earthquake gates act as barriers to rupture propagation, where material properties, rupture dynamics, and the availability and geometry of neighboring faults control the probability of throughgoing rupture. We map step-overs, bends, gaps, splays, and strands from the surface ruptures of 31 strike-slip earthquakes at 1:50,000 scale, classifying each population into breached and unbreached groups. We then calculate passing probability as a function of geometry for each group. We find that step-overs, gaps, and single bends halt ruptures more effectively than double bends and splays. We also observe that <20% of the ruptures stopped on straight fault segments. Based on our modeled probabilities, we estimate an event likelihood for each event as the joint passing probability of its breached gates and the probability of stopping on a straight segment along its rupture length. Event likelihood decreases with increasing magnitude, where the size and spacing of earthquake gates along the rupture support a barrier model for controlling earthquake size. We find that Coulomb stress change on a receiver fault describes the population of breached and unbreached step-overs observed, where ruptures seldom renucleate on receiver faults with stress change below a critical threshold of 20% of the stress drop. The distribution of breached and unbreached bends observed may be explained by the frictional strength amplification caused by the change in strike angle. At the scale of mapping considered here, double-bend length does not affect earthquake rupture arrest. Together, our probabilistic and mechanistic outcomes can be used to validate barrier breaching frequencies and conditions in long-term rupture simulators.

Introduction

Earthquake surface ruptures are composed of fault segments bound by gaps, step-overs, bends, and splay faults (Lettis et al., 2002; Wesnousky, 2006; Manighetti et al., 2007; Klinger, 2010; Oskin et al., 2012; Perrin et al., 2016; Hamling et al., 2017; Ross et al., 2019). These geometrical complexities, or earthquake gates, can act as barriers to rupture propagation, where the history of past earthquakes, rupture dynamics, material properties, and the availability and geometry of neighboring fault segments dictate the probability of throughgoing rupture. The role of geometrical complexities as earthquake gates (segment boundaries) was recognized from early rupture and fault maps (Bakun et al., 1980; Segall and Pollard, 1980; King and Nabelek, 1985; Sibson, 1985; Barka et al., 1988; Wesnousky, 1988). These observations motivated systematic mapping of geometrical complexities from surface ruptures to better constrain their relationship with earthquake propagation and arrest (e.g. Wesnousky, 2006; Wesnousky, 2008; Biasi and Wesnousky,

2016, 2017, 2021). Dynamic rupture models supplement empirical work by constraining the role of material properties and rupture dynamics in the mechanical behavior of earthquake gates (e.g. Harris and Day, 1993; Shaw and Dieterich, 2007; Lozos et al., 2011; Lozos et al., 2016; Share and Ben-Zion, 2018; Liu et al., 2021). Long-term paleoseismic and slip rate studies can decode the multi-cycle history of an earthquake gate, though this work is currently limited to a few continental fault systems (e.g. Shao et al., 2018; Elliott et al., 2018; Scharer and Yule, 2020; Howarth et al., 2021).

For continental strike-slip earthquakes where the down-dip extent of rupture is quickly saturated by the thickness of the seismogenic zone, earthquake gates pose an important control on rupture length, and thus on maximum magnitude. Therefore, the conditional passing probability of an earthquake gate given its geometry is one of the key ingredients in long-term rupture simulators used to generate forecasts of the extent, size, and frequency of events across a fault system (Field et al., 2015; Milner et al., 2022).

Wesnousky (2006) showed that $\sim$2/3 of the surface ruptures analyzed from a compilation of 22 strike-slip events ended in step-overs, where rupture propagation through step-overs occurred in $\sim$40% of the cases and did not occur past step-overs wider than 3-4 km. Biasi and Wesnousky (2016) found that 90% of the rupture termini occurred at mapped discontinuities. Within this dataset, step-overs wider than 4 km were breached only 8% of the time. Harris and Day (1993), using dynamic rupture models, found that larger releasing than restraining step-overs could be breached by propagating ruptures, a result of dynamic unclamping (e.g. Oglesby, 2005).

Propagation through bends is easier than through step-overs, as the rupture is not required to jump and renucleate (Magistrale and Day, 1999; Lozos et al., 2011). Biasi and Wesnousky (2017) found from a compilation of surface rupture maps that bends $>25^\circ$ were breached less than half of the time. Lozos et al. (2011) found that releasing bends $\sim<35^\circ$ and restraining bends $\sim<20^\circ$ were frequently breached in dynamic rupture models, though minor rotations in the stress field ($\sim10^\circ$) could force this behavior to switch, making rupture propagation easier through restraining bends instead of releasing bends. Similarly, Poliakov et al. (2002) and later Kame et al. (2003) found that ruptures prefer to branch onto splays on extensional configurations, though this behavior switched to compressional splays being favored as the angle between the maximum compressive stress and the fault decreases. They also found that wide splay angles could be easily breached but small splays were hard to breach due to stress interactions between the two fault branches. Fast rupture speeds could help overcome the effect of these interactions.

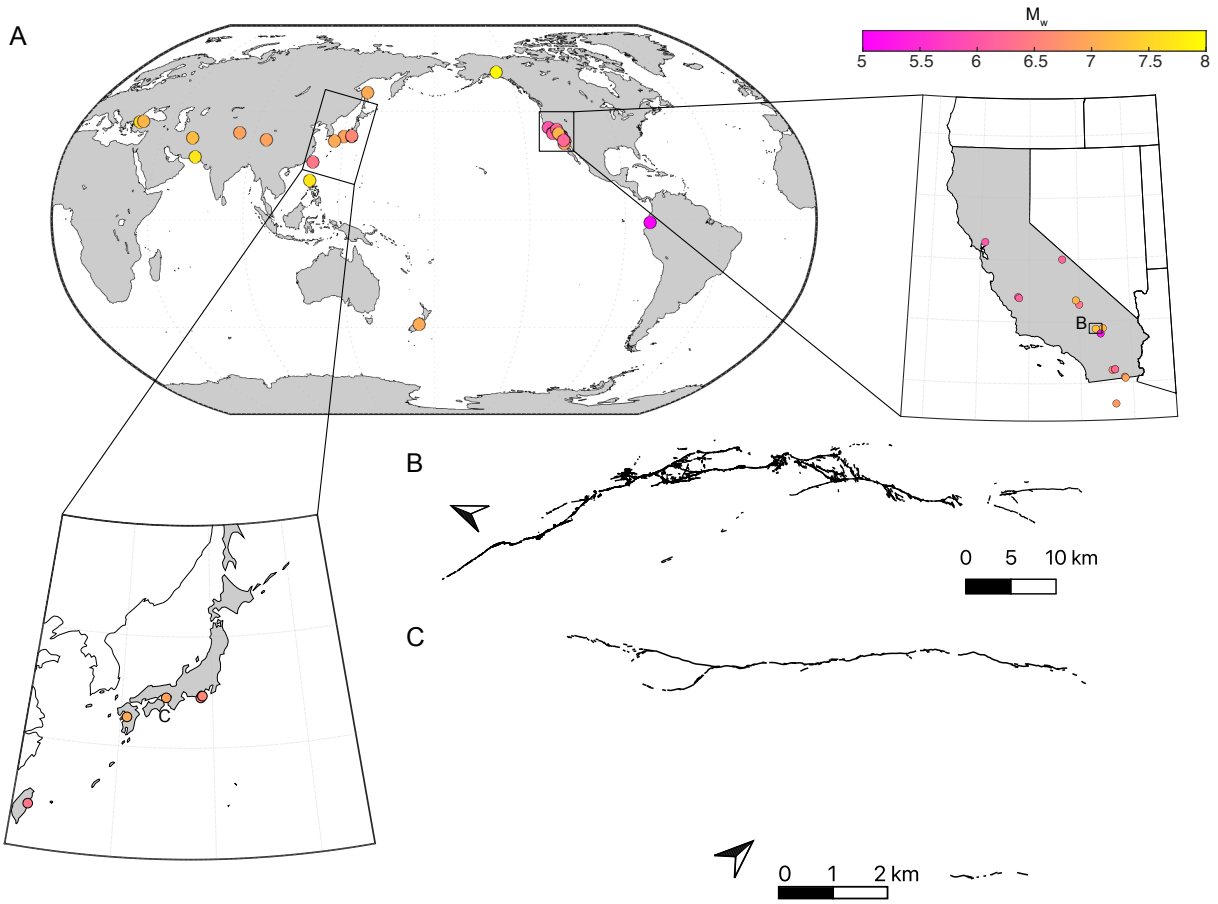

Figure 8: Surface rupturing strike-slip earthquakes in the FDHI database (Sarmiento et al., 2021). A: Epicentral locations of events, color-coded by moment magnitude. The insets show events in California, Baja California, and Japan. B: Surface rupture map of the Landers 1992 event in California. C: Surface rupture map of the 1995 Great Kobe earthquake in Japan, including a strand located 7 km from the main rupture. Note scale difference for these events.

Historical earthquake rupture maps provide essential tests for geometrical controls on rupture propagation. Previous work characterizing passing probabilities relied on coarse early rupture maps (Wesnousky, 2006) or opted to simplify rupture maps into ∼7-kilometer-long segments before characterizing earthquake gates to only capture crustal-scale geometrical complexity (Biasi and Wesnousky, 2016). In this study, we undertake mapping of geometrical complexities at 1:50,000 scale, which roughly corresponds with features > 100-500 meters in wavelength. While mapping fine-scale (meter) geometrical complexity is not relevant mechanically, as small discontinuities may be attributed to very local effects, earthquake gates in the hundreds of meters length scale have not been characterized and may be of mechanical importance. For example, the 2014 Napa earthquake terminated in a 750-meter-wide step-over, too small to be included in previous studies (e.g. Biasi and Wesnousky, 2016). Geometrical complexity also contains information about rupture

dynamics, where sub-kilometer gaps on the surface rupture have been linked to the transition to supershear rupture velocities (Jara et al., 2021).

With new surface rupture maps available from recent earthquakes and standardized ones for older events, it is now possible to characterize additional earthquake gates and revisit previous measurements at finer scales. We map bends, step-overs, gaps, and two additional types of earthquake gates: splays, and strands, using the unified Fault Displacement Hazard Initiative rupture database (Sarmiento et al., 2021). From these measurements, we analyze the effectiveness of each feature as an earthquake gate at the mapping scale and, for those with distinct breached and unbreached populations, we estimate the passing probabilities of the class of earthquake gate as a function of its geometry. Using these probability distributions, we analyze the joint probability of all of the observed breached gates and straight segments for each event and discuss the relationship of these probabilities to the observed earthquake magnitude and surface rupture length. We conclude by analyzing the stress conditions under which bends and step-overs are breached.

Methods

Earthquake Gate Mapping

The Fault Displacement Hazard Initiative (FDHI) database is hosted at and maintained by the Natural Hazards Risk & Resilience Research Center at the University of California, Los Angeles (Sarmiento et al., 2021). The database contains rupture maps and displacement, lithology, and other information for sixty-six surface-rupturing crustal earthquakes, with moment magnitudes ranging from 5.0 to 8.0. Thirty-one of these events are strike-slip (Figure 8). The database was compiled with a focus on rupture detail, completeness, accuracy, and consistency across datasets. Surface ruptures are mapped to 1-meter precision in the database, though individual maps differ in the level of detail captured in the surface rupture (e.g. Figure 8, B and C, and 9, B). This variability is in part related to the different degrees of complexity in the hosting fault system, and in part a result of differences in mapping methods and areal coverage across ruptures. We map earthquake gates from the surface ruptures in the FDHI database at a 1:50,000 scale, which roughly corresponds to mapping features with lengths exceeding 100-500 meters. At this scale, we expect the level of detail across ruptures to be roughly comparable.

Prior work has either relied on simplified rupture maps (e.g. Wesnousky, 2006) or simplified ruptures to segments long enough ($\sim$7 km) to be bounded by earthquake gates representative of the full seismogenic zone (Biasi and Wesnousky, 2017). We map earthquake gates directly from the surface rupture maps, without simplifying the rupture traces. An important consequence of our scale of choice (1:50,000) is that larger features (for example, the large, regional-scale releasing bend in the Balochistan earthquake which spans 6

km) are mapped into its smaller constituents that occur at the mapping scale (i.e. several shorter bends that make up the regional one).

The surface rupture maps in the FDHI database include ruptures classified as primary and distributed. The Landers and Ridgecrest (foreshock and mainshock) earthquakes have a substantially larger amount of distributed ruptures mapped than the remaining events. For consistency between events in the analysis, we do not consider the distributed ruptures from these events in our earthquake gate mapping. We characterize gates as restraining or releasing when possible, depending on the volumetric deformation fostered by the type of slip and the geometry of the fault segments. To do this, we assume all fault segments involved in the rupture have strike-slip kinematics consistent with the focal mechanism for the event. This is a reasonable approximation for all the strike-slip ruptures in the FDHI database except for the Denali earthquake, from which we remove the portion of the rupture that occurred on the Susitna Glacier Thrust, where the earthquake initiated (e.g. Crone et al., 2004). We also do not considered the zone of secondary, triggered normal faulting on the Volcanic Tableland west of the main rupture of the 1986 Chalfant earthquake (Lienkaemper et al., 1987).

We characterize five different types of earthquake gates in this study: step-overs, gaps, bends, splays, and strands (Figure 9). We distinguish between breached features where the rupture transferred through and continued for at least 1 kilometer, and unbreached features, where the rupture halted immediately or within 1 km past the gate. For the case of splays, we classify cases where the rupture transferred onto a splay (regardless of whether it also continued on the main fault), as ruptured and instances where an available intersecting splay fault was foregone as unruptured. Note the use of different terminology from breached and unbreached to indicate that at least one fault strand was always active past the splay (Figure 9).

For each of the gates of interest, we measure the relevant geometrical attribute. For bends and splays, this is the bend angle, which is the difference between the fault strike as it enters the feature and the fault strike as it exits the feature. In the case of multi-stranded bends, we map the bend strand with the smallest angle. We distinguish between single bends, where the fault strike changes once, and double bends, where the fault strike changes for a segment and then returns to the original strike (see examples in Figure 9). Step-overs occur where a fault ends and the rupture is forced to jump onto a neighboring segment or come to arrest. We also map locations where the rupture activates parallel to subparallel neighboring fault strands without reaching the terminus of the principal fault. By definition, strands may only exist as breached features, as there was no fault terminus that forced a jump. For step-overs and strands, we measure the distance between parallel fault segments at their minimum, orthogonal to the fault segments when possible. For gaps, we measure the length of the gap between the active rupture and another fault, or between parts of the active rupture if breached, in the fault-parallel direction. Note that we do not have the ability to distinguish

gaps that represent pauses on the rupture on the same fault versus gaps that represent the spacing between two sequential faults of parallel strike.

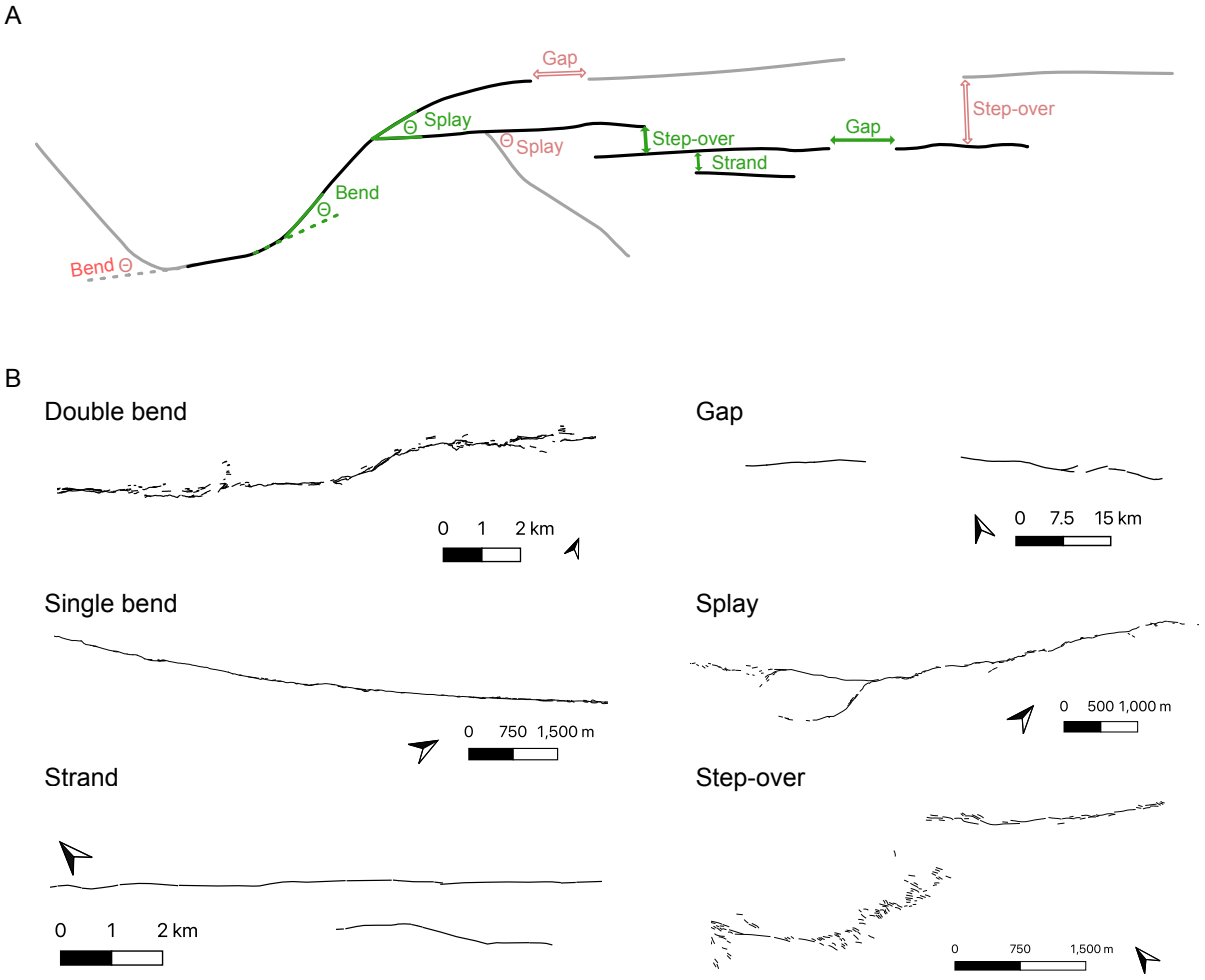

Figure 9: Earthquake gates mapped in this study. a: Simplified cartoon showing the features characterized in this study. The black lines denote the surface rupture whereas the light grey lines represent the regional faults that did not rupture during the event. The widths, lengths, and angles measured are shown in green for the breached features and in red for the unbreached features. b: Examples of breached earthquake gates from the FDHI surface rupture database (Sarmiento et al., 2021). The single and double bends are from the 2013 Balochistan earthquake in Pakistan. The strand is from the Parkfield 1996 surface rupture along the San Andreas Fault, the gap is from the 2010 Yushu earthquake in China, the splay is from the 1995 Kobe event in Japan, and the step-over is from the 1968 Borrego earthquake in California.

We rely on different active fault databases to characterize unbreached features, where we measure the angle or distance between the ruptured fault and unruptured active faults in the database. The reference databases we use are listed in Supplementary Table 2. For the United States, the resolution of the regional faults associated with the events in this study in the Qfaults database is comparable to the resolution of the primary rupturing faults in the FDHI database. For the Darfield event in New Zealand, we use the NZAFD

database, mapped at 1:250,000 (Langridge et al., 2016). The Active Faults of Eurasia Database (AFEAD) database for Eurasia, which we use for events in Turkey and Asia, is mapped at 1:500,000 scale (Bachmanov et al., 2021). Last, the GEM database, which we use only for the San Miguel and Pisayambo earthquakes in Mexico and Ecuador respectively, is mapped at 1:1,000,000 scale (Styron and Pagani, 2020). In the interest of classifying unbreached features as restraining or releasing, when the inactive fault kinematics are unknown, we assume these are the same as the rupturing faults'. When two unbreached step-overs may be measured at a fault's terminus, we map both of them, following the choice of previous workers (e.g. Wesnousky, 2006). Note that some events (e.g. Galway Lake and Ridgecrest foreshock, Figure 8) have unbreached step-overs at both of their termini with the same fault (e.g. the faults in the Landers event and the Garlock fault respectively), in which case both unbreached step-overs are mapped. When a gap and a step-over of the same size exist, and one gets breached but the other one does not, we map both the breached and unbreached features. The same occurs where there is a bend but the rupture instead skips the bend and jumps ahead to a more straight portion of the fault. This only occurs in the case of very similarly sized earthquake gates available at the same location, otherwise, we only map the smallest gate present.

Passing Probability and Event Likelihood Estimates

To determine whether the forms of geometrical complexity we map (Figure 9) act as barriers to rupture propagation, we analyze the distribution of breached and unbreached gates in terms of the geometrical attribute measured (angle or length). We look at the cumulative distribution functions of breached and unbreached gates and use a Kolmogorov-Smirnoff (KS) test to determine whether the breached and unbreached populations are statistically different.

For those features where the breached and unbreached populations are statistically different, we compute passing probabilities as a function of the geometrical characteristics of the gate. To do so, we use a logistic function, a model that describes the probability of a binary outcome (breached versus unbreached) as a continuous function of the geometrical properties of an earthquake gate. To fit logistic regressions through our data, we use the Python package scikit learn (Pedregosa et al., 2011). When fitting the regressions for earthquake gates that have very different numbers of breached and unbreached elements, we adjust the weight of each data point inversely proportional to the frequency of the class it belongs to. An advantage of using logistic regressions over past methods is that estimating probabilities does not rely on arbitrary binning of the data. We evaluate the performance of our logistic models for each type of earthquake gate using Receiver Operating Characteristic (ROC) scores and confusion matrices, which is standard procedure for these models.

To consider the role of earthquake gates in controlling earthquake moment magnitude, we introduce the

concept of earthquake likelihood as the joint probabilities of all the breached gates in an event:

$$log_{10}P_{EQ} = log_{10}P_c + \sum_{i=1}^{n} log_{10}P_i \tag{1}$$

Expressed as their log-likelihood (equation 1). Where each probability P_i is estimated by making a prediction for a gate of those characteristics from the logistic models. We also account for the probability of a rupture stopping on a straight segment between gates. To consider this, we compute the probability of ruptures continuing past a straight fault of length L:

$$P_c = (1 - P_s)^L \tag{2}$$

where L is the surface rupture length and P_s is given by:

$$P_s = \frac{n_{st}}{\Sigma L} \tag{3}$$

where n_{st} is the number of rupture termini on straight segments and ΣL is the total rupture length of all events combined. We find that $P_s = 8.16 \times 10^{-6}$ and for a rupture of length L, $log_{10}P_c \approx -\frac{P_s}{2.3}L$.

Distribution of earthquake gates

We mapped step-overs, bends, strands, gaps, and splays from the 31 strike-slip ruptures in the FDHI database (Sarmiento et al., 2021). To consider the size and geometry distribution of the earthquake gates we map, we estimate empirical cumulative distribution functions (ECDFs) for each population (bold lines in Figure 10). We find that the ECDFs are well fitted by log-normal distributions, shown by the dotted lines in Figure 10. Next, we describe the characteristics of the breached and unbreached groups for each type of gate, as well as restraining and releasing categories when available. We use the Kolmogorov-Smirnoff (KS) test to assess whether different subset groups of an earthquake gate are statistically different. We use the p-value returned by the test, which is the probability of rejecting the null hypothesis that samples in the two subset groups were drawn from the same distribution. The convention for statistical significance is $p<0.05$.

We mapped a total of 68 step-overs, where 20 are releasing and 48 are restraining. The widest breached step-over is a 1.4 km wide restraining step-over from the 2013 Balochistan earthquake. Figure 10 (top left) shows the cumulative distribution functions for breached and unbreached step-overs separated into restraining and releasing subgroups. The breached and unbreached step-over populations are distinct, though the restraining and releasing groups are statistically indistinguishable (p-values of 0.7 and 0.4 for breached and unbreached populations respectively). We also map 45 strands, the bulk of which are within 2 km of the

rupturing fault, though an exceptional case occurs where a strand is activated over 11 km from the rupturing fault during the Izmit earthquake.

We mapped a total of 153 gaps, where only 6 were unbreached (Figure 10). The largest breached gap we map is over 15 km long and is associated with the Yushu earthquake. Despite the low number of unbreached gaps mapped, the breached and unbreached CDFs are statistically distinct, with a p-value of 0.02. Mapping an unbreached gap requires the rupturing fault and faults of parallel strike ahead of it to have been mapped in the regional map to a sufficient resolution to include gaps in the fault system. We posit the low number of unbreached gaps we map reflects the limited resolution of the regional fault maps.

We map a total of 695 bends and analyze these separated into restraining and releasing, and single and double categories (Figure 10). The restraining and releasing classification applies only to double bends since the rupture propagation direction would need to be known to classify single bends. The largest breached single bend is 50° and the largest breached double bend is 47° and releasing. The largest restraining bend we map is 38°. Notably, we map only 17 bends (breached or unbreached) larger than 40°. Similarly to the step-over case, the breached and unbreached single and double bends are statistically different ($p=1.7x10^{-13}$ and p=0.01 respectively), but the restraining and releasing populations are not (p-values of 0.3 and 0.6 for breached and unbreached respectively). We map 71 splays. With a p-value of 0.06, the splays that were ruptured versus those that were foregone are not statistically different.

An important difference between characterizing earthquake gates from simplified rupture maps and the detailed rupture maps in the FDHI database is that the simplified rupture maps tend to overestimate the size of the earthquake gate. For example, the restraining step-over in the center of the Borrego earthquake rupture (Figure 9b) was measured as a 1.5 km wide step-over from a simplified map in Wesnousky (2006) whereas we measure its width to be only ∼800 meters. The Napa earthquake terminated on a step-over smaller than 1 km, which we map here but was not included in Biasi and Wesnousky (2017) because they only considered step-overs wider than 1 km. The opposite occurs for a few rupture termini, where Wesnousky (2006) mapped unbreached step-overs but we note the fault continued for over 1 km past the rupture terminus in the updated regional maps, so the events did not end at their mapped earthquake gate. This is the case, for example, for the northern tip of the 1968 Borrego earthquake, the southern tip of the Superstition Hills earthquake, and the southern terminus of the Imperial 1940 event. With the more refined maps, several of the step-overs mapped in previous work appear as hard-linked, so we no longer classify these as step-overs, but as breached double bends or splays instead, depending on what feature achieves the hard linkage. This is the case for a previously mapped step-over in the middle of the Superstition Hills surface rupture or several of the steps in the Landers earthquake which are hard linked by splay faults and were previously defined as "complex step-overs" (Biasi and Wesnousky, 2016).

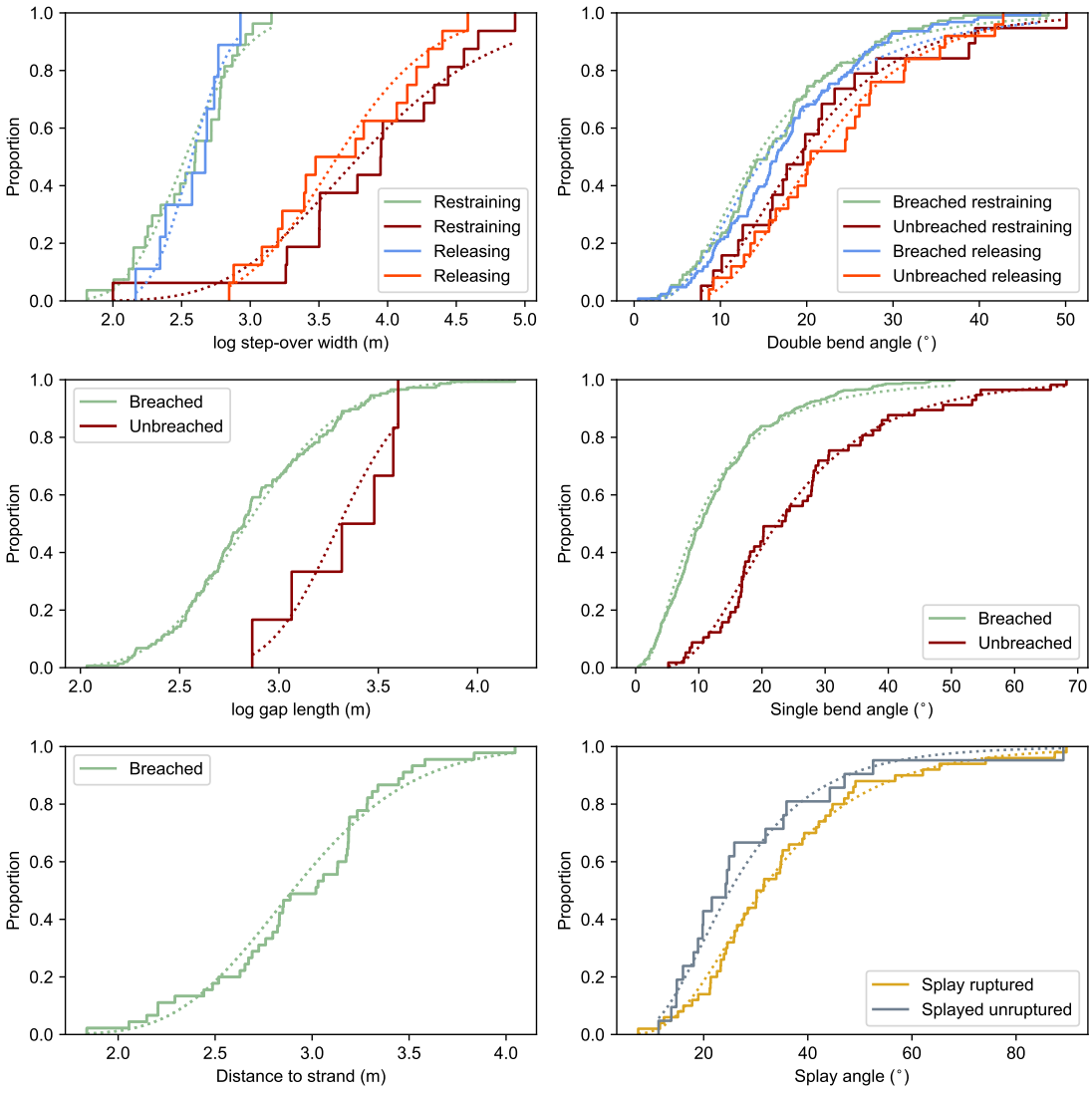

Figure 10: The solid lines show the empirical cumulative distribution function for the earthquake gates mapped in this study. Breached features are indicated in green or blue, and unbreached features are in red or orange. The dotted lines show a log-normal cumulative distribution fit for each ECDF. Top left: Restraining and releasing step-overs, parameterized based on the logarithmic (base 10) of width. Top right: Gap length. Middle left: Strands. Middle right: Double bends, separated into restraining and releasing categories, parameterized based on the bend angle. Bottom left: Single bends. Bottom right: Splays, separated into ruptured or unruptured.

Earthquake gates are not stationary features in the long-term evolution of faults. A reasonable expectation is that the number of earthquake gates on a fault will decrease as geometrical complexity gets smoothed with increasing slip (e.g. Wesnousky, 1988; Dolan and Haravitch, 2014; Perrin et al., 2021). As part of their evolution, step-overs can become hard-linked by fault segments, evolving into double bends (an example of a recently hard-linked step-over can be seen in Figure 15 in the appendix). We analyse our bend population by looking at two additional geometrical characteristics, a bend length (Lozos, 2011), and a proxy step-over

width (Figure 15 in the appendix). When we parameterize bends by their length or proxy step-over width (Figure 16 in the appendix), we find no distinguishing differences between the breached and unbreached bend populations. This suggests that step-overs that evolve into double bends become mechanically different features with much lower effectiveness as an earthquake gate. A potential implication of this observation is that the hard linkage of step-overs we observe at the surface persists at depth. This suggests that earthquake gates of small (<1 km) dimensions can span the entire seismogenic zone and play a role in rupture dynamics.

Rupture termination sometimes occurs on a straight portion of a fault, absent of earthquake gates, where the active fault continues for at least one kilometer past the rupture tip. This is the case for <20% of the events in this study, a result comparable to the 10% of Biasi and Wesnousky (2016).

Passing probabilities

For the earthquake gates that have statistically significantly different breached and unbreached populations, we estimate passing probability as a function of geometry (length or angle) using a logistic model. Because restraining and releasing features are not statistically different, we combine these classifications when estimating passing probabilities.

Our logistic regressions (Figure 11) suggest that step-overs wider than ∼1.1 km will be breached less than half of the time. Step-overs larger than 5 km will be breached around <1% of the time, consistent with the fact that they are not observationally documented in the FDHI rupture maps. The number of unbreached gaps we map is very small compared to the number of breached gaps. By weighting the gaps inversely proportional to frequency when fitting the regression (Pedregosa et al., 2011), we are able to balance the disproportionate number of breached and unbreached gaps, and estimate passing probabilities. The logistic models predict that gaps larger than ∼1.2 km will be breached less than half of the time, similar to our prediction for step-overs. Double bends >50° are predicted to be breached less than half of the time. For single bends, this occurs for angles >37°.

We assess the performance of our logistic regressions in predicting whether an earthquake gate will be breached based on its geometry using an ROC score and confusion matrix. ROC scores can range from 0.5 to 1, with increasing numbers indicating that more features have been correctly predicted by the logistic regression. Step-overs are the earthquake gates best described by a logistic model, with an excellent ROC score of 0.96. Gaps and single bends exhibit good ROC scores (>0.8). Double bends are the least well described by their logistic regression, with a poor ROC score of 0.64.

The confusion matrices for each model (figure 18 in the appendix) are consistent with their ROC scores. Only 3/32 unbreached step-overs are mispredicted as breached, whereas only one breached step-over was

mispredicted as unbreached. Therefore, step-over width is a strong predictor of whether a step-over will be breached during earthquake rupture or not. Two of the six unbreached gaps were mispredicted as breached. As previously mentioned, the limited ability to map unbreached gaps limits the applicability of the logistic regressions for this type of earthquake gate. The logistic regressions struggle to predict unbreached bends well as the populations of breached and unbreached bends largely span the same bend angles and are only separated by the changes in the frequency of that angle being breached or unbreached, which makes it difficult to predict with a binary classifier. Therefore, bend angle is only a strong predictor of whether a bend will be breached for gates that are very large in angle.

For step-overs 1.5-2.5, 2.5-3.5, and 3.5-4.5 km wide, Wesnousky (2006) obtained a passing probability of 50%, whereas our passing probabilities for step-overs of those size ranges are ∼33-12%, 5-1%, and <1% respectively. The 50% mark in Biasi and Wesnousky (2016) occurs at 3 km wide step-overs, a value that exceeds the largest observed breached step-overs in this study. The differences between our passing probabilities and those in previous work arise from the use of different rupture maps (simplified versus not) and mapping at a finer scale. Previous work has consistently found that releasing features are breached more easily due to dynamic unclamping (e.g. Harris and Day, 1993). Many of the large releasing step-over (>2 km width) in the surface ruptures we consider were hard-linked and therefore mapped as bends or splays in this study. Restraining step-overs are not as frequently hard-linked. Biasi and Wesnousky found the probability of a rupture propagating past a 25° bend was 50%, consistent with the passing probability estimated by Ozawa et al. (2023) using dynamic rupture models of bends. We predict much larger passing probabilities of >75% for single and double bends of that size, whereas our 50% mark occurs for bend angles exceeding 50° for double bends and 37° for single bends. Figure 19 in the appendix shows a comparison between the passing probabilities for double bends estimated in this study and those in Ozawa et al. (2023) and Biasi and Wesnousky (2017).

Our results suggest that single bends are more effective earthquake gates than double bends. In our work, bend length is not a good predictor of whether a bend will be breached (Figure 17 in the appendix). This may in part be because due to the scale we map at, large bends (such as that from the Balochistan earthquake discussed in the methods section), are broken down into smaller constituent bends. Note that only 25 bends exceeding 2 kilometers in length are contained within our dataset. Lozos (2011) found that all bends shorter than 2 km were breached in dynamic rupture models. For larger bends, trade-offs between bend angles and lengths result in a limiting size and angle at which bends are breached, so that, at a larger scale, double bends are indeed effective earthquake gates.

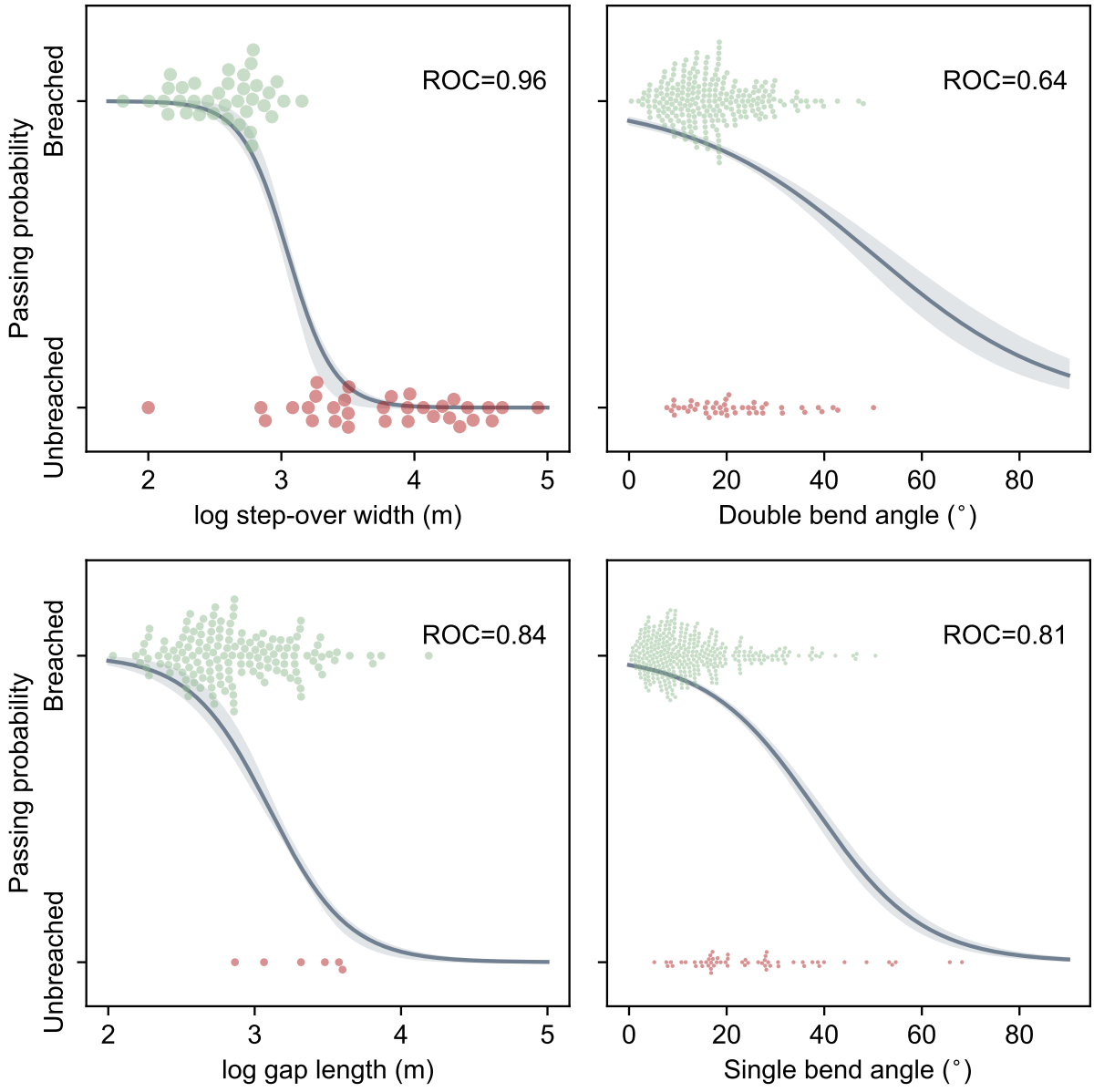

Figure 11: Logistic regressions (grey) showing the passing probabilities of step-overs, gaps, single, and double bends. The data are shown as beehive plots, which show all data points in each classification, breached in green and unbreached in red. The ROC score for each logistic regression is shown on the top right of each panel. The grey shading represents the 1 σ confidence intervals on the logistic fit from a bootstrapping analysis. Restraining and releasing features are combined. Top left: Passing probability as a function of step-over width. The logarithm is base 10. Top right: Passing probability as a function of double bend angle. Bottom left: Passing probability as a function of gap length. For fitting the gap data, each data point is weighted inversely proportional to the frequency of the class. Bottom right: Passing probability as a function of single bend angle.

Importantly, splays do not contribute to rupture propagation, in the sense that unbreached splays are foregone opportunities to activate or transfer the rupture to a second fault strand, but the rupture continues

instead on its main fault segment. There are only two splays that correlate with complete rupture arrest in our dataset. Splays appear to only really condition earthquake propagation insofar as the rupture will encounter a different set of future gates depending on what fault it travels on. Thus, a better conceptual model for splays may be a binary switch that affects the direction of rupture propagation but lacks the ability to bring it to arrest on most occasions. Most of the ruptures traveled under 3 km on the splay they transferred to, and are probably features that help accommodate the surficial strain during rupture propagation. In cases where the rupture traveled over 4-5 km on the splay fault, this fault became the primary fault hosting the earthquake.

Previous workers found a link between rupture arrest at splays related to the kinematics of the junction and the length of the fault branch (Poliakov et al., 2002; Kame et al., 2004; Bhat et al., 2007). Though we do not classify our splays into transpressional or transtensional because the direction of rupture propagation is not known, the fact that we only observe two complete rupture arrests at splays suggests that the presence of a splay plays a small role in the behavior of the rupture on the principal fault at the scale we map at, despite the fact that most splay branches mapped were relatively short, which should hinder rupture propagation by allowing the two fault segments to interact as the rupture stops on the shorter one (Bhat et al., 2007).

A barrier model for earthquake size

To consider the role of earthquake gates in controlling earthquake moment magnitude, we introduce the concept of the event likelihood as the joint probabilities of all the breached gates in an event (see equation 1 in the methods), computed based on the logistic models illustrated in Figure 11. The notion of event likelihood as expressed in equation 1 serves as a retrospective assessment of how likely an event of the magnitude was given the pre-existing geometrical complexity in the hosting fault system.

Figure 12 (top) shows the distribution of event likelihoods versus magnitude for the 31 strike-slip earthquakes in the FDHI database. Event likelihood consistently decreases with increasing magnitude for the magnitude range captured by the events in the database. The decrease is well described by an inverse power law with scaling exponent $\sim$1.8, though there is significant scatter between events. We do not consider the M_w 5 events in our fit because M_w 5 events rarely cause surface ruptures (Wells and Coppersmith, 1993; Pizza et al., 2023), and, when they do, the rupture is typically incomplete to the surface, resulting in the absence of a coherent rupture trace from which earthquake gates can be robustly mapped. We also do not consider gaps in the estimates of event likelihoods, as the unbreached gap data is very sparse. Nevertheless, we show results including gaps in Figure 21 in the appendix for completeness. Despite an increase in slope, the consistent decrease in event likelihood for increasing magnitude remains robust.

To further investigate this relationship, we compute event likelihoods as cumulative probabilities along each mapped rupture, evaluating how probability is reduced along the surface rupture length of each earthquake (Figure 12, bottom). The spacing between neighboring earthquake gates is log-normally distributed (figure 20 in the appendix), with an average spacing of $\sim$2 km. This is what causes the flat sections in the relationships in the upper left of Figure 12 (bottom). Beyond these flatter sections, where only the probability of ending on a straight segment decreases the likelihood, the cumulative log-likelihood of each event decreases following a similar slope. This suggests that the different breached earthquake gates contribute similarly to decreasing the likelihood of an event as they are encountered along the strike of the fault system.

The estimate of passing probabilities and analysis of the distribution of earthquake gate sizes are not very sensitive to variability in the level of completeness in the individual rupture maps. However, the comparison of different event probabilities to estimate a dependency on the magnitude and surface rupture length we do here is more sensitive to differences in how the events were mapped. These differences may be partly responsible for the degree of scattering in the two panels in Figure 12. Another possibility is that the variability can be explained by variations in maturity among the different hosting fault systems, as structural complexity decreases with increasing cumulative displacement on the fault (e.g. Wesnousky, 1988; Dolan and Haravitch, 2014). However, when we compare our event probabilities to cumulative fault displacement, a common proxy for fault maturity, we find no correlation (See Figure 22 in the appendix). Therefore, variations in mapping completeness and the natural variability of surface ruptures remain our preferred explanations for the scatter in Figure 12.

Though our observations are limited by the magnitude range of surface rupturing earthquakes in the FDHI database, the relationship between likelihood and surface rupture length and magnitude suggests that earthquake scaling is at least in part controlled by the number and characteristics of the earthquake gates present along the hosting fault system. The evolution of probability along rupture strike provides support for a barrier model for earthquake size (e.g. Aki, 1979; Aki, 1989), where relatively simple segments of the fault are bounded by hard geometrical barriers that must be breached for the rupture to continue. Previous empirical studies have also argued in favor of this model based on the segmentation of surface ruptures (e.g. King and Nabelek, 1985; Klinger et al., 2006; Rockwell and Klinger, 2013).

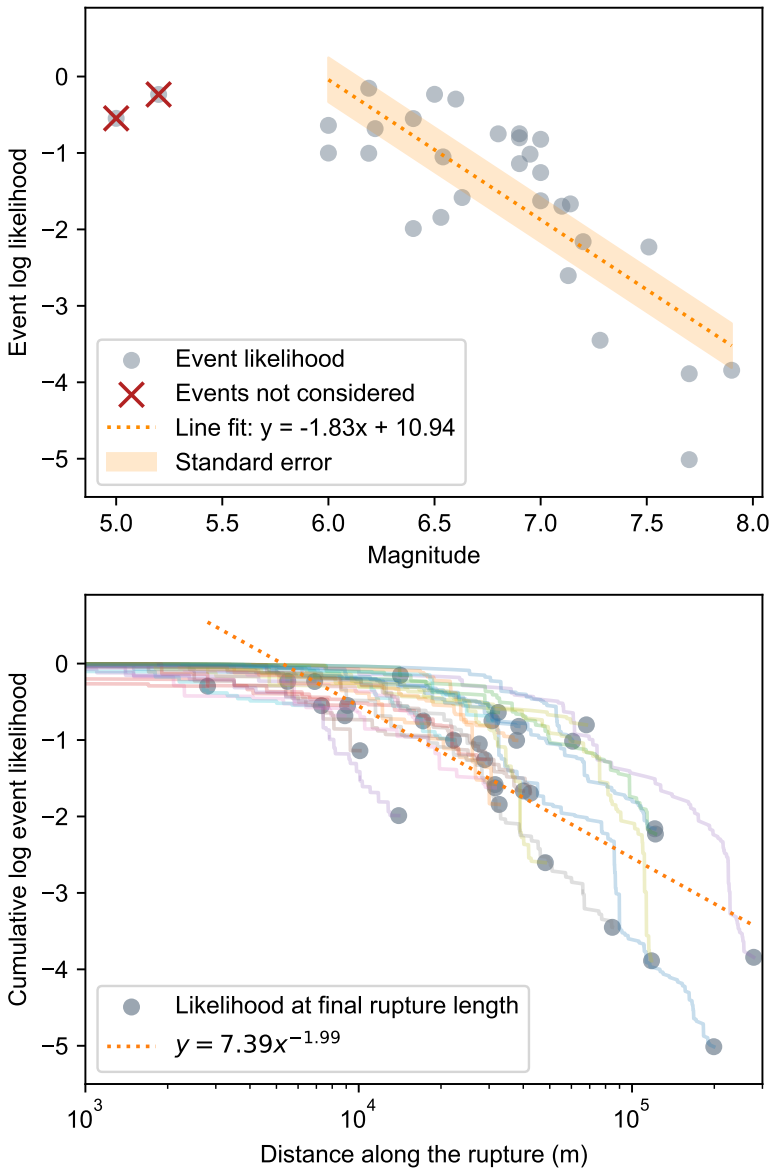

Figure 12: Top: Event likelihood versus magnitude for the 31 strike-slip earthquakes in the FDHI database (Sarmiento et al., 2021). Event likelihood is computed using equation 1 and the logistic model predictions from figure 11. Each scattered dot represents one event and the line represents the best fit for the evolution of event likelihood with magnitude. Bottom: Cumulative event likelihood versus distance along the surface rupture. Each colored line represents one event. The scattered dots indicate the final event likelihood at its final rupture length. The rupture lengths are based on the FDHI database event coordinate systems (ECS) reference lines (Sarmiento et al., 2021). The orange line represents the best fit to the final likelihood of each event.

Mechanical models for rupture propagation through step-overs and bends

We consider the mechanics that result in the populations of breached and unbreached step-overs and bends that we map. To examine the underlying mechanical conditions that result in step-over breaching, we perform a Coulomb stress analysis using the framework of linear elastic fracture mechanics, assuming that the fault segments on each side of the step-over are mode II fractures. The stress distribution around a sharp crack is given by:

$$\sigma_{ij} = \frac{K}{\sqrt{2\pi r}} f_{ij}(\theta) \tag{4}$$

where $K = \Delta\tau\sqrt{L}$ is the stress intensity factor that depends on the crack length behind the tip (L) and $\Delta\tau$, the difference between the imposed far-field stress and the stress resolved on the crack walls. Parameter r denotes the distance away from the crack tip in a linear elastic medium. The function $f_{ij}(\theta)$ describes the azimuthal distribution of the near-tip stress field and is dependent on the crack geometry (fracture mode) and stress direction/component. The standard solutions of $f_{ij}(\theta)$ for a mode II fracture in Cartesian coordinates are given by:

$$\begin{aligned} f_{yy} &= \sin\left(\frac{\theta}{2}\right)\cos\left(\frac{\theta}{2}\right)\cos\left(\frac{3\theta}{2}\right) \\ f_{xy} &= \cos\left(\frac{\theta}{2}\right)\left[1 - \sin\left(\frac{\theta}{2}\right)\sin\left(\frac{3\theta}{2}\right)\right] \end{aligned} \tag{5}$$

where θ is the angle from the crack tip, and yy and xy correspond to the normal and shear stress components respectively (Lawn, 1993). For a mode II fracture, the shear stress change is always positive, and the normal stress change is the opposite sign for restraining and releasing step-overs. Positive normal stress denotes tension. We assume that the rupture will re-nucleate on the receiving step-over and the most optimal angle where r in equation 4 is given by:

$$r = \frac{W}{sin\theta} \tag{6}$$

where W is the step-over width we map and θ is the angle that maximizes the Coulomb stress change ($\Delta\sigma_c = \tau_{ij} + \mu\sigma_{ij}$) based on equation 4, which will be dependent on the static friction coefficient of the receiver fault μ (dependency illustrated in Figure 23 in the appendix). This approach assumes the two fault segments separated by the step-over have parallel strikes.

We calculate the Coulomb stress change on a fault segment across a step-over using equation 4. This

requires knowledge of the widths of step-overs (Figure 10, top left), and the crack length behind a step-over since the nearest earthquake gate that is a step-over or a gap, both of which can be empirically determined from the surface rupture maps in the FDHI database. Because knowledge of the rupture propagation direction is limited, for breached step-overs, we do not know which of the adjacent segments is the one the rupture jumped from, so, to make a conservative estimate, we choose the shorter one. Figure 24 in the appendix shows that larger breached step-overs are associated with longer cracks leading up to them.

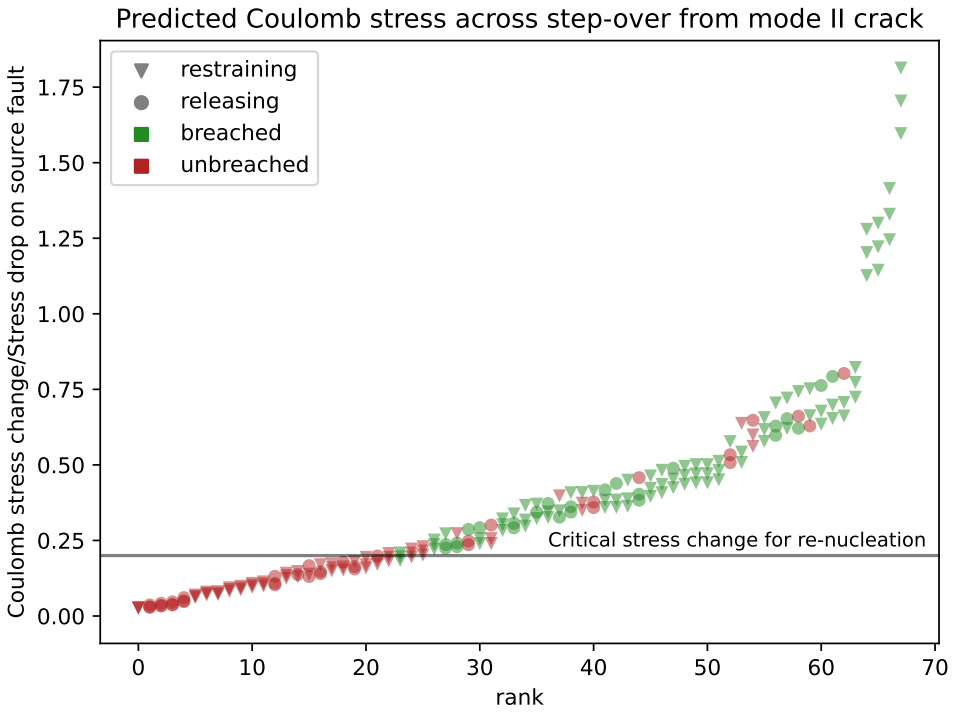

Figure 13: Ratio of Coulomb stress change to stress drop on receiver fault segments across the mapped step-overs calculated for friction coefficients μ of 0, 0.3, and 0.6. The data are ranked from lowest to highest stress ratio and color-coded by whether the step-over was breached or unbreached. Releasing step-overs are shown as circles whereas restraining step-overs are shown as inverted triangles. The black horizontal lines shows an apparent critical stress change ratio required for renucleation across the step-over.

We calculate the Coulomb stress change on the receiving fault segment across the step-over as a ratio of the stress drop in the source fault, using a range of possible friction values. Figure 13 shows all step-overs considered in this study, ranked by the predicted Coulomb stress change, for three candidate friction values. We find that step-overs across which the receiver segment experiences a stress change ratio smaller than 0.2 are not breached, suggesting that a large stress increase is needed to immediately overcome static friction and activate the fault across the step-over. Curiously, this stress change is at least 10 times larger than that associated with the triggering of aftershocks (e.g. King et al., 1994), and is also at odds with observations of widespread earthquake-triggered fracturing at the surface and aftershocks at depth (e.g. Rodriguez Padilla

et al., 2022).

There are five unbreached step-overs out of the sixty-eight step-overs considered in this study that experienced stress change ratios exceeding a value of 50% of the stress drop. Two of these step-overs were along the Denali surface rupture, where the earthquake favored propagation past a larger gap, instead of breaching either of the smaller step-overs available. Two of the other exceptions occurred at the termini of the Pisayambo and Napa ruptures, where long rupture segments end at 750 meters and 1.8 km wide step-overs respectively. The smallest unbreached step-over with a high stress ratio is barely 100 m wide and occurred at one of the complex rupture termini on the Hector Mine earthquake.

Previous studies have argued for the importance of rupture dynamics in facilitating rupture transfer past a step-over (e.g. Oglesby, 2008; Elliott et al., 2009). Besides the exceptions listed above, the simple static stress model for a receiver mode II crack illustrated in Figure 13 explains the population of breached and unbreached step-overs in the surface ruptures considered in this study very well. This model suggests that nucleation across step-overs requires a high stress change and has little dependence on the frictional strength of the receiver segment. Rupture dynamics, the integrated stress history on a fault segment, or rheological characteristics not considered in our simple model may help explain the exceptions listed above.

Rupture propagation past bends is a fundamentally different problem than on step-overs mechanically. Rupture propagation past step-overs is conditional on rupture re-nucleation on the neighboring segment, and therefore a rupture initiation problem. Rupture propagation past bends is instead a rupture arrest problem, as the rupture does not need to renucleate to overcome the bend (e.g. Magistrale and Day, 1999). Because ruptures do not need to renucleate on the bend but just continue propagating past it, the frictional strength of the bend, and the normal stress, exert a primary control on whether a bend will be breached or unbreached. To examine the underlying mechanical conditions that enable bends to be breached, we estimate the frictional amplification that fault segments undergo as they enter a bend:

$$A = \frac{\mu + tan(\theta)}{1 - \mu tan(\theta)} - \mu \tag{7}$$

where μ is the static friction coefficient and θ is the bend angle as defined in Figure 9. Amplification reflects the increase in frictional strength of the fault segment as a result of the change in strike angle, relative to the same stress field (Jaeger and Cook, 1979; Biasi and Wesnousky, 2017). Note this does not provide a solution for the frictional strength of the bend, but enables examining the effect of bend angle in strength in a general sense.

Biasi and Wesnousky (2017) proposed that the population of unbreached bends they mapped could be explained on the basis of the frictional strength increase induced by the presence of a bend on the fault

(Cook and Jaeger, 1979; equation 7). Figure 14 shows the expected frictional amplification for bend angles from 0 to 50° and friction coefficients of 0.3, 0.6, and 0.8.

Most bends we map have angles smaller than 30°. For low angles, the bend amplification values in Figure 7 are very similar to each other. Because the bend amplification coefficient increases non-linearly, the few large breached bends we map (>40°) must have relatively low frictional strength to have been breached, otherwise, their frictional amplification factor would be too large for slip to reasonably occur on the fault segment. Equation 7 shows asymptotic behavior followed by a reversal in sign given by the change in the direction of the resolved shear force on the bend (Jaeger and Cook, 1979). This behavior occurs at angles of ∼50, 60, and 75° for $\mu = 0.8$, 0.6, 0.3 respectively, and it places a physical limit on the bend angle given the strength of the preceding fault segment. All of our breached bends have angles below these critical values for friction coefficients below 0.6.

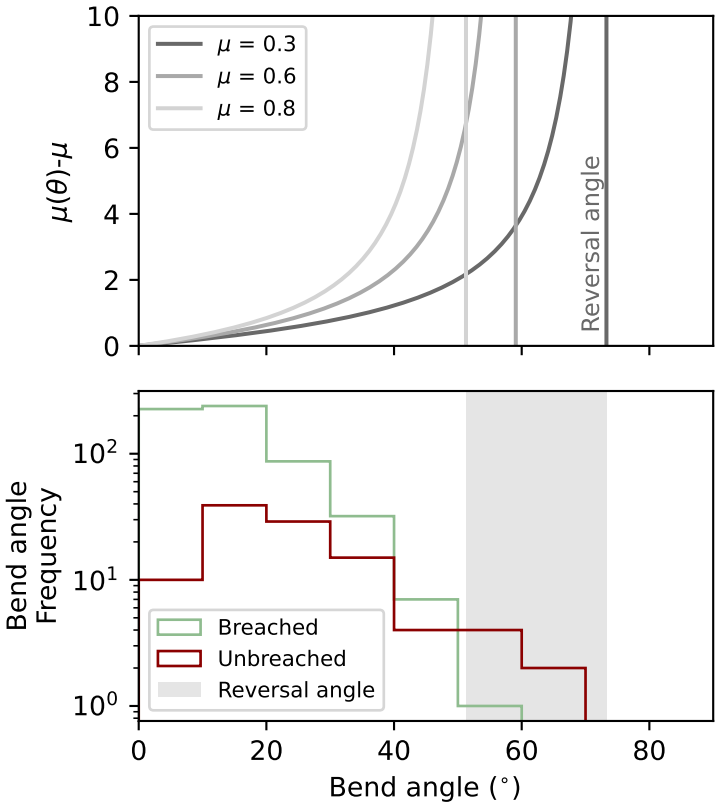

Figure 14: Top: Bend amplification factor ($\mu(\sigma) - \mu$, equation 7) for bend angles from 0 to 80° for different static friction coefficients, shown by the grey lines. Note the amplification calculation does not account for whether the bend occurs in a releasing or a restraining configuration. Bottom: Frequency distribution of breached and unbreached bend populations, single and double bends combined.

Conclusions

We map step-overs, bends, gaps, splays, and strands along the surface rupture maps of 31 strike-slip earthquakes at 1:50,000 scale. We characterize features as breached and unbreached based on whether the rupture propagated past and, when possible, as restraining or releasing based on kinematic relationships.

When fitting a logistic model to estimate passing probabilities as a function of geometry, we find that step-over width is an excellent predictor of whether a step-over will be breached, with step-overs wider than $\sim$1.1 km being breached less than half of the time. Bends are less effective earthquake gates than step-overs, and bend angle is a limited predictor of whether a bend will be breached, although the ratio of unbreached to breached bends increases consistently with increasing bend angle. The logistic models predict that double bends $>50^\circ$ are breached less than half of the time. For single bends, this occurs for angles $>37^\circ$. We find double bends behave differently than step-overs with the same geometry, suggesting the hard-linkage persists at depth. We map only 6 unbreached gaps, which limits our ability to estimate robust passing probabilities for them, though, using the limited data available, the logistic model predicts that gaps >1.2 km long will be breached less than half of the time, consistent with the passing probabilities of step-overs. Splays control the direction of rupture propagation by determining on what fault the rupture will continue to grow, though they rarely (only twice in this dataset) bring ruptures to complete arrest. These new empirically determined passing probabilities can be used to calibrate long-term rupture simulators (e.g. Field et al., 2015).

We use the passing probabilities of the breached earthquake gates in each event to estimate a retrospective event likelihood that captures the likelihood of that earthquake given the complexity of the hosting fault system. We find that event likelihood decreases with increasing event magnitude. Gate size and spacing are both log-normally distributed. The cumulative likelihood along rupture strike supports a barrier model for controlling earthquake size, where relatively straight fault segments are bound by hard geometrical barriers that must be breached in order for the rupture to continue growing.

We use a simple model for the Coulomb stress change on a receiver fault across a step-over to estimate the stress change on each of the mapped step-overs. We find that there is a critical stress change threshold that separates the unbreached and breached population of step-overs, where step-overs that experienced a stress change $\sim<0.2$ of the stress drop were never breached. This result has little dependence on the friction of the receiver fault. We also find that frictional strength amplification as a function of bend angle provides a good general framework to describe breached and unbreached bend populations.

References

1. Aki, K. (1989). Geometric features of a fault zone related to the nucleation and termination of an earthquake rupture. In Proceedings of Conference XLV. Fault Segmentation Controls of Rupture Initiation and Termination (pp. 1-9).

2. Aki, K. (1979). Characterization of barriers on an earthquake fault. Journal of Geophysical Research: Solid Earth, 84(B11), 6140-6148.

3. Bachmanov, D.M., Trifonov, V.G., Kozhurin, A.I. and Zelenin E.A.: AFEAD v.2021 Active Faults of Eurasia Database, https://doi.org/10.13140/RG.2.2.10333.74726, 2021.

4. Bakun, W. H., Stewart, R. M., Bufe, C. G., & Marks, S. M. (1980). Implication of seismicity for failure of a section of the San Andreas fault. Bulletin of the Seismological Society of America, 70(1), 185-201.

5. Barka, A. A., & Kadinsky-Cade, K. (1988). Strike-slip fault geometry in Turkey and its influence on earthquake activity. Tectonics, 7(3), 663-684.

6. Biasi, G. P., & Wesnousky, S. G. (2016). Steps and gaps in ground ruptures: Empirical bounds on rupture propagation. Bulletin of the Seismological Society of America, 106(3), 1110-1124.

7. Biasi, G. P., & Wesnousky, S. G. (2017). Bends and ends of surface RupturesBends and ends of surface ruptures. Bulletin of the Seismological Society of America, 107(6), 2543-2560.

8. Biasi, G. P.,& Wesnousky, S. G. (2021). Rupture passing probabilities at fault bends and steps, with application to rupture length probabilities for earthquake early warning. Bulletin of the Seismological Society of America, 111(4), 2235-2247.

9. Bhat, H. S., Olives, M., Dmowska, R., & Rice, J. R. (2007). Role of fault branches in earthquake rupture dynamics. Journal of Geophysical Research: Solid Earth, 112(B11).

10. Crone, A. J., Personius, S. F., Craw, P. A., Haeussler, P. J., & Staft, L. A. (2004). The Susitna Glacier thrust fault: Characteristics of surface ruptures on the fault that initiated the 2002 Denali fault earthquake. Bulletin of the Seismological Society of America, 94(6B), S5-S22.

11. Dolan, J. F., & Haravitch, B. D. (2014). How well do surface slip measurements track slip at depth in large strike-slip earthquakes? The importance of fault structural maturity in controlling on-fault slip versus off-fault surface deformation. Earth and Planetary Science Letters, 388, 38-47.

12. Elliott, A. J., Dolan, J. F., & Oglesby, D. D. (2009). Evidence from coseismic slip gradients for dynamic control on rupture propagation and arrest through stepovers. Journal of Geophysical Research: Solid Earth, 114(B2).

13. Field, E. H., Biasi, G. P., Bird, P., Dawson, T. E., Felzer, K. R., Jackson, D. D., ... & Zeng, Y. (2015). Long-term time-dependent probabilities for the third Uniform California Earthquake Rupture Forecast (UCERF3). Bulletin of the Seismological Society of America, 105(2A), 511-543.

14. Guo, H., Lay, T., & Brodsky, E. E. (2023). Seismological Indicators of Geologically Inferred Fault Maturity. Authorea Preprints.

15. Hamling, I. J., Hreinsdóttir, S., Clark, K., Elliott, J., Liang, C., Fielding, E., ... & Stirling, M. (2017). Complex multifault rupture during the 2016 M w 7.8 Kaikōura earthquake, New Zealand. Science, 356(6334), eaam7194.

16. Harris, R. A., & Day, S. M. (1993). Dynamics of fault interaction: Parallel strike-slip faults. Journal of Geophysical Research: Solid Earth, 98(B3), 4461-4472.

17. Howarth, J. D., Barth, N. C., Fitzsimons, S. J., Richards-Dinger, K., Clark, K. J., Biasi, G. P., ... & Sutherland, R. (2021). Spatiotemporal clustering of great earthquakes on a transform fault controlled by geometry. Nature Geoscience, 14(5), 314-320.

18. Jaeger J. C., & Cook N. G. W. 1979. Fundamentals of Rock Mechanics , Chapman and Hall, London, United Kingdom.

19. Jara, J., Bruhat, L., Thomas, M. Y., Antoine, S. L., Okubo, K., Rougier, E., ... & Bhat, H. S. (2021). Signature of transition to supershear rupture speed in the coseismic off-fault damage zone. Proceedings of the Royal Society A, 477(2255), 20210364.

20. Kame, N., Rice, J. R., & Dmowska, R. (2003). Effects of prestress state and rupture velocity on dynamic fault branching. Journal of Geophysical Research: Solid Earth, 108(B5).

21. King, G., & Nábělek, J. (1985). Role of fault bends in the initiation and termination of earthquake rupture. Science, 228(4702), 984-987.

22. Klinger, Y., Michel, R., & King, G. C. (2006). Evidence for an earthquake barrier model from Mw$\sim$ 7.8 Kokoxili (Tibet) earthquake slip-distribution. Earth and Planetary Science Letters, 242(3-4), 354-364.

23. Klinger, Y. (2010). Relation between continental strike-slip earthquake segmentation and thickness of the crust. Journal of Geophysical Research: Solid Earth, 115(B7).

24. Langridge, R. M., Ries, W. F., Litchfield, N. J., Villamor, P., Van Dissen, R. J., Barrell, D. J. A., ... & Stirling, M. W. (2016). The New Zealand active faults database. New Zealand Journal of Geology and Geophysics, 59(1), 86-96.

25. Lawn, B. (1993). Fracture of brittle solids.

26. Lettis, W., Bachhuber, J., Witter, R., Brankman, C., Randolph, C. E., Barka, A., ... & Kaya, A. (2002). Influence of releasing step-overs on surface fault rupture and fault segmentation: Examples from the 17 August 1999 Izmit earthquake on the North Anatolian fault, Turkey. Bulletin of the Seismological Society of America, 92(1), 19-42.

27. Lienkaemper, J. J., Pezzopane, S. K., Clark, M. M., & Rymer, M. J. (1987). Fault fractures formed in association with the 1986 Chalfant Valley, California, earthquake sequence: preliminary report. Bulletin of the Seismological Society of America, 77(1), 297-305.

28. Liu, D., Duan, B., Prush, V. B., Oskin, M. E., & Liu-Zeng, J. (2021). Observation-constrained multicycle dynamic models of the Pingding Shan earthquake gate along the Altyn Tagh Fault. Tectonophysics, 814, 228948.

29. Lozos, J. C., Oglesby, D. D., Duan, B., & Wesnousky, S. G. (2011). The effects of double fault bends on rupture propagation: A geometrical parameter study. Bulletin of the Seismological Society of America, 101(1), 385-398.

30. Lozos, J. C. (2016). A case for historic joint rupture of the San Andreas and San Jacinto faults. Science advances, 2(3), e1500621.

31. Magistrale, H., & Day, S. (1999). 3D simulations of multi-segment thrust fault rupture. Geophysical Research Letters, 26(14), 2093-2096.

32. Manighetti, I., Campillo, M., Bouley, S., & Cotton, F. (2007). Earthquake scaling, fault segmentation, and structural maturity. Earth and Planetary Science Letters, 253(3-4), 429-438.

33. Milner, K. R., Shaw, B. E., & Field, E. H. (2022). Enumerating plausible multifault ruptures in complex fault systems with physical constraints. Bulletin of the Seismological Society of America, 112(4), 1806-1824.

34. Oglesby, D. D. (2005). The dynamics of strike-slip step-overs with linking dip-slip faults. Bulletin of the Seismological Society of America, 95(5), 1604-1622.

35. Oglesby, D. (2008). Rupture termination and jump on parallel offset faults. Bulletin of the Seismological Society of America, 98(1), 440-447.

36. Oskin, M. E., Arrowsmith, J. R., Corona, A. H., Elliott, A. J., Fletcher, J. M., Fielding, E. J., ... & Teran, O. J. (2012). Near-field deformation from the El Mayor–Cucapah earthquake revealed by differential LIDAR. Science, 335(6069), 702-705.

37. Pedregosa, F., Varoquaux, G., Gramfort, A., Michel, V., Thirion, B., Grisel, O., ... & Duchesnay, E. (2011). Scikit-learn: Machine learning in Python. the Journal of machine Learning research, 12, 2825-2830.

38. Perrin, C., Manighetti, I., Ampuero, J. P., Cappa, F., & Gaudemer, Y. (2016). Location of largest earthquake slip and fast rupture controlled by along-strike change in fault structural maturity due to fault growth. Journal of Geophysical Research: Solid Earth, 121(5), 3666-3685.

39. Perrin, C., Waldhauser, F., & Scholz, C. H. (2021). The shear deformation zone and the smoothing of faults with displacement. Journal of Geophysical Research: Solid Earth, 126(5), e2020JB020447.

40. Pizza, M., Ferrario, M. F., Thomas, F., Tringali, G., & Livio, F. (2023). Likelihood of Primary Surface Faulting: Updating of Empirical Regressions. Bull. Seismol. Soc. Am, 20, 1-13.

41. Poliakov, A. N., Dmowska, R., & Rice, J. R. (2002). Dynamic shear rupture interactions with fault bends and off-axis secondary faulting. Journal of Geophysical Research: Solid Earth, 107(B11), ESE-6.

42. Rockwell, T. K., & Klinger, Y. (2013). Surface rupture and slip distribution of the 1940 Imperial Valley earthquake, Imperial fault, southern California: Implications for rupture segmentation and dynamics. Bulletin of the Seismological Society of America, 103(2A), 629-640.

43. Rodriguez Padilla, A. M., Oskin, M. E., Milliner, C. W., & Plesch, A. (2022). Accrual of widespread rock damage from the 2019 Ridgecrest earthquakes. Nature Geoscience, 15(3), 222-226.

44. Ross, Z. E., Idini, B., Jia, Z., Stephenson, O. L., Zhong, M., Wang, X., ... & Jung, J. (2019). Hierarchical interlocked orthogonal faulting in the 2019 Ridgecrest earthquake sequence. Science, 366(6463), 346-351.

45. Sarmiento, A., Madugo, D., Bozorgnia, Y., Shen, A., Mazzoni, S., Lavrentiadis, G., Dawson, T., Madugo, C., Kottke, A., Thompson, S., Baize, S., Milliner, C., Nurminen, F., Boncio, P., and Visini, F. (2021). Fault Displacement Hazard Initiative Database, UCLA B. John Garrick Institute for the Risk Sciences, Report GIRS-2021-08, doi: 10.34948/N36P48.

46. Scharer, K. M., & Yule, D. (2020). A maximum rupture model for the southern San Andreas and San Jacinto faults, California, derived from paleoseismic earthquake ages: Observations and limitations. Geophysical Research Letters, 47(15), e2020GL088532.

47. Segall, P., & Pollard, D. D. (1980). Mechanics of discontinuous faults. Journal of Geophysical Research: Solid Earth, 85(B8), 4337-4350.

48. Shao, Y., Liu-Zeng, J., Oskin, M. E., Elliott, A. J., Wang, P., Zhang, J., ... & Li, Z. (2018). Paleoseismic investigation of the Aksay Restraining Double Bend, Altyn Tagh Fault, and its implication for barrier-breaching ruptures. Journal of Geophysical Research: Solid Earth, 123(5), 4307-4330.

49. Share, P. E., & Ben-Zion, Y. (2018). A bimaterial interface along the northern San Jacinto fault through Cajon Pass. Geophysical Research Letters, 45(21), 11-622.

50. Shaw, B. E., & Dieterich, J. H. (2007). Probabilities for jumping fault segment stepovers. Geophysical Research Letters, 34(1).

51. Sibson, R. H. (1985). Stopping of earthquake ruptures at dilational fault jogs. Nature, 316(6025), 248-251.

52. Styron, R., & Pagani, M. (2020). The GEM global active faults database. Earthquake Spectra, 36(1), 160-180.

53. U.S. Geological Survey, 2020, Quaternary Fault and Fold Database for the Nation, accessed [Month, Day, Year], at https://doi.org/10.5066/P9BCVRCK

54. Wells, D. L., & Coppersmith, K. J. (1993). Likelihood of surface rupture as a function of magnitude. Seismological Research Letters, 64(1), 54.

55. Wesnousky, S. G. (1988). Seismological and structural evolution of strike-slip faults. Nature, 335(6188), 340-343.

56. Wesnousky, S. G. (2006). Predicting the endpoints of earthquake ruptures. Nature, 444(7117), 358-360.

57. Wesnousky, S. G. (2008). Displacement and geometrical characteristics of earthquake surface ruptures: Issues and implications for seismic-hazard analysis and the process of earthquake rupture. Bulletin of the Seismological Society of America, 98(4), 1609-1632.

Appendix

Table 2: Reference maps of active faults to measure unbreached feature characteristics with respect to.

Reference Fault Map	Location	References
Quaternary Fault and Fold Database of the United States	United States	USGS and CGS
New Zealand Active Faults Database (NZAFD)	New Zealand	Langridge et al. (2016)
The Active Faults of Eurasia Database (AFEAD)	Europe and Asia	Bachmanov et al. (2021)
GEM Global Active Faults Database	Central and South America	Styron and Pagani (2020)

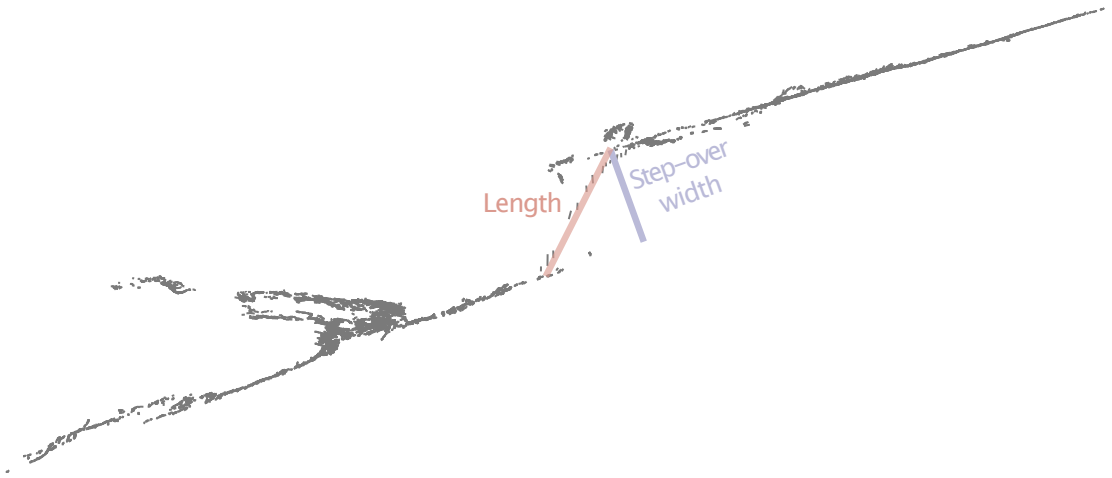

Figure 15: Releasing double bend from the 2014 Yutian earthquake. The rupture map is shown in grey. The pink and purple lines show the bend length as defined by Lozos (2011) and the proxy step-over width respectively.

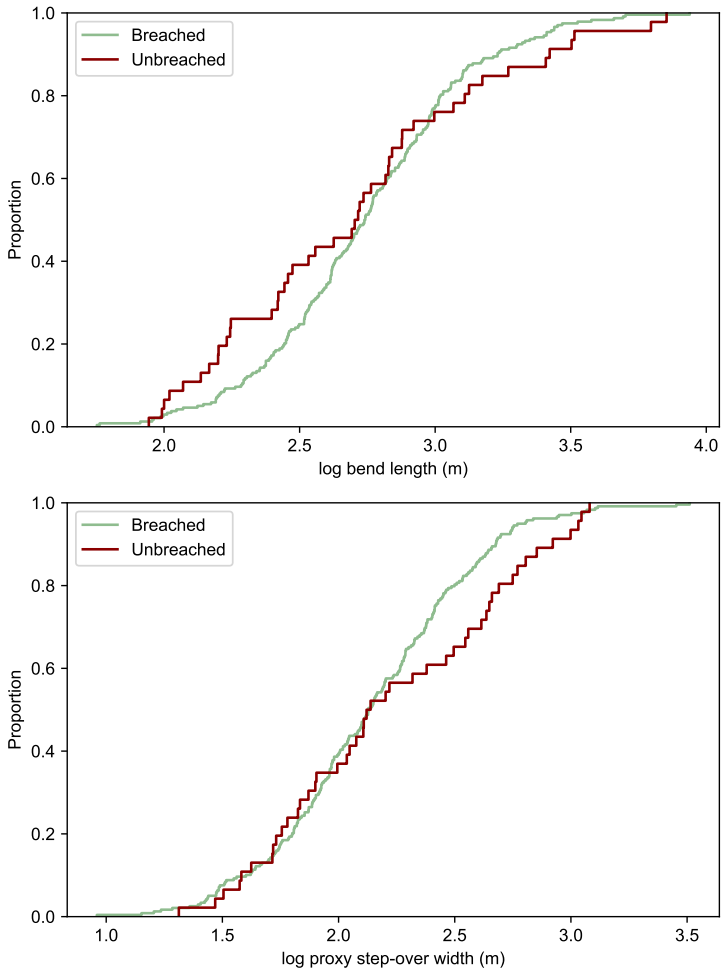

Figure 16: Cumulative distribution function of the breached and unbreached proxy step-over width (top) and length (bottom) for double bends.

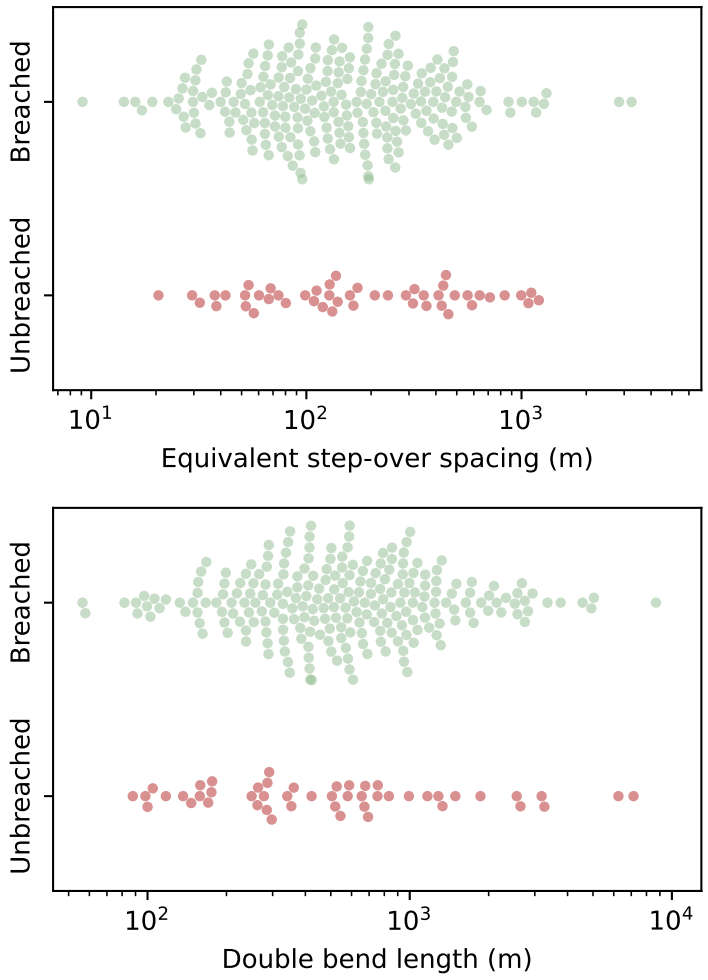

Figure 17: Beehive plots showing the proxy step-over width (top) and bend length (bottom) for the breached and unbreached double bends in this study.

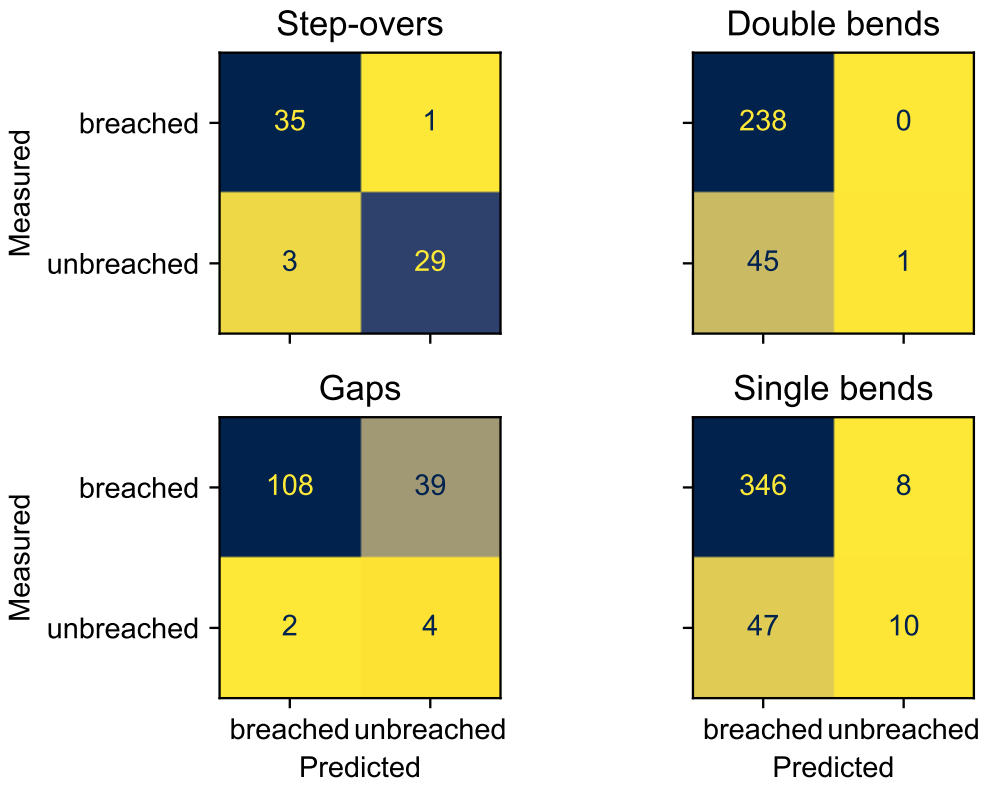

Figure 18: Confusion matrices for the logistic models for step-overs, single and double bends, and gaps in Figure 11.

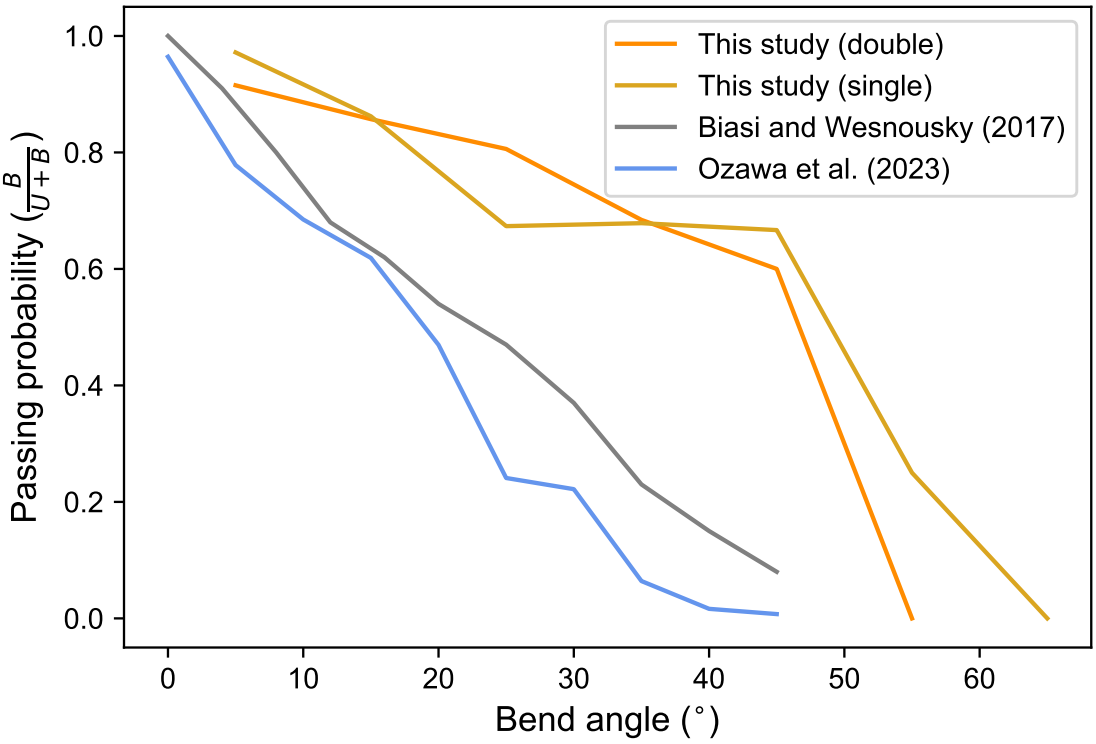

Figure 19: Comparison of the passing probabilities for different bend angles estimated in Biasi and Wesnousky (2017), Ozawa et al. (2023), and this study. Passing probability estimated as the number of breached bends per bin over the total number of bends in that bin. Note that the Biasi and Wesnousky (2017) passing probabilities include both single and double bends without discriminating between them, and the Ozawa et al. (2023) passing probabilities only include double bends.

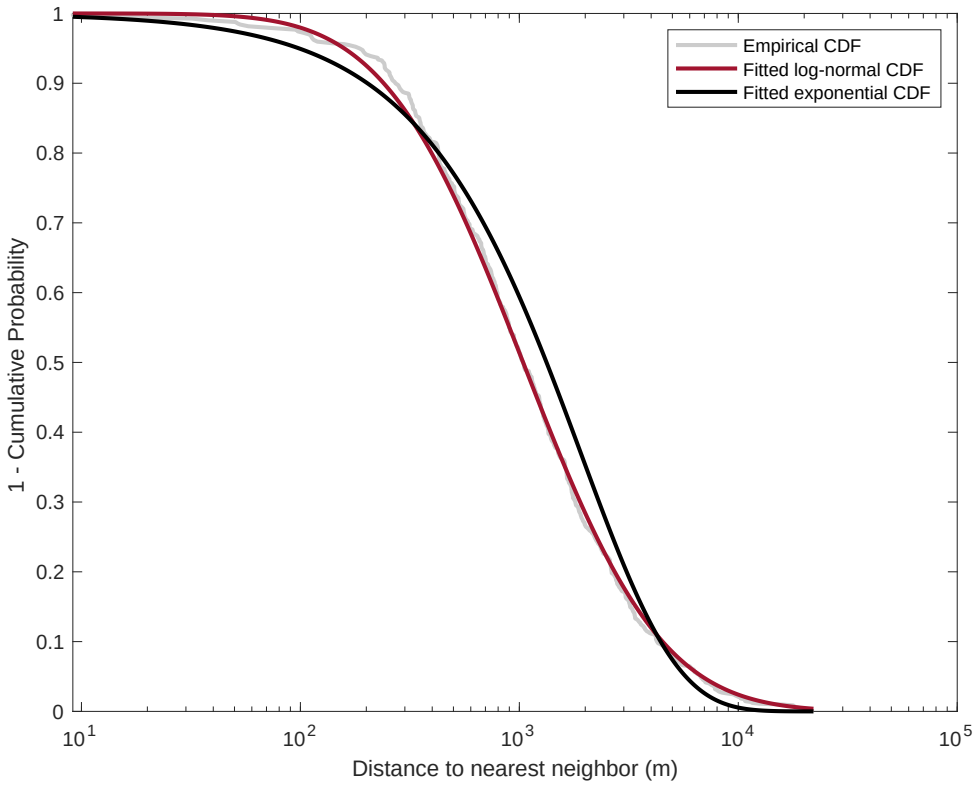

Figure 20: Empirical complementary cumulative distribution function (grey) of the distances to nearest neighbor for all breached earthquake gates. Complementary cumulative distribution functions for an exponential and a log-normal fit are shown in black and red respectively.

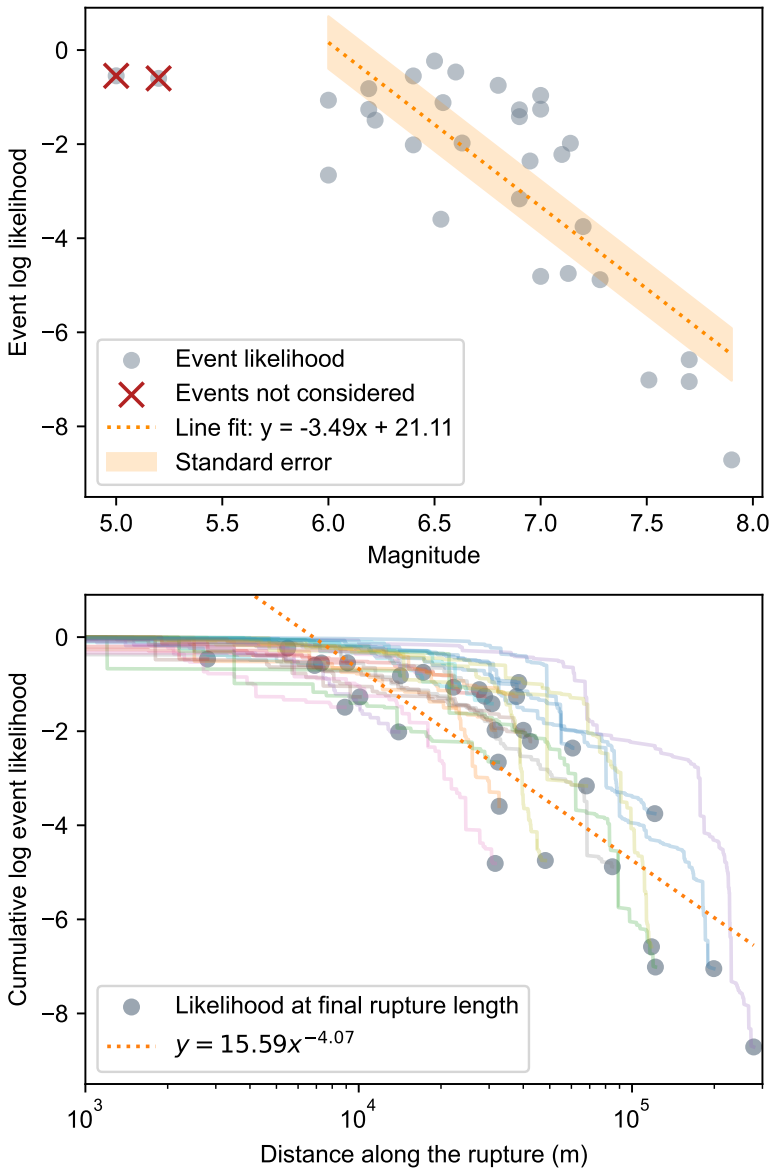

Figure 21: Top: Event likelihood versus magnitude for the 31 strike-slip earthquakes in the FDHI database (Sarmiento et al., 2021). Event likelihood is computed using equation 1 and the logistic model predictions from figure 11. Each scattered dot represents one event and the line represents the best fit for the evolution of event likelihood with magnitude. Bottom: Cumulative event likelihood versus distance along the surface rupture. Each colored line represents one event. The scattered dots indicate the final event likelihood at its final rupture length. The rupture lengths are based on the FDHI database ECS reference lines (Sarmiento et al., 2021). The orange line represents the best fit to the final likelihood of each event. This is the equivalent of Figure 12 in the main text but gap passing probabilities are included when computing event likelihood.

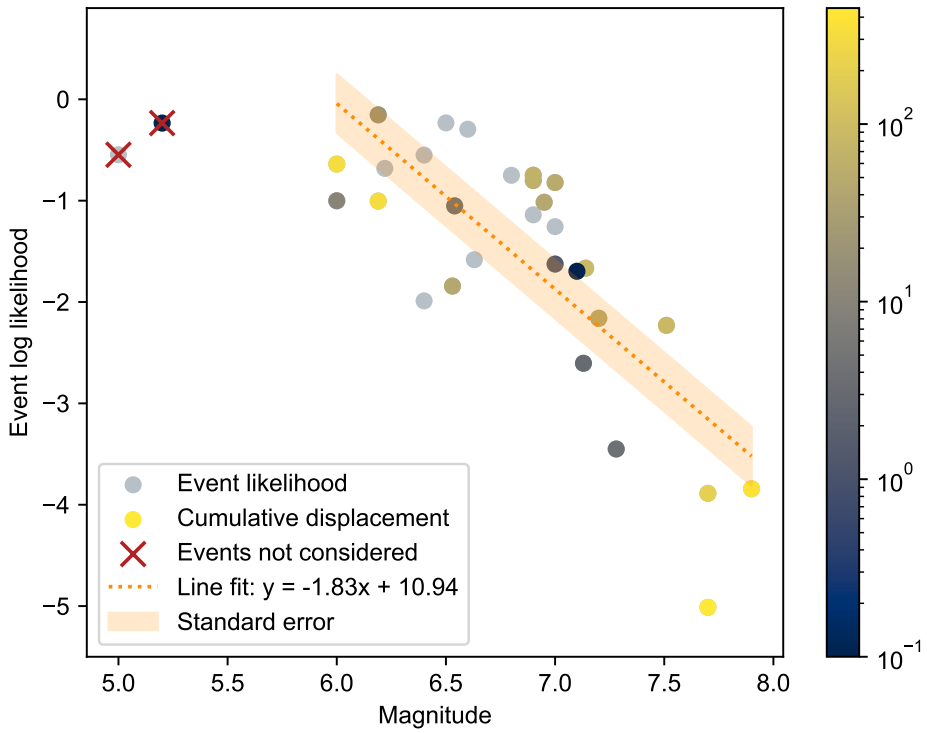

Figure 22: Event likelihood versus magnitude for the 31 strike-slip earthquakes in the FDHI database (Sarmiento et al., 2021). Event likelihood is computed using equation 1 and the logistic model predictions from figure 11. Each scattered dot represents one event and the line represents the best fit for the evolution of event likelihood with magnitude. Each point is color-coded by the logarithm of the cumulative displacement of the host fault. Cumulative displacements from the compilation in Guo et al. (2023).

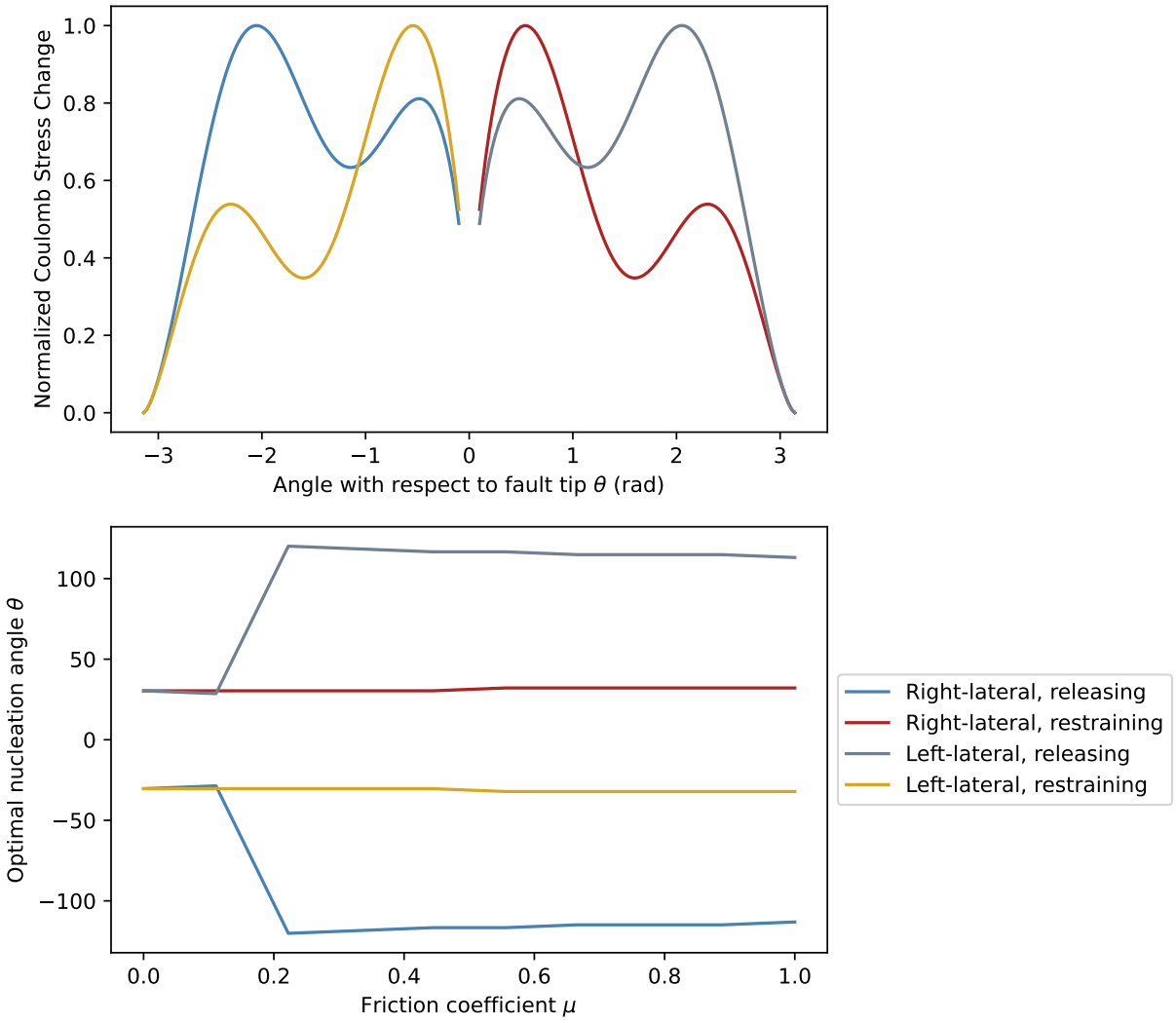

Figure 23: Top: Normalized Coulomb stress change versus angle with respect to the crack tip for μ=0.4. The Coulomb stress change is estimated from the shear and normal stresses calculated from equation 4 and normalized by subtracting the minimum Coulomb stress from every value, and dividing by the range of Coulomb stress values. Bottom: evolution of the optimal nucleation angle θ with friction coefficient μ.

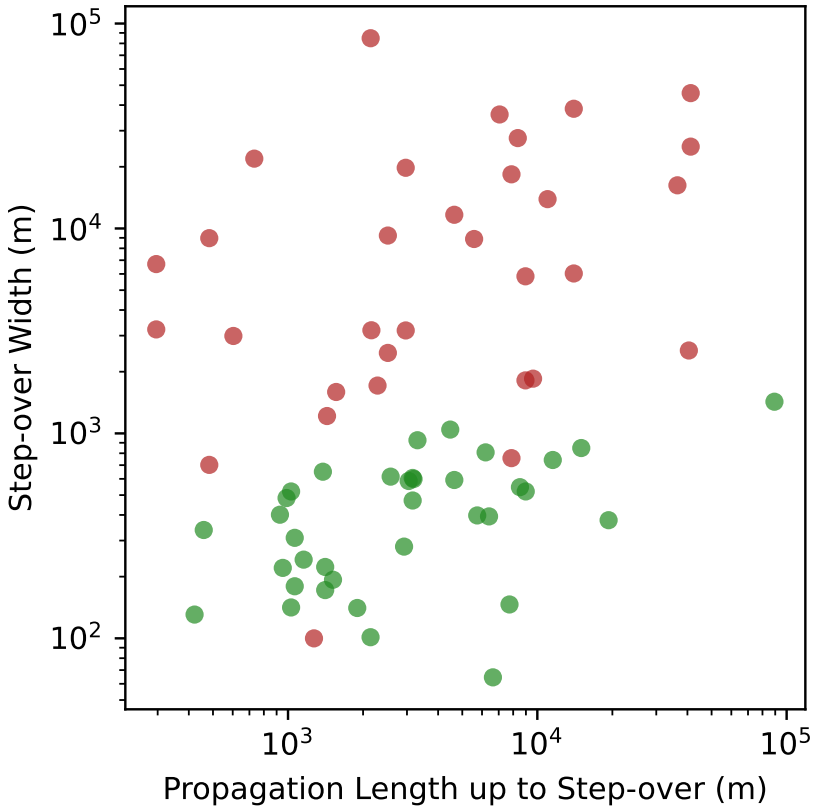

Figure 24: Step-over width versus minimum rupture length leading up to the step-over. Note half lengths are used in estimating the stress ratios in Figure 13. Points are color-coded by breached (green) and unbreached (red) categories.

Chapter 2: Joint earthquake ruptures of the San Andreas and San Jacinto faults

Abstract

Large, multi-fault earthquakes increase the threat of strong ground shaking and reshape the probability of future events across a system of faults. Fault junctions act as conditional barriers, or earthquake gates, that stop most earthquakes but permit junction-spanning events when stress conditions are favorable. Constraining the physical conditions that favor multifault earthquakes requires information on the frequency of isolated events versus events that activate faults through the junction. Measuring this frequency is challenging because dating uncertainties limit correlation of paleoseismic events at different faults, requiring a direct approach to measuring rupture through an earthquake gate. We show through documentation and finite-element modeling of secondary fault slip that co-rupture of the San Andreas and San Jacinto faults (California, USA) through the Cajon Pass earthquake gate occurred at least three times in the past 2000 years, most recently in the historic 1812 earthquake. Our models show that gate-breaching events taper steeply and halt abruptly as they transfer slip between faults. Comparison to independent chronologies shows that 20%–23% of earthquakes on the San Andreas and the San Jacinto faults are co-ruptures through Cajon Pass.

Introduction

Junctions of high-slip-rate faults with the potential to rupture together occur adjacent to high population centers across the world, including San Francisco and Los Angeles, Istanbul, Tehran, and Wellington. Fault junctions may act as earthquake gates, inhibiting most events from propagating past the barrier but permitting rare junction-spanning events to occur when stress conditions are favorable. Multi-fault earthquakes can produce greater-magnitude events than earthquakes confined to a single fault and lead to longer-sustained and more-widespread strong ground motions as well as larger and longer surface fault rupture. These outsized events are challenging to predict from traditional seismic hazard approaches, hindering forecasting of moderate and large earthquakes across a fault system (Field et al., 2015). Thus, constraining the mechanics and frequency of such events are key components of physics-based probabilistic hazard assessment and setting insurance costs. Validating the frequency of these earthquakes is challenging because the observational record is limited and uncertainties in the geologic record complicate correlation of events from fault to fault (Scharer and Yule, 2020).

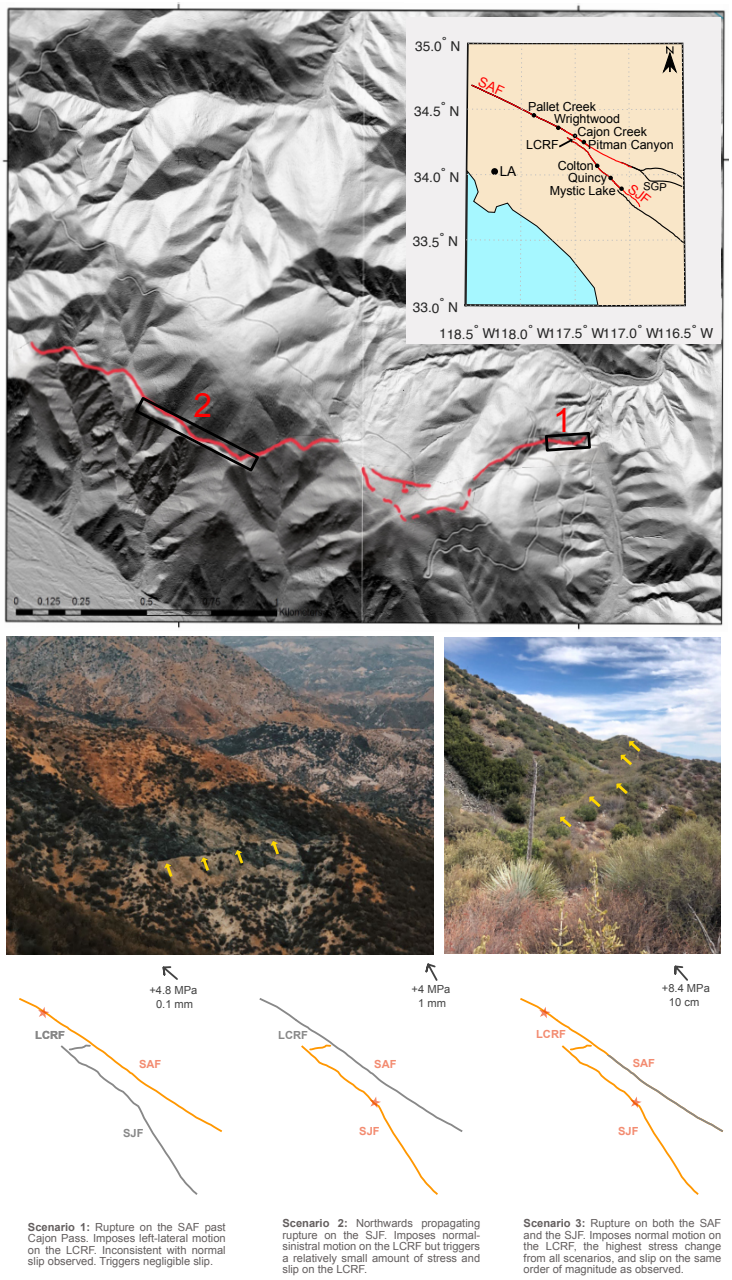

Figure 25: Top: Lidar shaded-relief map of Lytle Creek Ridge fault (LCRF; red lines, dotted where inferred) in Cajon Pass (California, USA). Star denotes location of paleoseismic trench. Inset shows the San Andreas fault (SAF) and San Jacinto fault (San Jacinto fault) in southern California, with paleoseismic sites. LA—Los Angeles; SGP—San Gorgonio Pass. Middle left: Bedrock exposure of the LCRF (indicated by yellow arrows) cutting the Pelona Schist. Middle right: Uphill-facing scarp of the LCRF cutting through Lytle Creek Ridge. Bottom: Rupture scenarios and resulting slip on the LCRF. Rupturing faults are orange, and faults with no slip are gray. Sketches are based on Coulomb models (Toda et al., 2011) for stress increase and optimal slip direction on the LCRF in response to rupture on the San Andreas fault (left), rupture on the San Jacinto fault (center), and rupture on both the San Andreas and San Jacinto faults (right) (Figure 30). The highest stress change, with slip direction consistent with that observed in outcrop, occurs for the case with slip on both the San Andreas and San Jacinto faults. Arrows indicate slip vector on the LCRF, followed by stress change on the LCRF and magnitude of triggered slip.

Collectively, the San Andreas fault and San Jacinto fault carry the majority of Pacific–North America plate motion through southern California and produce frequent, large, surface-rupturing earthquakes (Fialko, 2006; Rockwell et al., 2016). The San Jacinto fault terminates in a 2.5-km-wide releasing step-over with the San Andreas fault at Cajon Pass (34.3117°N, 117.4750°W), where their surface traces do not intersect (Morton et al., 2006). The potential for rupture transfer through this step-over has been demonstrated through dynamic modeling and by synthetic earthquake catalogs (Anderson et al., 2003; Field et al., 2015; Lozos, 2016) but previously lacked direct observational constraints. Earthquake chronologies from paleoseismic sites are available for the San Andreas fault (Biasi et al., 2002; Scharer et al., 2007) and the San Jacinto fault (Rockwell et al., 2015; Onderdonk et al., 2018). However, the alignment of the northernmost San Jacinto fault with major river canyons draining the eastern San Gabriel Mountains presents a challenging geomorphic setting for recording earthquake event chronologies within the earthquake gate.

We identified and mapped the Lytle Creek Ridge fault (LCRF), a low-angle normal fault that bridges the releasing step-over between the San Jacinto fault and the San Andreas fault (Figure 25). The LCRF strikes west over a distance of at least 2 km and dips north at 25°–30°. McCalpin and Hart (2003) previously identified scarps on the LCRF as a sackung formed by collapse of the nearby ridge line. However, based on its gentle dip and because its mapped trace crosses over the ridge crest, we interpret the LCRF as a low-angle normal fault that roots into the San Andreas fault at a shallow depth (Figure 29). Normal slip on the LCRF requires strong, local dilation to overcome the north-south contraction of the Transverse Ranges regime (Yang and Hauksson, 2013). The conditions for dominantly normal slip on the LCRF occur in the presence of right-lateral slip that tapers northward on the San Jacinto fault and are plausible both through slip on the San Jacinto fault alone and through co-rupture of both faults (see the Supplemental Material and Figure 30). However, triggered slip on the LCRF large enough to match observations in our paleoseismic trench requires slip on both the San Andreas fault and the San Jacinto fault (Figure 25).

Chronology and Slip of Events in the Lytle Creek Ridge Fault

The timing and number of paleoseismic events in the LCRF establish the frequency of co-rupture of the San Jacinto fault and the San Andreas fault through Cajon Pass. By documenting the amount of triggered slip observed in each event, we also constrain the amount of slip that occurred on these faults when mechanical conditions favored linkage. The chronology of LCRF slip events, based on ^{14}C ages of charcoal samples from the trench and pollen analysis of invasive species (see the Supplemental Material; Table 3), shows that at least three earthquakes have bridged the Cajon Pass earthquake gate in the past 2000 years (Figure 26). These events exhibit apparent vertical offset in the 50 cm to 1 m range, distributed between a low-angle

master normal fault and a graben system of minor faults that root into the LCRF. The LCRF is exposed at the contact with bedrock at the bottom of the hanging-wall stratigraphic sequence (Figure 26). The oldest event exposed in our trench ruptured to the top of unit 150 (Figure 26), a 2-m-thick angular gravel and cobble debris-flow deposit, and is capped by gravelly sand unit 144. Colluvium sourced from the scarp is mixed in with unit 144 and coarsens toward the principal splay fault. Our Bayesian model of radiocarbon ages (see the supplemental Material) places this event before A.D. 623 CE (Figure 31). The penultimate event in the trench ruptured to the top of unit 140, and is capped by the growth strata of units 135 and 130; radiocarbon ages yield a range of A.D. 615–906.

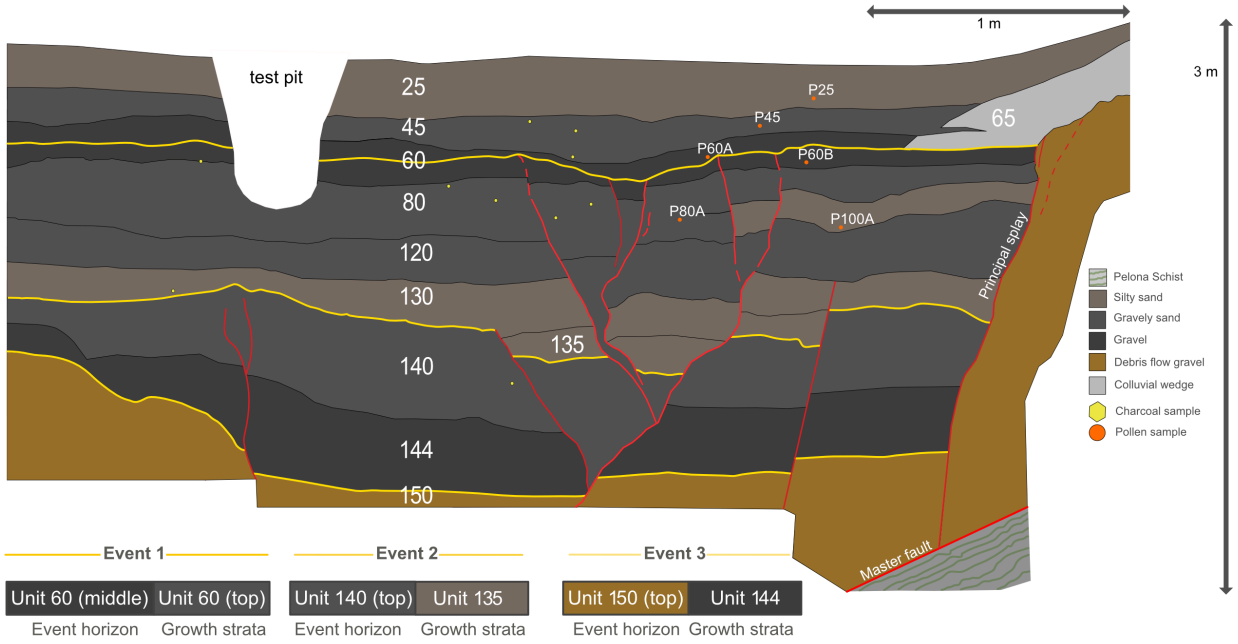

Figure 26: Trench log of the Lytle Creek Ridge fault in Cajon Pass (California, USA) showing structure of the southern wall (see the Supplemental material for details of the trench). Red lines represent faults and fractures. Event horizons and growth strata are listed under the log, and units are color-coded by grain size.

The most recent fault rupture reaches the top of unit 60B, with infilling above this event horizon by unit 60A and by a colluvial wedge contributing material from the footwall. Pollen analyses of samples from the stratigraphic sequence reveal that a significant portion of the pollen is invasive to California. Samples in units 45 and 60A accumulated in the time interval between A.D. 1848, the first appearance in the sequence of the invasive species Spanish broom, and 1890, the first appearance of Russian thistle. Samples from underlying units (60B–150) were presumably deposited before 1839 because they do not contain evidence for tamarisk (Figure 32). This suggests that the most recent event to rupture through Cajon Pass and induce slip on the LCRF corresponds to the 1812 earthquake on the San Andreas fault, and correlates to the most recent large

earthquake recorded at Onderdonk et al.'s (2018) Mystic Lake paleoseismic site on the San Jacinto fault, which they interpreted to have occurred in 1812.

Frequency of Multi-Fault Earthquakes through Cajon Pass

We compare our chronology of LCRF events with the existing chronologies for the southern San Andreas fault and northern San Jacinto fault to constrain the timing of possible joint ruptures and the relationship of these to prior events that did not breach the Cajon Pass earthquake gate (Figure 27). This allows establishment of the relative frequency of shared events between the San Andreas fault, the San Jacinto fault, and the LCRF. The LCRF has hosted three events in the past ∼2000 yr, resulting in a recurrence interval of ∼660 yr. The probability density functions reflecting the ages of the two older events in the LCRF are too broad for direct comparison to the well-established chronologies in Wrightwood (Scharer et al., 2007) and Mystic Lake (Onderdonk et al., 2018), north and south of Cajon Pass on the San Andreas fault and the San Jacinto fault, respectively (Figure 27). It is possible, however, to compare the frequency of events at these paleoseismic sites with the total number of events at the LCRF to establish the portion of shared events. There are three events in our LCRF trench, 13 events at the Mystic Lake site along the San Jacinto fault, and 15 events at the Wrightwood site along the San Andreas fault. This suggests that 20% (3 of 15) and 23% (3 of 13) of events are shared, respectively, between the San Andreas fault and the San Jacinto fault[1]. The most recent event to have bridged the step-over is the 1812 historical earthquake, which appears in the paleoseismic sites of Pallet Creek and Wrightwood on the San Andreas fault and at Mystic Lake on the San Jacinto fault and is now confirmed to have bridged the gap as recorded by the LCRF.

We also compared our results to the most recent Uniform California Earthquake Rupture Forecast (UCERF3; https://www.scec.org/ucerf; Field et al., 2015), which accounts for the possibility of joint rupture of the San Jacinto fault-San Andreas fault through Cajon Pass. UCERF3 predicts an annual rate of shared events comparable to the frequency of events recorded by the LCRF (1.5 events per 1000 yr) (Figure 27). Scharer and Yule (2020) developed a 1500 yr maximum rupture model for the San Andreas fault and the San Jacinto fault based on radiocarbon ages from paleoseismic trenches throughout California. Their model is compatible with our findings, and when considered together with our results (Figure 27), shows that co-rupture of the San Andreas fault and San Jacinto fault through Cajon Pass occurred more frequently (20%–23%) than through the San Gorgonio Pass earthquake gate (13%) (Scharer and Yule, 2020) (SGP in Figure 25).

[1]The predicted passing probability for a step-over 2-2.5 km wide from the logistic models in chapter 1 is 12-19%, comparable to the frequency estimated here.

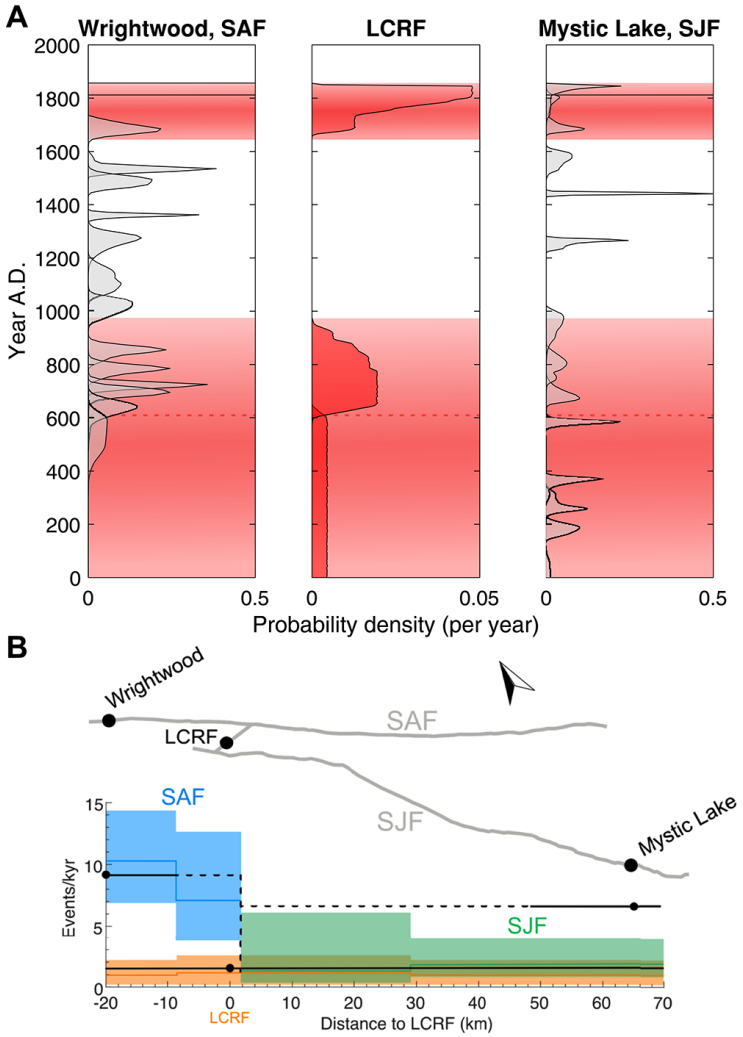

Figure 27: (A) Comparison of seismic event histories recorded at paleoseismic neighboring sites at the northern San Jacinto fault (SJF) and San Andreas fault (SAF) in California (USA). Red shaded rectangles outline the areas spanned by probability density functions of events recorded in the Lytle Creek Ridge fault (LCRF) trench. The Wrightwood chronology is from Scharer et al. (2007), and the Mystic Lake chronology is from Onderdonk et al. (2018). (B) Comparison between event rates from the paleoseismic record and the third Uniform California Earthquake Rupture Forecast (UCERF3; https://www.scec.org/ucerf). Black lines indicate paleoseismic event rates from Wrightwood, Mystic Lake, and the LCRF; black dots denote trench locations. Colored lines represent UCERF3 event rates for the San Andreas fault (blue), San Jacinto fault (green), and shared (orange); shaded areas represent the model range.

Mechanical Conditions of Junction-Spanning Events

Because the LCRF is too short and shallow to be seismogenic on its own, large slip events on the LCRF must be driven by strains imposed by rupture events on the San Andreas fault or San Jacinto fault. We use the A.D. 1812 and 1857 historical events as case examples to understand the conditions that induce slip on the LCRF. We rely on these two events because there are slip distributions available from prior studies and

the induced slip on the LCRF may be compared to our slip measurements from the trench.

Based on correlation with sparse paleoseismic data and historic reports of damage to Spanish California missions, Lozos (2016) modeled the ∼M7.5 1812 earthquake as a multi-fault event that originated around the Mystic Lake paleoseismic site on the San Jacinto fault and propagated northward, breaching the Cajon Pass step-over and transferring slip onto the San Andreas fault. We used the finite-element model PyLith (Aagaard et al., 2013; https://geodynamics.org/cig/software/pylith/) to test potential quasistatic slip distributions for the northern San Jacinto fault in the 1812 event (Figures 33 and 34). We imposed slip on the San Andreas fault and the San Jacinto fault based on the preferred model outcomes from the Lozos (2016) dynamic simulations. We kept the San Andreas fault slip distribution and the San Jacinto fault slip distributions consistent with the Lozos result from Mystic Lake to Colton, the northernmost paleoseismically verified point in the model. From this point northward, we tested ∼30 slip distributions for the northern San Jacinto fault entering the Cajon Pass step-over.

Models were assessed based on the amount of slip they trigger on the LCRF. Plausible slip distributions trigger between 50 cm and 1 m of slip on the LCRF, consistent with the slip measured in our trench for the most recent event. Models that impose slip comparable to observations require at least 5 m of slip on the San Jacinto fault north of the Colton site, tapering steeply within Cajon Pass, losing ∼1 m of slip per kilometer of fault length approaching the step-over, and halting abruptly 1–3 km north of the LCRF (Figure 28). This result is consistent with prior observations that steep slip gradients and abruptly halting ruptures promote linkage across step-overs (Scholz and Lawler, 2004; Elliott et al., 2009).

To explore the possibility that the 1857 earthquake on the San Andreas fault also triggered slip on the LCRF, we modeled the 1857 event based on the surface displacements documented by Sieh (1978) and Zielke et al. (2012). The slip distribution of Sieh (1978), which places the southern terminus of the rupture north of Pitman Canyon, imposes little to no slip (<0.1 cm) on the LCRF (Figure 35). Zielke et al. (2012) reported several slip measurements south of where Sieh (1978) placed the end of the 1857 rupture. We considered only the slip measurements classified as high quality by Zielke et al. (2012), which impose ∼10 cm of slip on the LCRF (Figure 28). The slip measurements in both studies are not age constrained and could combine slip from the 1812 and 1857 events north of Cajon Pass, and thus serve as the upper bound for slip on the 1857 event. Nevertheless, both slip distributions trigger negligible (<10 cm) slip on the LCRF when compared to the slip recorded in our trench for the most recent event (>50 cm). Together with the pollen data, our modeling supports evidence that the most recent event to overcome the Cajon Pass earthquake gate was the 1812 historical earthquake, not the 1857 Fort Tejon earthquake (which likely remained confined to the San Andreas fault). This strengthens the case for co-rupture in 1812 made by prior work (Grant-Ludwig et al., 2015; Lozos, 2016; Onderdonk et al., 2018).

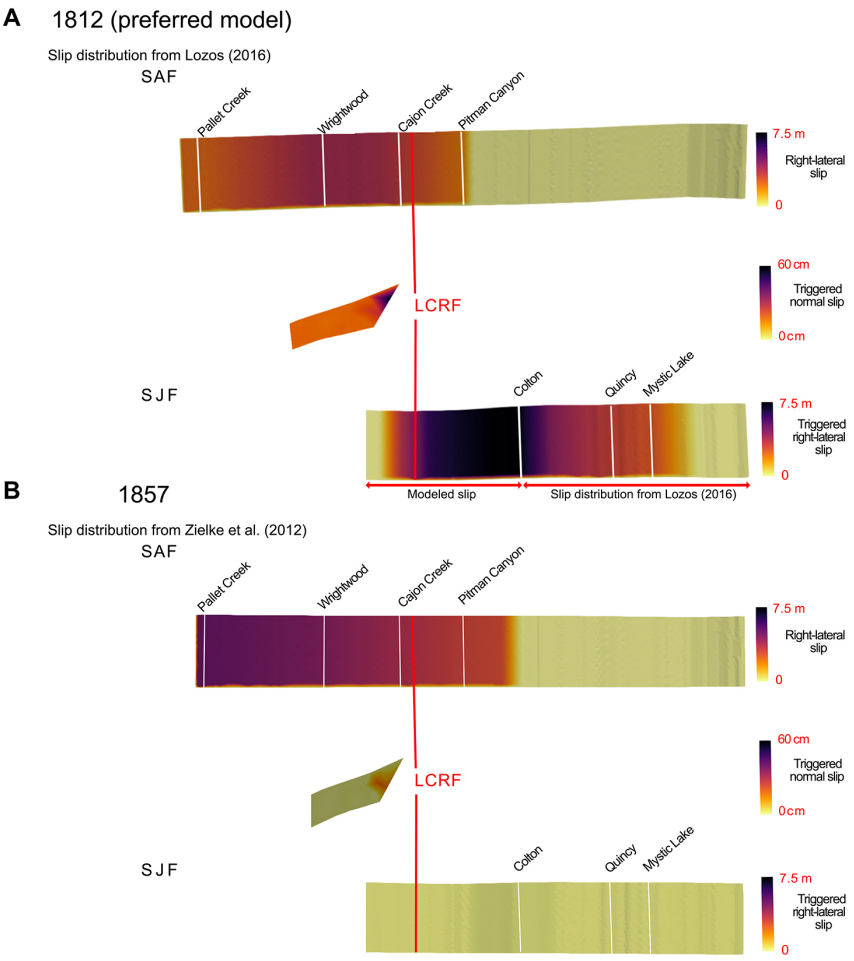

Figure 28: Slip models for the A.D. 1812 and 1857 earthquakes through Cajon Pass (California, USA). (A) Preferred slip model for the 1812 event. Right-lateral slip imposed on the San Jacinto fault and San Andreas fault is based on final slip distributions in the preferred model of Lozos (2016). Slip north of the Colton paleoseismic site (see Figure 25) on the San Jacinto fault is based on a model that triggers the amount of slip measured in the Lytle Creek Ridge fault (LCRF) trench from a suite of tests (Fig. 34). (B) The 1857 event model based on the slip distributions of Zielke et al. (2012).

Heterogeneous stress fields resulting from prior events exert a first-order control of the initiation, arrest, and propagation of the next earthquake (Harris et al., 1991). This behavior is particularly crucial at step-overs, where residual stresses from prior events may determine whether the next rupture is able to overcome the gap, and ultimately regulate the behavior of the earthquake gate over multiple earthquake cycles (Wang et al., 2020). The high slip and steep taper that the 1812 model predicts suggests that the 1812 event released residual stress built up from prior events that terminated on the San Jacinto fault but did not bridge the step-over.

Conclusions

The chronology of rupture events recorded by our LCRF stratigraphic sequence establishes that the San Andreas and the San Jacinto faults have ruptured together at least three times in the past 2000 yr, most recently in the historical 1812 earthquake, preceded by events between A.D. 615 and 906, and between 485 B.C. and A.D. 623. The frequency of events recorded by the LCRF suggests that 20%–23% of events on the adjacent San Andreas and San Jacinto faults may be joint ruptures through Cajon Pass. Mechanical modeling of 0.5–1-m-scale slip on the LCRF in 1812 shows that slip on the San Jacinto fault must have tapered steeply and halted abruptly within 3 km of our trench site. Conversely, the 1857 earthquake triggered <10 cm of slip on the LCRF, confirming that this event did not jump to the San Jacinto. The frequency of events spanning the junction of the San Andreas and San Jacinto faults provides crucial information for long-term hazard estimates for California. The LCRF highlights the potential of small faults that do not contribute to seismic moment release or control large-scale rupture behavior to reveal the mechanics of major faults through earthquake gates.

References

1. Aagaard, B.T., Knepley, M.G., and Williams, C.A., 2013, A domain decomposition approach to implementing fault slip in finite-element models of quasi-static and dynamic crustal deformation: Journal of Geophysical Research: Solid Earth, v. 118, p. 3059–3079, https://doi .org/10.1002/jgrb.50217.

2. Anderson, G., Aagaard, B.T., and Hudnut, K., 2003, Fault interactions and large complex earthquakes in the Los Angeles area: Science, v. 302, p. 1946–1949, https://doi .org/10.1126/science.1090747.

3. Biasi, G.P., Weldon, R.J., II, Fumal, T.E., and Seitz, G.G., 2002, Paleoseismic event dating and the conditional probability of large earthquakes on the southern San Andreas fault, California: Bulletin of the Seismological Society of America, v. 92, p. 2761–2781, https://doi .org/10.1785/0120000605.

4. Elliott, A.J., Dolan, J.F., and Oglesby, D.D., 2009, Evidence from coseismic slip gradients for dynamic control on rupture propagation and arrest through stepovers: Journal of Geophysical Research, v. 14, B02313, https://doi .org/10.1029/2008JB005969.

5. Fialko, Y., 2006, Interseismic strain accumulation and the earthquake potential on the southern San Andreas fault system: Nature, v. 441, p. 968–971, https://doi .org/10.1038/nature04797.

6. Field, E.H., et al., 2015, Long-term time-dependent probabilities for the third Uniform California Earthquake Rupture Forecast (UCERF3): Bulletin of the Seismological Society of America, v. 105, p. 511–543, https://doi .org/10.1785/0120140093.

7. Grant Ludwig, L., Brune, J.N., Anooshehpoor, A., Purvance, M.D., Brune, R.J., and Lozos, J.C., 2015, Reconciling precariously balanced rocks (PBRs) with large earthquakes on the San Andreas fault system: Seismological Research Letters, v. 86, p. 1345–1353, https://doi .org/10.1785/0220140239.

8. Harris, R.A., Archuleta, R.J., and Day, S.M., 1991, Fault steps and the dynamic rupture process: 2-D numerical simulations of a spontaneously propagating shear fracture: Geophysical Research Letters, v. 18, p. 893–896, https://doi .org/10.1029/91GL01061.

9. Lozos, J.C., 2016, A case for historic joint rupture of the San Andreas and San Jacinto faults: Science Advances, v. 2, e1500621, https://doi .org/10.1126/sciadv.1500621.

10. McCalpin, J.P., and Hart, E.W., 2003, Ridge-top spreading features and relationship to earthquakes, San Gabriel Mountains region, Southern California: Part A. Distribution and description of ridgetop depressions (sackungen), in Hart, E.W., ed., Ridge-Top Spreading in California; Contributions toward understanding a significant seismic hazard: California Geological Survey Open-File Report 1, CD 2003-05, 2 CD-ROMs.

11. Morton, D.M., and Miller, F.K., 2006, Geologic map of the San Bernardino and Santa Ana 30' × 60' quadrangles, California: U.S. Geological Survey Open-File Report 2006-1217, scale 1:100,000, 4 sheets, https://doi .org/10.3133/ofr20061217.

12. Onderdonk, N., McGill, S., and Rockwell, T., 2018, A 3700 yr paleoseismic record from the northern San Jacinto fault and implications for joint rupture of the San Jacinto and San Andreas faults: Geosphere, v. 14, p. 2447–2468, https://doi .org/10.1130/GES01687.1.

13. Rockwell, T.K., Dawson, T.E., Ben-Horin, J.Y., and Seitz, G., 2015, A 21-event, 4,000-year history of surface ruptures in the Anza seismic gap, San Jacinto fault, and implications for long-term earthquake production on a major plate boundary fault: Pure and Applied Geophysics, v. 172, p. 1143–1165, https://doi .org/10.1007/s00024-014-0955-z.

14. Rockwell, T., Scharer, K.M., and Dawson, T.E., 2016, Earthquake geology and paleoseismology of major strands of the San Andreas fault system, in Anderson, R., and Ferriz, H., eds., Applied Geology in California: Association of Environmental & Engineering Geologists Special Publication 26: Redwood City, California, Star Publishing, p. 721–756.

15. Scharer, K.M., and Yule, D., 2020, A maximum rupture model for the southern San Andreas and San Jacinto faults, California, derived from paleoseismic earthquake ages: Observations and limitations: Geophysical Research Letters, v. 47, e2020GL088532, https://doi .org/10.1029/2020GL088532.

16. Scharer, K.M., Weldon, R.J., Fumal, T.E., and Biasi, G.P., 2007, Paleoearthquakes on the southern San Andreas fault, Wrightwood, California, 3000 to 1500 BC: A new method for evaluating paleoseismic evidence and earthquake horizons: Bulletin of the Seismological Society of America, v. 97, p. 1054–1093, https://doi .org/10.1785/0120060137.

17. Scholz, C.H., and Lawler, T.M., 2004, Slip tapers at the tips of faults and earthquake ruptures: Geophysical Research Letters, v. 31, L21609, https://doi .org/10.1029/2004GL021030.

18. Sieh, K.E., 1978, Slip along the San Andreas fault associated with the great 1857 earthquake: Bulletin of the Seismological Society of America, v. 68, p. 1421–1448.

19. Toda, S., Stein, R.S., Sevilgen, V., and Lin, J., 2011, Coulomb 3.3: Graphic-rich deformation and stress-change software for earthquake, tectonic, and volcano research and teaching—User guide: U.S. Geological Survey Open-File Report 2011-1060, p. 63, https://doi .org/10.3133/ofr20111060.

20. Wang, H., Liu, M., Duan, B., and Cao, J., 2020, Rupture propagation along stepovers of strike-slip faults: Effects of initial stress and fault geometry: Bulletin of the Seismological Society of America, v. 110, p. 1011–1024, https://doi .org/10.1785/0120190233.

21. Yang, W., and Hauksson, E., 2013, The tectonic crustal stress field and style of faulting along the Pacific North America Plate boundary in Southern California: Geophysical Journal International, v. 194, p. 100–117, https://doi .org/10.1093/gji/ggt113.

22. Zielke, O., Arrowsmith, J.R., Ludwig, L.G., and Akciz, S.O., 2012, High-resolution topography-derived offsets along the 1857 Fort Tejon earthquake rupture trace, San Andreas fault: Bulletin of the Seismological Society of America, v. 102, p. 1135–1154, https://doi .org/10.1785/0120110230.

Appendix: Methods

Conditions for triggering the LCRF

Rupture conditions for LCRF triggering The LCRF is a low-angle, shallow normal fault, located between the San Andreas and the San Jacinto faults, which by itself is too shallow (Supplemental Figure 29) and too short to be seismogenic or act directly to transfer slip between these faults. Thus, slip on the LCRF is most likely a quasistatic response to slip on these faults or to strong shaking. Normal motion on the LCRF requires strong dilation that overcomes the regional north-south contraction of the Transverse Ranges (Yang and Hauksson, 2013). Strong dilation is expected adjacent to a right-lateral fault rupture, on either or both the San Andreas and the San Jacinto faults, that terminates within Cajon Pass. To test the imposed stress and the optimal slip direction of the LCRF in response to rupture on either or both of the San Andreas and the San Jacinto faults, we build a suite of Coulomb stress models (Supplemental Figure 30)(Toda et al., 2011). In the models, slip on the neighboring part of the San Andreas fault or San Jacinto fault is tapered to simulate a stress drop of approximately 6 MPa. Based on our Coulomb models, the conditions necessary for dominantly normal slip occur in the presence of right-lateral slip that tapers northward on the San Jacinto fault (Supplemental Figure 30, middle and right). A scenario involving tapered slip on both the San Andreas and the San Jacinto faults (Supplemental Figure 30, right) triggers double the stress change on the LCRF than the scenario involving the San Jacinto fault alone (Supplemental Figure 30, middle). Rupture that terminates on the San Andreas without stepping over induces a stronger component of left-lateral slip than normal slip on the LCRF, inconsistent with our field observations. To further distinguish between our two favorable Coulomb stress models, we built a finite element mesh in Trelis (Supplemental Figure 33) based on the mesh in Lozos et al. (2016). The details of the mesh and inclusion of the LCRF are given in the finite element modeling section of this appendix. Extending the slip distributions used in our Coulomb stress models to more realistic, non-planar faults, we allow the LCRF to slip in response to rupture of the San Andreas and the San Jacinto fault. The summary of these models and our Coulomb stress models are in Figure 25 of the main manuscript. Modeled slip on the San Jacinto fault only imposes $\sim$1 mm of normal slip on the LCRF (Figure 25, bottom middle), which would not be distinguishable from our paleoseismic record. While different slip conditions (larger slip, steeper slip tapers) on the San Jacinto fault would trigger larger slip on the LCRF, an increase of over two orders of magnitude would be required to match the >50cm of slip recorded per event in our trench. Slip on both the San Jacinto fault and the San Andreas imposes $\sim$10 cm of normal slip on the LCRF (Figure 25, bottom left). The slip per event observed in the trench (50 cm-1 m) exceeds this number by at least a factor of 5. This mismatch would be overcome by larger slip on the San Jacinto fault and the San Andreas, or steeper slip tapers on these faults. Our models for the 1812 event show

such a case (see main manuscript and finite element models section). Thus, while the LCRF may preserve a record of slip on the northern San Jacinto fault alone, the large slip events described in this manuscript are most likely the product of co-rupture of the San Andreas and the San Jacinto faults. While we cannot rule out the possibility of lingering Coulomb stresses from ruptures promoting rupture on the adjacent fault, large slip on the LCRF requires steep slip tapers, which are a feature of linked earthquake rupture (Elliott, Dolan, and Oglesby, 2009; Scholz and Lawler, 2004) favoring co-rupture as the main mechanism driving the large slip we observe in the trench.

Trenching

The excavation site for the trench was chosen based on the availability of ponded sediment that would record fault slip. Because the LCRF scarp ruptures through a ridge, depocenters are scarce. A team excavated a 15 m long, 1.5m wide, ∼2-3 m deep trench where the uphill-facing fault scarp dams a small, ephemeral channel draining the crest of Lytle Creek Ridge (Figure 25). The strata in the trench were numbered by age, increasing downward. The numbering scheme was developed as trenching proceeded, with gaps between numbers left to accommodate units not yet characterized or subdivided. The trench interpretation is shown in Figure 26. We only show the westernmost 5 meters of the trench, because the remaining 10 meters were not faulted.

Radiocarbon dating

We collected charcoal samples to constrain the age of the stratigraphic units and earthquake event horizons. We collected over 120 samples spanning the entire stratigraphic sequence of the trench. Collection of multiple samples per unit is essential because age determination using detrital charcoal is limited by the effects of inheritance during growth and transport of burned vegetation to the depocenter. We selected and prepared 40 samples in the Keck Center for Accelerator Mass Spectrometry (KeckCAMS) Laboratory at the University of California, Irvine following the standard pre-treatment, combustion, and graphite reduction processes. The selected samples were then measured by the KeckCAMS, and calibrated to calendar years with the Intcal13 radiocarbon calibration curve (Ramsey, 2009; Reimer et al., 2013). We then used OxCal v.4.2., a software for Bayesian analysis of geochronology data, to re-calibrate the probability distribution functions of sample ages to account for stratigraphic ordering (Lienkaemper and Ramsey, 2009) and construct a depth profile of units that then could be used to interpret the timing of events in the trench. Because samples from different layers overlap in age and reversals are common, only the youngest age per unit was included in the Oxcal model. The ages for all samples are shown in Table 3. Pollen analysis is required to refine stratigraphic ages younger than ∼1650A.D., because of non-unique calibration of ^{14}C dates during this time.

We collected pollen samples from every fine-grained unit in the stratigraphic sequence to obtain additional dating constraints. Pollen analysis bypasses the inheritance problem in the radiocarbon ages but only extends back to the early 1600s.

Invasive pollen species analysis

We collected nine samples from the trench for palynological analysis (Figure 26) from the uppermost strata of the trench. All samples were soil-like sediments, presumably a mixture of aeolian sand, colluvial material, and an organic fraction, mostly fine woody dust, microcharcoals, phytoliths, and pollen. To determine the pollen concentration per sample, two Lycopodium tablets (BATCH N177745) were added to each sample (15 g) before the beginning of treatment. We used the standard Faegri-Iversen potassium hydroxide, hydrochloric acid, and acetolysis method for extracting pollen from a mixture of sand, silt, and clay, but with some necessary additions. After the dissolution of carbonates and silicates, the remaining fraction was filtered several times to remove particles coarser than 70 microns, and those finer than 7 microns. From the remaining purified sediment, pollen was extracted using a sodium polytungstate heavy liquid flotation method. The slides are prepared using glycerin and sealed with a varnish. The objective of our palynological analysis was to identify pollen species non-native to California and to find the possible first appearance of the introduced species. This method was successfully used in the past for dating seismic events in California (e.g. Fumal et al., 2002). Historical records suggest that invasive plant species emerged in California generally in the 18th century (Mensing and Byrne, 1998). We compiled a list of all existing plant species in the Cajon Pass area based on references of plant atlas Calflora (Calflora, 2020). We selected a group of non-native plants from the general list, including 63 different plant genera and a total of 123 species. We then assembled an atlas of pollen images of each invasive species and used it for pollen identification. From 450 to 2050 pollen grains (both introduced and native) were counted for each sample, except for two bottom-most samples (P100 A and P130A) which did not have statistically sufficient pollen. Twenty-seven different invasive species were identified. The absolute and relative amounts of each species of pollen are presented in repository https://doi.org/10.1130/GEOL.S.17051585.v1. with the date of their introduction to California. A kite diagram (Figure 32) represents frequencies of occurrence of introduced species along a time transect. We use the year of introduction of the invasive pollen species present in our samples as constraints in our Bayesian models. Aerial pollen transport occurs at a rate of ∼2-20km/yr (Pysek and Humle, 2005). The trenching site is downwind from the two nearest missions, and ∼100 km away from Los Angeles. To account for the transportation delay in our Oxcal model, we treat our pollen constraints as uniform probability density functions that start at the year of introduction of the species and extend for 20 years, resulting in a right-triangle truncation of the event PDF (see the example for pollen sample 1 below). We choose 20 years as a

conservative range based on the transportation rate range of Pysek and Humle (2005).

Finite element modeling

Because the LCRF is too short and shallow to be seismogenic, large slip events on the LCRF must be driven by strains imposed by rupture events on the San Andreas or San Jacinto faults. Using mechanical modeling, we can use the magnitude of LCRF slip to constrain these strains, and thus the amount and gradient of slip on the northern San Jacinto in these events. We focus on the 1857 event versus the 1812 event given the pre-existing slip distributions available. This process is described in the main body of this manuscript. We mesh the San Andreas and San Jacinto faults based on the USGS Quaternary Faults Database surface traces with simplified geometries at depth (Lozos, 2016, Supplemental figure 33) using the commercial finite element meshing software Trelis. We use the San Bernardino and Claremont strands of the San Andreas and the San Jacinto respectively (Lozos, 2016). The faults are embedded in a homogeneous, elastic crustal volume 16 km deep, following the work of Lozos (2016). Because the LCRF is most likely aseismic unless it is being driven by the San Andreas and/or the San Jacinto, there is no microseismicity that can aid in mapping its subsurface geometry. Based on its outcrop pattern and dip in the trench, we interpret the LCRF intersects the rough topography of the Lytle Creek Ridge at a shallow angle, resulting in a complex surface trace that is unlikely to be representative of the subsurface geometry. To avoid unrealistic complexity, we mesh the LCRF as a planar, low-angle normal fault using the westerly strike and 30° dip measured in the field at six different locations. Our models assume there are no residual stresses in the LCRF from prior events or tectonic loading that would facilitate triggering from the imposed displacements on the San Andreas and San Jacinto. We use finite element code Pylith (Aagard et al., 2013) to impose kinematic slip on the San Andreas and the San Jacinto faults. The parameters used in the simulations are listed in Supplemental Table 4. In these quasistatic models, the LCRF slips when the static value of friction is overcome and the fault is assumed to be cohesionless. The LCRF ruptures through a range of materials present at different sections of the Pelona Schist, including through bands of serpentine and tonalitic intrusions. We tested a range of friction values to determine the sensitivity of slip on the LCRF to this parameter and found negligible differences within the range of μ = 0.2-0.6. For the final models, we assumed a coefficient of static friction of 0.4.

Supplemental references

1. Bronk Ramsey, C., 2009, Bayesian analysis of radiocarbon dates: 233 Radiocarbon, v. 51, p. 337–360, https://doi.org/10.1017/S0033822200033865.

2. Calflora, 2021, Information on California 235 plants for education, research and conservation: Berkeley, California, The Calflora 236 Database, https://www.calflora.org/ (accessed 10 August 2019).

3. Lienkaemper, J.J., 256 and Bronk Ramsey, C., 2009, OxCal: Versatile tool for developing paleoearthquake 257 chronologies—A primer: Seismological Research Letters, v. 80, p. 431–434, 258 https://doi.org/10.1785/gssrl.80.3.431.

4. Mensing, S., and Byrne, R., 1998, 275 Pre-mission invasion of Erodium cicutarium in California: Journal of Biogeography, 276 v. 25, p. 757–762, https://doi.org/10.1046/j.1365-2699.1998.2540757.x.

5. Pyšek, P., and Hulme, P.E., 2005, 287 Spatio-temporal dynamics of plant invasions: Linking pattern to process: Écoscience, 288 v. 12, p. 302–315, https://doi.org/10.2980/i1195- 6860-12-3-302.1.

6. Reimer, P.J., et al., 2013, IntCal13 and 290 Marine13 radiocarbon age calibration curves 0– 50,000 years cal BP: Radiocarbon, 291 v. 55, p. 1869–1887.

Supplemental figures

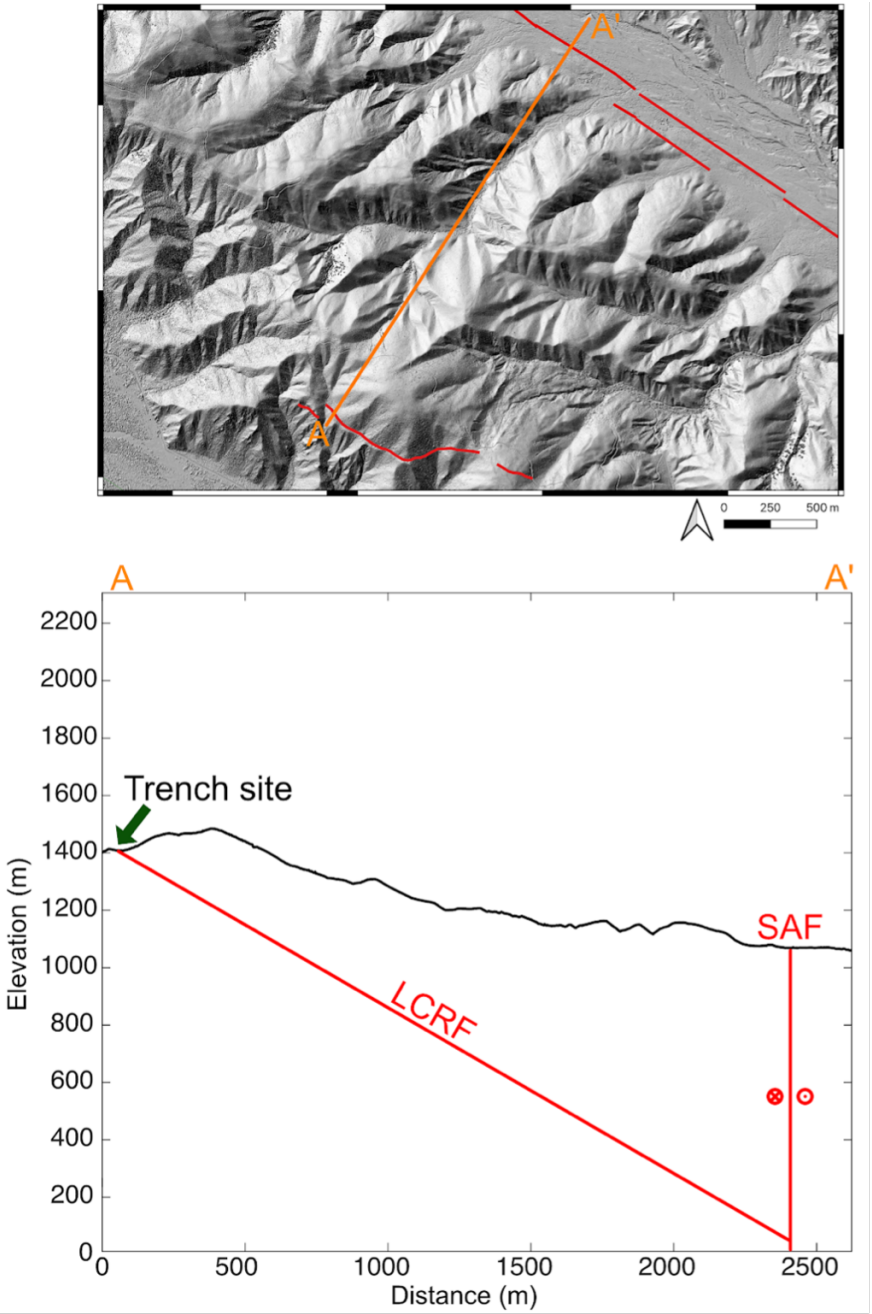

Figure 29: Cross-section of the Lytle Creek Ridge Fault (LCRF) based on measurements of strike and dip collected in the field. The LCRF roots into the San Andreas fault at a shallow depth.

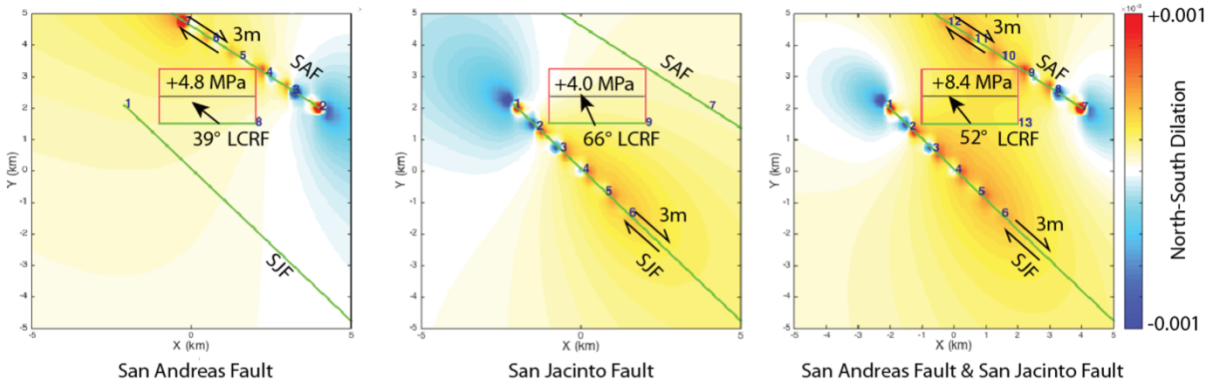

Figure 30: Coulomb models (Toda et al., 2011) for stress increase and optimal slip direction on a 30° north-dipping LCRF in response to rupture on the vertical San Andreas fault (left), San Jacinto fault (middle), or both (right). Color corresponds to change in north-south dilational strain. In each case, slip is tapered to simulate constant stress drop of approximately 6 MPa, driving a comparable stress increase on LCRF. Highest stress change, with slip direction consistent with that observed in outcrop, occurs for the case where slip occurs on the San Andreas fault and San Jacinto fault.

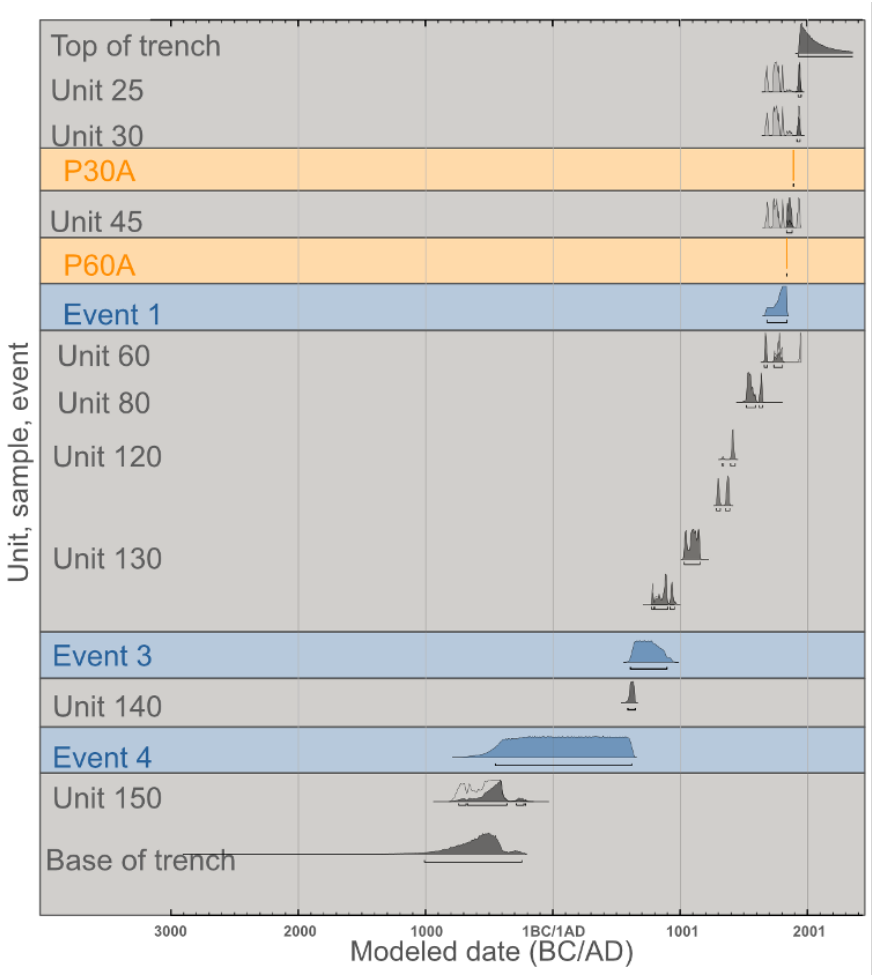

Figure 31: Modeled age of radiocarbon samples and events based on charcoal and invasive pollen species samples produced using OxCal software (Ramsey, 2009). Radiocarbon ages calibrated with the IntCal09 calibration curve (Reimer et al. 2013). The event ages are based on the ages of units above and below the event horizon. Darker probability density function (PDF) shading indicates trimming of age ranges based on stratigraphic constraints. Table 3 lists the radiocarbon samples with their respective carbon content and ages, following stratigraphic order.

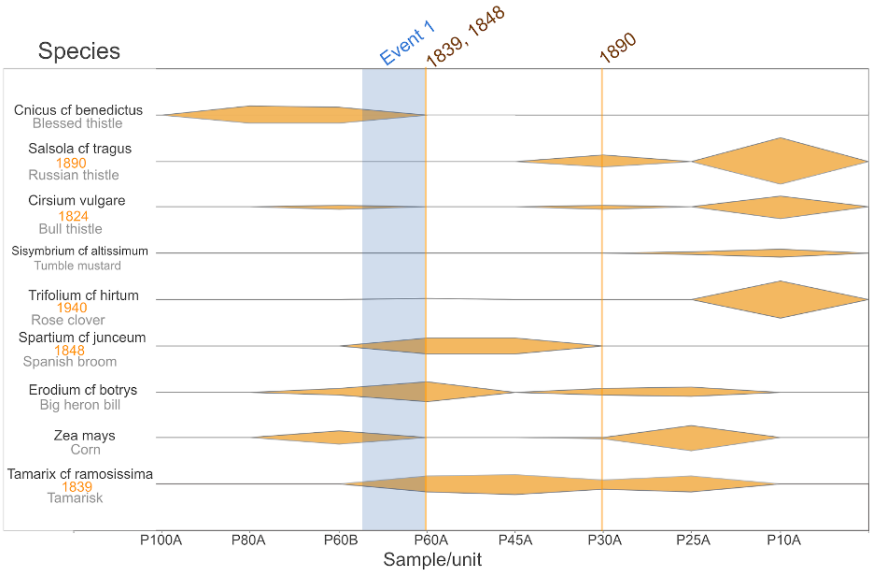

Figure 32: The kite diagram plots the appearance of pollen of plants introduced to California as a percentage. The percentage of introduced species has been calculated from the total pollen, including native species, found in the sample and taken as 100%. Only nine species out of twenty-three found were selected for the diagram as the most representative. The complete data is available from https://doi.org/10.1130/GEOL.S.17051585.v1. The X-axis represents sampling sites according to their order in the stratigraphic section and does not necessarily coincide with the timeline.

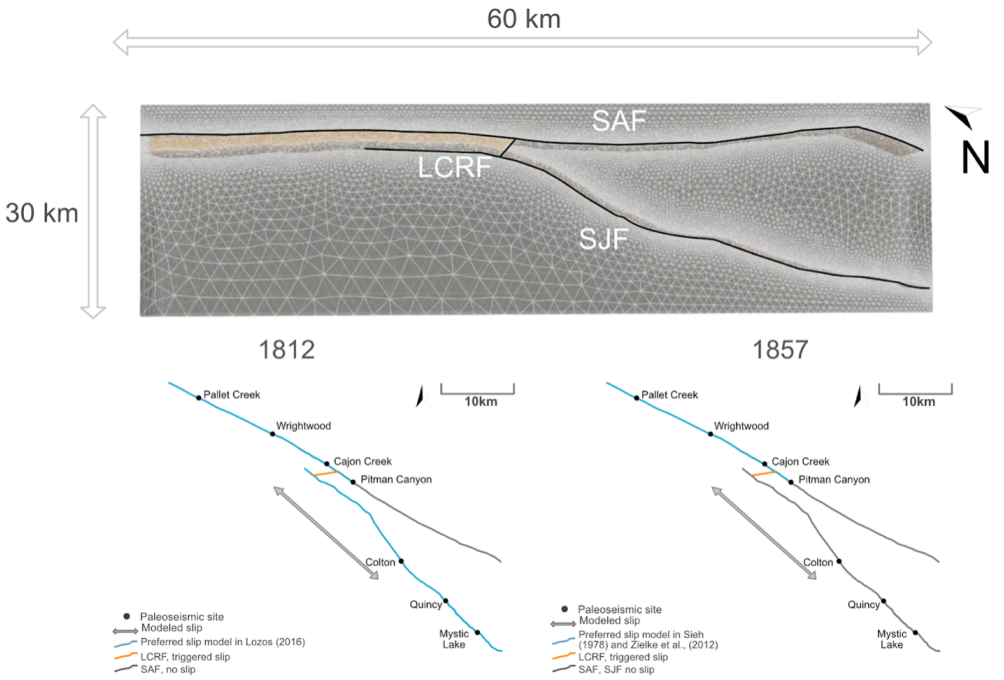

Figure 33: Top: Finite element mesh reproducing fault geometries in the Cajon Pass area. The San Andreas and the San Jacinto faults are based on the SCEC Community Fault Model's tsurfs. The geometry of the LCRF is a planar approximation projected from strike and dip measurements collected in the field. Bottom left: Slip model setup for the 1812 earthquake. Bottom right: Slip model setup for the 1857 earthquake.

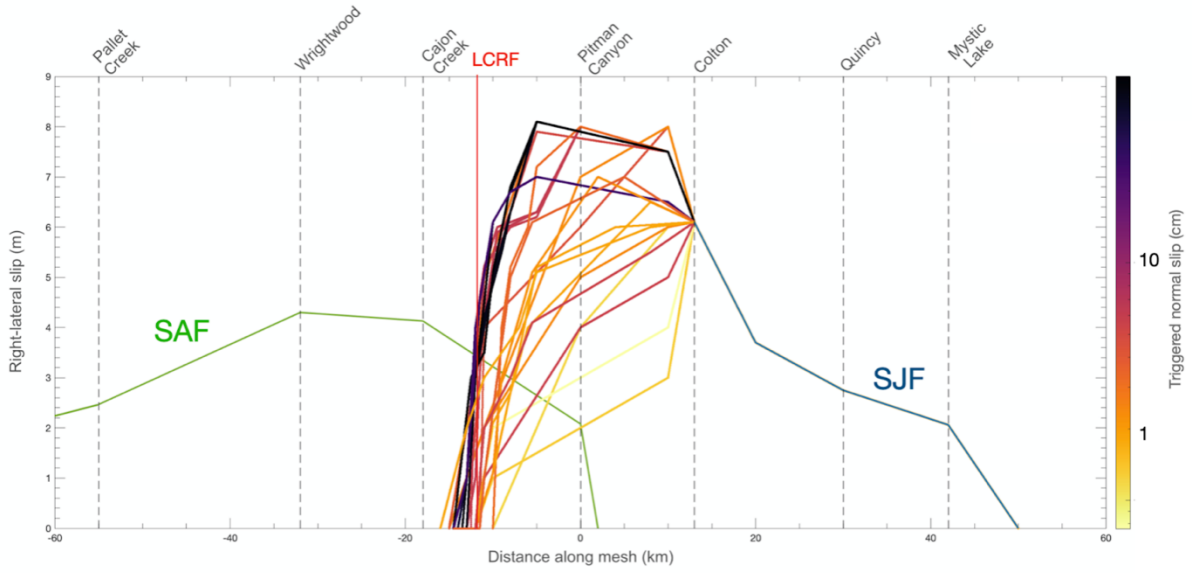

Figure 34: Slip models for the 1812 events through Cajon Pass. The grey and green lines are right-lateral slip imposed on the San Jacinto fault and the SAF based on the final slip in the preferred model in Lozos (2016). We test a suite of slip distributions on the San Jacinto fault north of Colton. The lines associated with these slip distributions are color-coded by the normal slip those distributions trigger on the LCRF.

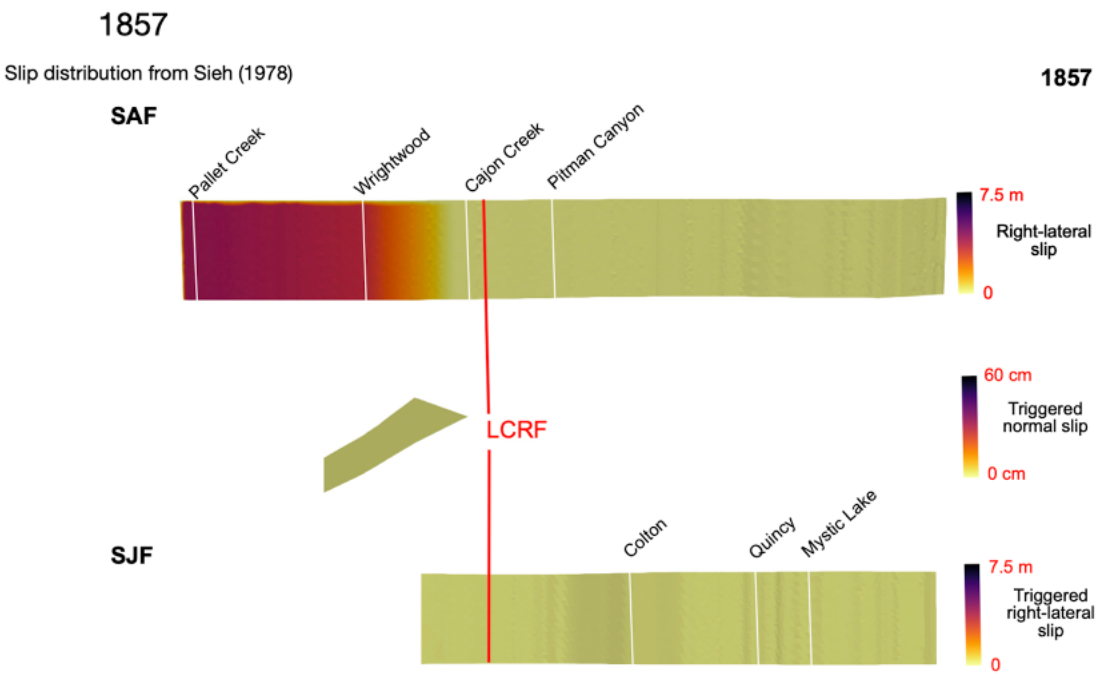

Figure 35: Model for the 1857 event based on the slip distributions in Sieh (1978).

Table 3: Radiocarbon samples with their respective carbon content and ages, following stratigraphic order.

UCIAMS	Sample name	Trench Unit	fraction modern	±	D14C (%)	±	14C age (BP)	±
217654	LCRF-C14-79	25	0.980419	0.001596	-19.581438	1.596372	160	15
217646	LCRF-C14-53	30	0.981020	0.001642	-18.980397	1.642009	155	15
217649	LCRF-C14-59	30	0.911506	0.001673	-88.493561	1.672737	745	15
217630	LCRF-C14-1 .20mgC	40	0.924420	0.001776	-75.579551	1.775605	630	20
217637	LCRF-C14-30	45	0.872747	0.001611	-127.252838	1.611181	1095	15
217643	LCRF-C14-34	45	0.981591	0.001530	-18.408918	1.530351	150	15
217632	LCRF-C14-13	50	0.853135	0.001264	-146.864671	1.264341	1275	15
217631	LCRF-C14-2	50-60	0.955100	0.001800	-44.900000	1.800000	370	15
217638	LCRF-C14-32	60	0.976567	0.001607	-23.433351	1.606992	190	15
217635	LCRF-C14-26	75	0.848542	0.001317	-151.458037	1.317146	1320	15
221704	LCRF-C14-96 .094mgC	80	0.853623	0.001945	-146.376798	1.944710	1270	20
217651	LCRF-C14-66	80	0.962498	0.001537	-37.502452	1.537312	305	15
217634	LCRF-C14-17	90	0.830550	0.001619	-169.449939	1.619130	1490	20
217633	LCRF-C14-15	100	0.853231	0.001261	-146.768579	1.261110	1275	15
217644	LCRF-C14-39	120	0.985515	0.001537	-14.485180	1.536885	115	15
217647	LCRF-C14-55	120	0.737201	0.001310	-262.798663	1.309976	2450	15
217650	LCRF-C14-61	120	0.935737	0.001453	-64.263172	1.453125	535	15
217652	LCRF-C14-70	120	0.922012	0.001365	-77.987986	1.364599	650	15
221707	LCRF-C14-100	120-130	0.735400	0.001200	-264.600000	1.200000	2470	15
221696	LCRF-C14-89 .24mgC	130	0.889493	0.001365	-110.506817	1.365232	940	15
221697	LCRF-C14-91	130	0.731280	0.001363	-268.719751	1.362685	2515	15
221698	LCRF-C14-93	130	0.865514	0.001345	-134.486397	1.345357	1160	15
221699	LCRF-C14-94	130	0.735469	0.001138	-264.530981	1.138396	2470	15
221703	LCRF-C14-95	130	0.735153	0.001087	-264.846613	1.087421	2470	15
221705	LCRF-C14-97	130	0.736536	0.001310	-263.463892	1.310065	2455	15
221706	LCRF-C14-98 .054mgC	130	0.728216	0.002924	-271.783722	2.924247	2550	35
217636	LCRF-C14-29	130	0.737878	0.001149	-262.121737	1.148607	2440	15
217645	LCRF-C14-48	140	0.835745	0.001409	-164.254999	1.408532	1440	15
217648	LCRF-C14-58	140	0.695740	0.001090	-304.259504	1.089859	2915	15
221708	LCRF-C14-102	144	0.631794	0.000958	-368.205915	0.958084	3690	15
221709	LCRF-C14-103 .054mgC	144-146	0.626001	0.002994	-373.999229	2.993574	3765	40
217653	LCRF-C14-71	150	150.000000	0.005925	-259.069790	5.924571	2410	70

Table 4: Parameters used in the finite element models of the 1812 and 1857 events.

Parameter	Value
Density crust	From SCEC CVM-S
Vs	From SCEC CVM-S
Vp	From SCEC CVM-S
Static friction coefficient (LCRF)	0.4
Cohesion (LCRF)	0 MPa
Element size	∼100 m (near field) ∼1000 m (far field)

Chapter 3: Accrual of widespread rock damage from the 2019 Ridgecrest earthquakes

Abstract

Inelastic processes from earthquakes contribute to the formation of fault damage zones that constitute a permanent sink of strain energy, modify the elastic properties of the shallow crust and amplify near-field ground shaking. Constraints on the extent of inelastic deformation differ depending on the dataset and methodology used. Here we combine fracture, strain and aftershock maps from the 2019 Ridgecrest earthquakes to reconcile the properties of damage zones across different spatial scales and resolutions. The decay of inelastic deformation with distance from the fault is well described by an inverse power law, extends beyond 20 km from the faults and is insensitive to lithology and slip magnitude. The damage decay is continuous without breaks in scaling, suggesting that a single mechanism dominates yielding. On the basis of our fracture density distribution, we predict an average reduction in shear rigidity of about 20% in bedrock and 40% in alluvium immediately adjacent to the fault, declining to less than 1% at 100 m. Our observations reveal how macroscopic fracturing generates intense near-fault damage and that widespread damage accrues regionally over multiple earthquake cycles.

Introduction

Long-term tectonic deformation is often interpreted through block models where rigid micro-plates are delimited by faults (Loveless and Meade, 2010; Evans et al., 2016). This model of crustal deformation is favoured by field and geodetic observations showing that strain is maximized and focused within a narrow band along the fault, with the remainder (20–40%) smoothly distributed in the adjacent 0.1–1.0 km (Shelef and Oskin, 2010; Milliner et al., 2016; Scott et al., 2018). Inelastic strain that occurs within this damage zone is accommodated by a suite of dissipative processes, including fracturing, warping, block rotations and granular yielding (Milliner et al., 2016; Shipton et al., 2006). These processes account for a slip deficit on the fault (Dolan and Haravitch, 2014), constitute a strain energy sink (Shipton et al., 2006) and contribute to weakening the host lithology, causing permanent changes to the physical properties of the crust (Cochran et al., 2009). Thus, the extent and properties of the damage zone are fundamental elements in long-term models of crustal deformation, probabilistic fault displacement hazard assessment and seismic shaking predictions.

Damage zones manifest as a tabular volume of fractured and warped rock surrounding the main fault plane (Brock and Engelder, 1977). Within this volume, fracture density decays with distance from the primary fault (Chester et al., 2005; Mitchell and Faulkner, 2009; Savage and Brodsky, 2011). Damage zones

have also been characterized by the concentration of seismicity surrounding faults (Powers and Jordan, 2010; Perrin et al., 2021). Geodetically, damage zones are described as areas of reduced shear rigidity (Fialko, 2004) or, for directly imaged earthquake ruptures, the area where strain exceeds the elastic limit of the material (Scott et al., 2018; Barnhart et al., 2020; Milliner et al., 2021). Seismologically, damage zones are measured as a volume of decreased shear-wave velocity surrounding a fault that hosts guided waves (Li et al., 2006; Qiu et al., 2021).

The 2019 Ridgecrest sequence (Figure 36) ruptured an orthogonal set of strike-slip faults in a moment magnitude (M_W) 6.4 foreshock followed by a M_W 7.1 mainshock (Ross et al., 2019; Liu et al., 2019; Fialko and Jin, 2021). The event was extensively monitored, offering the opportunity to investigate the extent and physical properties of the damage zone through an integrated approach. Geodetic studies of the Ridgecrest earthquakes yield differing views of inelastic deformation. Optical image correlation defines a 30- to 100-m-wide zone of inelastic strain centred on the rupture (Barnhart et al., 2020; Milliner et al., 2021) and wider zones of diffuse deformation (0.6–2.0 km) receiving contributions from both elastic and inelastic processes (Antoine et al., 2021). Synthetic aperture radar (SAR) phase gradient maps also illuminate a wide (>1 km) zone of secondary-fault-zone deformation, including both discrete frictional slip and elastic deformation of secondary-fault damage zones, driven by Coulomb stress change (Xu et al., 2020). Seismological studies show 0.2–2.0 km waveguide and low-velocity zones that vary along strike (Qiu et al., 2021). To reconcile these spatially variable constraints on the extent of damage, we combine aftershocks (Ross et al., 2019), strain maps (Milliner et al., 2021), post-earthquake lidar data (Hudnut et al., 2020) and rupture maps (Ponti et al., 2020; Rodriguez Padilla et al., 2022). The combination of datasets allows us to characterize the damage zone in detail and across different spatial scales and to assess sensitivity to fault slip, lithology and data resolution.

High-resolution coverage of the Ridgecrest earthquakes

We incorporate three independent surface-rupture mapping datasets. Rodriguez Padilla et al. (2022) used 2- to 20-cm-per-pixel unmanned aerial vehicle (UAV) imagery 28 and 5-cm-per-pixel aerial imagery (Pierce et al., 2020) to map fractures from the Ridgecrest earthquakes (Figure 36a,c). Ponti et al. (2020) mapped the surface rupture from field observations and geodetic data. We generate a third rupture map from 0.5-m-resolution lidar collected a month after the mainshock (Figure 36a)(Hudnut et al., 2020). To examine fracturing at depth, we incorporate aftershocks from the Southern California Seismic Network (SCSN) and quake template matching (QTM) earthquake catalogues (Ross et al., 2019; Hauksson, 2020) (Figure 36b). Last, we consider the distribution of surficial strain mapped from satellite imagery cross correlation. We

use the fault-parallel shear strains measured from profiles oriented perpendicular to the primary rupture and stacked over a 138 m distance along strike (Extended Data Figure 40) (Milliner et al., 2021). We find inelastic strains ($> 10^{-3}$) are limited to 30–100 m from the fault. Beyond 1 km, strains become too small to resolve with this approach.

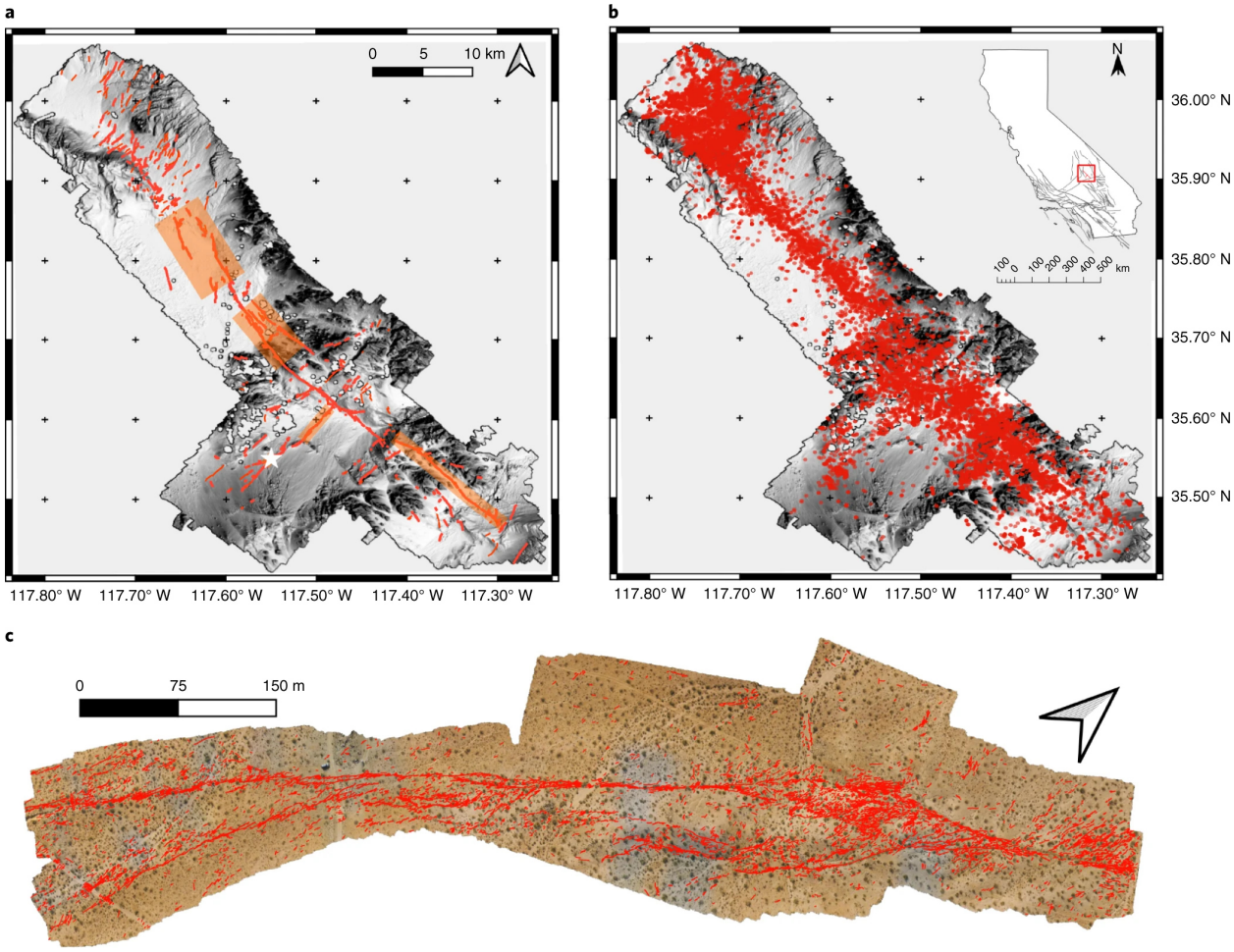

Figure 36: Distribution of surficial fractures and aftershocks. a, Surface fracturing mapped from the Ridgecrest lidar data (Hudnut et al., 2020). The orange rectangles highlight the areas where the rupture was mapped from high-resolution aerial imagery (Pierce et al., 2020). b, Distribution of aftershocks from the Ridgecrest QTM catalogue spanning the sequence from 4 July to 25 July 2019 (Ross et al., 2019). c, Surface fracturing mapped from UAV imagery (Pierce et al., 2020; Rodriguez Padilla et al., 2022). The imagery corresponds to the white star on a.

Distribution of inelastic deformation

To investigate the distribution of inelastic deformation with distance from the fault, we quantify the decay of fracture density, aftershock density and strain intensity for stacked profiles across the rupture. We measure the nearest distance between each damage feature and the main fault: in two dimensions for the fractures

and strain maps and in three dimensions for the aftershocks. We find that feature density with distance defines an inverse power law, with a break in scaling nearest to the fault that varies by feature type. We fit these damage distributions with the relationship proposed by Powers and Jordan (2010), where the decay with distance from the fault is defined by the density at the fault ν_o, a parameter defining the distance between the origin and a break in scaling d, the sharpness of the corner m and γ, which is the slope of the decay at distance $x >> d$:

$$\nu(x) = \nu_o \left(\frac{d^m}{|x|^m + d^m} \right)^{\frac{\gamma}{m}} \tag{8}$$

We use an ensemble sampler for Markov chain Monte Carlo to fit equation 8 to our datasets, assuming that $\nu(x)$ within each bin samples a Poisson distribution (Powers and Jordan, 2010) (Figure 37a). The maximum likelihood values of γ range from 0.8 to 1.1 and overlap within uncertainty (Figure 37b).

Equation 8 has two corner-defining parameters, d and m. We hold m=2 as the quality of fits does not vary significantly with corner sharpness (Powers and Jordan, 2010). The corner position d is farthest out for the aftershocks at 50 m but sits between 0 and 10 m for the higher-spatial-resolution lidar, field and imagery-derived fracture datasets (Figure 37c) and cannot be resolved for the strain data.

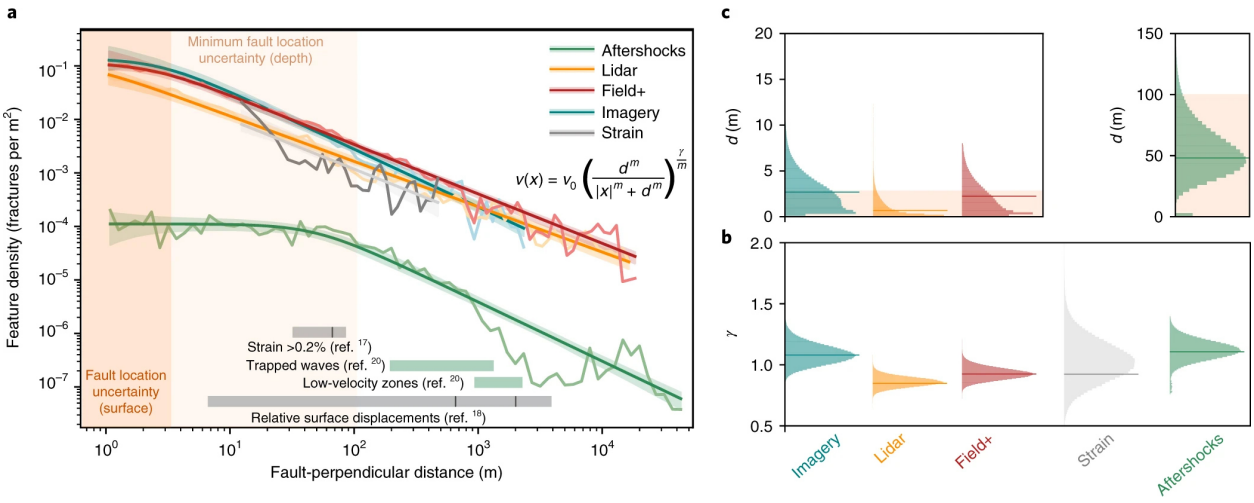

Figure 37: Fracture density, aftershock density and strain intensity decay with fault-perpendicular distance. a, The decay of aftershocks (depth <5 km)(Hauksson, 2020) is shown in green, and the remaining curves represent our lidar-derived fracture map, the field- and geodesy-based fracture map of Ponti et al. (2020), the fractures mapped from imagery in Rodriguez Padilla et al. (2022) and our fault-perpendicular strain profiles (Milliner et al., 2021). The green and grey rectangles represent prior constraints of the average zone of inelasticity (Qiu et al., 2020; Milliner et al., 2021; Antoine et al., 2021), where the solid line represents the average and the shaded box represents the reported range (foreshock and mainshock, respectively, from Antoine et al., 2021). b,c, Box plots showing the maximum likelihood fit (solid line) and fit range (histograms) for parameters γ (b) and d (c) in equation 8 for each distribution in a.

We compare our distributions to constraints on the extent of inelastic deformation obtained from previous

studies of the Ridgecrest earthquakes (Milliner et al., 2021; Antoine et al., 2021; Qiu et al., 2021) shown by the grey and green bars in Figure 37a. The corners (d) captured by the datasets analysed in our study do not overlap with the edges or extent of the zones of inelasticity estimated in previous work. For the high-resolution lidar, field and imagery datasets, d is on the order of the spatial error of the main rupture trace location, and the fits allow for the absence of a corner (d=0). For the aftershock data, d is comparable to the ∼100 m horizontal location uncertainty of events used to define subsurface fault geometry (Plesch et al., 2020). Binned by depth (Extended Data Figure 41), we find that d migrates outwards, consistent with increasing location error with distance from instrumentation at the surface. We interpret that corner location is an artefact of data resolution and fault location uncertainty and does not define the width of an inner damage zone (Powers and Jordan, 2010; Perrin et al., 2021). Instead, the damage zone surrounding faults is defined by the power-law decay of fracture density that lacks a clearly defined edge. The variability of damage-zone width imaged with different techniques may reflect, at least in part, different levels of sensitivity to damage intensity. For example, the width of the zone of relative surface displacement captured from optical image correlation (Antoine et al., 2018) greatly exceeds the zone where this strain exceeds the elastic limit (Milliner et al., 2021).

To investigate the sensitivity of the damage zone to lithology, we filter fractures cutting sediment or bedrock. We find that fracture density in sediment is ∼1.5–4 times higher than that of bedrock at a given distance from the fault; however, the decay of fracture density with distance is indistinguishable (Figure 38b and Extended Data Figure 42). The reduced fracture density in bedrock may reflect greater cohesion, whereas the similar decay exponents support that the mechanism responsible for the nucleation of fractures operates under the same stress conditions irrespective of the material.

To evaluate along-strike variability and assess the sensitivity of the damage zone to on-fault slip, we compute the decrease in fracture density with fault-perpendicular distance and the average and variance of slip for the sections mapped from high-resolution imagery (Figure 38c,d) (Milliner et al., 2021; Rodriguez Padilla et al., 2022). Despite variability in fracture density, we find no correlation with the corner, slope and overall fracture density with slip magnitude. Instead, the decay of fracture density with distance is remarkably consistent throughout the rupture (Extended Data Figure 42).

We compare our fracture maps with the strain maps derived from optical image correlation, where the strain magnitude is estimated using the second invariant of the finite strain tensor (Milliner et al., 2021). Fracture orientations exhibit variability but are most frequent at small angles from the main faults (Extended Data Figured 43 and 44), suggesting a large portion of the cracks formed in shear. This is consistent with image correlation maps (Milliner et al., 2021; Antoine et al., 2021), which show shear dominates deformation <100 m from the fault. To first order, areas of high fracture density and high strain overlap (Extended

Data Figure 45). Our fracture maps also show areas of high fracture density disconnected from the main rupture that are not resolved with the optical matching technique because cumulative displacements are too small (<20 cm). This illustrates that there are contributions to inelastic deformation below the resolution of current geodetic techniques, highlighting the value of post-earthquake high-resolution orthophotography.

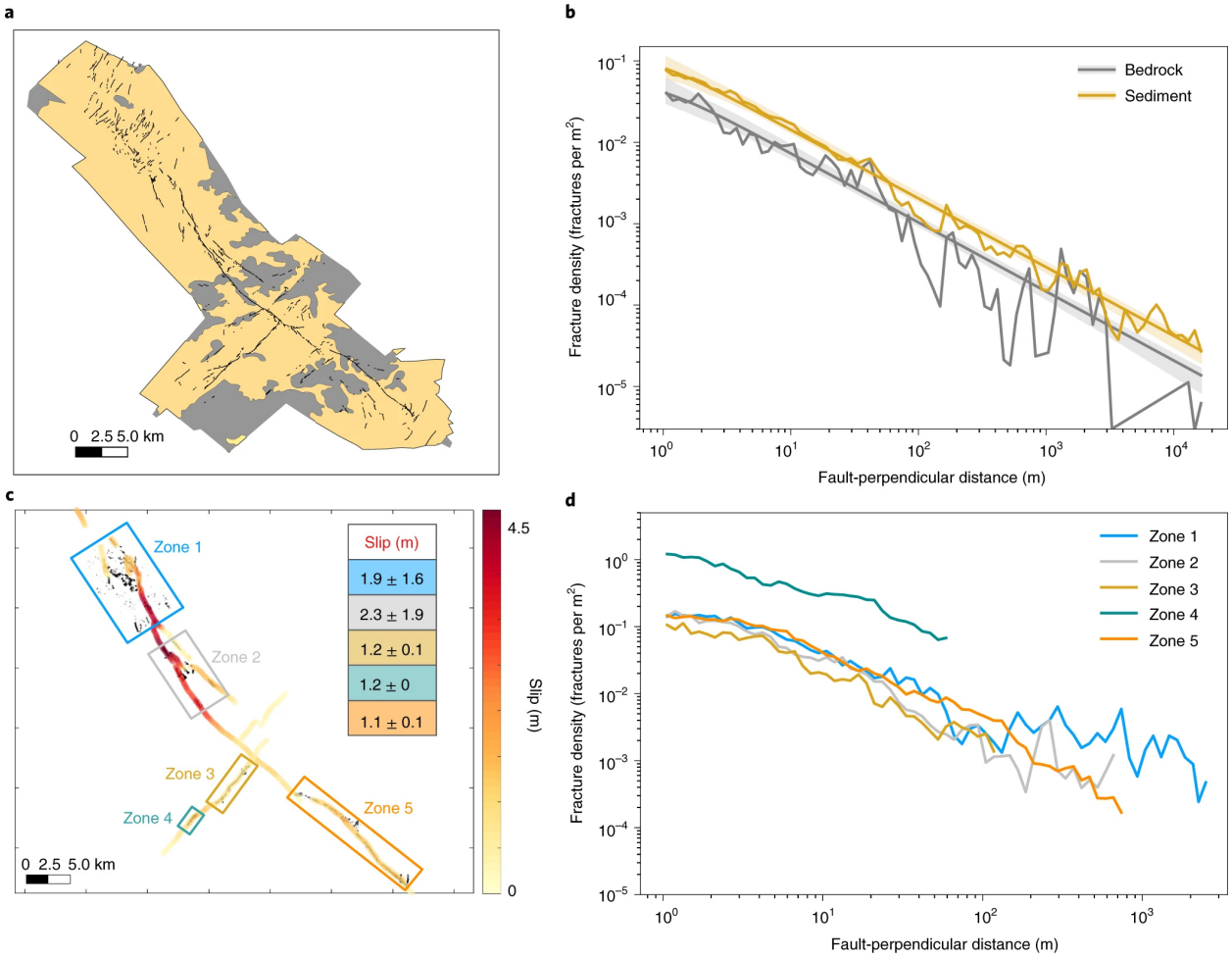

Figure 38: Decay of fracture density with fault slip and lithology. a, Simplified geologic map of the Ridgecrest area with the fractures mapped from lidar shown in black. b, Decay in fracture density in bedrock and sediment. c, Map view of the zones with high-resolution imagery where fractures are shown in black and the boxes represent the extent of the imagery for each section. The faults are colour-coded by slip magnitude measured with image cross-correlation techniques (Milliner et al., 2021). The table represents the average slip and its variance for each box. d, Fracture density with distance from the fault. Each line is colour-coded according to the boxes in c.

Implications for damage zone evolution

The coverage of the deformation field of the Ridgecrest earthquakes was unprecedented in terms of data diversity, resolution and surficial extent. The wide footprint of inelastic deformation observed may be a representative feature of earthquakes on faults in their early stages of evolution (Perrin et al., 2021) that has

remained relatively undocumented due to limited data extent. Whether widespread inelastic deformation also occurs with earthquakes on mature faults awaits future events with comparable data coverage to Ridgecrest.

Comparison of the damage distribution generated from different datasets of varying resolution suggests that the break in scaling frequently reported in damage-zone studies (Powers and Jordan, 2010; Perrin et al., 2021) is probably an artefact of data resolution and not a physically meaningful parameter. Our data suggest that, in aggregate, damage zones manifest as a continuum of decaying deformation intensity. This warrants caution in the use of a single dataset for determining the effective edge of damage zones in numerical models and probabilistic displacement hazard analysis. Whether the mechanism responsible for triggering fractures and aftershocks is static or dynamic stress cannot be resolved from the damage decay exponent alone (Felzer and Brodsky, 2006; Richards-Dinger et al., 2010), but the consistent decay exponents exhibited by all datasets suggests a single mechanism dominates yielding within 20 km of the fault.

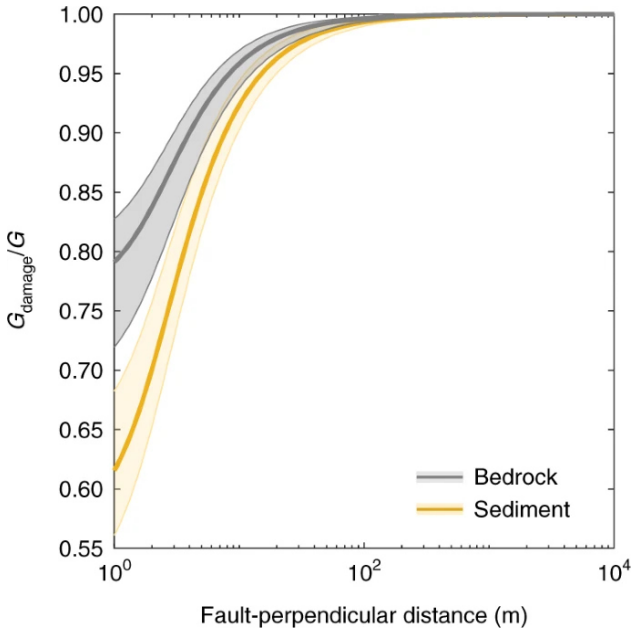

Figure 39: Decrease in shear rigidity as a result of coseismic fracturing. $\frac{G_{damage}}{G}$ represents the ratio of the shear modulus of the damaged material to the shear modulus of the intact material. We estimate the average decrease for bedrock (grey) and sediment (yellow). The shaded regions denote the shear modulus decrease within a standard deviation of the posterior spread of the damage decay fit derived from the high-resolution imagery, shown by the solid lines.

On the basis of the relationship between fracture density and shear rigidity (Budiansky and O'Connell, 1976), we estimate how much fracturing contributed to rigidity decrease in the volume of rock surrounding the Ridgecrest faults. This requires integrating both the density and length distribution of mapped fractures (see Methods). From this analysis, we predict a decrease in shear modulus by ∼40% immediately adjacent to the fault in sediment, and a decrease by ∼20% in bedrock, declining to <1% at 100 m (Figure 39). These

estimates are within the rigidity decrease range geodetically estimated in Xu et al. (2020) and seismologically in Qiu et al. (2021) and Zhou et al. (2022). Although our estimates are based on the fracture density mapped at the surface, we note that the width of reduced rigidity we predict compares favourably to the width and velocity structure of trapped-wave zones observed post-seismically at Ridgecrest that extend 3–5 km downdip and remain constant in width (Qiu et al., 2021; Zhou et al., 2022).

Our analysis also shows that low levels of rigidity reduction may be expected far from the principal rupture trace. This finding is supported by regional reductions in shear-wave velocity after the Ridgecrest earthquakes (Lu and Ben-Zion, 2021). These measurements from the far field, averaging through a large crustal volume surrounding the faults, show a ubiquitous, small- ($\sim$2%) velocity reduction, which may be akin to the widespread damage we map at the surface. Damage zones are geodetically and seismologically detected along faults in the late stages of their interseismic period (Cochran et al., 2009), suggesting that a portion of the coseismic damage we map is irrecoverable. Over time, the upper crust transected by zones of closely spaced faulting, such as the eastern California shear zone, receives inelastic contributions from earthquakes on multiple sources, becoming weakened compared with regions outside of the zone of faulting.

Fault and fracture mapping, aftershocks and strain maps from the Ridgecrest earthquakes show widespread damage with a power-law decay with distance from the principal faults. These observations simultaneously reveal the role of macroscopic fracturing in generating intense near-fault damage and how widespread damage may accumulate regionally over long timescales. We conclude that the upper crust (at least to 3 km depth) of an active plate boundary zone evolves into a widely damaged volume that is permanently deformed by contributions from each earthquake. This cumulative damage reduces shear rigidity, which focuses elastic deformation into fault zones, elevates fracture permeability, absorbs shear strain throughout the lifetime of faulting and may facilitate the stability of distributed, intersecting fault networks, such as evident in the eastern California shear zone. Distributed deformation of weakened plate boundary zones is thus a consequence of, and enabled by, seismogenic deformation on localized faults.

References

1. Antoine, S. L. et al. Diffuse deformation and surface faulting distribution from submetric image correlation along the 2019 Ridgecrest, California, ruptures. Bull. Seismol. Soc. Am. 111, 2275–2302 (2021).

2. Barnhart, W. D., Gold, R. D. & Hollingsworth, J. Localized fault-zone dilatancy and surface inelasticity of the 2019 Ridgecrest earthquakes. Nat. Geosci. 13, 699–704 (2020).

3. Brock, W. G. & Engelder, T. Deformation associated with the movement of the Muddy Mountain

overthrust in the Buffington window, southeastern Nevada. Geol. Soc. Am. Bull. 88, 1667–1677 (1977).

4. Budiansky, B. & O'connell, R. J. Elastic moduli of a cracked solid. Int. J. Solids Struct. 12, 81–97 (1976).

5. Chester, J. S., Chester, F. M. & Kronenberg, A. K. Fracture surface energy of the Punchbowl fault, San Andreas system. Nature 437, 133–136 (2005).

6. Cochran, E. S. et al. Seismic and geodetic evidence for extensive, long-lived fault damage zones. Geology 37, 315–318 (2009).

7. Dolan, J. F. & Haravitch, B. D. How well do surface slip measurements track slip at depth in large strike-slip earthquakes? The importance of fault structural maturity in controlling on-fault slip versus off-fault surface deformation. Earth Planet. Sci. Lett. 388, 38–47 (2014).

8. Evans, E. L., Thatcher, W. R., Pollitz, F. F. & Murray, J. R. Persistent slip rate discrepancies in the eastern California (USA) shear zone. Geology 44, 691–694 (2016).

9. Felzer, K. R. & Brodsky, E. E. Decay of aftershock density with distance indicates triggering by dynamic stress. Nature 441, 735–738 (2006).

10. Fialko, Y. Probing the mechanical properties of seismically active crust with space geodesy: study of the coseismic deformation due to the 1992 M 7.3 w Landers (Southern California) earthquake. J. Geophys. Res. Solid Earth 109, B03307 (2004).

11. Fialko, Y. & Jin, Z. Simple shear origin of the cross-faults ruptured in the 2019 Ridgecrest earthquake sequence. Nat. Geosci. 14, 513–518 (2021).

12. Hauksson, E. et al. Caltech/USGS Southern California Seismic Network (SCSN) and Southern California Earthquake Data Center (SCEDC): data availability for the 2019 Ridgecrest sequence. Seismol. Res. Lett. 91, 1961–1970 (2020).

13. Hudnut, K. W. et al. Airborne lidar and electro-optical imagery along surface ruptures of the 2019 Ridgecrest earthquake sequence, Southern California. Seismol. Res. Lett. 91, 2096–2107 (2020).

14. Li, Y.-G., Chen, P., Cochran, E. S., Vidale, J. E. & Burdette, T. Seismic evidence for rock damage and healing on the San Andreas fault associated with the 2004 M 6.0 Parkfield earthquake. Bull. Seismol. Soc. Am. 96, S349–S363 (2006).

15. Liu, C., Lay, T., Brodsky, E. E., Dascher-Cousineau, K. & Xiong, X. Coseismic rupture process of the large 2019 Ridgecrest earthquakes from joint inversion of geodetic and seismological observations. Geophys. Res. Lett. 46, 11820–11829 (2019).

16. Loveless, J. P. & Meade, B. J. Geodetic imaging of plate motions, slip rates, and partitioning of deformation in Japan. J. Geophys. Res. Solid Earth 115, B02410 (2010).

17. Lu, Y. & Ben-Zion, Y. Regional seismic velocity changes following the 2019 Mw 7.1 Ridgecrest, California earthquake from autocorrelations and P/S converted waves. Geophys. J. Int. 228, 620–630 (2021).

18. Milliner, C. W. D., Dolan, J. F., Hollingsworth, J., Leprince, S. & Ayoub, F. Comparison of coseismic near-field and off-fault surface deformation patterns of the 1992 Mw 7.3 Landers and 1999 Mw 7.1 Hector Mine earthquakes: implications for controls on the distribution of surface strain. Geophys. Res. Lett. 43, 10115–10124 (2016).

19. Milliner, C. et al. Bookshelf kinematics and the effect of dilatation on fault zone inelastic deformation: examples from optical image correlation measurements of the 2019 Ridgecrest earthquake sequence. J. Geophys. Res. Solid Earth 126, e2020JB020551 (2021).

20. Mitchell, T. M. & Faulkner, D. R. The nature and origin of off-fault damage surrounding strike-slip fault zones with a wide range of displacements: a field study from the Atacama fault system, northern Chile. J. Struct. Geol. 31, 802–816 (2009).

21. Perrin, C., Waldhauser, F. & Scholz, C. H. The shear deformation zone and the smoothing of faults with displacement. J. Geophys. Res. Solid Earth 126, e2020JB020447 (2021).

22. Pierce, I., Williams, A., Koehler, R. D. & Chupik, C. High-resolution structure-from-motion models and orthophotos of the southern sections of the 2019 Mw 7.1 and 6.4 Ridgecrest earthquakes surface ruptures. Seismol. Res. Lett. 91, 2124–2126 (2020).

23. Plesch, A., Shaw, J. H., Ross, Z. E. & Hauksson, E. Detailed 3D fault representations for the 2019 Ridgecrest, California, earthquake sequence. Bull. Seismol. Soc. Am. 110, 1818–1831 (2020).

24. Ponti, D. J. et al. Documentation of surface fault rupture and ground- deformation features produced by the 4 and 5 July 2019 Mw 6.4 and Mw 7.1 Ridgecrest earthquake sequence. Seismol. Res. Lett. 91, 2942–2959 (2020).

25. Powers, P. M. & Jordan, T. H. Distribution of seismicity across strike-slip faults in California. J. Geophys. Res. Solid Earth 115, B05305 (2010).

26. Qiu, H. et al. Seismic imaging of the Mw 7.1 Ridgecrest earthquake rupture zone from data recorded by dense linear arrays. J. Geophys. Res. Solid Earth 126, e2021JB022043 (2021).

27. Richards-Dinger, K., Stein, R. S. & Toda, S. Decay of aftershock density with distance does not indicate triggering by dynamic stress. Nature 467, 583–586 (2010).

28. Rodriguez Padilla, A. M. et al. Near-field high-resolution maps of the Ridgecrest earthquakes from aerial imagery. Seismol. Res. Lett. 93, 494–499 (2022).

29. Ross, Z. E. et al. Hierarchical interlocked orthogonal faulting in the 2019 Ridgecrest earthquake sequence. Science 366, 346–351 (2019).

30. Savage, H. M. & Brodsky, E. E. Collateral damage: evolution with displacement of fracture distribution and secondary fault strands in fault damage zones. J. Geophys. Res. Solid Earth 116, B03405 (2011).

31. Scott, C. P. et al. The M 7 2016 Kumamoto, Japan, earthquake: 3D deformation along the fault and within the damage zone constrained from differential lidar topography. J. Geophys. Res. Solid Earth 123, 6138–6155 (2018).

32. Shelef, E. & Oskin, M. Deformation processes adjacent to active faults: examples from eastern California. J. Geophys. Res. Solid Earth 115, B05308 (2010).

33. Shipton, Z. K., Evans, J. P., Abercrombie, R. E. & Brodsky, E. E. in Earthquakes: Radiated Energy and the Physics of Faulting (eds Abercrombie, R. et al.) 217–222 (American Geophysical Union, 2006).

34. Xu, X. et al. Surface deformation associated with fractures near the 2019 Ridgecrest earthquake sequence. Science 370, 605–608 (2020).

35. Zhou, Z., Bianco, M., Gerstoft, P. & Olsen, K. High-resolution imaging of complex shallow fault zones along the July 2019 Ridgecrest ruptures. Geophys. Res. Lett. 49, e2021GL095024 (2022).

Appendix: Methods

Rupture mapping

To map fractures from the lidar data, we rely on lidar hillshade maps generated at different sun angles, a slope map and an aspect map. Through the combination of these datasets, we ensure that fractures of all orientations are included in the map.

Strain calculations

To measure the two-dimensional (2D) inelastic strains associated with the 2019 Ridgecrest earthquake sequence, we used sub-pixel image correlation of optical satellite imagery to retrieve horizontal displacement maps of the coseismic rupture, which are presented in Milliner et al. (2021). The horizontal displacement field is estimated by correlating one pair of SPOT-6 satellite imagery (pixel resolution of 1.5 m) using the sub-pixel image correlation software COSI-Corr (Leprince et al., 2007). Here the pre-event image was acquired before the foreshock and the post-event image after the mainshock; therefore, the displacement maps contain surface motion associated with both events. Using the phase correlation method in COSI-Corr with a correlation window size of 32 $\times$ 32 pixels that samples the images every 4 pixels, produces a horizontal displacement map at 6 m resolution. From these displacement maps, we derive two types of strain measurements.

The first type is 1D fault-parallel strain profiles (shown in Extended Data Figure 40), and the second is 2D strain maps showing the overall strain magnitude (Extended Data Figure 45). To measure fault-parallel shear strain, we first measure fault-parallel displacement using profiles orientated perpendicular to the rupture trace that stacks motion in the along-strike direction over a 138 m distance. The fault-parallel shear strain is then estimated from the gradient of the fault-parallel displacement using a finite-difference approximation method with a kernel of 12 m. As the gradient is sensitive to noise in the displacement maps, we apply a non-local means filter that helps suppress noise but preserve non-local changes, or edges, associated with differential surface motion caused by the surface rupture. The compiled strain profiles are shown in profile coordinates in Extended Data Figure 40.

The strain maps are calculated by estimating the 2D finite strain tensor that is outlined in Milliner et al. (2021). The strain magnitude is then estimated from the finite strain tensor by calculating the second strain invariant, which characterizes the magnitude of the deviatoric component of the finite strain tensor.

Damage decay plots and fitting

Plesch et al. (2020) used the earthquake catalogues and image data to generate a detailed 3D map of the subsurface geometry of the faults involved in the Ridgecrest sequence. To quantify the decay in aftershock density, we measure the shortest distance between every aftershock and the nearest location on a fault plane in the Plesch model. We use the SCSN catalogue to estimate the decay in fault-perpendicular seismicity in Figure 37 because this catalogue was used by Plesch et al. (2020) to determine the location of the fault planes at depth. We consider events starting on 1 July 2019 to the end of the year. We also find a similar distribution of fault-perpendicular seismicity using events in the QTM catalogue (Ross et al., 2019) but with

a larger d value that results from location shifts relative to the SCSN catalogue and fault model. This is shown in the Supplementary Information.

To quantify the decay in fracture density, we measure the nearest distance between each fracture in the fracture maps (imagery, lidar based, and field and geodesy based) and the surface expression of the faults in Plesch et al. (2021) mapped in the field. We omit the faults in the north tip and cross-fault at the south tip in Plesch et al. (2021) from our fracture decay analysis because they do not match the strike of the main surface rupture and they lack a clear field expression and, thus, are likely not responsible for that distributed fracturing.

In this analysis, fractures are discretized into evenly spaced points at 1 m increments so that fracture length does not bias the fracture counts. Fractures shorter than 1 m are represented by a single point. Because fault dips are close to vertical, the surface distances between the fractures and the closest point along the surface rupture are a good estimate. Because the spatial errors in aftershocks are substantially larger than the uncertainty in fracture location and the error in strain, we consider only aftershocks where the hypocentral location is resolved with an uncertainty lower than 100 m.

Once the minimum distance for each fracture or aftershock is computed, we bin them into 100 bins that are log spaced from the origin to the farthest point in the dataset spanning the most distance. We first normalize each of the bins by bin size and then by rupture length of the dataset. The plots in Figures 37 and 38 and Extended Data Figure 41 show the normalized damage decay for each dataset.

We then apply the functional fit of Powers and Jordan (2010) (equation 8) to each damage decay curve. To fit our data with the model of Powers and Jordan (2010), we use an implementation of the affine-invariant ensemble sampler for Markov-chain Monte Carlo (Goodman and Weare, 2010; Foreman-Mackey et al., 2013), assuming that $\nu(x)$ within each bin samples a Poisson distribution (Powers and Jordan, 2010). We apply a uniform distribution to ν_o (10^{-5}-10 fractures per square metre), d (0–3,000 m), and γ (0.5–2.0) as our priors. We run the fits for 20,000 iterations, preceded by a burn-in phase of 10,000 iterations. We use an ensemble of 200 walkers (Foreman-Mackey et al., 2013).

We estimate the uncertainty in the location of the fault plane by measuring the distance between the location of the mapped main fault trace and the main fault trace in the high-resolution imagery. The average difference is reported as the spatial uncertainty in the location of the fault trace at the surface in Figure 37. Plesch et al. (2020) determined the location of the fault planes at depth on the basis of the SCSN catalogue (Hauksson, 2020). The average horizontal spatial uncertainty for the earthquakes in the catalogue ($\sim$100 m) serves as a minimum constraint on the fault location uncertainty at depth, as reported in Figure 37.

To ensure that minor cracks (centimetre scale) that are probably shallow and detected only from the high-resolution imagery data do not bias the scaling, we fit equation 8 on groups of downsampled fracture

populations, where fractures of lengths shorter than 1 m were removed. The maximum likelihood fit parameters for datasets incorporating <1 m fractures are essentially indistinguishable. The resulting plots are provided in the Supplementary Information.

Strain maps and fracture density comparisons

We compare fracture density and strain intensity, expressed as a scalar quantity by the second invariant of the strain tensor, to analyse similarities and differences in the spatial distribution of both quantities. To approximate the kernel size of the strain maps (12 m), we calculate fracture density over 10 m kernels. We compare strain maps and fracture density for two of the sectors where high-resolution maps based on UAV imagery are available (Extended Data Figure 45).

Decrease in shear modulus associated with damage in bedrock and sediment

We use our fits to the decay of fracture density with distance from the fault for the cracks mapped from high-resolution imagery (Figure 37) to estimate the decrease in shear rigidity associated with fracturing during the Ridgecrest earthquakes. For this dataset, the maximum likelihood fit for $\nu_o = 0.15$, $d = 1.99$ and $\gamma = 1.06$.

Following the approach of Powers and Jordan (2010), we keep m constant at 2. From our fit to distributions of sediment and bedrock fractures (Figure 38), we find that the fracture density at a given location is larger in sediment than in bedrock by a factor of ∼1.5–4. Thus, we can estimate an intercept ν_o= 0.06 and assess the decrease in shear rigidity for bedrock and sediment separately. The fractures we map are a subset of a population encompassing fractures much smaller than those we measure. We derive a weighted fracture distribution ML^2 on the basis of extrapolation of our mapped fracture lengths to account for the entire population below a maximum length, L_{max} = 10 m (note that mapped fractures rarely exceed this length)(Budiansky and O'Connell, 1976). We assume that cracks have a constant aspect ratio. The full derivation is provided in the Supplementary Information. We combine our weighted fracture length population with the spatial distribution of total fracture length to estimate the decrease in shear rigidity associated with fracturing, expressed as the ratio of the shear modulus of the damaged material (G') to the shear modulus of the intact material (G):

$$\frac{G'}{G} = 1 - \frac{32}{45}\frac{(1-\zeta)(5-\zeta)}{(2-\zeta)}\epsilon \tag{9}$$

where ζ is the Poisson's ratio of the solid and ϵ is a crack density parameter given by:

$$\epsilon = \frac{3\pi}{16GE(k)K(k)} ML^2 \tag{10}$$

where $E(k)$ and $K(k)$ are complete elliptical integrals of the first and second kind (Budiansky and O'Connell, 1976). For circular cracks, as we assume for our analysis, $E(k) = 1.5708$ and $K(k) = 1.5708$. ML^2 is a moment distribution of fracture lengths given by:

$$ML^2 = \nu \frac{\beta - 1}{2 - \beta} L_* I \tag{11}$$

where ν is the fracture density at a given distance from the fault, β is the exponent of the power law that describes the distribution of fracture lengths (1.9), L_* is a normalizing characteristic length = 1 m and I is an integral that accounts for the effect of fractures ranging in length from $L_{min} = 0$ m to $L_{max} = 10$ m:

$$I = \left(\frac{L_{max}}{L_*} \right)^{2-\beta} - \left(\frac{L_{min}}{L_*} \right)^{2-\beta} \tag{12}$$

Note that this approach is insensitive to whether the fractures are newly nucleated coseismically or are pre-existing cracks that were reactivated.

Appendix references

1. Foreman-Mackey, D., Hogg, D. W., Lang, D. & Goodman, J. emcee: the MCMC hammer. Publ. Astron. Soc. Pac. 125, 306–312 (2013).

2. Goodman, J. & Weare, J. Ensemble samplers with affine invariance. Comm. App. Math. Comp. Sci. 5, 65–80 (2010).

3. Leprince, S., Barbot, S., Ayoub, F. & Avouac, J.-P. Automatic and precise orthorectification, coregistration, and subpixel correlation of satellite images, application to ground deformation measurements. IEEE Trans. Geosci. Remote Sens. 45, 1529–1558 (2007).

Extended Data Figures

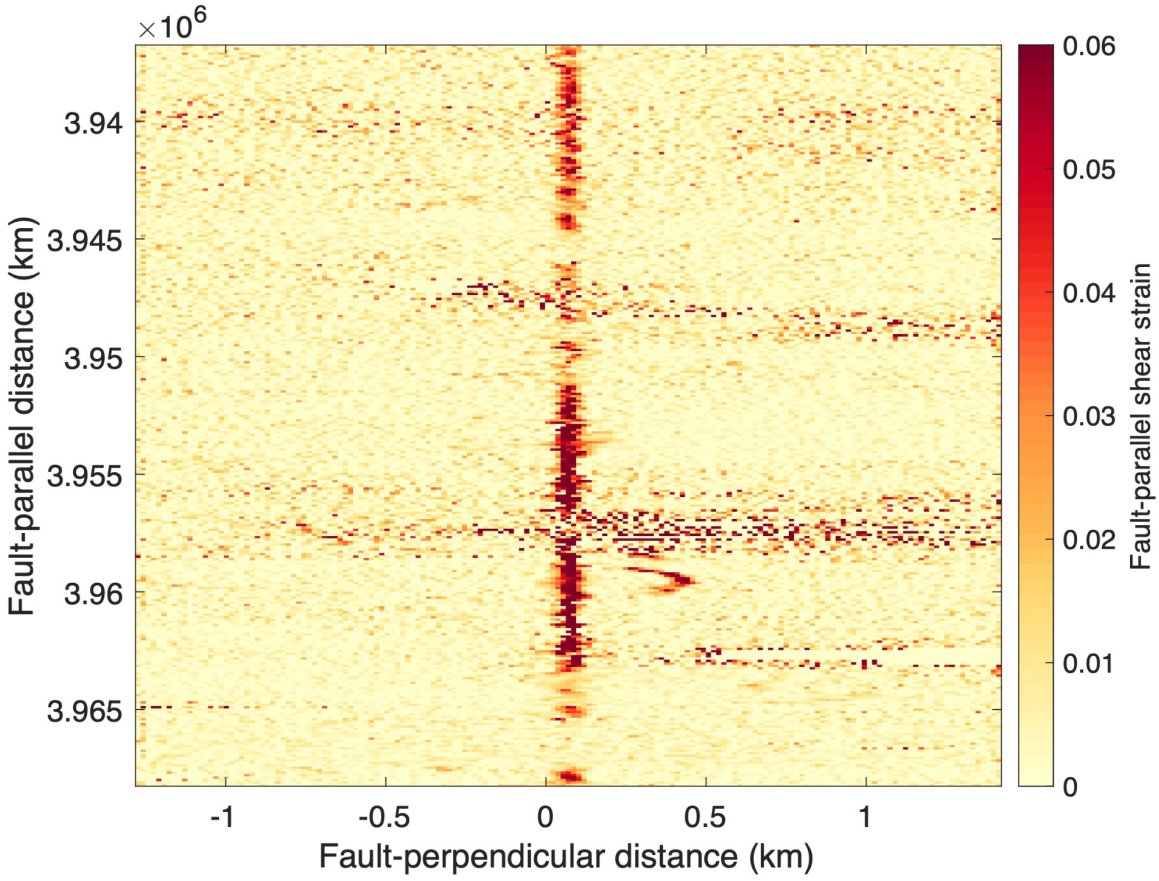

Figure 40: Stacked profiles of fault-parallel shear strain from satellite cross-correlated imagery. Stacked profiles of fault-parallel shear strain from satellite cross-correlated imagery (Milliner et al., 2021). Each profile stacks horizontal fault-parallel displacement over a 138-meter window along strike. Strain is then calculated from the fault-parallel displacement profile over a 12-meter kernel across strike by taking the first derivative using a central-difference finite approximation.

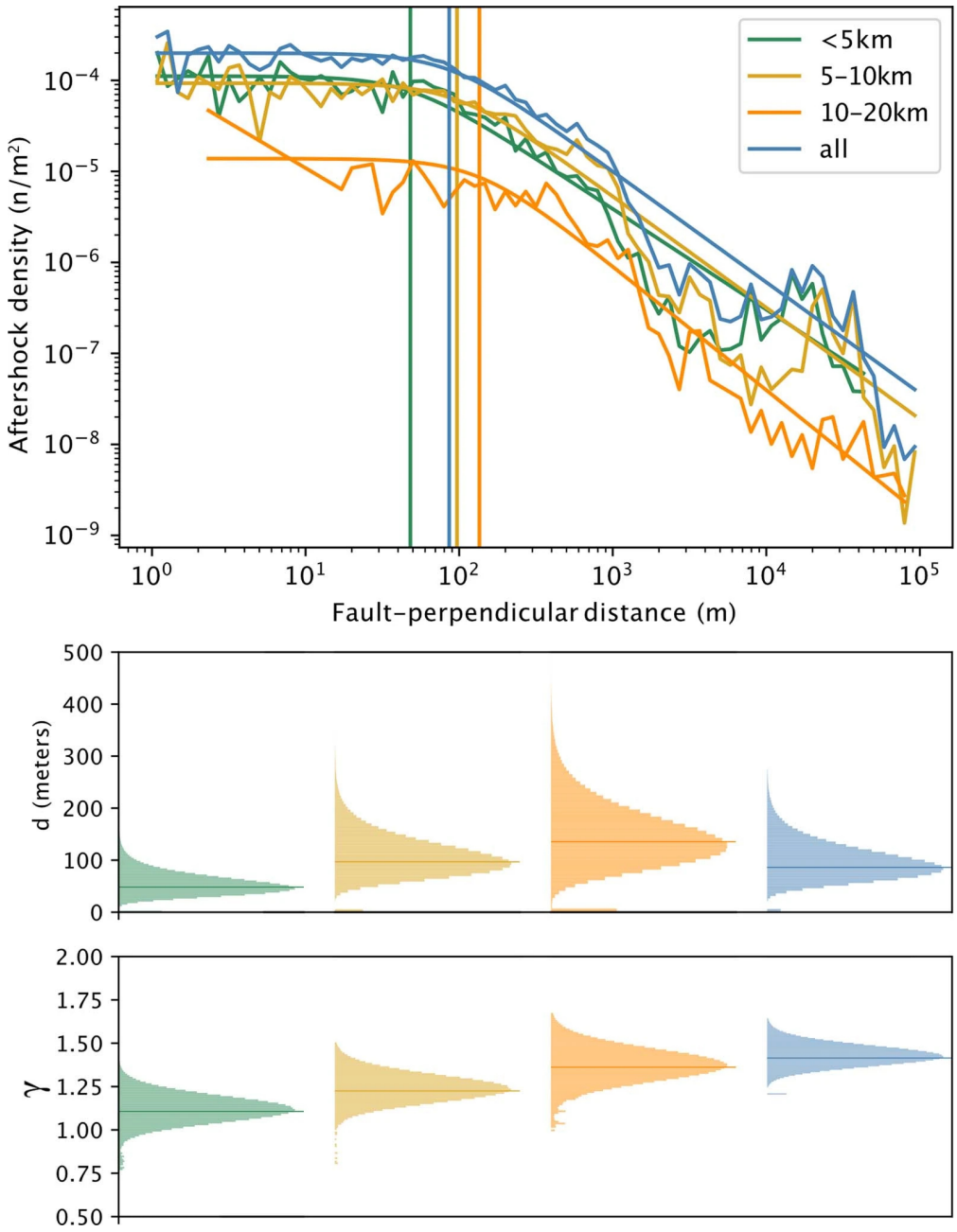

Figure 41: Decay in aftershock density with fault-perpendicular distance for different depth intervals. Top: Decay in aftershock density with fault-perpendicular distance for different depth intervals. The vertical lines represent the break in scaling d for each group of aftershocks. Bottom: Range of γ and d fits. The vertical lines represent the maximum likelihood value.

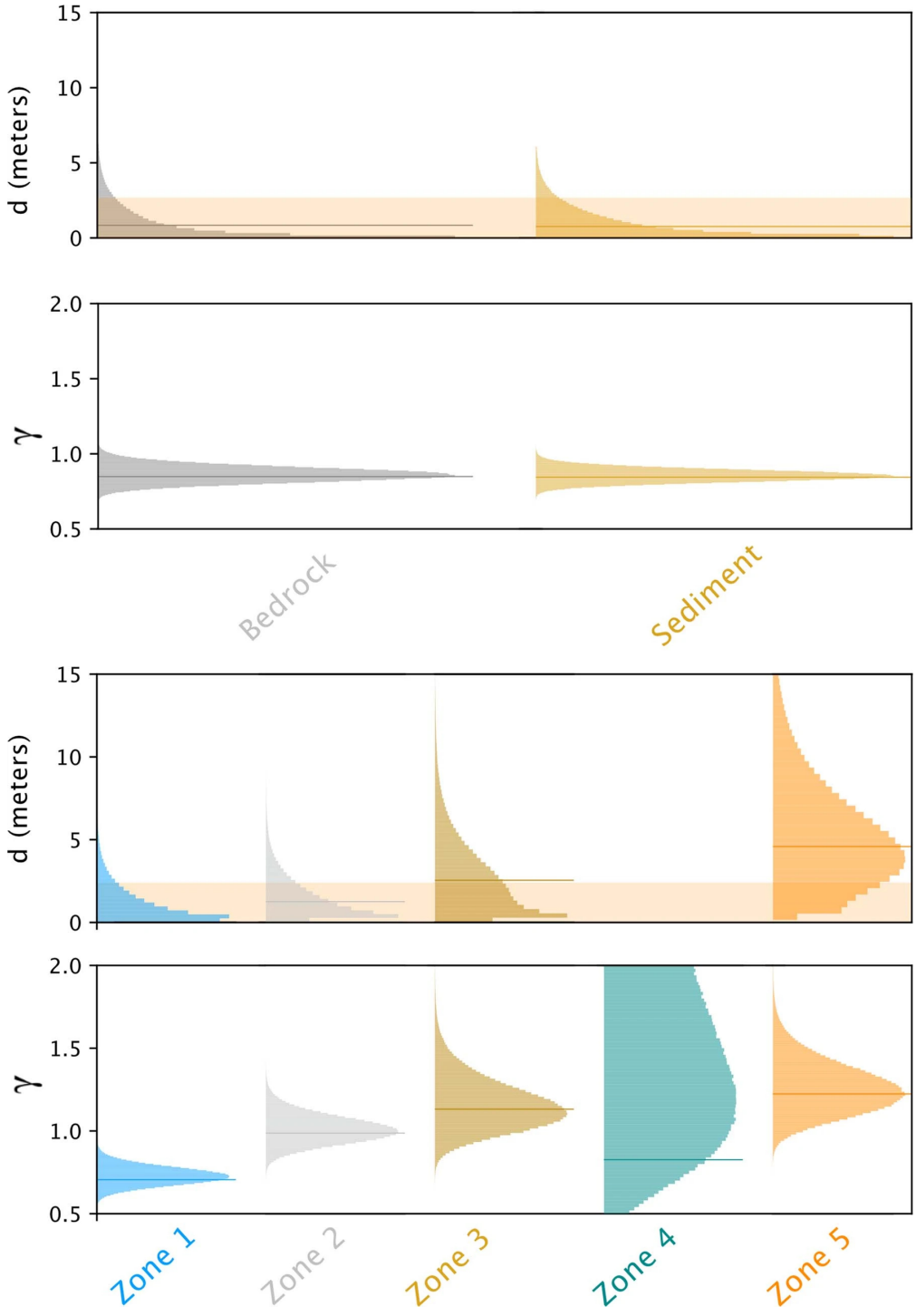

Figure 42: Maximum likelihood distribution of parameters in Equation 8 for the distributions in figure 38 (main). Top: Fit range (histograms) for parameters d and γ in equation 8 for the bedrock and sediment distributions in figure 38 of the manuscript. Bottom: fit range for parameters d and γ in equation 8 for zones 1 through 5 in figure 38 of the manuscript. The vertical lines represent the maximum likelihood value. The shaded orange section indicates the fault location uncertainty at the surface.

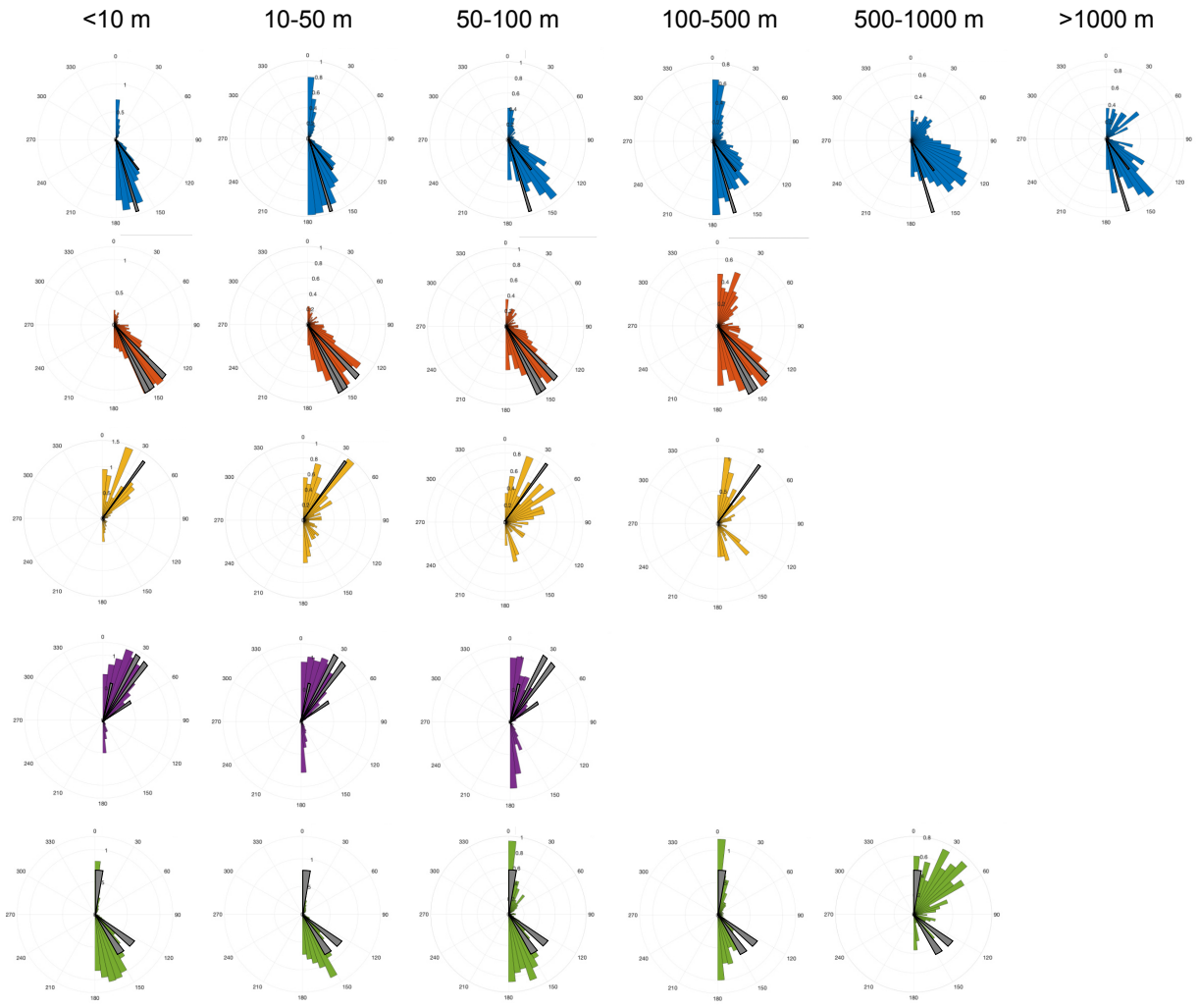

Figure 43: Distribution of fracture orientation with fault-perpendicular distance. Distribution of fracture orientation with distance away from the fault for zones 1–5 from top to bottom (Figure 38). Fractures are shown in color and faults are shown in grey. Fracture orientation abundances are normalized by the total number of fractures in the rose diagram.

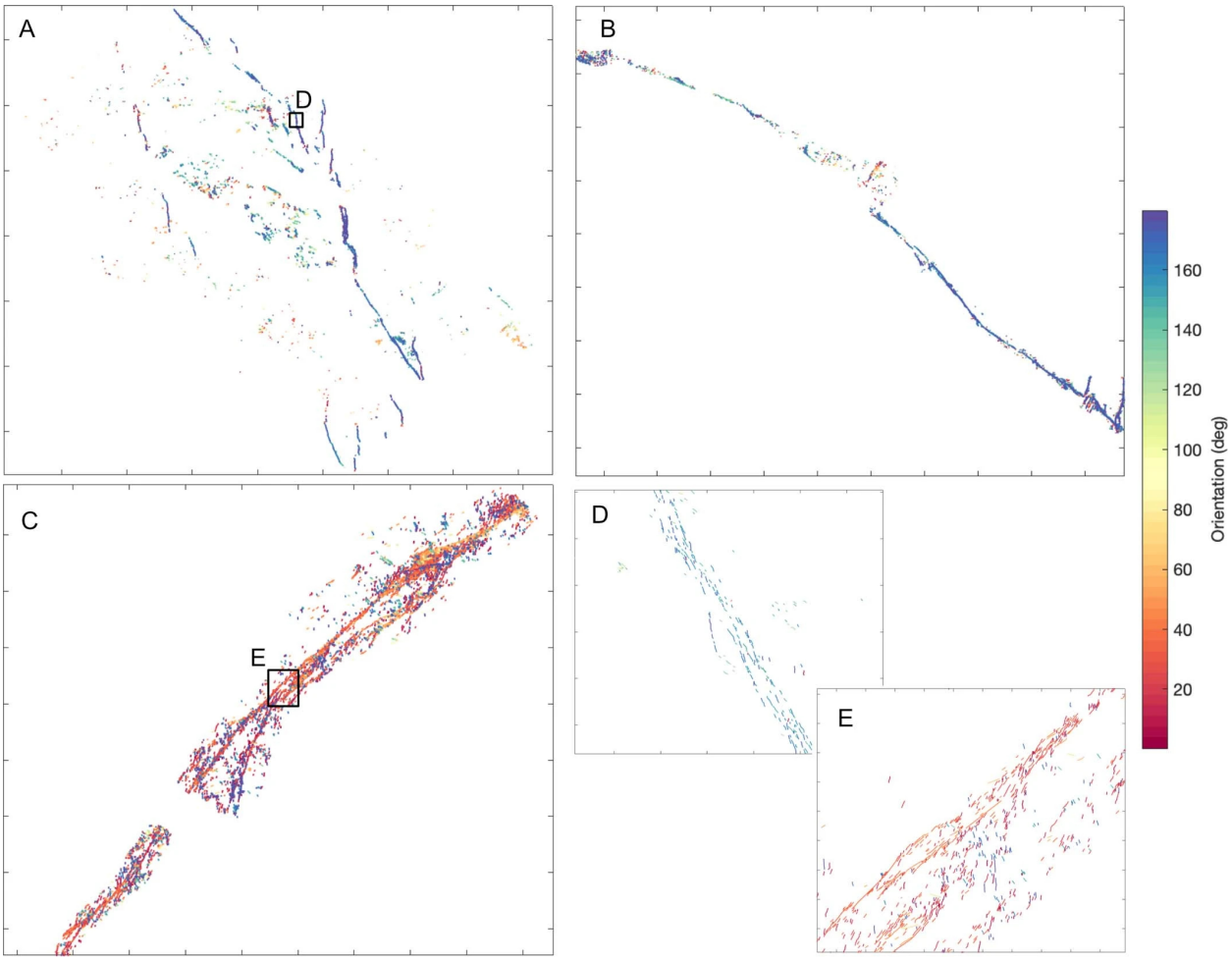

Figure 44: Map view of fracture orientations at select locations. Map view of fracture orientations. A, B, and C show the distribution of fractures through zones 1, 4, and 5 in Fig. 38 D and E show insets into regions of A and C to highlight variability along the rupture and organization of fractures at narrow angles from one another.

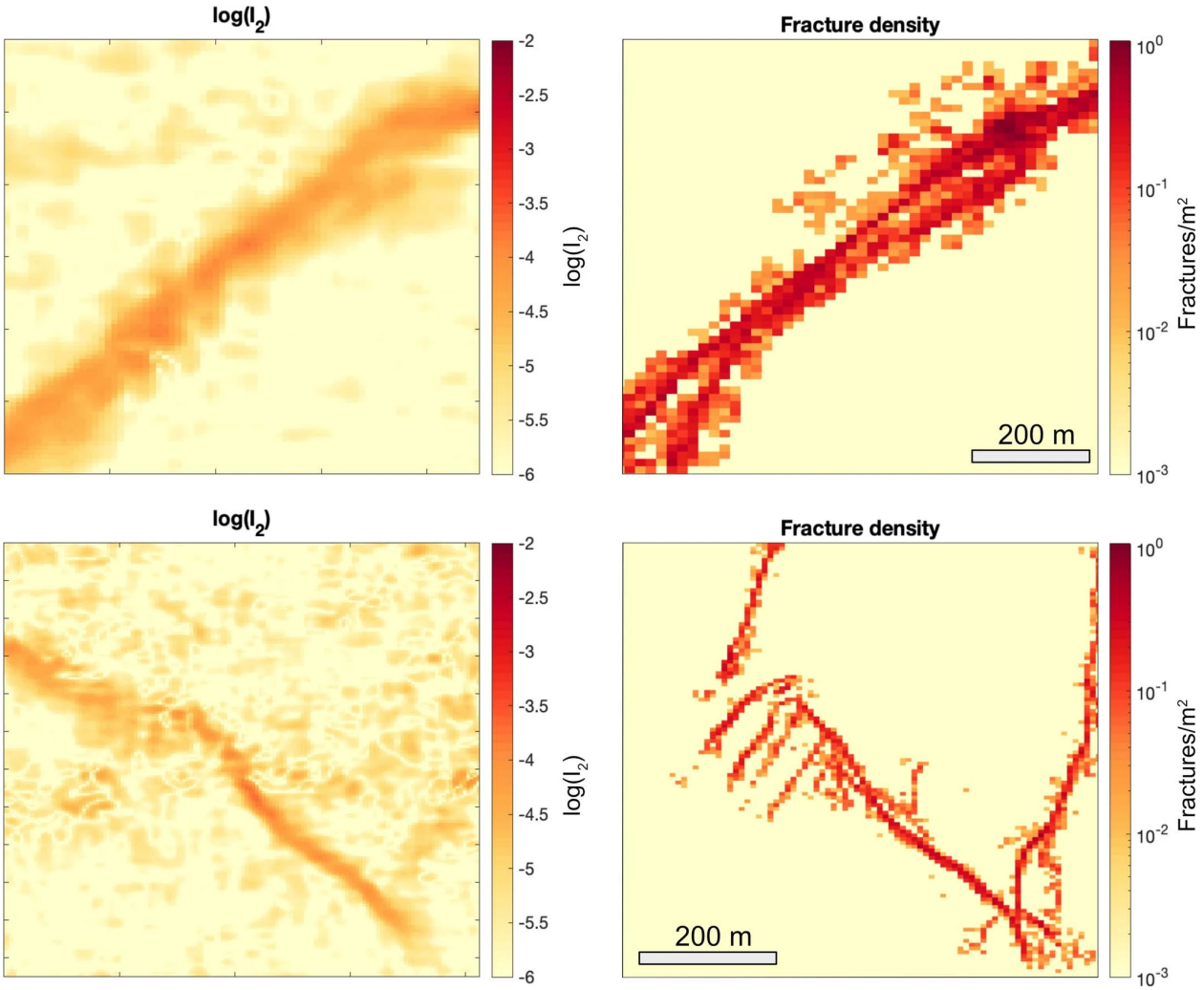

Figure 45: Strain and fracture density maps. Strain and fracture density maps from high-resolution imagery for the middle of the foreshock (a and b) and the southern tip of the mainshock (c and d). Strain is calculated over a 12-meter kernel and fracture density is calculated over a 10 meter kernel.

nature portfolio

https://doi.org/10.1038/s41561-021-00888-w

Supplementary information

Accrual of widespread rock damage from the 2019 Ridgecrest earthquakes

In the format provided by the authors and unedited

Fracture Size and Moment Distributions

We fit the cumulative distribution of individual mapped fracture lengths as a linear relationship in log-log space,

$$log[N(L > L_o)] = -\beta log\left(\frac{L_o}{L*}\right) + log[N(L > L^*)A_r] \tag{1}$$

where $N_o = N(L > L*)A_r$ is the total number of fractures of length greater than a normalizing length, L^*, measured over a contributing area, A_r. This analysis yields a power-law relationship for cumulative fractures of length greater than L_o:

$$N(L > L_o) = N_o\left(\frac{L_o}{L*}\right)^{-\beta}. \tag{2}$$

If we set L^* to a minimum observed fracture length, and normalize by N_0, this may be expressed as a cumulative distribution function (CDF),

$$CDF(L) = 1 - \left(\frac{L}{L*}\right)^{-\beta}, \tag{3}$$

which may be differentiated to derive a probability distribution function (PDF),

$$PDF(L) = \frac{d}{dL}CDF(L) = \frac{\beta}{L^*}\left(\frac{L}{L^*}\right)^{-\beta-1}. \tag{4}$$

The sum of all fracture lengths longer than L_o is given by:

$$N_o\int_{L_o}^{\infty} PDF(L)LdL. \tag{5}$$

$$N_o\frac{\beta}{\beta-1}L^*\left(\frac{L_o}{L^*}\right)^{1-\beta} \tag{6}$$

Replacing L_o with L^* yields the sum of observed fracture lengths (within the contributing area, A_r):

$$\nu = N_oL^*\frac{\beta}{\beta-1} \tag{7}$$

Budiansky and O'Connell (1976) derive a modified shear modulus due to fracturing in terms of the probability mass function of fracture lengths, which we derive by multiplying the PDF of fracture lengths by N_o:

$$PMF(L) = N_o\frac{\beta}{L*}\left(\frac{L}{L^*}\right)^{-\beta-1}. \tag{8}$$

From this they derive a moment distribution of fracture lengths, $M\langle L^2\rangle$:

$$M\langle L^2\rangle = \int_{L_{min}}^{L_{max}} L^2 PMF(L), \tag{9}$$

$$M\langle L^2\rangle = N_o \beta L^{*\beta} \int_{L_{min}}^{L_{max}} L^{1-\beta} = \frac{N_o \beta L^{*\beta}}{2-\beta} L^{2-\beta}\Big|_{L_{min}}^{L_{max}}. \tag{10}$$

In the original work of Budiansky and O'Connell (1976), the bounds of this integral range from 0 to infinity. We have to make a choice about both bounds. We can integrate from zero fracture length or the smallest fracture in our distribution, one meter. Evaluating this integral also requires choosing the largest fracture that matters. Few of the fractures we map exceed 100m length, and at this length its doubtful that the effects on shear modulus are uniform. Fortunately, the integral, I, yields very similar values for a wide range of fracture sizes.

$$M\langle L^2\rangle \approx \frac{N_o \beta L^{*2}}{2-\beta} I \tag{11}$$

$$I = \left[\left(\frac{L_{max}}{L^*} \right)^{2-\beta} - \left(\frac{L_{min}}{L^*} \right)^{2-\beta} \right] \tag{12}$$

Values of I range from 0.58 for the range from 1 meter to 100 meters, to 1.25 for the range from 0 to 10m, to 1.58 for the range from 0 to 100m.

Combining eq. 7 with eq. 11 yields an expression for $M\langle L^2\rangle$ in terms of the cumulative length of mapped fractures:

$$M\langle L^2\rangle \approx \nu \frac{\beta - 1}{2-\beta} L^* I. \tag{13}$$

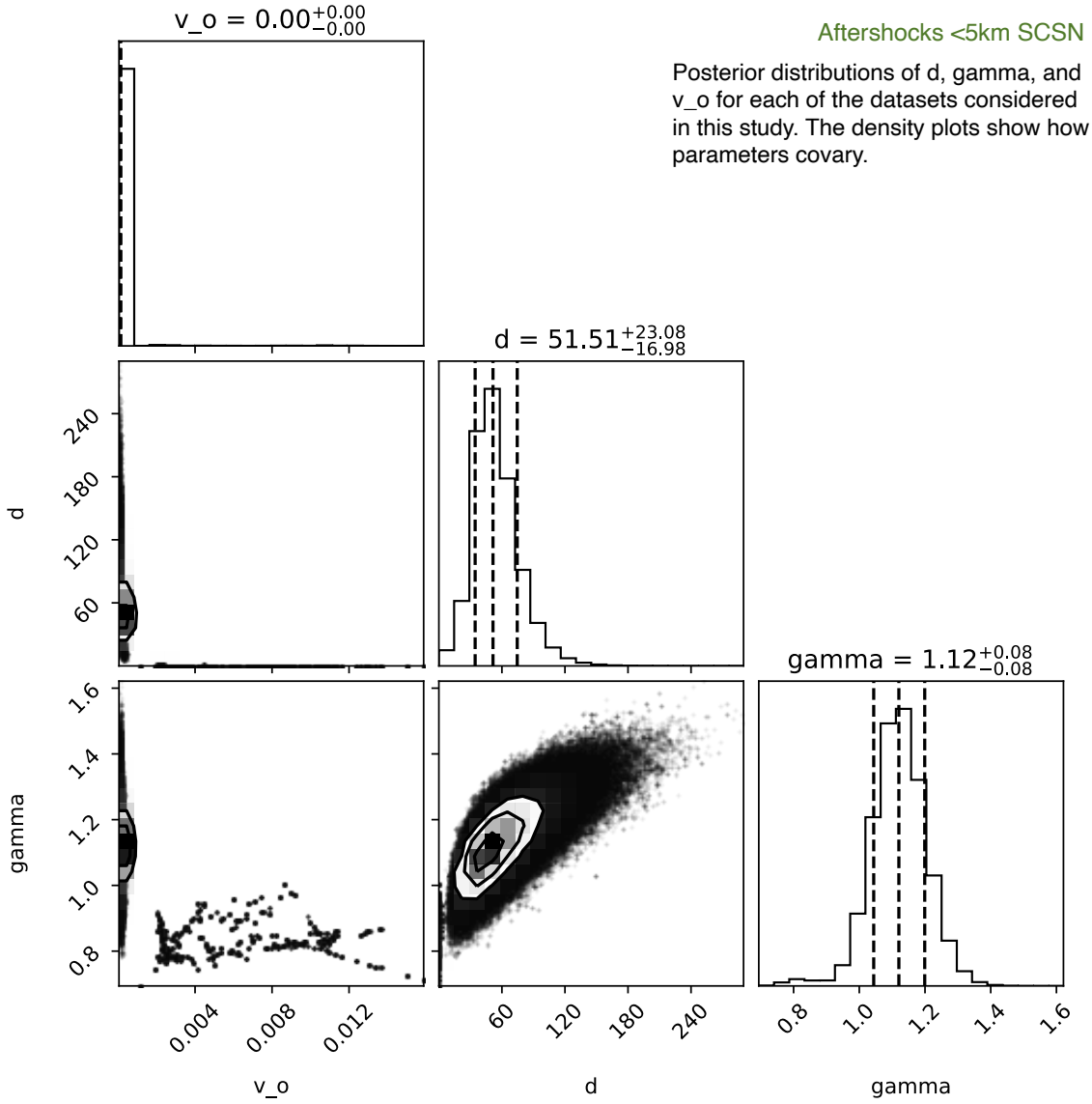

Aftershocks <5km SCSN

Posterior distributions of d, gamma, and v_o for each of the datasets considered in this study. The density plots show how parameters covary.

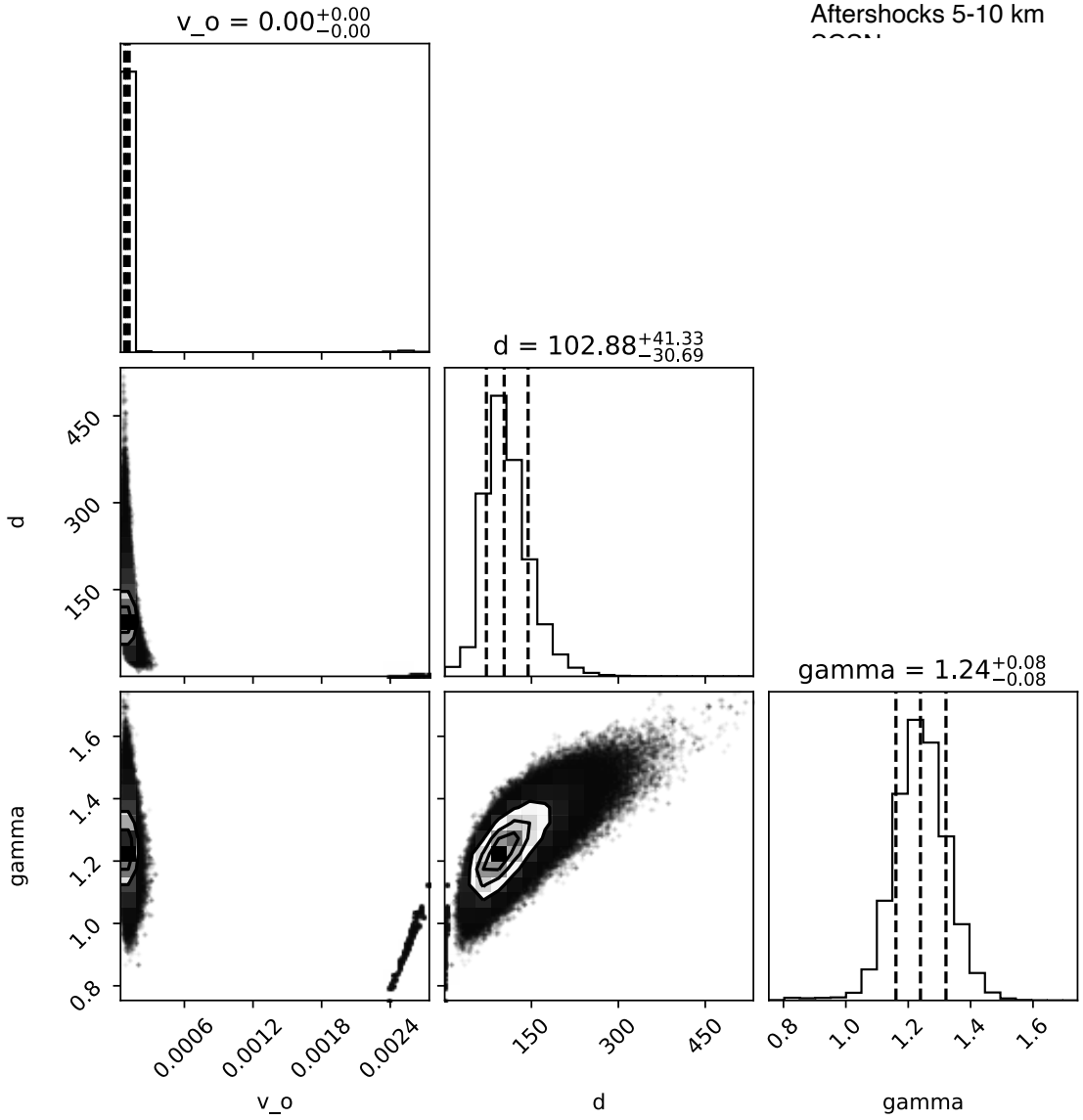
Aftershocks 5-10 km
v_o = 0.00$^{+0.00}_{-0.00}$
d = 102.88$^{+41.33}_{-30.69}$
gamma = 1.24$^{+0.08}_{-0.08}$
d
gamma
v_o
d
gamma
150
300
450
0.8
1.0
1.2
1.4
1.6
0.0006
0.0012
0.0018
0.0024

Afershocks 10-20 km SCSN

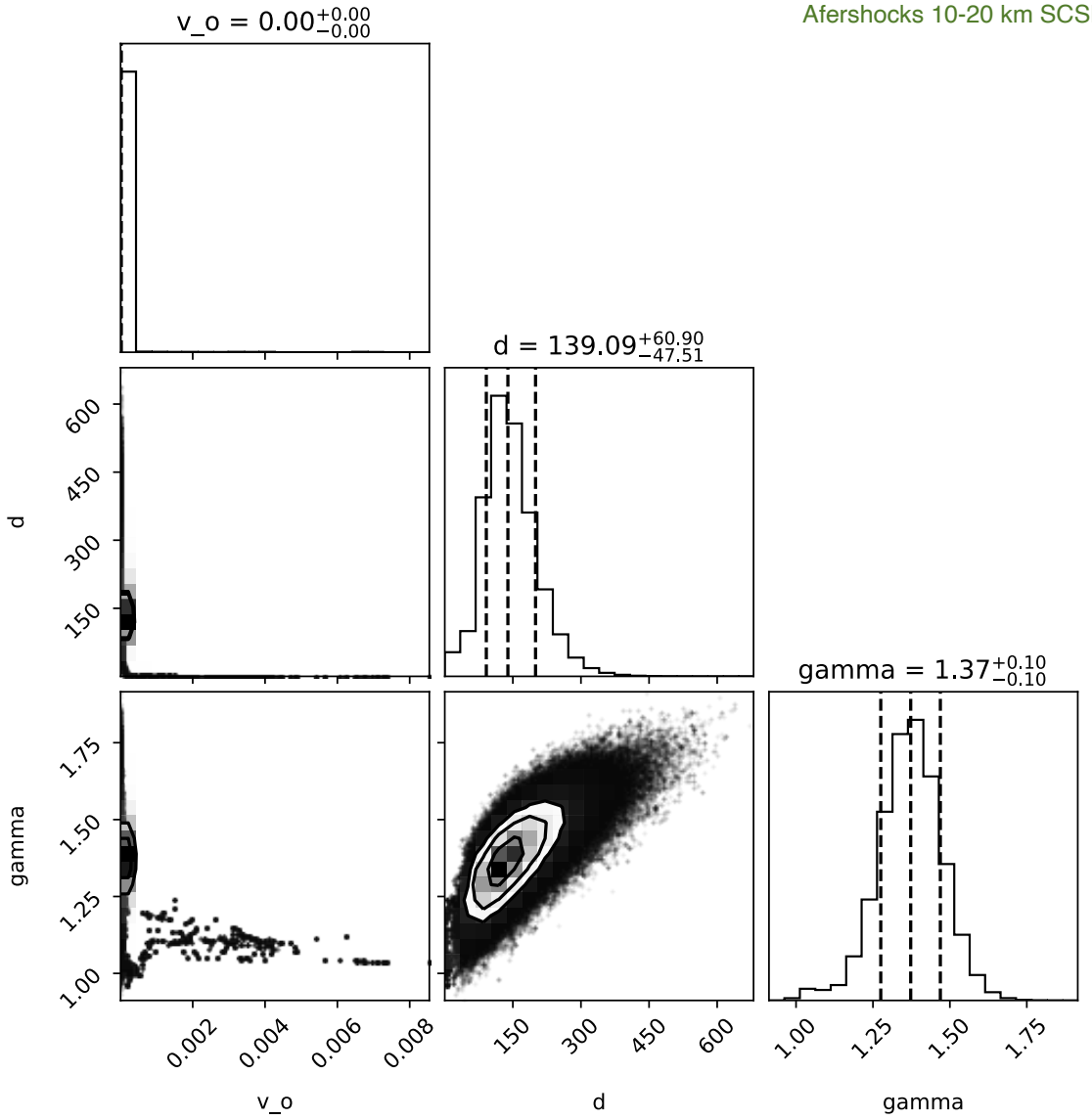

All aftershocks SCSN

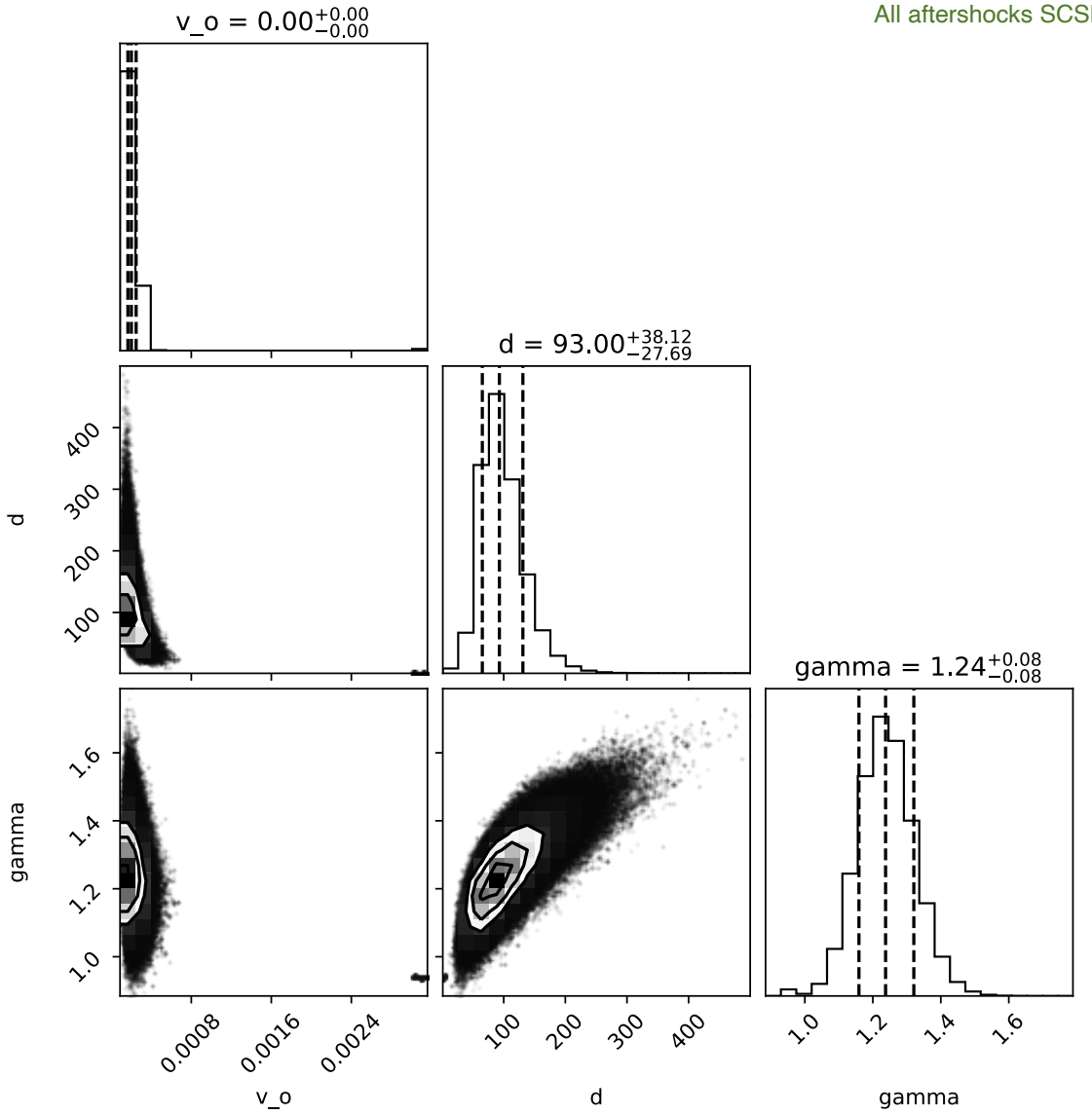

Ponti et al. (2020) fractures

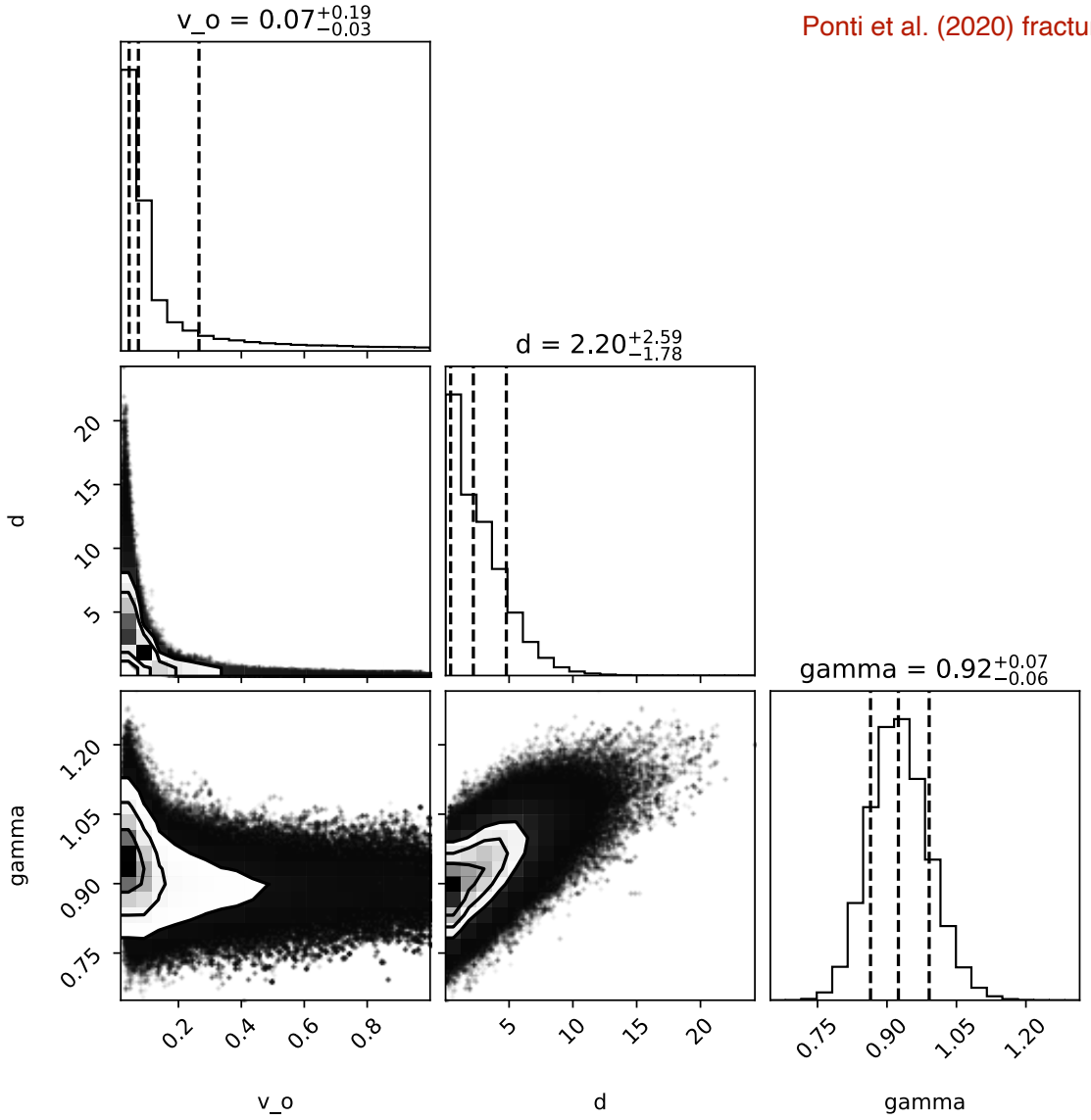

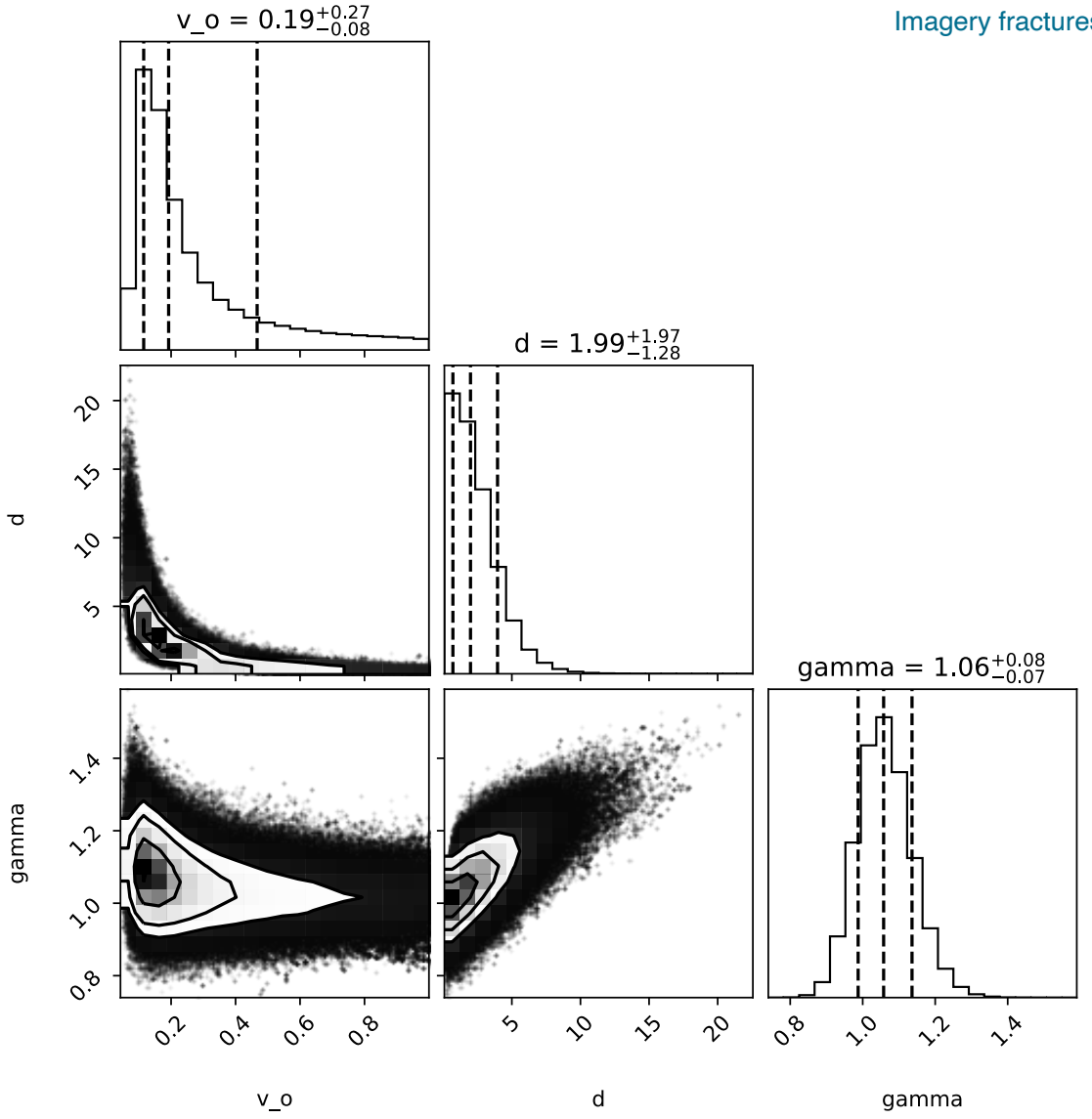
v_o = 0.19$^{+0.27}_{-0.08}$
d = 1.99$^{+1.97}_{-1.28}$
gamma = 1.06$^{+0.08}_{-0.07}$
v_o
d
gamma

Lidar fractures

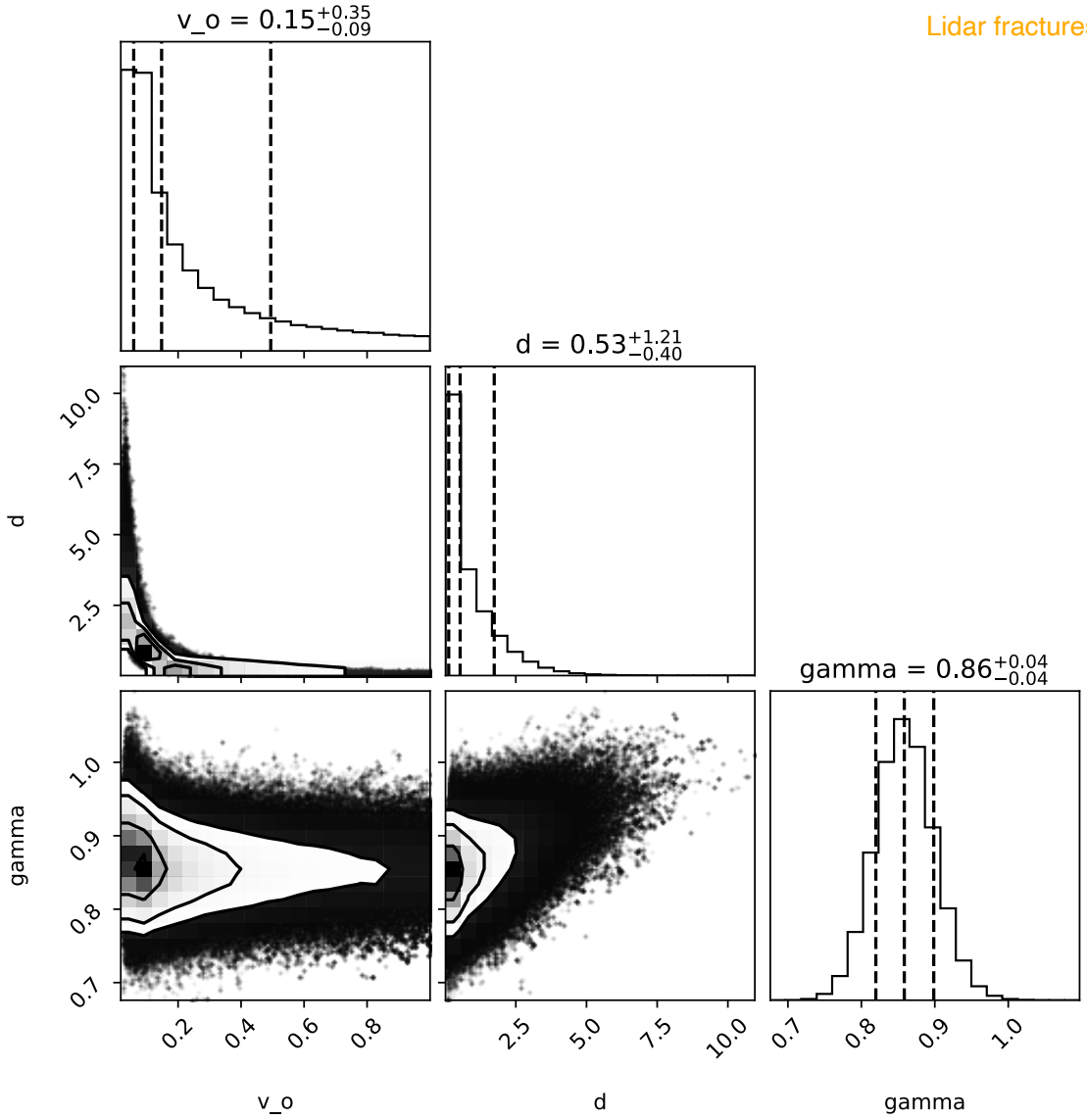

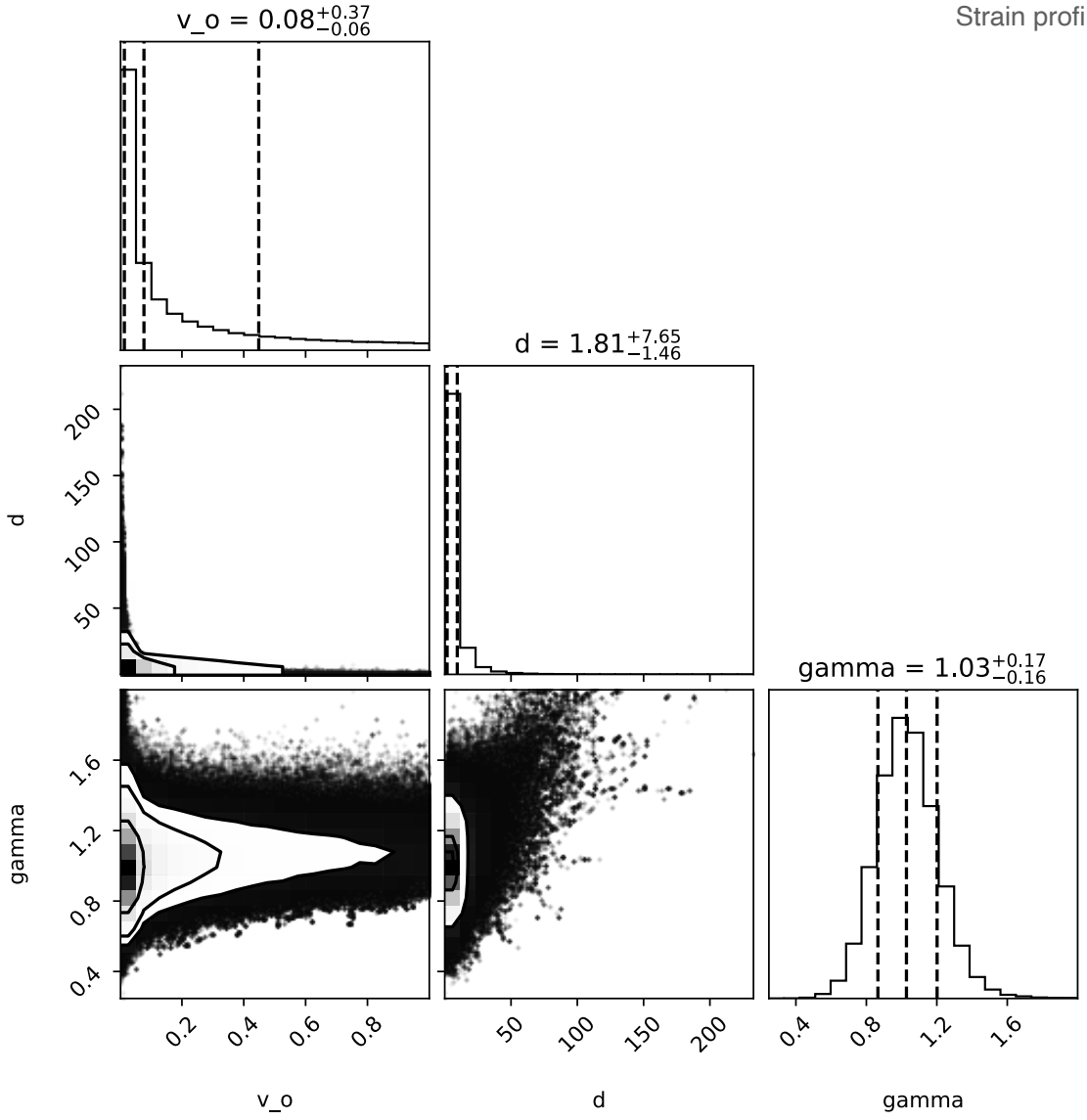
v_o = 0.08^{+0.37}_{-0.06}
d = 1.81^{+7.65}_{-1.46}
gamma = 1.03^{+0.17}_{-0.16}
v_o
d
gamma

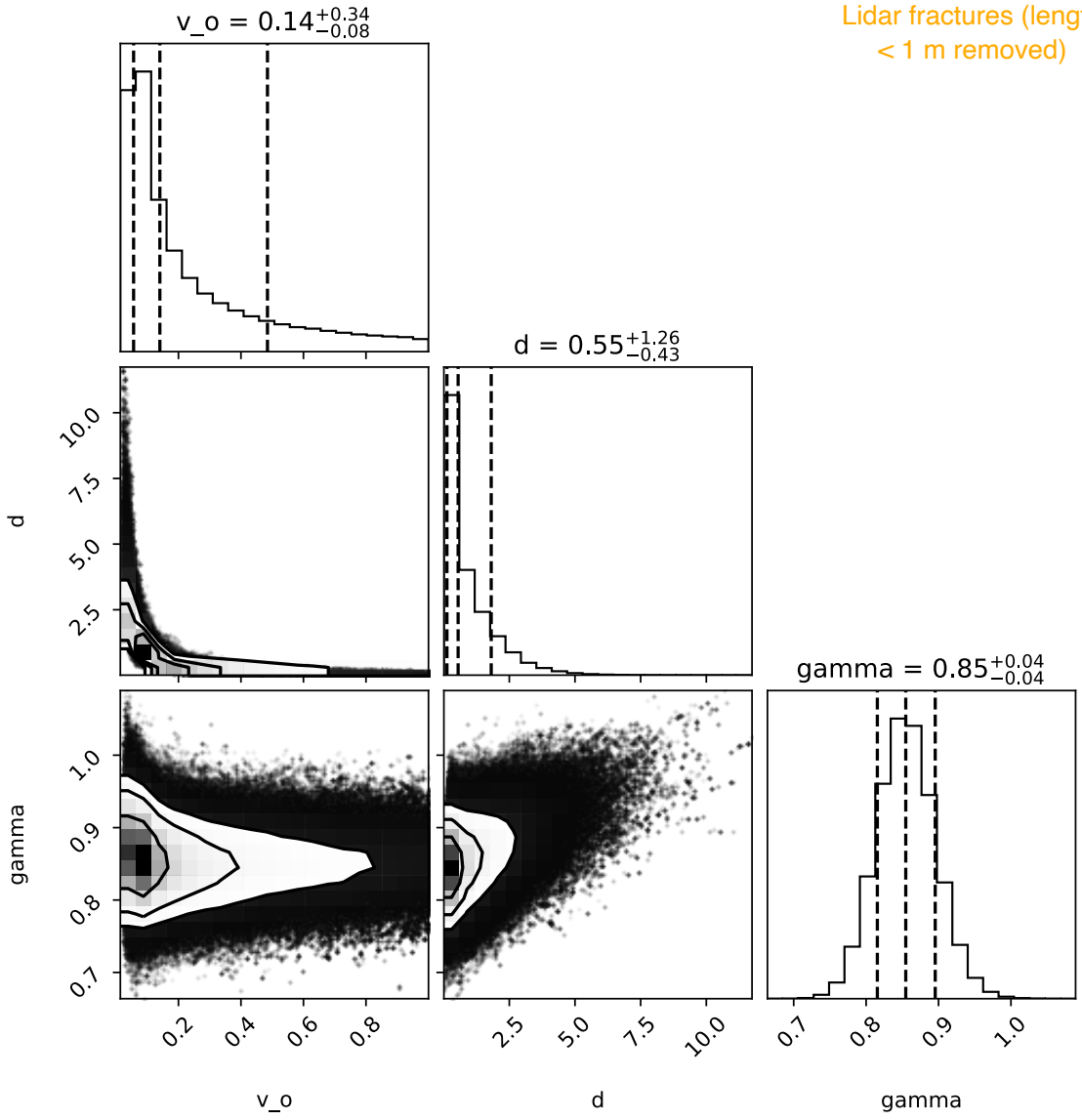
v_o = 0.14$^{+0.34}_{-0.08}$
d = 0.55$^{+1.26}_{-0.43}$
gamma = 0.85$^{+0.04}_{-0.04}$
Lidar fractures (length < 1 m removed)
v_o
d
gamma
0.2
0.4
0.6
0.8
2.5
5.0
7.5
10.0
0.7
0.8
0.9
1.0

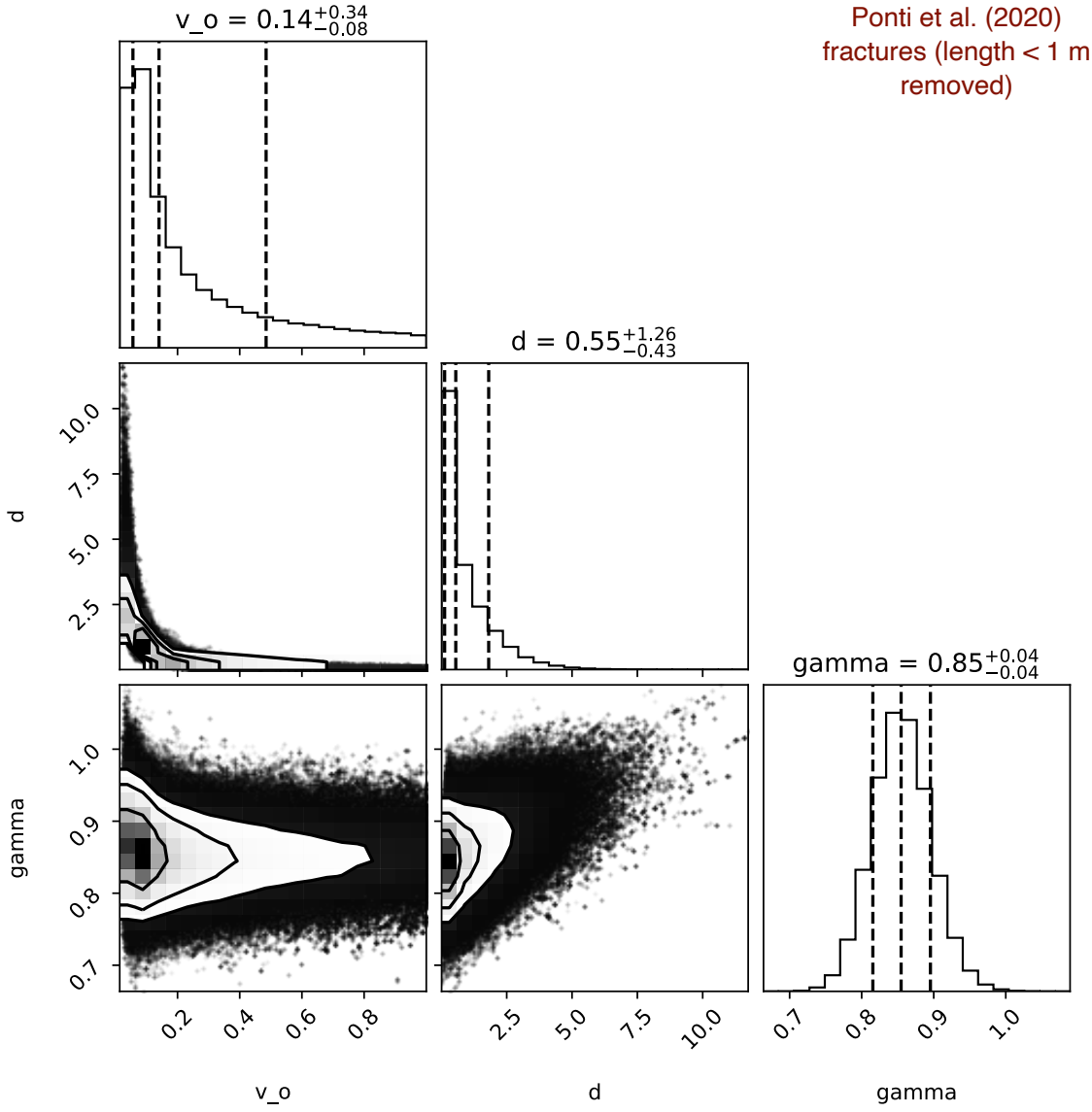

Ponti et al. (2020)
fractures (length < 1 m
removed)

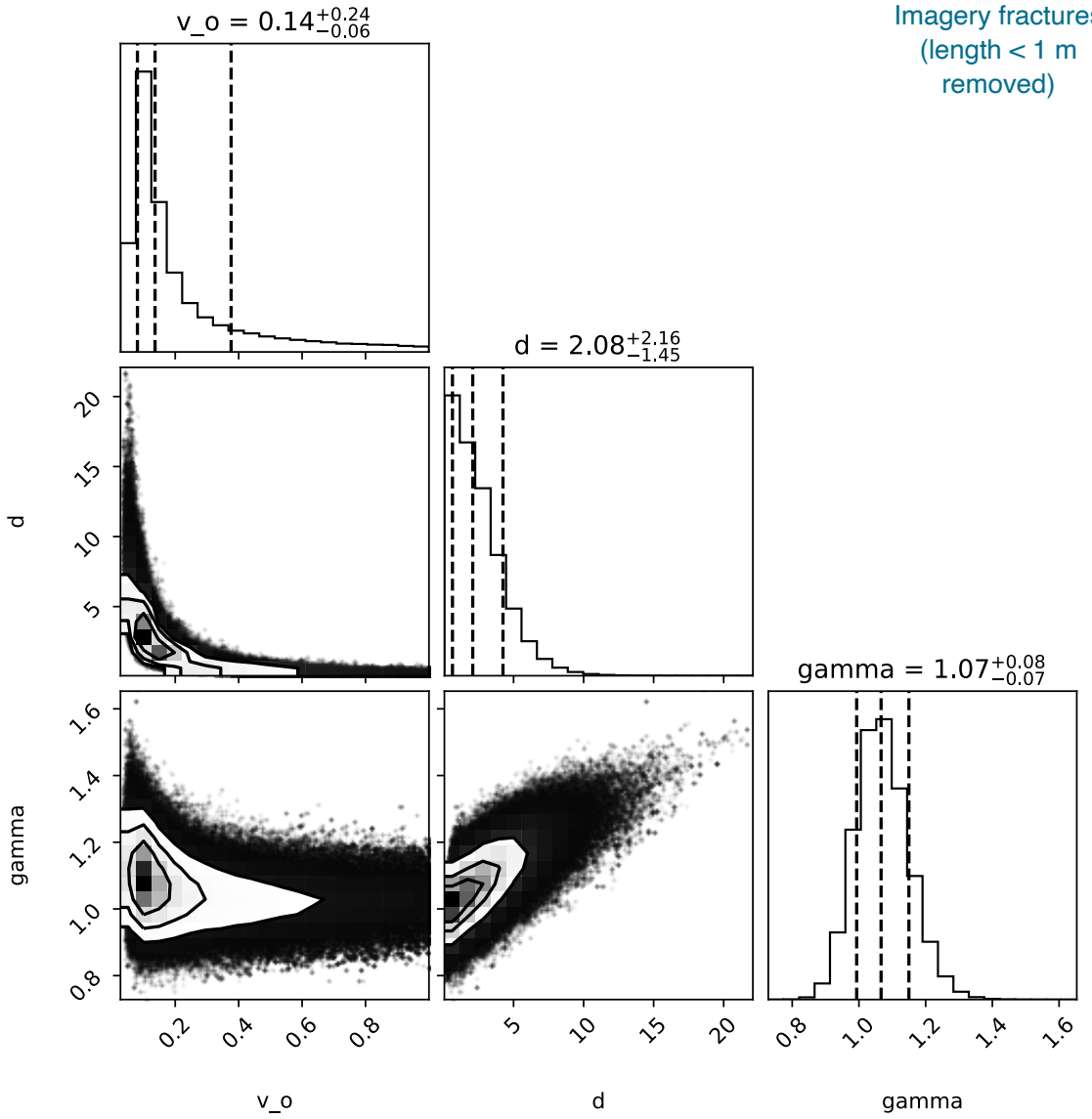
v_o = 0.14$^{+0.24}_{-0.06}$
d = 2.08$^{+2.16}_{-1.45}$
gamma = 1.07$^{+0.08}_{-0.07}$
Imagery fractures (length < 1 m removed)
v_o
d
gamma
0.2
0.4
0.6
0.8
5
10
15
20
0.8
1.0
1.2
1.4
1.6

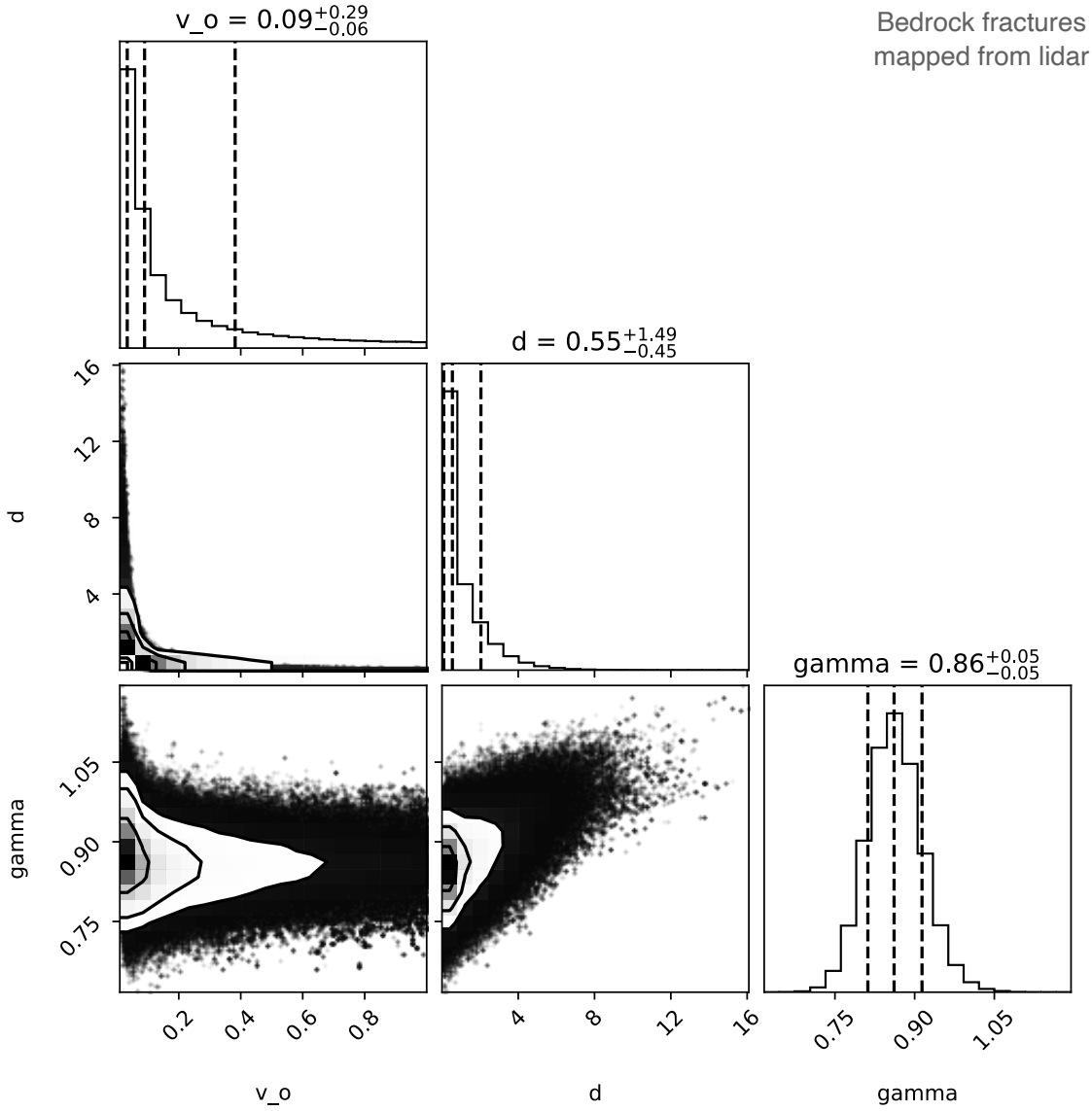

Bedrock fractures
mapped from lidar

Sediment fractures
mapped from lidar

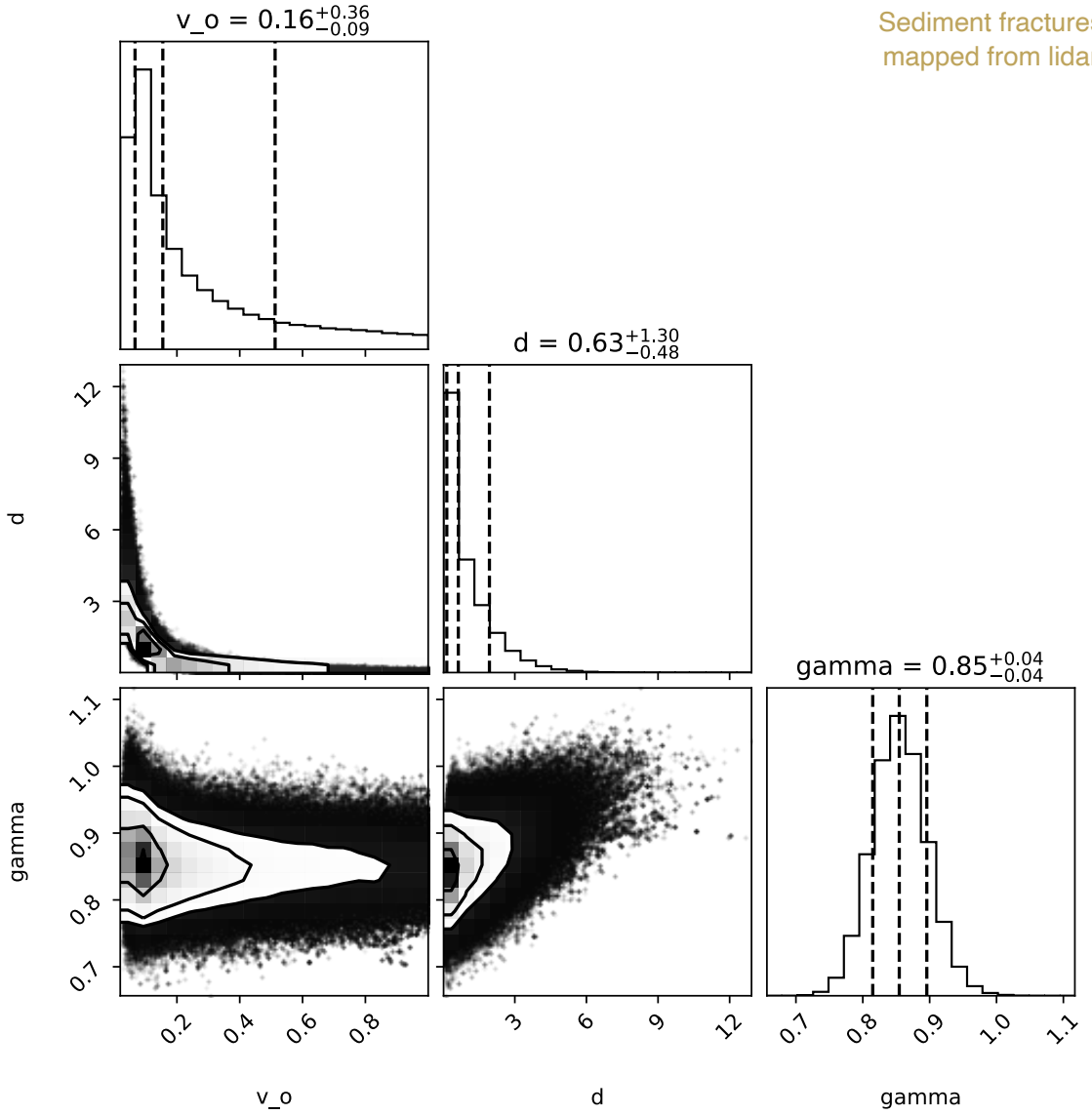

Imagery (zone 1)

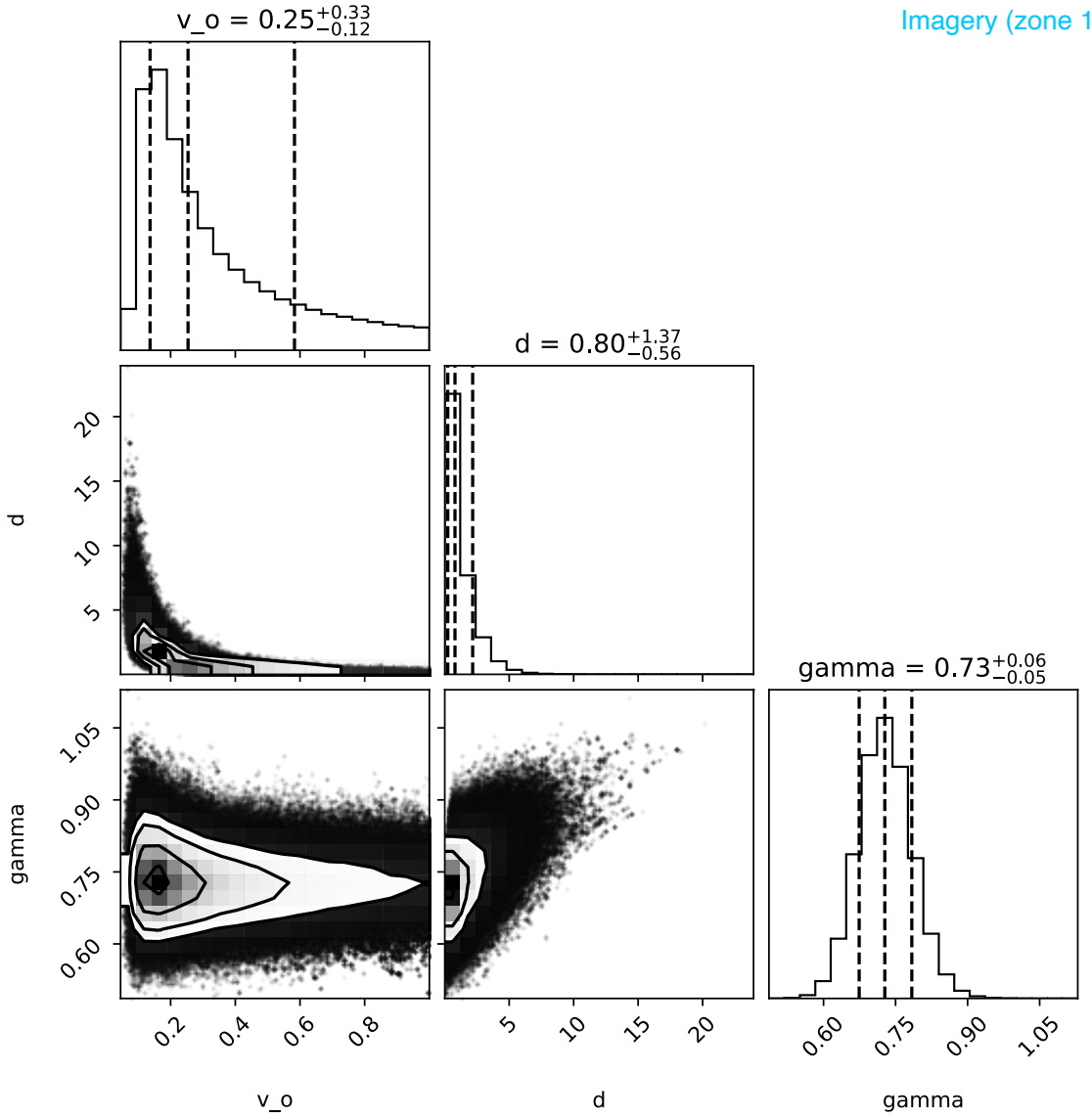

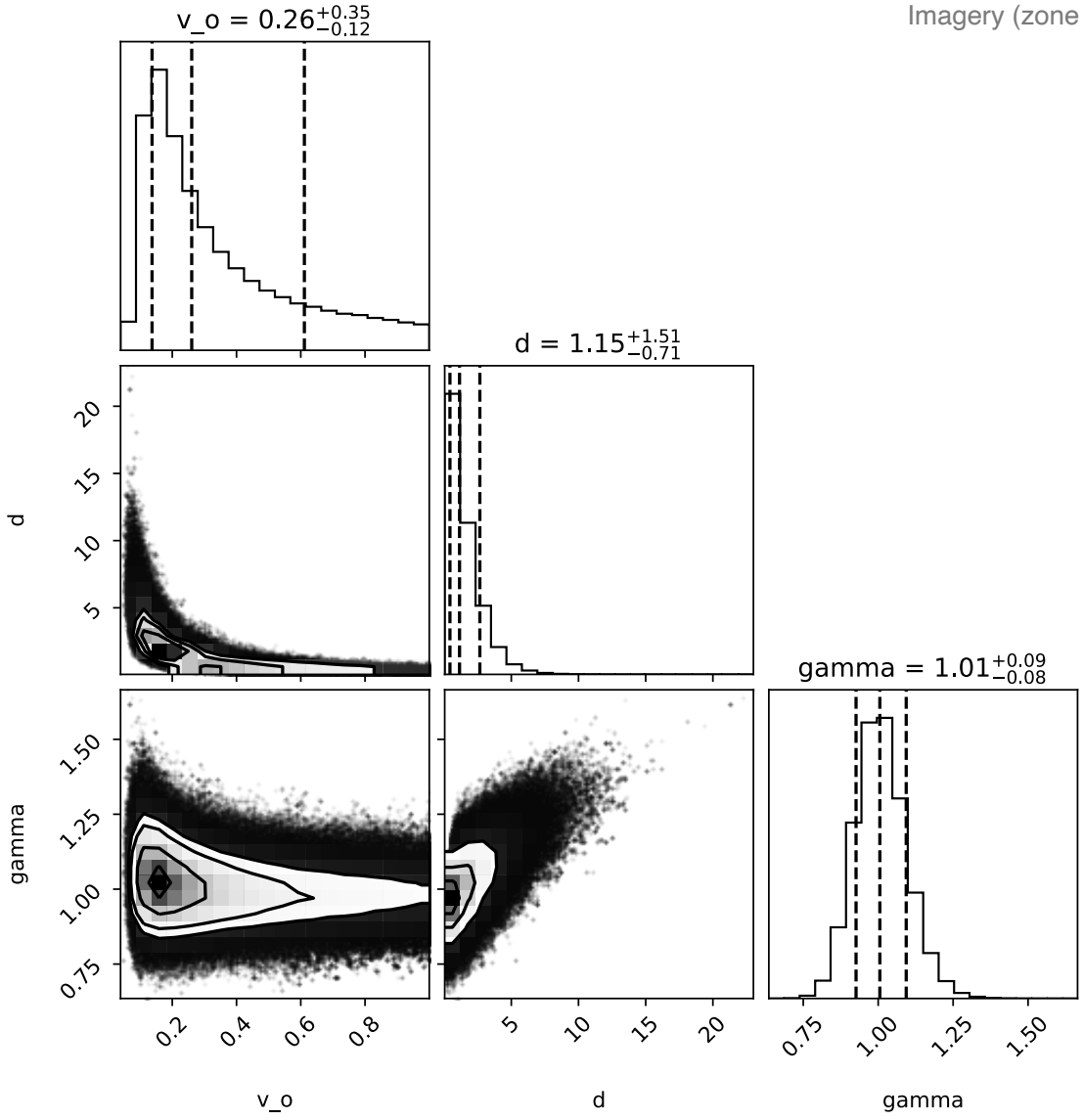
v_o = 0.26^{+0.35}_{-0.12}
d = 1.15^{+1.51}_{-0.71}
gamma = 1.01^{+0.09}_{-0.08}
v_o
d
gamma

Imagery (zone 3)

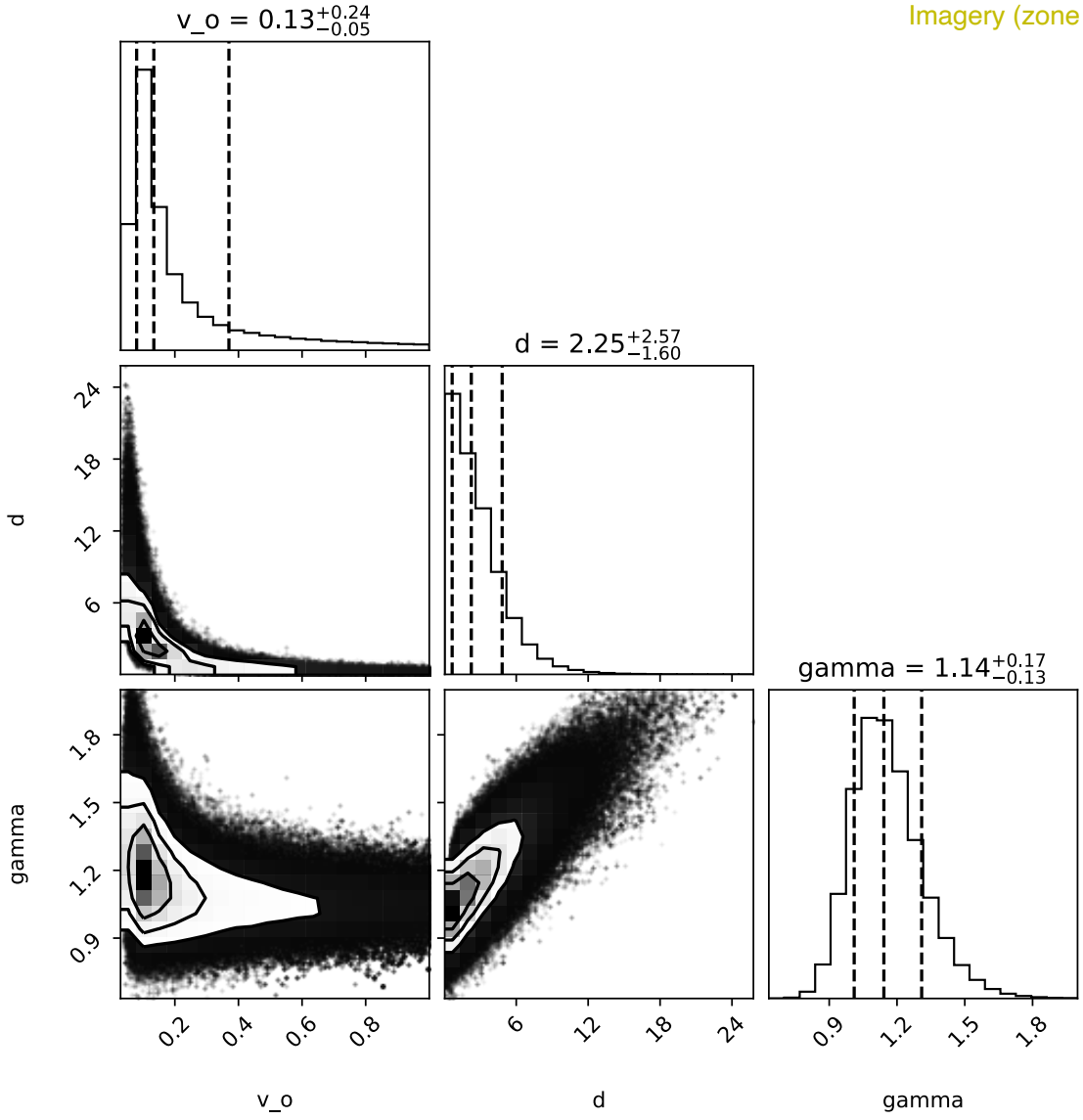

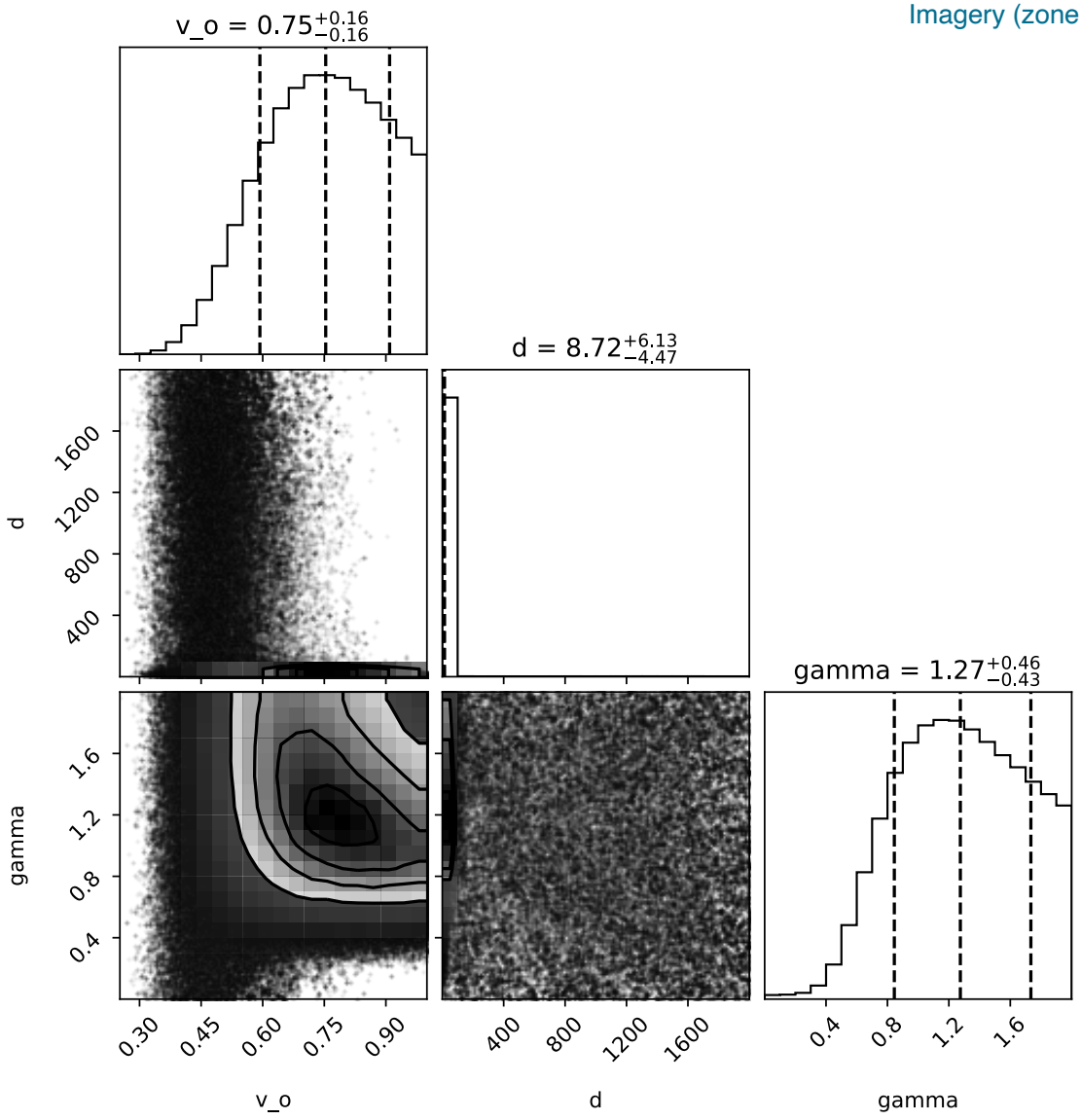
v_o = 0.75^{+0.16}_{-0.16}
d = 8.72^{+6.13}_{-4.47}
gamma = 1.27^{+0.46}_{-0.43}
v_o
d
gamma
0.30
0.45
0.60
0.75
0.90
400
800
1200
1600
0.4
0.8
1.2
1.6

Imagery (zone 5)

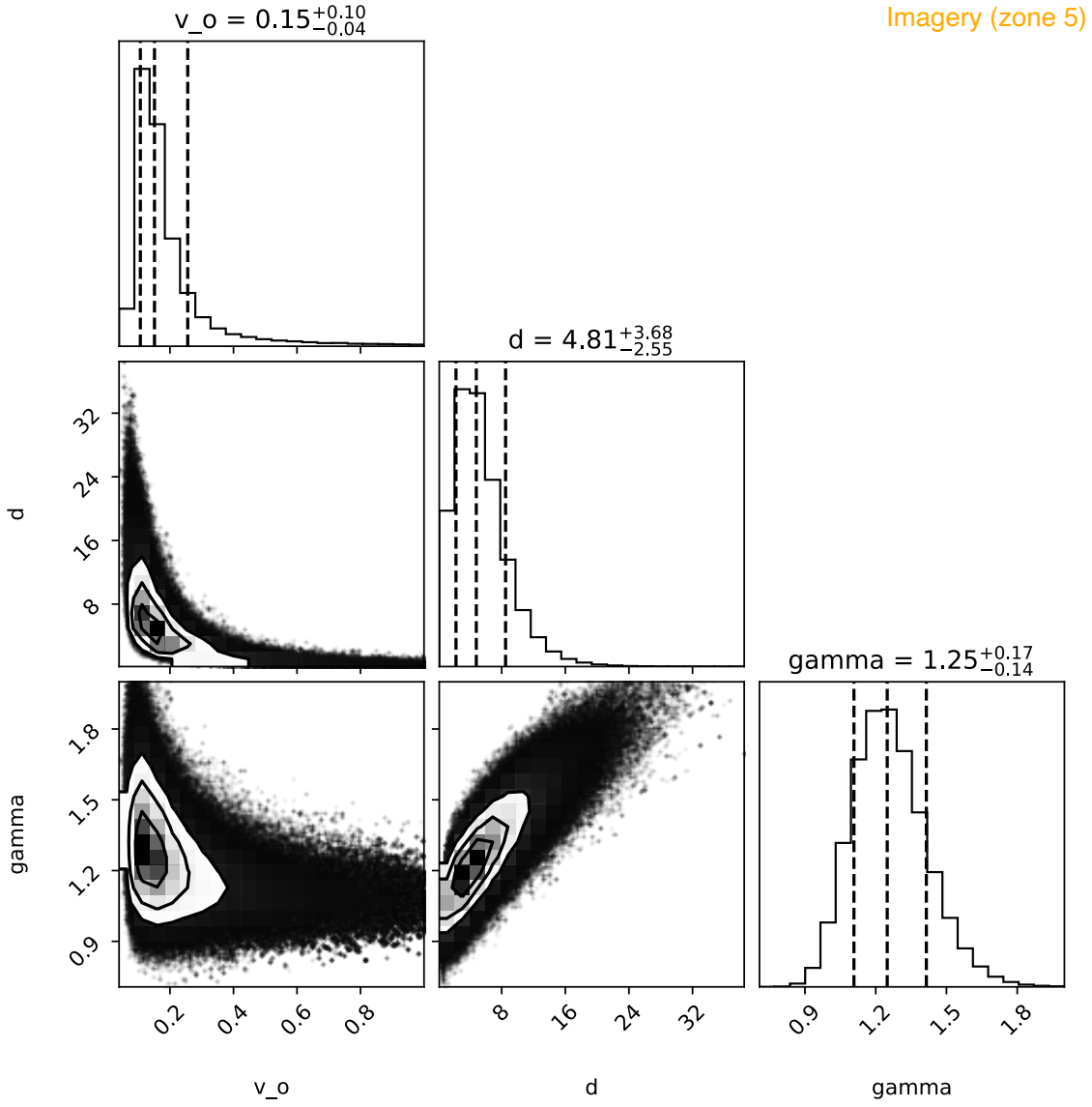

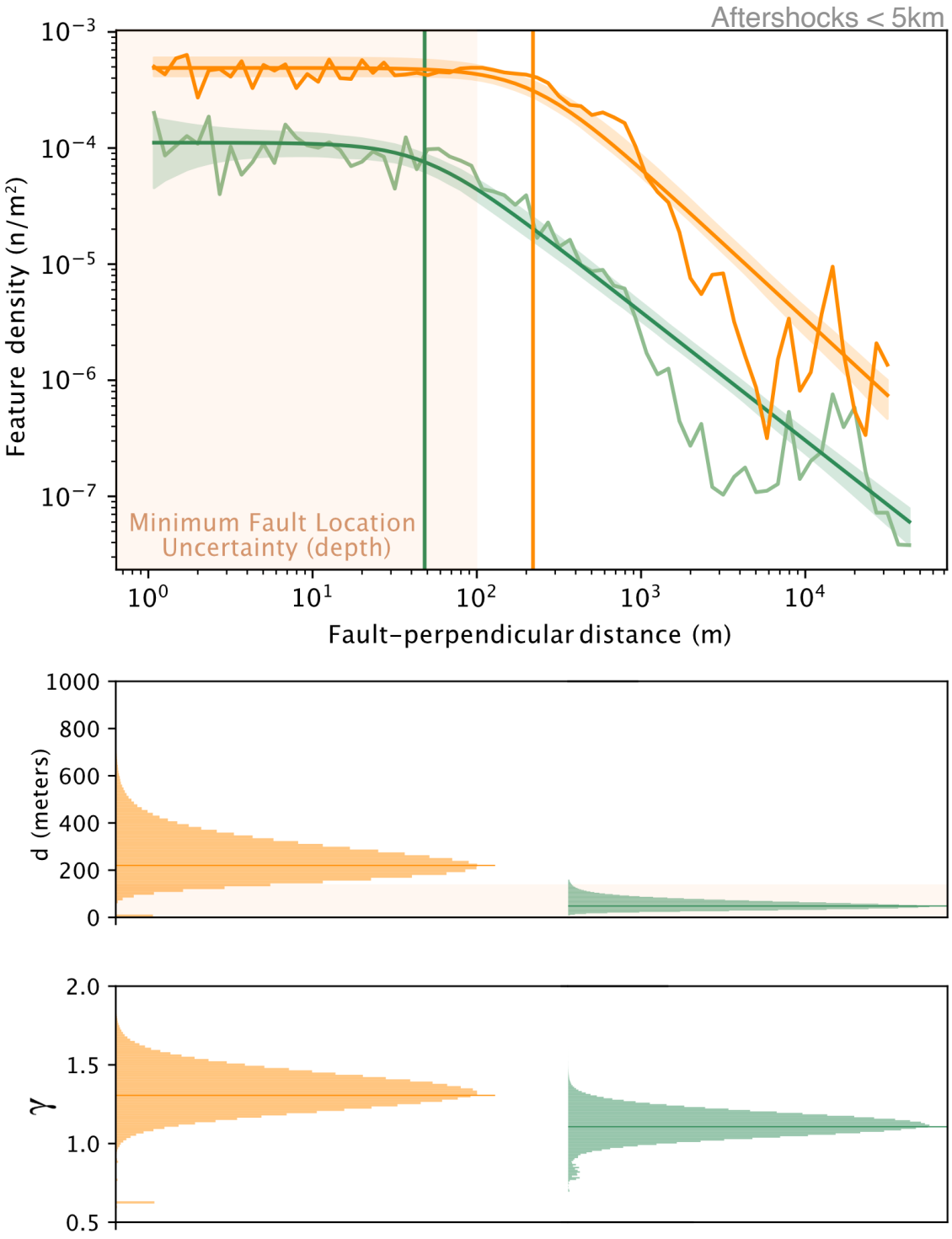
Aftershocks < 5km
Feature density (n/m²)
Minimum Fault Location Uncertainty (depth)
Fault-perpendicular distance (m)
d (meters)
γ

Chapter 4: Displacement hazard from distributed ruptures in strike-slip earthquakes

Abstract

Widespread distributed fracturing during earthquakes threatens infrastructure and lifelines. We combine high-resolution rupture maps from the five major surface-rupturing strike-slip earthquakes in southern California and northern Mexico since 1992 to incorporate the displacements produced by distributed ruptures into a probabilistic displacement hazard analysis framework. Through analysis of the spatial distribution of mapped ruptures and displacements for each of these events, we develop a magnitude-dependent expression for the probability per unit area of finding a distributed rupture that accommodates a displacement that exceeds a displacement threshold at a given distance from the principal fault. Our model is best applied to estimating expected distributed displacements for strike-slip earthquakes, similar to those analyzed, with widespread ruptures across immature fault zones.

Introduction

Displacements from surface-rupturing earthquakes directly threaten infrastructure and lifelines in tectonically active regions. Probabilistic fault displacement hazard analysis (PFDHA) addresses this challenge by providing estimates of the likelihood and distribution of surface displacements during fault rupture (e.g., Youngs et al., 2003; Petersen et al., 2011; Moss and Ross, 2011; Takao et al., 2013; Nurminen et al., 2020; Wang and Goulet, 2021; Scott et al., 2023). Over the past few years, earth scientists and engineers have joined efforts in generating standardized empirical databases to constrain fault displacement hazard models (Sarmiento et al., 2021; Nurminen et al., 2022). The data these efforts are based on has improved due to increased coverage of surface rupturing earthquakes (e.g., airborne lidar, Chen et al., 2015; Hudnut et al., 2020), better post-earthquake response coordination (e.g. Civico et al., 2018, Mattioli et al., 2020, Baize et al., 2022), and advances in the repeat frequency and resolution of geodetic methods (e.g. Milliner and Donnellan, 2020; Xu et al., 2020).

We present a fault displacement model focused on distributed ruptures for strike-slip faults using data from five major surface rupturing earthquakes in the Eastern California Shear Zone and Northern Mexico. These events left behind impressive footprints of broadly distributed ruptures in the desert that have been carefully mapped: the Landers (1992), Hector Mine (1999), El Mayor-Cucapah (2010), and Ridgecrest (2019 foreshock and mainshock) earthquakes (Sieh et al., 1993; Lazarte et al., 1994; Treiman et al., 2002; Hudnut et al., 2002; Fletcher et al., 2014; Teran et al., 2015; Milliner et al., 2015; Milliner et al., 2016;

Ponti et al., 2020; DuRoss et al., 2020; Rodriguez Padilla et al., 2022a). The hazard posed by distributed ruptures remains poorly characterized for strike-slip earthquakes, challenging the ability of engineers and other stakeholders to evaluate the associated risk. In this contribution, we use surface rupture maps and displacement measurements from these well-documented earthquakes to help fill this data gap. To do so, we develop a relationship for the probability per unit area of finding a rupture at a distance away from the principal fault that will have a displacement greater than a threshold. This relationship may be used by end-users to quantify surface displacement hazard in a probabilistic framework that can inform the design and evaluation of lifelines and engineered structures located near or across active fault zones.

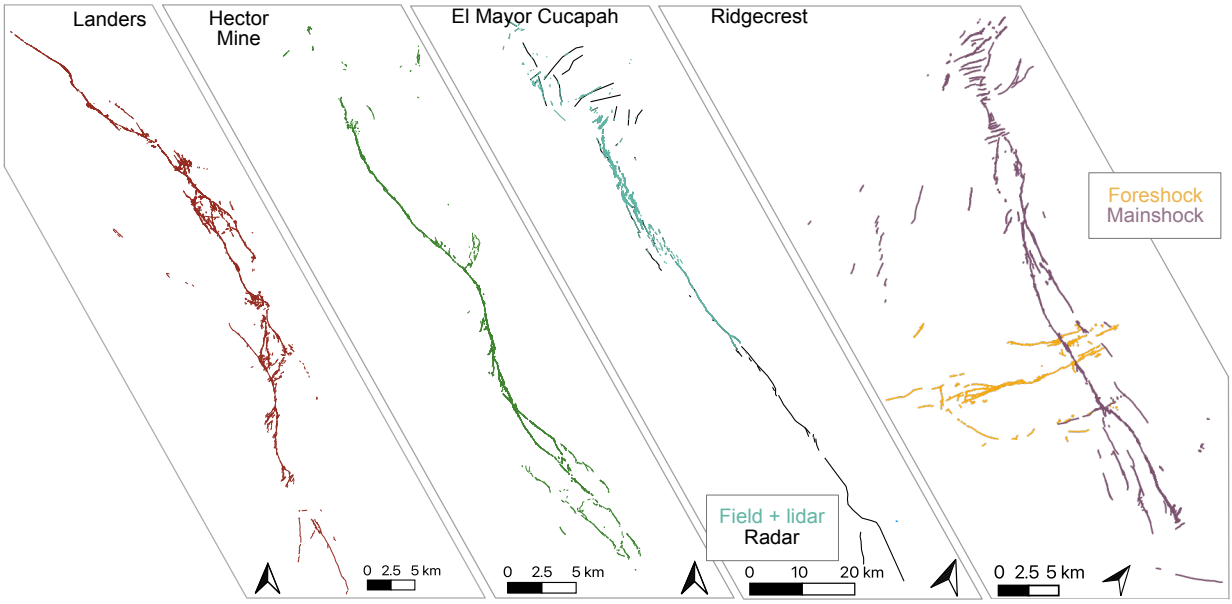

Figure 46: Surface rupture maps from the Landers, Hector Mine, El Mayor-Cucapah, and Ridgecrest earthquakes from the Fault Displacement Hazard Initiative (FDHI) database (Sarmiento et al., 2021). The black lines in the El Mayor-Cucapah rupture are simplified traces mapped from radar data and excluded in this study. The turquoise lines were mapped from field and lidar data and included here. The purple lines in the Ridgecrest map represent the mainshock rupture map and the orange lines represent the foreshock rupture map.

Surface rupture and displacement measurements

The Fault Displacement Hazard Initiative (FDHI) database, hosted and maintained by the Natural Hazards Risk & Resilience Research Center at the University of California, Los Angeles, includes 66 surface-rupturing earthquakes of all faulting styles, with moment magnitudes ranging from 5.0 to 8.0 (Sarmiento et al., 2021). The database incorporates surface rupture maps and displacement measurements for each of the events. The displacements are attributed with location, amount, and sometimes, direction. The ruptures are classified as primary or secondary. For the strike-slip events considered in this study, ruptures occur in a continuum of

decaying density (see methods section), without a distinct change from localized or primary to distributed or secondary, and thus we classify all ruptures in the FDHI database for these events as distributed for the purpose of our study.

We select five strike-slip events from the FDHI rupture database to incorporate into our model: the 1992 M_W7.3 Landers, 1999 M_W 7.1 Hector Mine, 2010 M_W 7.2 El Mayor-Cucapah, and 2019 Ridgecrest earthquakes (separated into M_w 6.4 foreshock and M_w 7.1 mainshock; Figure 46). We choose these events because they are well-mapped, occurred on relatively immature faults (<25 km cumulative displacement), and share the same regional tectonic setting (Eastern California Shear Zone and northern Baja California transtensional rift).

The surface rupture maps in the FDHI database include some variability in completeness and mapping style. Overall, the near-field region of these earthquakes (<1 km from the principal rupture trace) is mapped at a similar resolution, while the far-field has some variability in spatial completeness and resolution. Specifically, the rupture map for the El Mayor-Cucapah earthquake includes ruptures mapped from radar data at its northern end into southern California and its southern end through the Colorado River Delta (Figure 46)(Fletcher et al., 2014). These rupture traces are depicted more simply than the field- and lidar-based ruptures, and may introduce an unrealistic bias in the rupture population. Accordingly, we remove these radar-based rupture traces from our dataset. Similarly, the foreshock and mainshock Ridgecrest maps contain some ruptures that are doubly mapped, redundant from the original maps of Ponti et al. (2020) and DuRoss et al. (2020), which are both included in the FDHI database maps of the Ridgecrest events. When there are redundant features, we remove the simpler traces.

A displacement model for distributed ruptures from surface rupture and displacement maps

Our model estimates the probability per unit area of finding a rupture at a distance x away from the principal rupture with slip greater than a threshold S_0. Computing this probability requires knowledge of the spatial distribution of ruptures and the displacements that these ruptures could accommodate. We address the former through analysis of the distribution of rupture density and the latter by examining the distribution of surface displacements measured for each of our selected events. The distributed displacement hazard results from the joint probability,

$$P(S > S_0|x, M_W) = P(rupture|x)P(S > S_0|x, rupture, M_W), \tag{13}$$

where $P(S > S_0|x, M_w)$ is the probability per unit area of finding a rupture at a distance away from the

fault, resulting from an event of a given magnitude, that will have a displacement greater than the threshold S_0. $P(rupture|x)$ is the probability of rupture per unit area occurring at that location of distance x from the principal rupture. $P(S > S_0|x, rupture, M_w)$ is the displacement exceedance, a probability of finding a displacement that exceeds that threshold at a given distance from the fault, given the presence of a rupture, for a given earthquake magnitude.

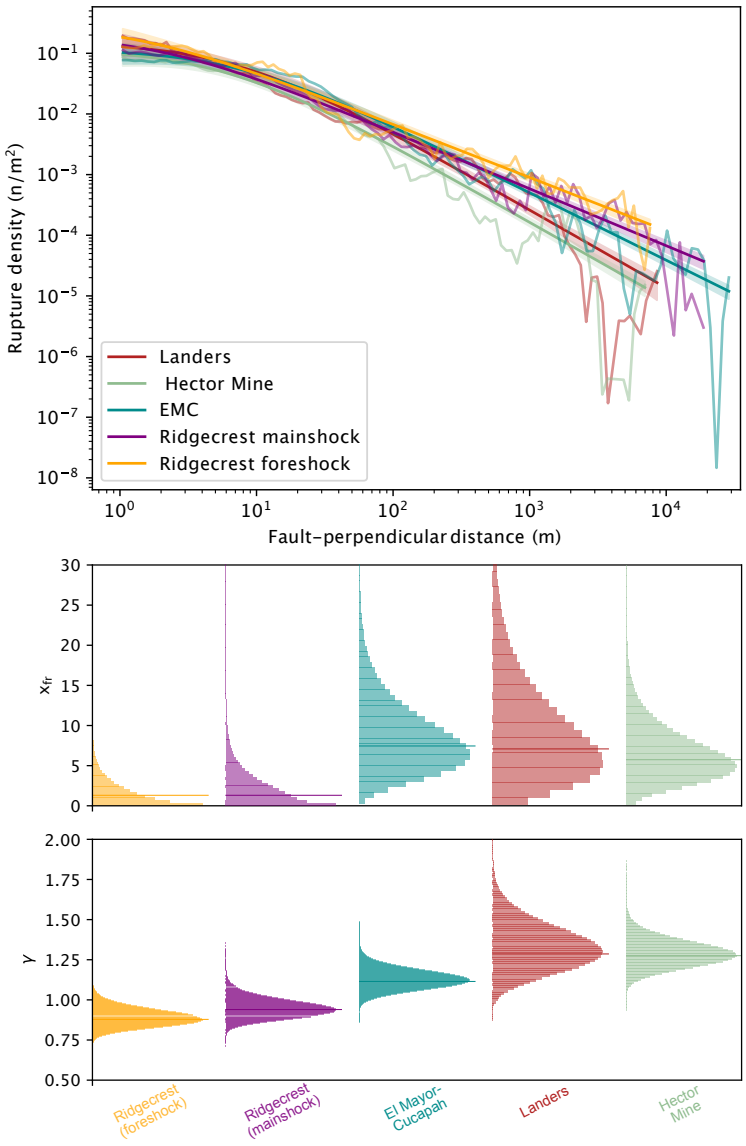

Figure 47: Top: Rupture density distribution (i.e. the probability of finding a rupture per unit area) for the Landers, Hector Mine, El Mayor-Cucapah, and Ridgecrest earthquakes. The Ridgecrest foreshock and mainshock are shown as separate events. The shaded region represents the fits within one standard deviation of the maximum likelihood fit, shown as the bold line, fit using equation 14. The bottom graphs show the distribution of posterior values for x_{fr}, the uncertainty on the location of the principal fault trace, and for γ, the scaling exponent of the density-distribution.

The probability of observing a rupture at a given distance away from the principal rupture (the first term in equation 13) can be estimated from the spatial distribution of fracture density (e.g. Rodriguez Padilla et al., 2022b), which is given by the inverse power-law:

$$\nu(x) = \nu_o \left(\frac{x + x_{fr}}{x_{fr}} \right)^{-\gamma} \tag{14}$$

Where ν_o is the rupture density at the origin in number of ruptures per unit square meter area, and x_{fr} is a normalizing constant related to the uncertainty of the location of the principal fault trace in meters (Rodriguez Padilla et al., 2022b). The exponent γ is the slope of the decay of rupture density with distance, for values of $x >> d$ in log-log space, or scaling exponent. $\nu(x)$ is the probability of a rupture occurrence per unit square meter area.

We use equation 14 to calculate the rupture density distribution (and thus the probability of finding a rupture per unit area) for the Landers, Hector Mine, El Mayor-Cucapah, and Ridgecrest earthquakes based on the surface rupture maps for these events in the FDHI database (Figure 47). To do this, we discretize individual ruptures into 1-meter spaced points so that mapping choices do not bias the rupture density estimates (Rodriguez Padilla et al., 2022b). We measure the shortest distance between each discretized point and the principal rupture, without considering the azimuth of the point (i.e., whether points are ahead of a fault tip and parallel to the rupture, or they are along the rupture and therefore perpendicular to it). The principal rupture trace for each event (i.e., the fault with respect to which fault-perpendicular distance is measured) is simplified from the ruptures mapped as primary in each of the rupture maps in the FDHI rupture database (Figure 53 in the appendix), with the exception of the Ridgecrest mainshock where a second fault in the middle of the dry lake bed was added based on the mapping of Rodriguez Padilla et al. (2022b).

Table 5: Distribution of best-fit parameters for each event and the general model in equation 13.

Parameter	Landers	Hector Mine	El Mayor-Cucapah	Ridgecrest (foreshock)	Ridgecrest (mainshock)	General model
ν_o	0.15	0.12	0.12	0.31	0.20	0.13
x_{fr} (meters)	7.0	5.7	7.5	1.3	2.0	6.7
γ	1.29	1.28	1.11	0.88	0.94	1.19
β (meters)	2.1	4.2	3.1	1.0	2.9	$\beta(M_W)$
n	0.37	0.40	0.42	0.51	0.36	0.41

We fit each parameter in equation 14 to the rupture data using an ensemble sampler Monte Carlo Markov Chain (see supplementary methods section). The maximum likelihood fits and posterior distributions for x_{fr} and γ are shown in Figure 47 and provided in Table 5. Note that the rupture distributions appear to be independent of earthquake magnitude, with all events having similar rupture densities ν_o at the fault, hence

the magnitude-independence of the first term in equation 13.

To assess displacement exceedance (second term in equation 13), we include only the displacements in the FDHI database (supplementary Figure 54) measured in the field, and exclude measurements derived from other techniques, such as image correlation. This is to ensure that the displacement measurements we consider are collected over apertures consistent with the width of individual ruptures. Among the field measurements, we select those labeled as "net preferred" for our models, as these are the measurements recommended for analysis by the FDHI database authors. The vast majority of the displacements in the database are lateral and therefore record shear, with a minor portion of them recorded in absolute terms, where multiple directional components are recorded as a ratio, representing a mixed-mode fracture. Because of the limited information available on fracture mode and displacement direction, our models are constructed without consideration of these parameters.

Coseismic displacements are highest along the principal rupture trace and decline to lower values on more distant distributed ruptures. We find that the mean displacement values from the FDHI database, binned with respect to distance to the principal fault trace, may be modeled as an inverse power-law described by:

$$\lambda(x) = \beta \left(\frac{x + x_S}{x_S} \right)^{-n} \tag{15}$$

where λ is the mean of the displacement at every distance bin, β is the average displacement at the origin, x is the location away from the principal fault trace in meters, x_S is a normalization factor held constant at 1 meter (see supplementary methods in the appendix), and n, which is the slope of the relationship between mean displacement and distance in log-log space, or the scaling exponent. We fit equation 15 to the distribution of average displacements with distance for each of the events using an ensemble sampler for Monte-Carlo Markov Chain (see appendix for detailed method). The maximum likelihood fits and posterior distributions for β and n are shown in Figure 48 and provided in Table 5. Values of β range from 1 meter for the Ridgecrest foreshock to 4.2 meters for the Hector Mine event, broadly consistent with the average slip at the fault in each earthquake.

We find that the values of n agree between the different events, averaging around 0.4, though the fits of equation 15 to the displacements vary in quality between events, with the Ridgecrest foreshock and the Hector Mine events being not well characterized by the power-law decay in equation 15. This poor characterization arises from the broader zone of similar average displacement measurements near the principal fault trace, and much higher scatter in the further (>1 km from the fault in Hector Mine and >50 m from the fault in the Ridgecrest foreshock) displacements measured in the field (Figure 48). This is clear in the residuals of the fit of equation 15 to the field displacement data from these two events (Figure 55 in the appendix). In

the case of the Ridgecrest foreshock, the constant average displacement values near the principal fault may arise from incomplete rupture to the surface, which may be a magnitude-dependent characteristic. This is something we do not address in our model. The spatial distribution of mean displacement is well described by equation 15 for the Ridgecrest mainshock, the Landers, and the El Mayor-Cucapah events, as shown by the generally low residuals (<20% of β) of the fit of equation 15 to the field displacement data (figure 55 in the appendix).

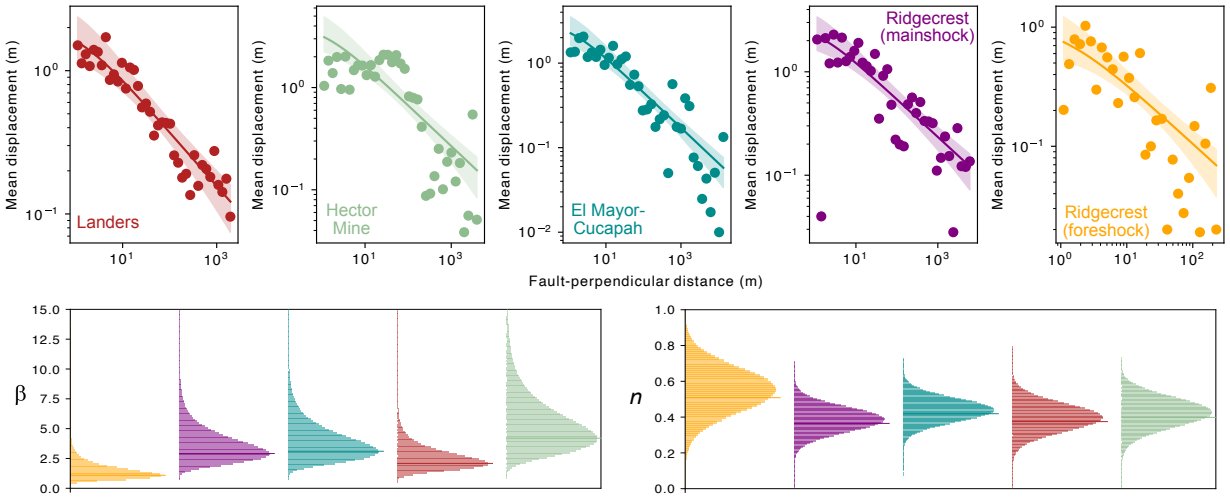

Figure 48: Distribution of average displacement measured in the field for the Landers, Hector Mine, El Mayor-Cucapah, and Ridgecrest earthquakes. The scattered dots on the top plot represent the field displacement data for each event from the FDHI database (Sarmiento et al., 2021). The solid lines represent the maximum likelihood fits to the distribution and the shaded area shows the 1σ posterior distribution from a Markov Chain Monte Carlo fit. The bottom panels show the posterior distributions of β and n fit using equation 15.

Within each distance bin (see supplementary methods for details), we find that the population of field displacement measurements can be described by exponential or log-normal distributions (Figure 49). Both the exponential and log-normal models fit the data comparatively well for the range of observed slip values near the fault (Figure 49) for the Ridgecrest mainshock, the Ridgecrest foreshock, the Landers, and the Hector Mine events. The El Mayor-Cucapah empirical cumulative distribution function (ECDF) is best described by the uniform cumulative distribution function (CDF), though none of the distributions tested describe the data exceptionally well. For all events, beyond the range of observable displacements, the log-normal and exponential distributions would make different predictions that would result in slightly different probabilistic models in the latter steps in this method. Without observational data spanning higher slip values, we prefer the simpler form and less heavy-tailed behavior of the exponential relationship.

This exponential relationship holds up well for all of the distance bins analyzed, as shown by the observation of similar values for the mean and the standard deviation of displacement measurements within each

bin (supplementary figure 56). The distribution of displacements within a distance bin can thus be described as follows:

$$f(S|x) = \frac{1}{\lambda} e^{\frac{-S}{\lambda}} \tag{16}$$

where λ, the mean of the displacement at every distance bin, is the output of equation 15. Combining equations 15 and 16 yields:

$$f(S|x) = \frac{1}{\beta} \left(\frac{x + x_S}{x_S} \right)^n e^{-\frac{S}{\beta}\left(\frac{x+x_S}{x_S}\right)^n} \tag{17}$$

Equation 17 is a probability density function (PDF) of observed displacements with distance x from the principal fault trace. We integrate this PDF from S_0, the threshold displacement of interest, to S_{max}, the maximum observed slip in an event (note that we expect $S_{max} \geq \beta$), to solve for the probability of observing a displacement that exceeds S_0 on an observed rupture given an earthquake magnitude (second term of equation 13):

$$\begin{aligned} P(S > S_0|x, rupture, M_W) = \int_{S_0}^{S_{max}} & \frac{1}{\beta} \left(\frac{x + x_S}{x_S} \right)^n \\ & e^{-\frac{S}{\beta}(\frac{x+x_S}{x_S})^n} dS \\ & = -e^{-\frac{S}{\beta}(\frac{x+x_S}{x_S})^n} \Big|_{S_0}^{S_{max}} \end{aligned} \tag{18}$$

Note that in evaluating this integral, the term containing S_{max} is small, so that as long as $S_0 << S_{max}$, this term can be ignored. This limits the appropriate application of our model to predicting the probability of distributed displacements above a threshold that is a fraction (i.e. 10%) of the slip measured on the primary fault trace. This limitation is appropriate because solving only for the probability of large slip values would be akin to predicting the presence of another primary fault trace, which is not the objective of this model. With this application in mind, completing the integration of equation 18 yields:

$$P(S > S_0|x, rupture, M_W) = e^{\frac{-S_0}{\beta}(\frac{x+x_S}{x_S})^n} \tag{19}$$

The displacement threshold, S_0, may be adjusted by end-users for different engineering applications. Combining the probabilities in equations 14 and 19 yields the solution to equation 13:

$$P(S > S_0|x, M_W) = \nu_o \left(\frac{x + x_f}{x_f} \right)^{-\gamma} e^{\frac{-S_0}{\beta}\left(\frac{x+x_S}{x_S}\right)^n} \tag{20}$$

Note that the magnitude-dependence in this model arises from parameter β, the average displacement on the fault.

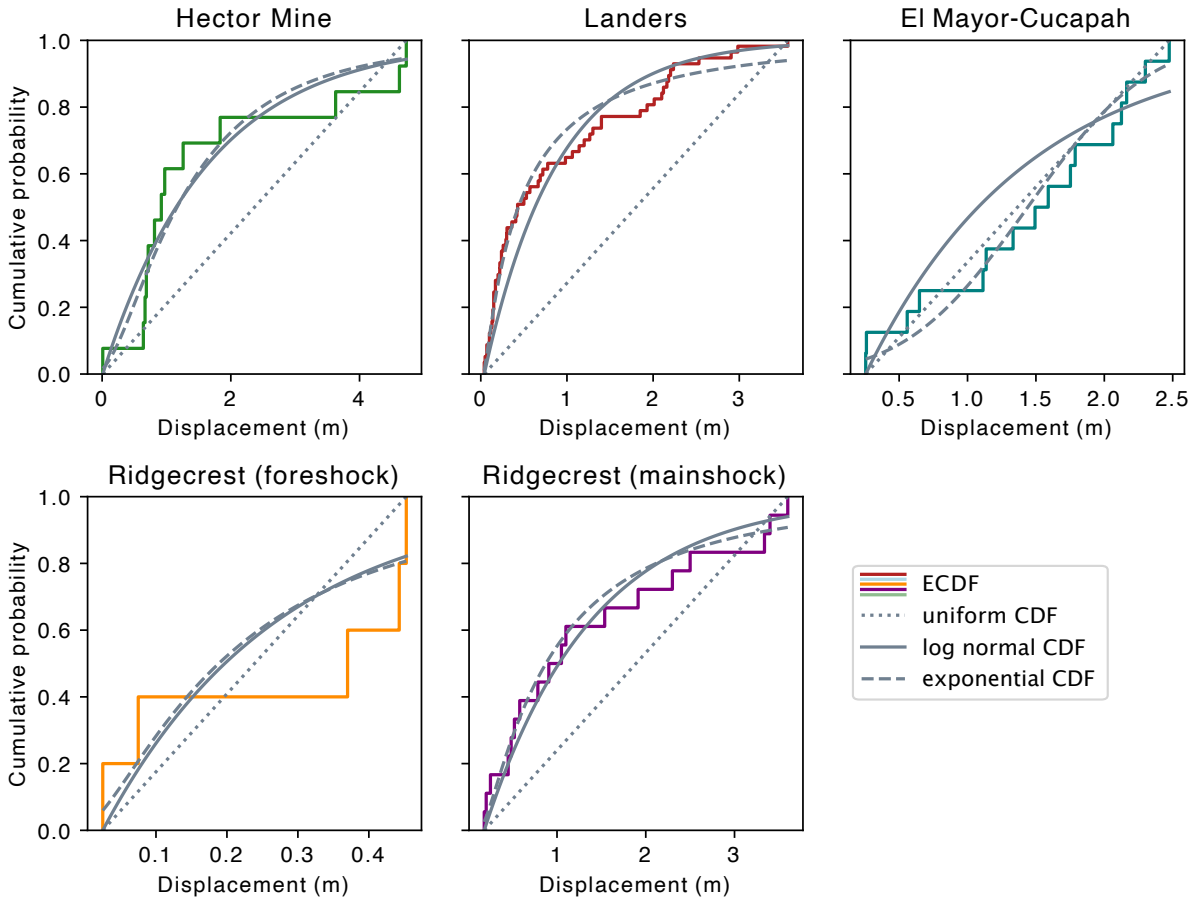

Figure 49: Empirical cumulative distribution functions (ECDF) of the displacements within 6-8 meters away from the fault for the Landers, Hector Mine, El Mayor-Cucapah, and Ridgecrest earthquakes. The cumulative distribution functions fit for exponential, log-normal, and uniform distributions are also shown on top of the ECDF.

Figure 50 shows the relationship in equation 20 for each dataset for x= 1 to x=10 kilometers away from the fault, consistent with the extent of ruptures shown in Figure 47, with example values of S_0 of 0.01, 0.1, and 0.5 meters. The probabilities of finding a rupture that hosts displacements larger than 1 cm near the fault exceed 10% for all of the events considered here, reaching 20% for the Ridgecrest foreshock (Figure 50, left). Despite the smaller magnitude, the Ridgecrest foreshock has the highest rupture density predicted at the fault, which results in higher probabilities $P(S > S_0)$, despite the lower value of β, at this displacement threshold. $P(S > S_0)$ decreases rapidly with distance for all events, even for this small value of S_0, such that the probability of finding a rupture that hosts a displacement larger than 1 cm is lower than 1 in 1,000 beyond 300 m-1 km from the primary fault trace depending on the event.

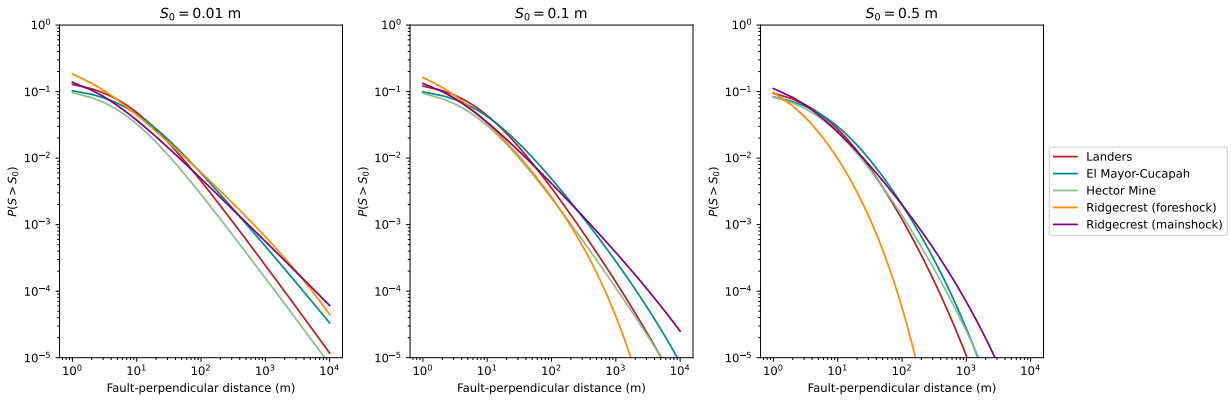

Figure 50: Curves showing the probability per square meter of finding a rupture hosting a displacement that exceeds threshold S_0 for the Landers, Hector Mine, El Mayor-Cucapah, and Ridgecrest earthquakes. The models are generated using equation 20. We show models for $S_0 = 0.01$ m, 0.1 m, and 0.5 m.

The surface rupture hazard curves for the Ridgecrest mainshock, Landers, El Mayor-Cucapah, and Hector Mine events look very similar for $S_0 = 1$ cm to those for $S_0 = 10$ cm. The variability of $P(S > S_0)$, about a factor of 2, at the intercept, arises largely from the variability in rupture density for the different events and likely reflects the natural variability that may be expected for these events and low displacement thresholds, regardless of magnitude (Figure 50, center). The magnitude-dependence of the model becomes clear with increasing distance away from the fault, given by the larger slope of $P(S > S_0)$ for the smaller-magnitude Ridgecrest foreshock. This pattern becomes even more obvious for the $P(S > S_0)$ curves where $S_0 = 0.5$ meters (Figure 50, right). At this displacement threshold, the effect of magnitude, captured by parameter β, trumps that of rupture density at the intercept and the Ridgecrest foreshock has a lower probability of finding a rupture hosting a displacement larger than 0.5 meters than that of the mainshock or Landers. When $S_0 = 0.5$ m, $P(S > S_0)$ becomes lower than 1 in 10,000 at about 500 m-1 km from the fault for the Ridgecrest mainshock, the Landers, the Hector Mine, and the El Mayor-Cucapah events. This hazard level is crossed at about 200 m from the fault for the Ridgecrest foreshock.

A generalized rupture-displacement probability model

The individual models of $P(S > S_0)$ for each event (Figure 50) can be used to inform a general model that is representative of events like these, i.e., those dominated by distributed deformation, largely rupturing through sediment, hosted by immature fault zones.

To estimate the first term of $P(S > S_0)$ for the general model, which is independent of earthquake magnitude, we combine the rupture distributions from the FDHI database from these five earthquakes and estimate a general relationship for rupture density with fault-perpendicular distance using equation 14 (figure

57 in the appendix). This is possible because the parameters describing the spatial distributions of rupture density for all events overlap within error, irrespective of magnitude or other event characteristics.

The second term in $P(S > S_0)$ is magnitude-dependent and therefore requires more careful examination to be generalized. The scaling exponent, n, that describes the spatial distribution of mean displacement is very consistent for the M_W 7.1 Ridgecrest mainshock, the M_W 7.3 Landers, and the M_W 7.2 El Mayor-Cucapah events, and the distribution of field displacements for these events is well described by equation 15, as captured by the low residuals (figure 55 in the appendix). Thus, to estimate n in our general model, we combine the posterior distributions of n from the Landers, El Mayor-Cucapah, and Ridgecrest mainshock displacement distributions (Figure 58 in the appendix). We find that n is normally distributed with a mean value of 0.41 and a standard deviation of 0.07.

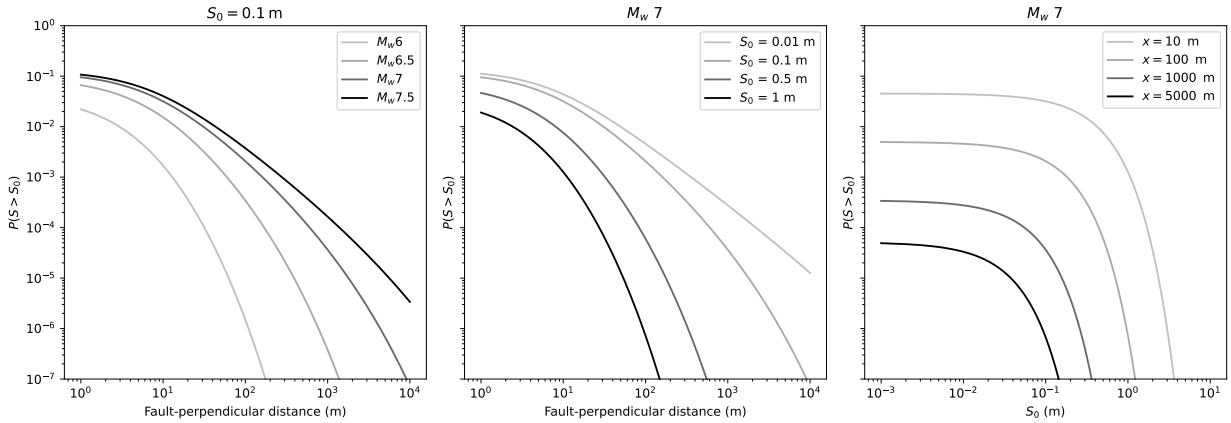

Figure 51: Curves showing the probability per square meter of finding a rupture hosting a displacement that exceeds threshold S_0 as a function of distance from the fault for a surface-rupturing strike-slip earthquake. The models are generated using equation 20. On the left, we show models for M_W = 6, 6.5, 7, and 7.5, where S_0 = 0.1 m. On the center, we show models for S_0 = 0.01, 0.1, 0.5, and 1 meter, for a M_W 7 event. On the right, we show probability ($P(S > S_0)$) versus displacement hazard curves for an M_W 7 event at distances of 10 m, 100 m, 1 km, and 5 km from the fault.

The magnitude-dependence of our probabilistic displacement model arises from parameter β, which we propose may be estimated using the empirical relationship for average displacement as a function of magnitude using the displacement measurements in the FDHI database:

$$log_{10}(\beta) = bM_W - a \tag{21}$$

where $a = 6.8701$ and $b = 0.9629$ are the regression coefficients, determined for strike-slip earthquakes in the regression in Figure 59 in the appendix. The standard error of β depends on magnitude and is given by:

$$\sigma\beta(M_W^*) = \sqrt{\frac{\sum (S - \hat{S})^2}{N-2}} \sqrt{\frac{1}{N} + \frac{(M_W^* - \overline{M_W})^2}{(\sum (M_W - \overline{M_W})^2}} \tag{22}$$

where N is the number of events in the regression, $\overline{M_W}$ is the mean magnitude, M_W^* is the selected magnitude, M_W is the observed magnitude, S is the observed slip, and $\hat{S}$ is the predicted slip at that magnitude. The standard error as a function of magnitude is shown in Figure 61 in the appendix.

We rely on the displacements labeled as "preferred" in the FDHI database to estimate the mean displacement for each strike-slip event. We are not able to use displacements measured in the field only because six of the strike-slip events in the database had displacements measured fully remotely.

Two examples of the general model are shown in Figure 51. One for events of M_W = 6, 6.5, 7 and 7.5, all with S_0 = 0.1 m (Figure 51, left), and a second for values of S_0 = 0.01, 0.1, 0.5, and 1 m for an M_W 7 event (Figure 51, center). The magnitude dependence of $P(S > S_0)$ for a fixed displacement threshold S_0 manifests as an increasingly wider hazard envelope, i.e. slope decreases and intercept increases with increasing magnitude. For a fixed magnitude, the slope describing the probability $P(S > S_0)$ increases with increasing displacement threshold S_0, and the intercept decreases. The relationship of $P(S > S_0)$ and displacement threshold (Figure 51, right) shows an increasingly larger hazard envelope (i.e. larger probability for a given displacement threshold), for smaller distances x to the fault.

Parameter uncertainty estimates

For the probabilistic displacement model $P(S > S_0)$ to provide a robust result, we need to account for the uncertainties in the parameters in the model. The sources of uncertainty in the model are the fitting error in the exponent n that describes the PDF of displacements for an event, the uncertainty in the average displacement at the fault, β, and the uncertainty in the fits to x_{fr}, ν_o, and γ, which describe the spatial distribution of rupture density.

To combine the errors in both terms in equation 20, we make a prediction for $P(S > S_0)$ under each set of samples from our suite of 5000 combined parameter sets. The parameters in the first term of equation 20, which describe the spatial distribution of rupture density, are correlated, so they must be sampled from the same state of the Markov chain for this correlation to be preserved (Figure 60 in the appendix). The parameters in the displacement term in equation 20 are normally distributed. To account for the variability of parameter n, we draw samples from a normal distribution with the mean and standard deviations reported in the previous section. The uncertainty of the average displacement β is given by the standard error of the regression that describes the scaling of mean displacement with magnitude. To account for the expected variability in β, we sample from a normal distribution where the mean is given by the best-fit value from

our linear regression to the data in the FDHI database, and the standard error of the regression serves as the standard deviation of the distribution.

A general model with $S_0 = 0.1$ m and M_W 7, with uncertainties, as well as the model residuals resulting from the 5000 iterations of Monte Carlo sampling are shown in Figure 52. The incompleteness of the rupture maps in the far field contributes to the conical shape of the uncertainty distribution, which is largely inherited from the uncertainty in the rupture density and average displacement scaling exponents, γ and n. We estimate the one standard error by estimating the envelope of model fits at the 16^{th} and 84^{th} percentiles (1σ). Based on these envelopes, we expect variability in probability below one order of magnitude for $P(S > S_0)$ within 3 kilometers of the fault, increasing up to 6 orders of magnitude at 10 km away from the fault. The standard error can be described by the expression:

$$\sigma_M = \tau e^{x^{0.15}} \tag{23}$$

where $\tau \approx 5x10^{-2}$ for the 84% percentile and $\tau \approx -0.10$ for the 16% percentile. The fits of equation 23 to the model fits are shown in red in Figure 52.

We provide a Jupyter Notebook (`https://github.com/absrp/PFDHA_strikeslip`) that allows end-users to generate their own model for $P(S > S_0)$. The only inputs required are a displacement threshold S_0 and an earthquake moment magnitude (M_W). The model outputs $P(S > S_0)$ curves with a best-fit model and an analytically defined uncertainty range using equation 23.

Model discussion and limitations

The model we develop in this contribution is based on rupture maps and field displacement measurements from select events in the Eastern California Shear Zone and northern Baja California. From our limited number of available surface rupturing events with high-resolution maps, there arise some challenges and assumptions in this model that limit its application.

Magnitude-dependence

Rupture density has no observable dependence on earthquake magnitude within the events studied, which span a range of magnitudes between M_W 6.4-7.3. However, this could change with an expanded dataset of high-resolution maps from more events. We find that, with the data available, the distributed rupture densities at the principal fault vary by less than a factor of 10. The rupture density variability documented by Rodriguez Padilla et al. (2022b) between different portions of the Ridgecrest 2019 surface ruptures, which they found to be independent of the displacement magnitude at the surface, exceeds this level of variability.

Additionally, the ruptures we use as model inputs largely occurred through sediment, which may exert an important effect on rupture density. This is consistent with the work of Petersen et al. (2011), who found no dependence between the probability of observing a rupture off-fault and the magnitude of the event. Hence there is no basis at this time to develop a magnitude-dependent estimator of distributed rupture density.

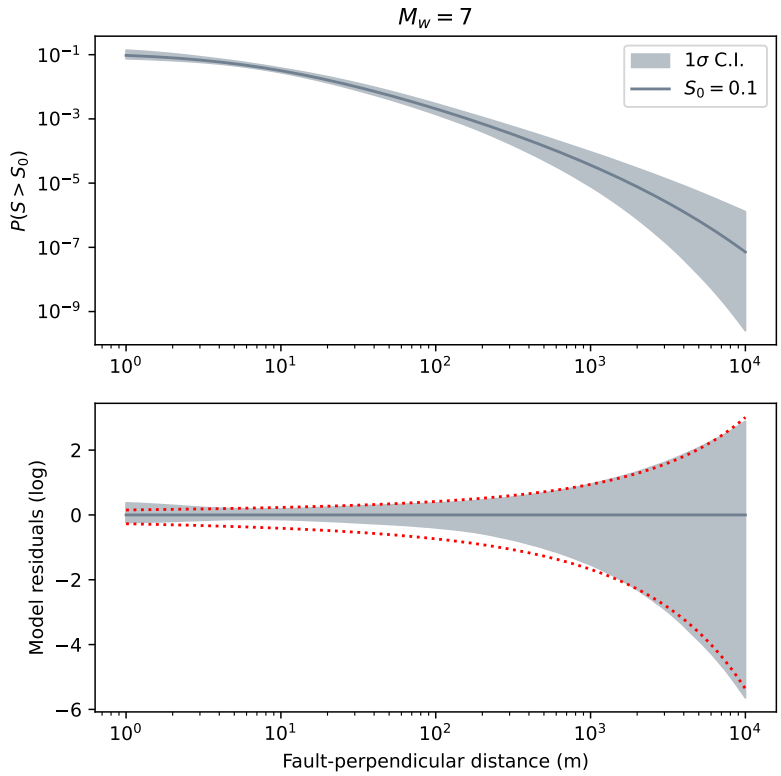

Figure 52: Top: PFDHA model expressing the probability of finding a rupture hosting a displacement that exceeds threshold $S_0 = 0.1$ m for a surface-rupturing strike-slip earthquake of M_W 7. The model is generated using equation 20. The shading represents the 1σ confidence intervals. The solid line represents the best-fit model. Bottom: Model residuals (log). The dotted red line represents the fit of equation 23 to the logarithm of the residuals. A version of this plot showing the 95% confidence intervals is shown in the appendix (Figure 62).

It is reasonable to expect some association between the maximum distance from the fault at which ruptures are observed and earthquake magnitude, but no such relation can be derived from our study. The maximum distance observable is currently limited by the footprint available to map. Similarly, while the rupture tips tend to have more distributed ruptures extending away from them, the currently incomplete azimuthal coverage of ruptures precludes determining whether a higher frequency and extent of distributed ruptures at fault tips stem from a mapping bias or a physical feature (e.g. resulting from rupture directivity effects). Long-range azimuthal coverage for future events should enable assessing the potential effect of magnitude on the maximum distance from the fault at which we observe ruptures, as well as diversity in

azimuthal behavior.

The magnitude dependence in the models for individual events and for our general model is captured in parameter β, the expected average displacement measured at the primary fault. This parameter separates the Ridgecrest foreshock from the other events distinctly. For the other, M_W 7.1 to 7.3 events, the average displacements reflect variability that exceeds the expected differences as a function of magnitude within this narrow magnitude range, making the events indistinguishable from each other. An important implicit assumption in our model is that the event assessed has an observable surface rupture. The likelihood of an event having a surface rupture, which we do not account for, depends on event magnitude (e.g. Wells and Coppersmith, 1993), and is accounted for in models that consider hazard for a fault over multiple events (e.g., Petersen et al., 2011). Because our models are built to consider single events, we do not include a rate parameter that accounts for the frequency distribution of large events on a fault or its slip rate (e.g., Petersen et al., 2011). Note that our model produces higher probabilities of observing a rupture (Equation 14) than previous models accounting for distributed ruptures (Petersen et al., 2011). These differences largely stem from the use of different input data.

Sources of uncertainty

Proper identification of the principal rupture trace is fundamental for the appropriate application of our model. The assumption of $S_0 << S_{max}$ in this model, required to obtain the expression in equation 19, underscores that our model is not appropriate to deduce the probability of large slip on a distributed rupture. This is a minor limitation in the sense that, a second rupture hosting a large slip is likely to be identified as an additional principal fault trace. Examples of this kind of categorization exist for the Ridgecrest mainshock and the El Mayor-Cucapah events (see figure 53 in the appendix), where multiple, parallel ruptures are classified as principal fault traces. Note that our model is not conditioned on prior knowledge of whether a fault exists or not (i.e., the model does not account for a site-specific understanding of the presence or absence, and age, of minor faults or shears).

Even when the principal rupture trace has been properly localized, there remains a small knee in the curve of $P(S > S_0)$ in the very near-fault region, inherited from parameter x_{fr} in the expression that describes the distribution of rupture density (equation 14). Parameter x_{fr} captures the uncertainty in the location of this primary rupture trace and is on the order of a few meters for the events with high-resolution maps we use in this study. The uncertainty in the fault location is an important parameter to consider in fault hazard assessments (e.g., Chen and Petersen, 2019; Scott et al., 2023). We expect that the uncertainty in the principal fault trace location for faults without recent surface ruptures should be, at a minimum, comparable to the values of x_{fr} deduced from these datasets. Thus, we consider x_{fr} a useful parameter to incorporate

into our model, as it results in a more conservative, wider zone of, high $P(S > S_0)$ near the fault. More conservative approaches to the error in the fault trace are given in Petersen et al. (2011) and Scott et al. (2023).

The Landers, Hector Mine, Ridgecrest, and El Mayor-Cucapah earthquakes show similar rupture distributions. The slopes (γ) or scaling exponents of rupture density that yield the probability of finding a rupture at a given distance from the fault overlap within error (Figure 47), though the exponents for the Ridgecrest foreshock and mainshock are comparatively lower than those for the other events. We suspect the gentler slope of the Ridgecrest events partly results from the inclusion of far-field features mapped as simplified lines based on geodetic observations, and from the more thorough far-field coverage during the field mapping. The variation of rupture densities at distances beyond 3 kilometers away from the main rupture likely results from variable mapping extent (e.g. far-field coverage is not complete for each event). Incomplete far field map coverage is accounted for in our uncertainties and reflected in the increase in uncertainty in our model with fault-perpendicular distance seen in Figure 52.

An important consideration regarding our model uncertainties is that the posterior distributions shown in Figures 47 and 48 only represent how well the models (equations 14 and 15) fit the spatial distributions of rupture density and average displacement. These distributions omit the epistemic uncertainty carried by these rupture maps and displacement measurements, which is associated with variability in mapping completeness throughout, as well as in individual mapper decisions when deciding where to place ruptures. The displacement distributions are also affected by the individual location errors for each displacement measurement. We expect larger location errors in the displacement measurements from the Landers and Hector Mine events, which predate the relaxation of selective availability for GPS locations.

Recommendations for future data collection

The epistemic uncertainties in these models could be largely mitigated through the data collection process in future surface-rupturing earthquakes. In the case of the rupture distributions, even coverage of the area surrounding the fault should largely reduce the far-field variability in the distributions and help establish whether a relationship between the location of the furthest rupture observed is magnitude-dependent. For the displacements, more careful documentation of the complete displacement range within the fault zone, without bias toward larger displacements, is necessary. This could be achieved through even sampling of displacement measurements along the principal rupture zones. In addition, careful documentation of the direction of displacement and separation of horizontal and vertical components would enable an expansion of this model to include displacement direction, an important component of assessing rupture hazard to engineered structures.

The characteristics of the events considered in this study make our model suitable for application to other faults in immature fault zones (<25 km of cumulative displacement) where large amounts of distributed deformation are expected, and in landscapes dominated by extensive sediment cover. Our framework may not be appropriate for more mature fault zones with a higher degree of strain localization (Dolan and Haravitch, 2014). Because the bulk of the surface ruptures we analyze occurred in sediment, the application of this model for events predominantly in bedrock remains to be tested. Last, events with substantial blind faulting may cause largely different distributed deformation patterns at the surface (e.g. Koehler et al., (2021), where a continuous, primary rupture trace cannot be defined, a requirement for the model proposed here.

Preliminary model implementation recommendations

In this contribution, we present a framework for how a distributed displacement model may approach the problems of distributed rupture density and displacement exceedance along strike-slip faults. In this section, we provide a set of preliminary guidelines to inform how practitioners and other users should consider the implementation of this framework to sample sites. This is a very general approach that does not take into account the peculiarities of specific structures (e.g. Valentini et al., 2021), only considering the dimensions and orientation of the site.

From a hazard assessment perspective, we are interested in any scenario that includes at least one rupture hosting a displacement exceeding a threshold S_0 within the dimensions (A) of the site. The probability of this event is given by:

$$P_{site}(x, M_W, A) = 1 - \prod_{A} P(S < S_0 | x, M_W, \delta a) \tag{24}$$

For simplicity, equation 24 assumes that the solutions for $P(S < S_0)$ are independent of each other for each area δa ($1m^2$ throughout this study). This is an assumption we made for the ruptures and the displacements in the rupture-perpendicular direction when fitting their spatial distributions. We now make this assumption in the rupture-parallel direction as well. Consulting projects will often involve sites with footprints in the 50-200 m^2 range. We apply equation 24 to the simple case of a 1 by 50 m long site parallel to a fault, located at 10 m from it in the fault-orthogonal direction. For this site, $P_{site}(x, M_W, A) = 0.39$, for a M_W 7 event and a displacement threshold S_0=0.1 m. Sites with dimensions exceeding 1 m in the fault-perpendicular direction may require accounting for the dependence of $P(S > S_0)$ on x, especially in the very near field of the fault.

Conclusions

Using detailed rupture maps from the Ridgecrest, Landers, Hector Mine, and El Mayor-Cucapah earthquakes in southern California and northern Mexico, we develop a framework for PFDHA that estimates the probability per unit area of finding a rupture with a displacement exceeding a threshold S_0, located at a given distance away from a principal fault trace. This model may be best applied to assess rupture hazard for a site in the near-field region (<3 km) of immature strike-slip faults (<25 km of cumulative displacement) where widespread distributed fault ruptures are expected, such as in the Eastern California Shear Zone or the Walker Lake Belt of the western United States.

References

1. Baize, S., Amoroso, S., Belić, N., Benedetti, L., Boncio, P., Budić, M., ... & Ricci, T. (2022). Environmental effects and seismogenic source characterization of the December 2020 earthquake sequence near Petrinja, Croatia. Geophysical Journal International, 230(2), 1394-1418.

2. Chen, T., Akciz, S. O., Hudnut, K. W., Zhang, D. Z., & Stock, J. M. (2015). Fault-Slip Distribution of the 1999 M w 7.1 Hector Mine Earthquake, California, Estimated from Postearthquake Airborne LiDAR Data. Bulletin of the Seismological Society of America, 105(2A), 776-790.

3. Chen, R., & Petersen, M. D. (2019). Improved implementation of rupture location uncertainty in fault displacement hazard assessment. Bulletin of the Seismological Society of America, 109(5), 2132-2137.

4. R. Civico, S. Pucci, F. Villani, L. Pizzimenti, P. M. De Martini, R. Nappi & the Open EMERGEO Working Group (2018) Surface ruptures following the 30 October 2016 Mw 6.5 Norcia earthquake, central Italy, Journal of Maps, 14:2, 151-160, DOI: 10.1080/17445647.2018.1441756

5. Dolan, J. F., & Haravitch, B. D. (2014). How well do surface slip measurements track slip at depth in large strike-slip earthquakes? The importance of fault structural maturity in controlling on-fault slip versus off-fault surface deformation. Earth and Planetary Science Letters, 388, 38-47.

6. DuRoss, C. B., Gold, R. D., Dawson, T. E., Scharer, K. M., Kendrick, K. J., Akciz, S. O., ... & Zinke, R. (2020). Surface displacement distributions for the July 2019 Ridgecrest, California, earthquake ruptures. Bulletin of the Seismological Society of America, 110(4), 1400-1418.

7. Fletcher, J. M., Teran, O. J., Rockwell, T. K., Oskin, M. E., Hudnut, K. W., Mueller, K. J., ... & González-García, J. (2014). Assembly of a large earthquake from a complex fault system: Surface

rupture kinematics of the 4 April 2010 El Mayor–Cucapah (Mexico) Mw 7.2 earthquake. Geosphere, 10(4), 797-827.

8. Hudnut, K. W., Borsa, A., Glennie, C., & Minster, J. B. (2002). High-resolution topography along surface rupture of the 16 October 1999 Hector Mine, California, earthquake (M w 7.1) from airborne laser swath mapping. Bulletin of the Seismological Society of America, 92(4), 1570-1576.

9. Hudnut, K. W., Brooks, B. A., Scharer, K., Hernandez, J. L., Dawson, T. E., Oskin, M. E., ... & Sorhus, S. (2020). Airborne lidar and electro-optical imagery along surface ruptures of the 2019 Ridgecrest earthquake sequence, southern California. Seismological Research Letters, 91(4), 2096-2107.

10. Koehler, R. D., Dee, S., Elliott, A., Hatem, A., Pickering, A., Pierce, I., & Seitz, G. (2021). Field response and surface-rupture characteristics of the 2020 M 6.5 Monte Cristo range earthquake, Central Walker Lane, Nevada. Seismological Research Letters, 92(2A), 823-839.

11. Lazarte, C. A., Bray, J. D., Johnson, A. M., & Lemmer, R. E. (1994). Surface breakage of the 1992 Landers earthquake and its effects on structures. Bulletin of the Seismological Society of America, 84(3), 547-561.

12. Mattioli, G. S., Phillips, D. A., Hodgkinson, K. M., Walls, C., Mencin, D. J., Bartel, B. A., ... & Zaino, A. (2020). The GAGE data and field response to the 2019 Ridgecrest earthquake sequence. Seismological Research Letters, 91(4), 2075-2086.

13. Milliner, C. W., Dolan, J. F., Hollingsworth, J., Leprince, S., Ayoub, F., & Sammis, C. G. (2015). Quantifying near-field and off-fault deformation patterns of the 1992 Mw 7.3 Landers earthquake. Geochemistry, Geophysics, Geosystems, 16(5), 1577-1598.

14. Milliner, C. W. D., Dolan, J. F., Hollingsworth, J., Leprince, S., & Ayoub, F. (2016). Comparison of coseismic near-field and off-fault surface deformation patterns of the 1992 Mw 7.3 Landers and 1999 Mw 7.1 Hector Mine earthquakes: Implications for controls on the distribution of surface strain. Geophysical Research Letters, 43(19), 10-115.

15. Milliner, C., & Donnellan, A. (2020). Using daily observations from Planet Labs satellite imagery to separate the surface deformation between the 4 July Mw 6.4 foreshock and 5 July Mw 7.1 mainshock during the 2019 Ridgecrest earthquake sequence. Seismological Research Letters, 91(4), 1986-1997.

16. Moss, R. E. S., & Ross, Z. E. (2011). Probabilistic fault displacement hazard analysis for reverse faults. Bulletin of the Seismological Society of America, 101(4), 1542-1553.

17. Nurminen, F., Boncio, P., Visini, F., Pace, B., Valentini, A., Baize, S., & Scotti, O. (2020). Probability of occurrence and displacement regression of distributed surface rupturing for reverse earthquakes. Frontiers in Earth Science, 8, 581605.

18. Petersen, M. D., Dawson, T. E., Chen, R., Cao, T., Wills, C. J., Schwartz, D. P., & Frankel, A. D. (2011). Fault displacement hazard for strike-slip faults. Bulletin of the Seismological Society of America, 101(2), 805-825.

19. Ponti, D. J., Blair, J. L., Rosa, C. M., Thomas, K., Pickering, A. J., Akciz, S., ... & Zinke, R. (2020). Documentation of surface fault rupture and ground-deformation features produced by the 4 and 5 July 2019 Mw 6.4 and Mw 7.1 Ridgecrest earthquake sequence. Seismological Research Letters, 91(5), 2942-2959.

20. Rodriguez Padilla, A. M., Quintana, M. A., Prado, R. M., Aguilar, B. J., Shea, T. A., Oskin, M. E., & Garcia, L. (2022a). Near-Field High-Resolution Maps of the Ridgecrest Earthquakes from Aerial Imagery. Seismological Society of America, 93(1), 494-499.

21. Rodriguez Padilla, A. M., Oskin, M. E., Milliner, C. W., & Plesch, A. (2022b). Accrual of widespread rock damage from the 2019 Ridgecrest earthquakes. Nature Geoscience, 15(3), 222-226.

22. Sarmiento, A., Madugo, D., Bozorgnia, Y., Shen, A., Mazzoni, S., Lavrentiadis, G., Dawson, T., Madugo, C., Kottke, A., Thompson, S., Baize, S., Milliner, C., Nurminen, F., Boncio, P., and Visini, F. (2021). Fault Displacement Hazard Initiative Database, UCLA B. John Garrick Institute for the Risk Sciences, Report GIRS-2021-08, doi: 10.34948/N36P48.

23. Scott, C., Adam, R., Arrowsmith, R., Madugo, C., Powell, J., Ford, J., ... & Ingersoll, S. (2023). Evaluating how well active fault mapping predicts earthquake surface-rupture locations. Geosphere.

24. Sieh, K., Jones, L., Hauksson, E., Hudnut, K., Eberhart-Phillips, D., Heaton, T., ... & Zachariasen, J. (1993). Near-field investigations of the Landers earthquake sequence, April to July 1992. Science, 260(5105), 171-176.

25. Takao, M., J. Tsuchiyama, T. Annaka, and T. Kurita (2013). Application of probabilistic fault displacement hazard analysis in Japan, J. Jpn. Assoc. Earthq. Eng. 13, 17–36, doi: 10.5610/jaee.13.17.

26. Teran, O. J., Fletcher, J. M., Oskin, M. E., Rockwell, T. K., Hudnut, K. W., Spelz, R. M., ... & Morelan, A. E. (2015). Geologic and structural controls on rupture zone fabric: A field-based study of the 2010 Mw 7.2 El Mayor–Cucapah earthquake surface rupture. Geosphere, 11(3), 899-920.

27. Treiman, J. A., Kendrick, K. J., Bryant, W. A., Rockwell, T. K., & McGill, S. F. (2002). Primary surface rupture associated with the M w 7.1 16 October 1999 Hector mine earthquake, San Bernardino County, California. Bulletin of the Seismological Society of America, 92(4), 1171-1191.

28. Valentini, A., Fukushima, Y., Contri, P., Ono, M., Sakai, T., Thompson, S. C., ... & Youngs, R. R. (2021). Probabilistic fault displacement hazard assessment (PFDHA) for nuclear installations according to IAEA safety standards. Bulletin of the Seismological Society of America, 111(5), 2661-2672.

29. Wang, Y., & Goulet, C. (2021). Validation of fault displacements from dynamic rupture simulations against the observations from the 1992 landers earthquake. Bulletin of the Seismological Society of America, 111(5), 2574-2594.

30. Wells, D. L., & Coppersmith, K. J. (1993). Likelihood of surface rupture as a function of magnitude. Seismological Research Letters, 64(1), 54.

31. Wells, D. L., & Coppersmith, K. J. (1994). New empirical relationships among magnitude, rupture length, rupture width, rupture area, and surface displacement. Bulletin of the seismological Society of America, 84(4), 974-1002.

32. Xu, X., Sandwell, D. T., & Smith-Konter, B. (2020). Coseismic displacements and surface ruptures from Sentinel-1 InSAR: 2019 Ridgecrest earthquakes. Seismological Research Letters, 91(4), 1979-1985.

33. Youngs, R. R., Arabasz, W. J., Anderson, R. E., Ramelli, A. R., Ake, J. P., Slemmons, D. B., ... & Toro, G. R. (2003). A methodology for probabilistic fault displacement hazard analysis (PFDHA). Earthquake spectra, 19(1), 191-219.

Appendix

Supplementary figures

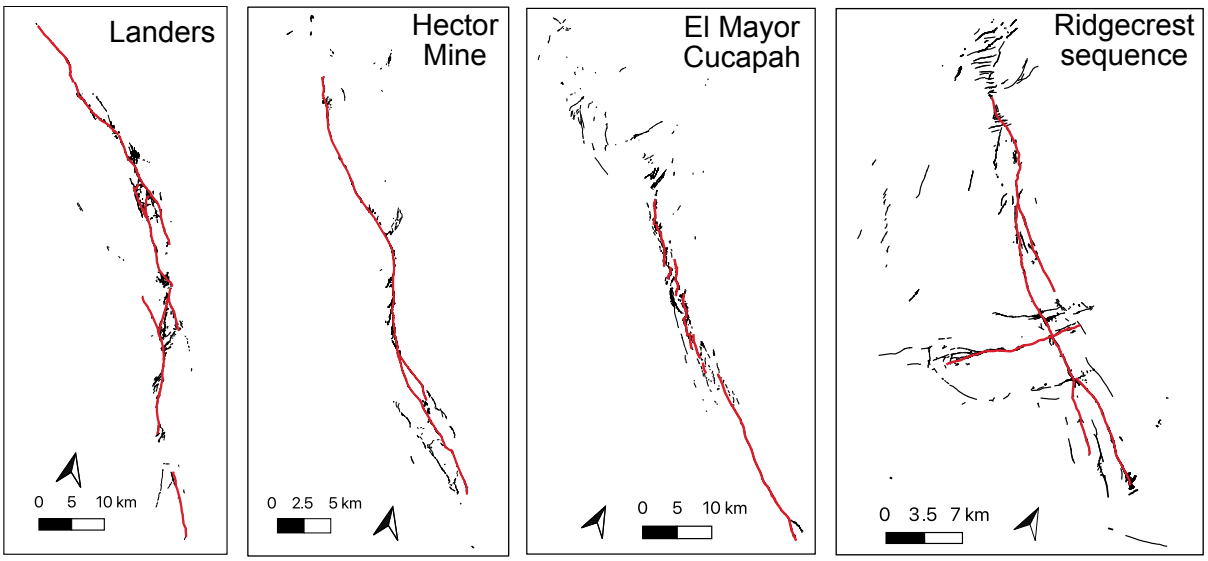

Figure 53: Distributed ruptures (black) and simplified principal rupture trace (red) for each event considered in this study.

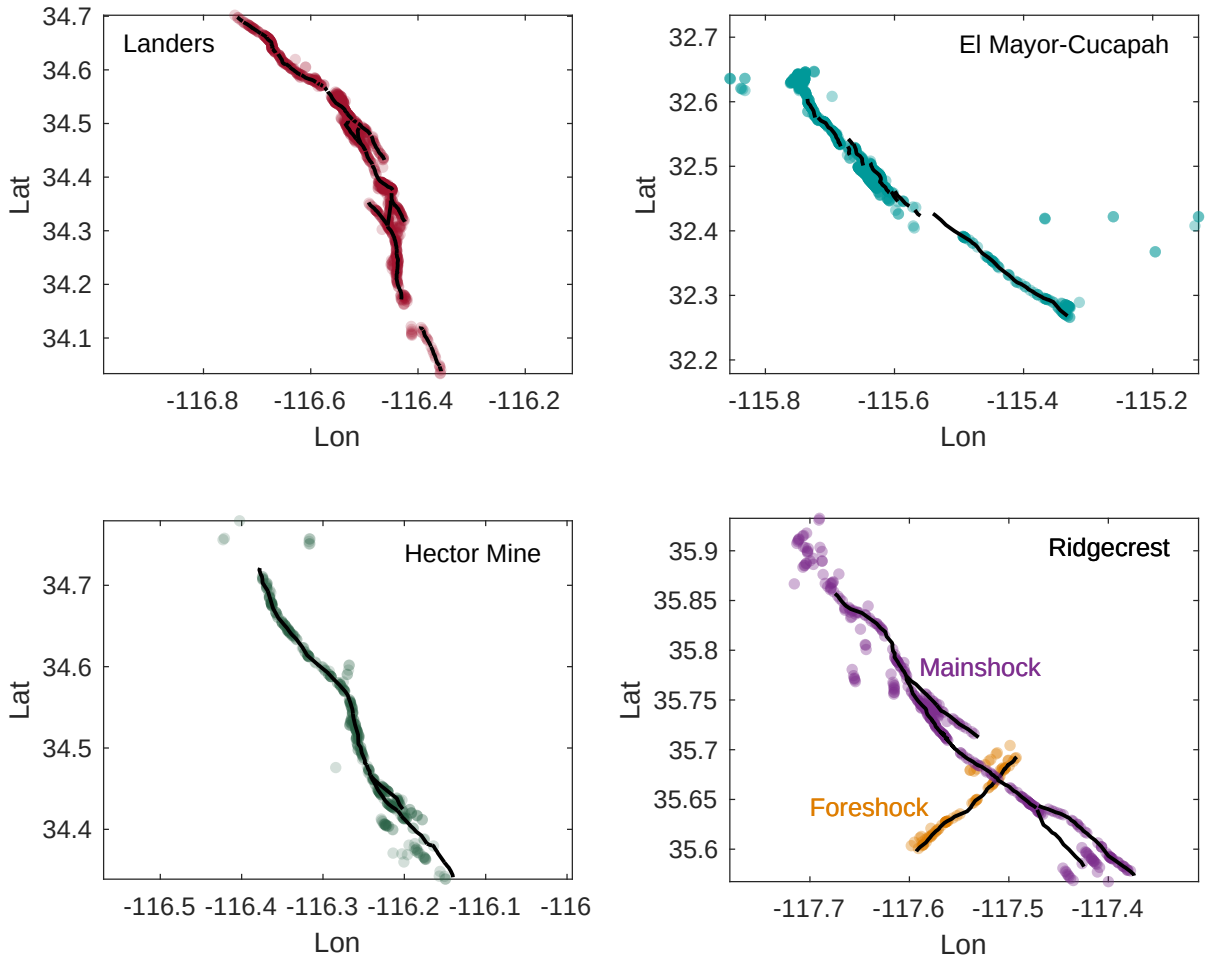

Figure 54: Displacement data from the Landers (red), Hector Mine (green), El Mayor-Cucapah (teal), and Ridgecrest earthquakes (foreshock in orange and mainshock in purple) plotted over the principal rupture trace of each event. The displacement data is sourced from the Fault Displacement Hazard Initiative database (Sarmiento et al., 2021) and we only consider measurements collected in the field. The principal rupture traces are roughly simplified from the ruptures classified as primary in the FDHI database (see figure 53) in the appendix.

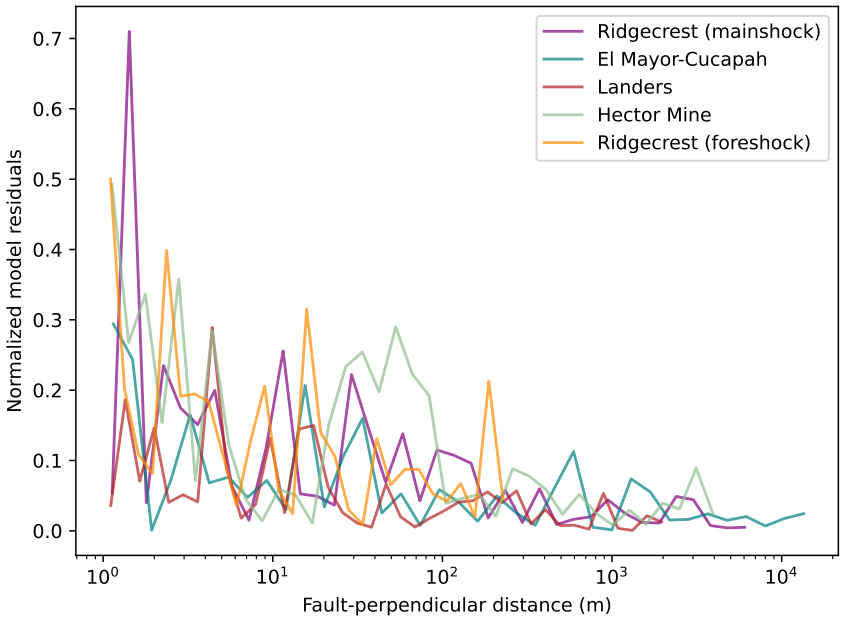

Figure 55: Model residuals from the best fits of equation 15 to the field displacement data in the FDHI database for each event (Figure 48). The residuals are normalized by the value of β for each event to account for the magnitude-dependence of displacement.

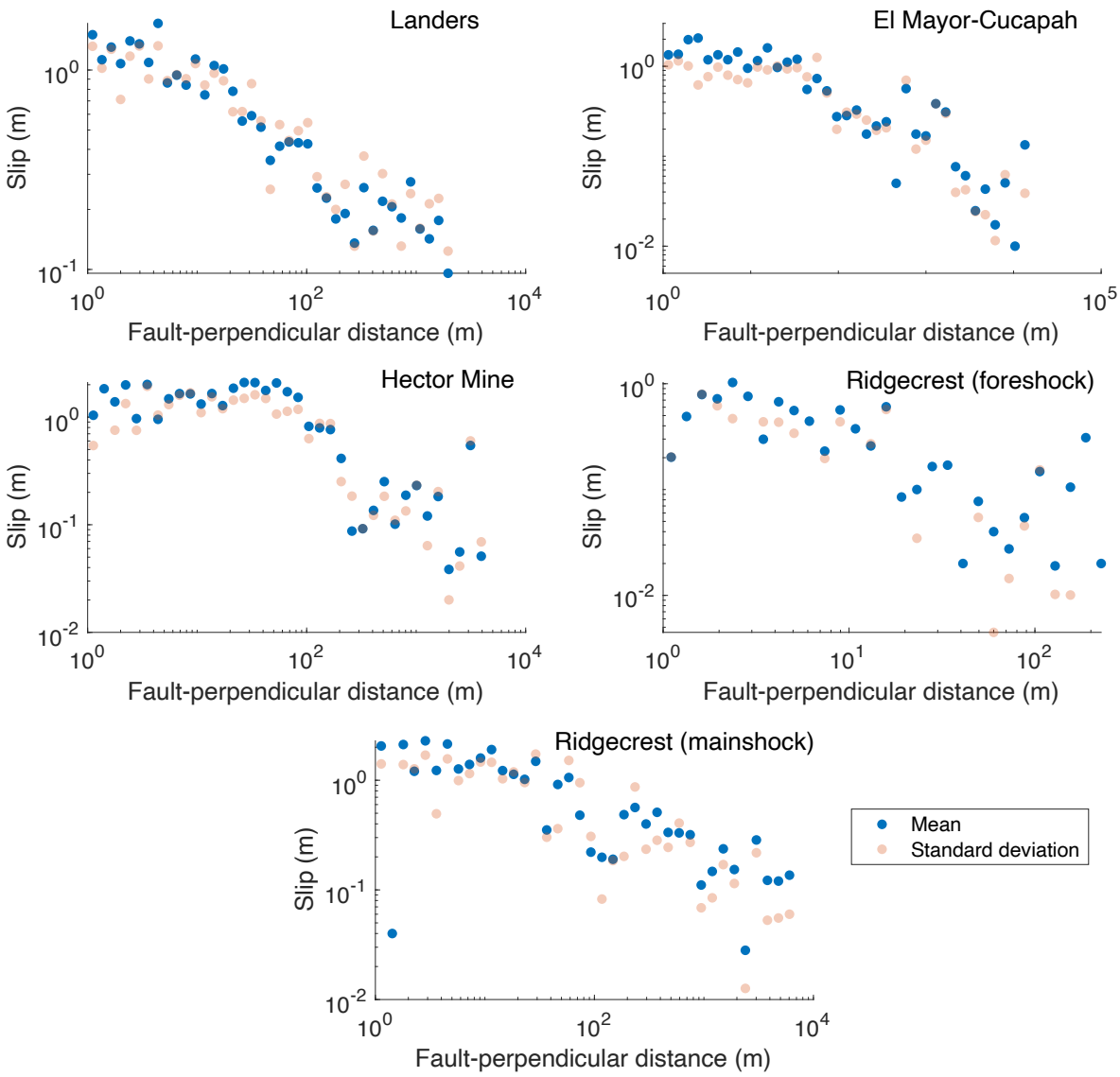

Figure 56: Mean (blue) and standard deviation (pink) of slip with fault-perpendicular distance for the Landers, Hector Mine, El Mayor-Cucapah, and Ridgecrest earthquakes. The consistent correlation of the mean and the standard deviation suggests the displacements are exponentially distributed within each distance bin.

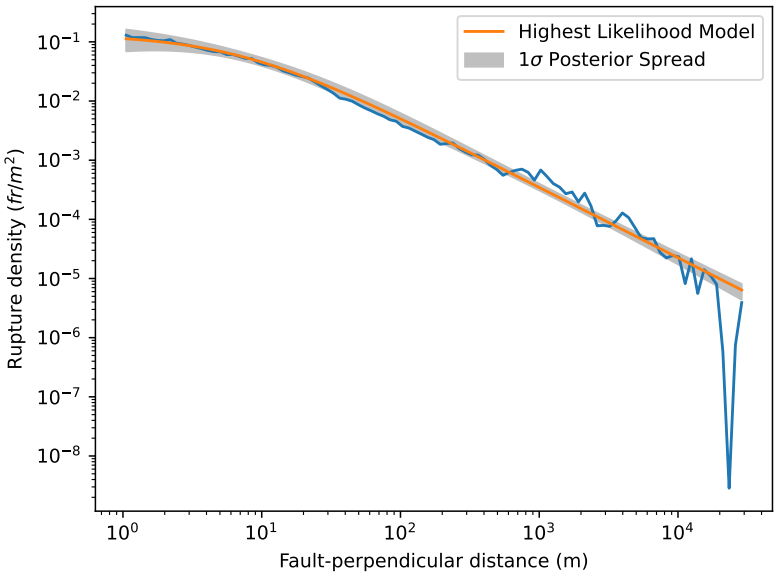

Figure 57: General model for the decay of rupture density with fault-perpendicular distance generated from combining the distributed rupture maps from the Landers, Hector Mine, El Mayor-Cucapah, and Ridgecrest earthquakes.

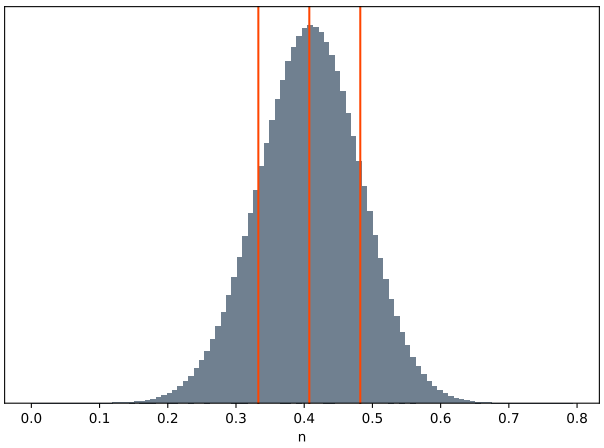

Figure 58: Concatenated posteriors for n in equations 15 and 20 from the Landers, Ridgecrest mainshock, and El Mayor-Cucapah event. Note that n is roughly normally distributed. The vertical red lines indicate the mean and data within one standard deviation of the mean.

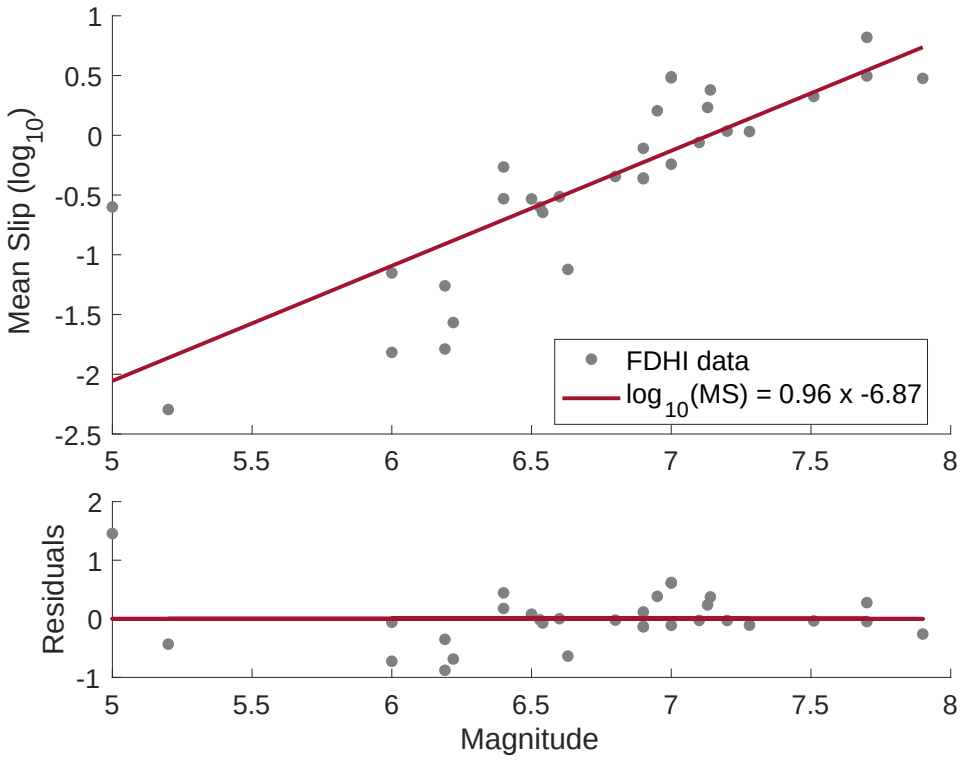

Figure 59: Top: Scaling of mean slip in meters with event magnitude for the strike-slip events in the FDHI database (Sarmiento et al., 2021). The best fit to the data using a least-squares approach is shown in the solid maroon line. Bottom: Model residuals.

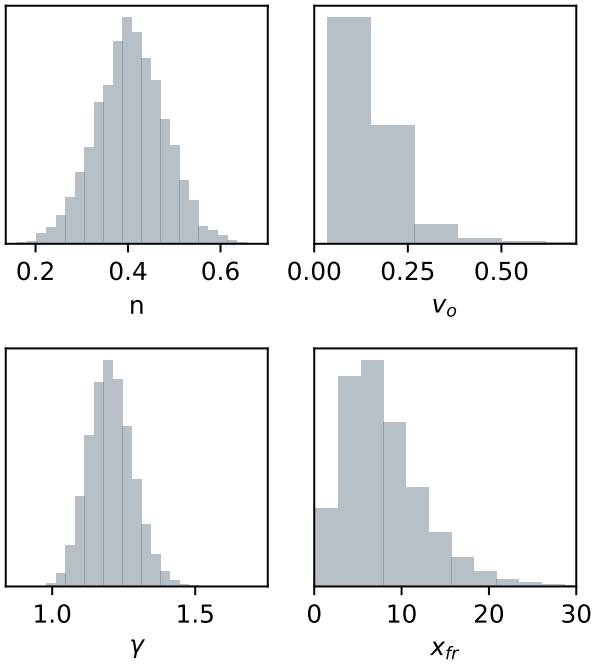

Figure 60: Distribution of parameters from equation 20. ν_o, x_{fr}, and γ are sampled from the posterior distributions of the fits in supplementary figure 57. n is sampled from a normal distribution where the mean and standard deviation of are calculated from the posterior distributions of the events well described by the displacement model in equation 15 (figure 58.)

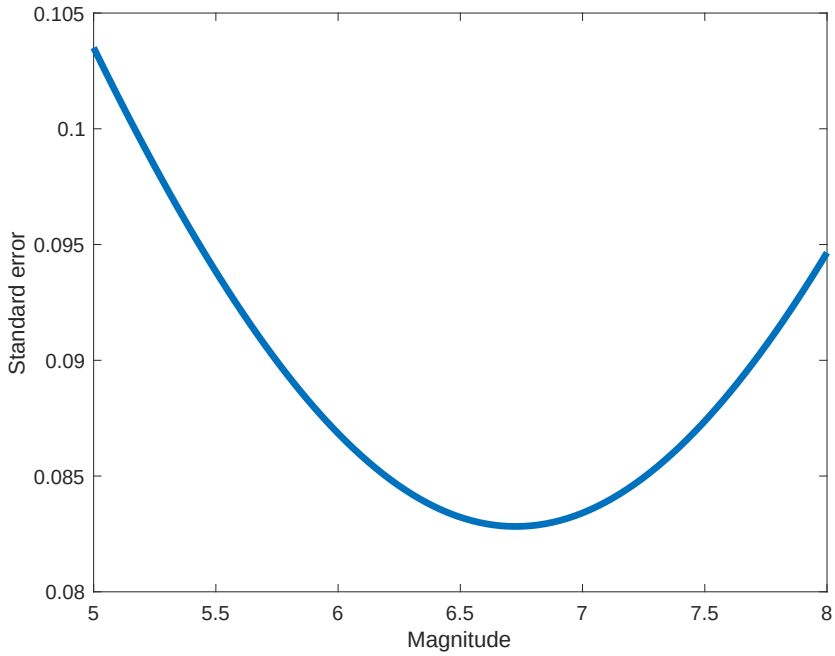

Figure 61: Standard error as a function of magnitude for the general model based on the standard error of the regression in figure 59.

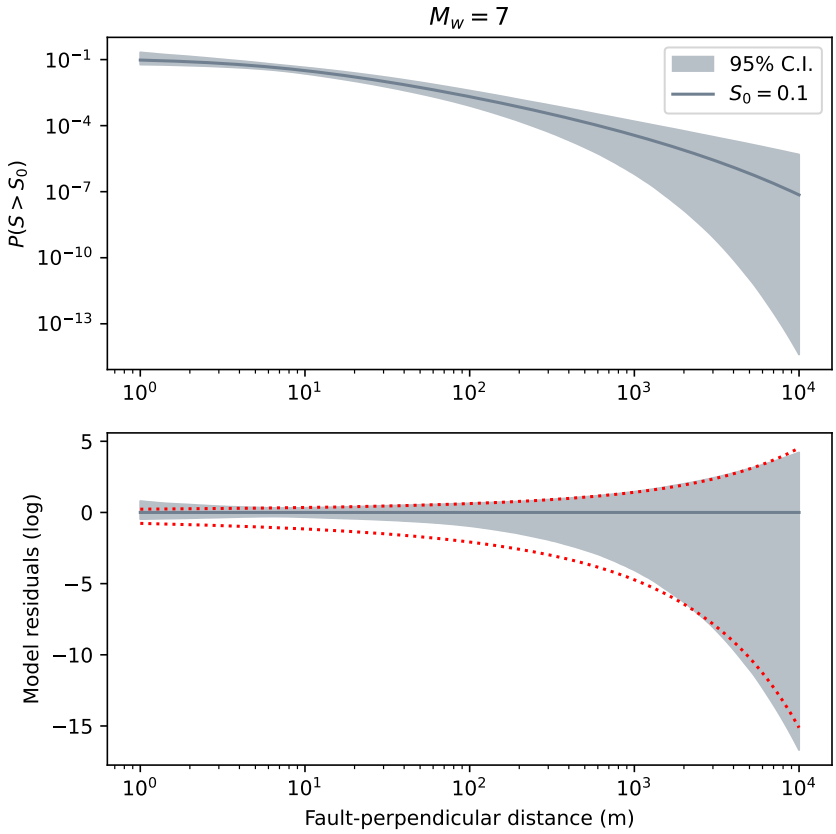

Figure 62: Top: PFDHA model expressing the probability of finding a rupture hosting a displacement that exceeds threshold $S_0 = 0.1$ m for a surface-rupturing strike-slip earthquake of M_W 7. The model is generated using equation 20. The shading represents the 95% confidence intervals. The solid line represents the best-fit model. Bottom: Model residuals. The dotted red line represents the fit of equation 23 logarithm of the residuals.

Supplementary methods

We build on the method in Rodriguez Padilla et al. (2022b) to estimate the decay of rupture density with fault-perpendicular distance for each event. We begin by discretizing every rupture into 1 m spaced points, to minimize the effect of mapper bias in rupture continuity. Next, we measure the distance between each point and the nearest point on the main rupture. The principal rupture is simplified for each event from the cracks defined as primary in the FDHI rupture database (supplementary figure 53). We then log bin the distances into 100 bins, from 0 to the furthest rupture from the main rupture, and count the number of rupture segments per bin. Last, we normalize each bin by its size, and the entire decay by the total length of the principal fault. This produces the decays shown in Figure 47.

We fit each decay with an affine-invariant ensemble sampler for Markov Chain Monte Carlo (Goodman and Weare, 2010; Foreman-Mackay et al., 2013) to estimate the maximum likelihood parameters for equation

14. As priors, we use uniformly distributed values of ν_o= (0,3), x_{fr}= (0, 100) meters, and γ = (0, 3). We assume that the error of $\nu(x)$ in each bin is Poisson-distributed, following the method of Powers and Jordan (2010). We employ an ensemble of 200 walkers, which run for 100,000 iterations, following a 10,000-iteration burn-in period.

We follow a similar approach to estimate the decay of average displacement with fault-perpendicular distance. We take the displacements from the FDHI database for each event and measure their distance to the principal rupture trace (supplementary figure 53). We then log-bin the distances into 40 bins, from 0 to the furthest rupture from the main rupture, and calculate the average displacement per bin. Note we use a smaller number of bins for the displacement data than the rupture locations (Figure 46) because of the smaller number of displacement measurements (Figure 54 in the appendix). This binning produces the decays shown in Figure 48. We fit each decay with an affine-invariant ensemble sampler for Markov Chain Monte Carlo (Goodman and Weare, 2010; Foreman-Mackay et al., 2013) to estimate the maximum likelihood parameters for equation 15. As priors, we use uniformly distributed values of β= (0,15) meters and n=(0,3). We employ an ensemble of 200 walkers, which run for 100,000 iterations, following a 10,000-iteration burn-in period. Note that we fix $x_S = 1$ meter in equation 15 because this provides a better model fit than letting x_S be a free parameter that is fit with the ensemble sampler for Markov Chain Monte Carlo and contributes to reducing uncertainty in the model fits. We also tested values of $x_S = 10$ meters, with worse residuals, thus the choice of $x_S = 1$ meter.

Supplementary references

1. Foreman-Mackey, D., Hogg, D. W., Lang, D., & Goodman, J. (2013). emcee: the MCMC hammer. Publications of the Astronomical Society of the Pacific, 125(925), 306.

2. Goodman, J., & Weare, J. (2010). Ensemble samplers with affine invariance. Communications in applied mathematics and computational science, 5(1), 65-80.

3. Powers, P. M., & Jordan, T. H. (2010). Distribution of seismicity across strike-slip faults in California. Journal of Geophysical Research: Solid Earth, 115(B5).

Chapter 5: Distributed yielding over multiple earthquake cycles

Abstract

High-resolution geodesy illuminates zones of subtle but long-wavelength warping extending 100 m to 3 km from faults where the coseismic bending strains approach the yield limit of rock without clearly exceeding it. This observation raises the question of whether folding accounts for widespread yielding in the upper crust. We use lidar data to measure coseismic and cumulative folding from five locales in western North America, supplemented by field observations at one location. Our lidar observations link coseismic to cumulative deformation and show that folding amplitude accumulates over multiple slip cycles, scaling as the square root of fault throw. The distribution of folding strains is well described by the decay of elastic stress surrounding a crack tip, though the strains exceed the elastic limit of rock by over an order of magnitude. Our field observations suggest that pre-existing fabrics in the rock mass help accommodate the large folding strains while maintaining the elastically created shape. Our lidar and field observations can be explained by a simple model where the rock mass deforms linearly with stress, though the shear modulus that defines the rate of change in deformation decreases once the yield stress of rock is exceeded, and continues to do so over successive earthquake cycles.

High-resolution observations of folding

The extent and timescales over which permanent deformation occurs in the shallow crust influences how much energy is available to generate ground shaking during future damaging earthquakes (e.g. Okubo et al., 2019). High-resolution geodesy reveals subtle coseismic folding extending hundreds of meters to kilometers from the primary fault (Oskin et al., 2012; Antoine et al., 2021; Milliner et al., 2023)(Figure 63). Near the fault, folding strains exceed the elastic limit of rock by over an order of magnitude (Oskin et al., 2012). Whether folding at larger distances is an elastic deformation feature or represents widespread distributed yielding in the bulk is hard to quantify from observations from individual earthquakes, as the coseismic folding strains approach the elastic limit of rock without clearly exceeding it. To test whether coseismically observed folding is a permanent deformation feature, we use lidar data to search for a signal of widely distributed, finite bulk deformation accumulated around faults over multiple earthquake cycles.

Airborne laser altimetry (lidar) data enables measuring the subtle shape of the landscape resulting from uplift or subsidence in a continuous way as it decays with distance away from a fault. Attributing deformation to elevation changes requires a landscape with low erosion rates where the original, unfaulted configuration is simple and known, so that deviations in elevation may be attributed to tectonic deformation. Normal faults

cutting through homogeneous lithologies constitute ideal natural laboratories to measure such deformation from high-resolution altimetry: For a typical, steeply dipping (>60°) normal fault, displacement is principally vertical. In this study, we consider three sites that host fault arrays in the western United States and meet these characteristics: the Volcanic Tableland of Bishop (CA), the Lake City fault zone in the Modoc Plateau (CA), and the Needles District in Canyonlands National Park (UT). High-resolution altimetry is available for the three locales, where the host lithologies are uniform and tabular, and erosion rates are low (see geologic background in the appendix).

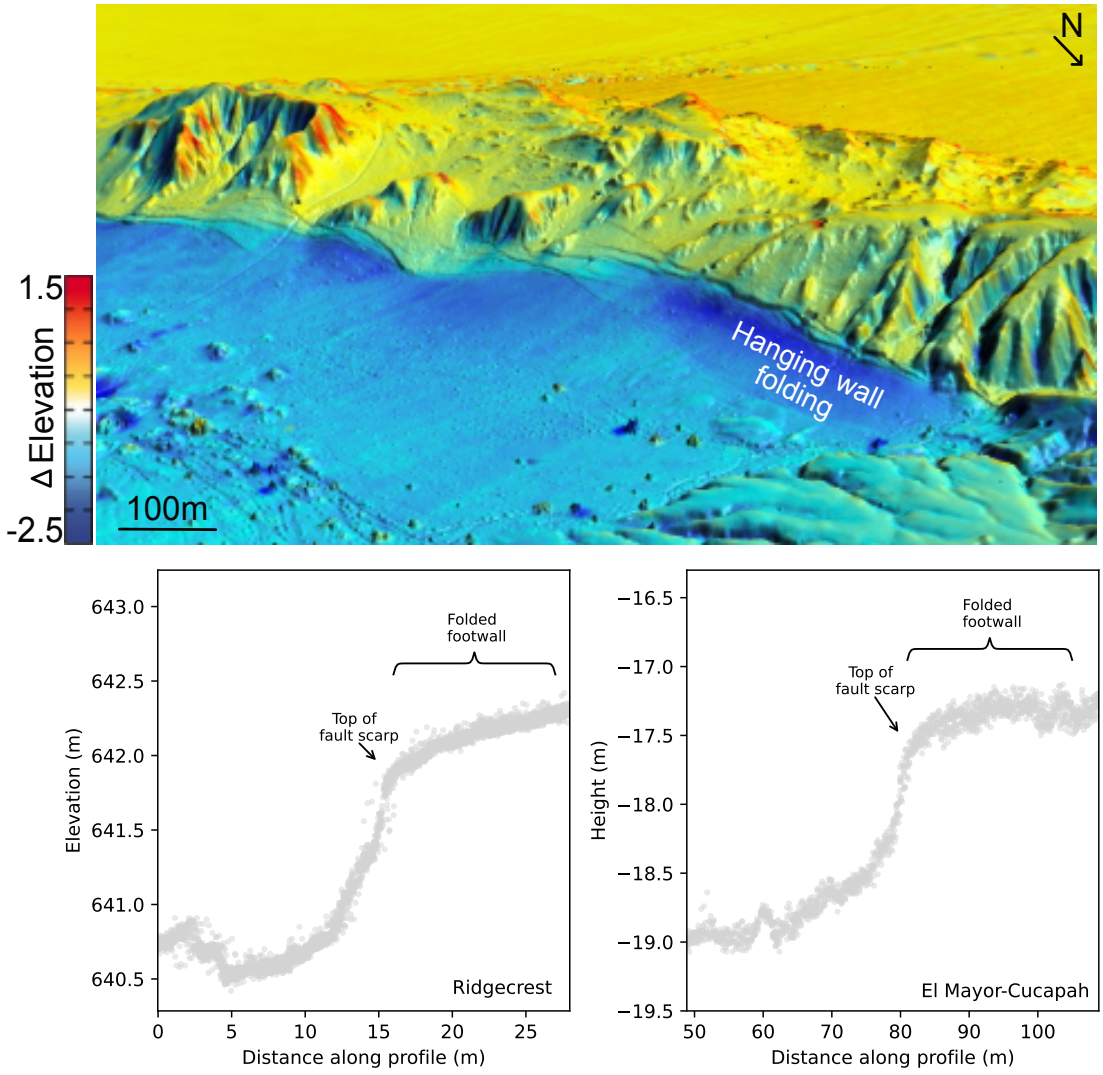

Figure 63: Top: Vertical displacements from topographic differencing plotted over post-earthquake topography of the 2010 El Mayor Cucapah earthquake (Oskin et al., 2012). The differencing highlights broad areas of deformation in the hanging wall of faults, one of them labeled in the plot as hanging wall folding. The distributed displacements extend beyond 100 meters from the fault. Bottom left: elevation profile through a scarp of the Paxton Ranch Fault from the Ridgecrest 2019 earthquakes, from the post-earthquake lidar point cloud. Bottom right: elevation profile through a scarp from the 2010 El Mayor Cucapah earthquake, from the post-earthquake lidar point cloud.

These study sites host active normal faults spanning throws under 1 meter to over 100 meters, and contrasting slip conditions. The faults in the Volcanic Tableland experience triggered slip when neighboring larger faults slip seismically (Lienkaemper et al., 1987; Pinter, 1995). Normal faults in the Modoc Plateau are seismogenic (Personious et al., 2009), whereas the faults in the Needles district slip aseismically due to dissolution and flow of underlying evaporites (Furuya et al., 2007; Kravitz et al., 2017). Using lidar data from each of these settings, we characterize fault throw and folding geometry to investigate the evolution of off-fault folding and its relationship to fault slip. We couple these observations of cumulative folding with coseismic folding measurements from post-earthquake lidar from the 2010 El Mayor Cucapah earthquake (Oskin et al., 2012) and the 2019 Ridgecrest earthquakes (Hudnut et al., 2020). We supplement our remote observations with field measurements from the Volcanic Tableland to quantify the distribution of folding strains, characterize some mechanisms responsible for accommodating widespread and continuous permanent deformation near faults, and investigate how the bulk rheology of the shallow crust evolves with cumulative number of earthquakes.

The geometry of off-fault folding

Deformation associated with normal faulting consists of a fault scarp that accommodates most of the displacement, and a surrounding deformation field dominated by folding of the hanging wall and the footwall. Scarp collapse obscures folding immediately adjacent to the fault, but erosion does not measurably affect folding beyond the scarp zone. To measure folding, we extract one meter-wide and up to several hundred-meter long fault-perpendicular swaths from the ground-classified lidar point cloud data. Using point-cloud data maximizes the data density available for measurement and avoids artefacts due to gridding. In some cases, we use the full, raw, unfiltered dataset to recover data lost due to classification errors. Because sedimentary basins tend to obscure folding in the hanging wall of normal faults, we conduct our measurements on folding of the footwalls.

We find that the distribution of elevations, and therefore the geometry of off-fault folding, is well described by a simple square-root relationship:

$$f(x) = c\sqrt{x} \tag{25}$$

Where c is the folding stretch factor, a pre-factor that describes the stretch of the function, and x is the distance from the top of the fault scarp, measured in meters (Figure 64, top left). Our approach to extracting the folding shape from the lidar point cloud and fitting this relationship is detailed in the supplementary methods section.

We fit over 250 folds at the three target locations using equation 25. Capturing the folding shape is limited by topographic noise and the distance to the nearest fault, as the deformation field of neighboring faults interact, which complicates describing subtle folds along small faults, and determining their extent or wavelength. Nevertheless, we find that, in the absence of large neighboring faults or other topographic obstacles, equation 25 typically describes the folding shape well >50 meters away from the top of the fault scarp (Figure 64, top left, Figure 69 in the appendix).

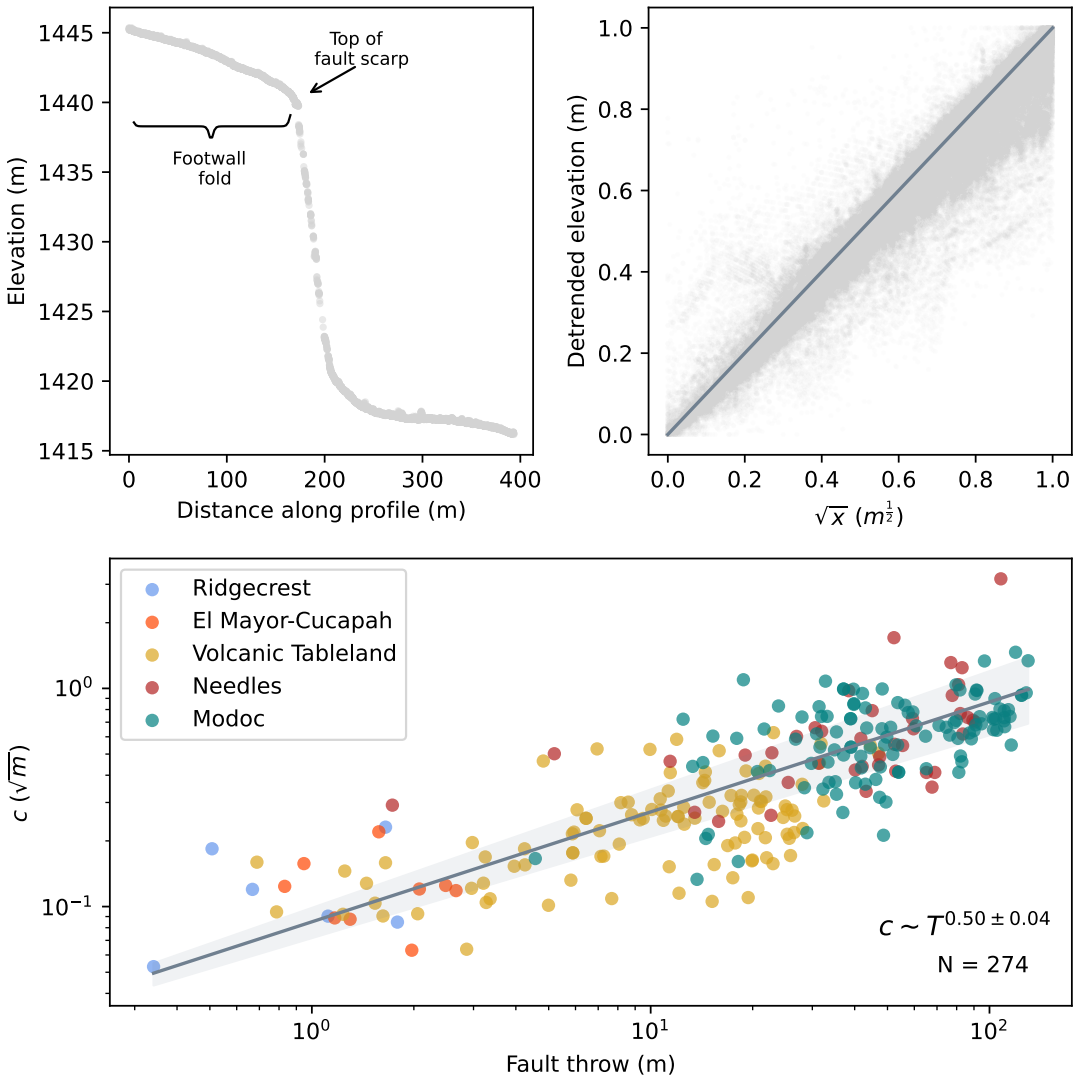

Figure 64: Top left: Elevation profile through a lidar point cloud swath of a fault in the Volcanic Tableland. The profile spans the footwall of the fault, the scarp, and the hanging wall. The end of the scarp and footwall fold are annotated. The hanging wall is also folded but may be partially buried. Top right: Normalized folding profiles through the footwalls of all faults considered in this study. The solid line shows the perfect fit of equation 25 to the elevation data. Bottom: Scaling of folding stretch factor c with fault throw. The grey shading shows the uncertainty in the power-law fit based on the standard errors of the intercept and the slope.

The largest faults considered in this study accommodate throws exceeding 100 meters. Reconstruction of the pre-faulted landscape, which is indispensable for our measurements of finite deformation, is typically not possible for major faults with throws that largely exceed those documented here. We observe that, as faults approach the largest throws we measure from our point clouds, especially in the Needles District, off-fault joints in the folded footwall begin to accumulate significant slip themselves, so that the fold becomes dissected by secondary faults with their own surrounding folding, and the distribution of footwall elevations is no longer well described by equation 25. The width of the scarp collapse zone also grows with fault throw, increasingly obscuring the zone of folding.

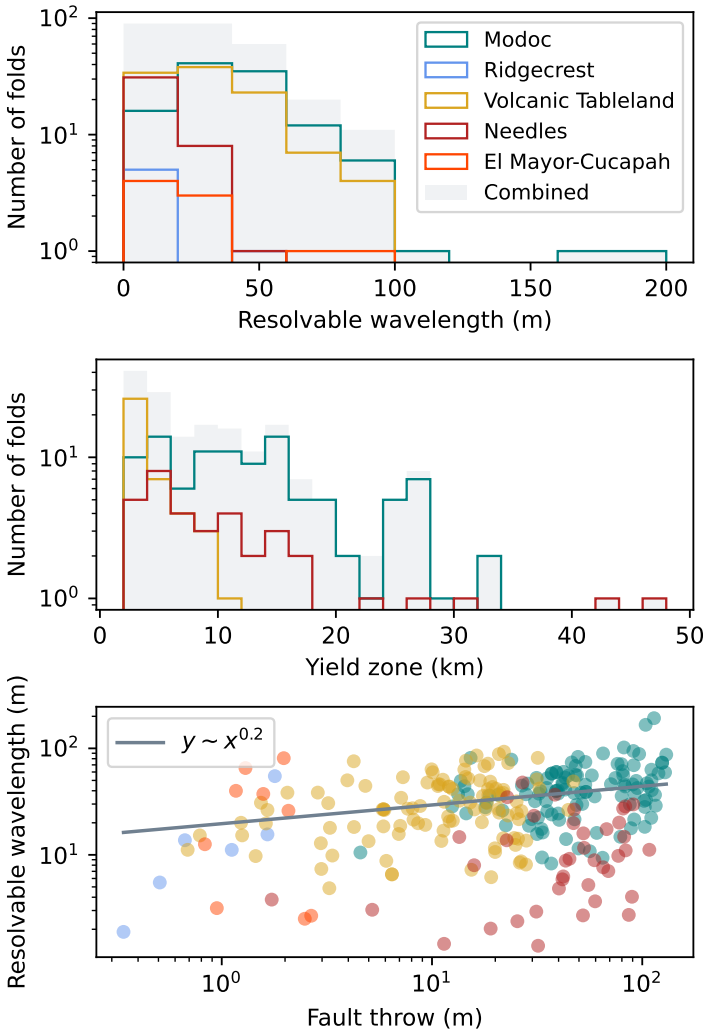

Figure 65: Top: Resolvable folding wavelengths measured. Middle: Predicted locations where folding shear strain will fall below the yield strain $3\text{x}10^{-3}$ (Michel and Avouac, 2006), given the measured value of c. Bottom: Scaling of resolvable wavelength with fault throw.

The lidar data captures an integrated history of the folding, but we can use fault throw as a proxy for

time, as faults accrue slip through incremental events so that throw is representative of the lifetime of a fault, given a slip rate (e.g. Cowie and Scholz, 1992). To consider the evolution of folding, we measure fault throw for all the faults along which we measured folding geometry, at the same location where folding geometry was estimated. Figure 64 shows folding stretch factor c versus fault throw for faults and cumulative folds in the Modoc Plateau, the Volcanic Tableland, and the Needles District. We supplement these cumulative folding measurements with 15 coseismic folding measurements collected along vertical scarps from the surface ruptures of the El Mayor Cucapah 2010 and Ridgecrest 2019 events. Our coseismic data is limited because we could only make folding measurements in sections where the ruptures captured by the post-earthquake lidar point clouds have sufficient vertical displacement and offset flat and simple landscapes.

We do not span a sufficiently large throw range or have enough data points to retrieve a robust relationship between throw and the folding stretch factor c for individual sites because of the large scatter in the relationship between the two variables (Figure 74 in the appendix). However, by combining the data from the five sites, we are able to observe a consistent scaling of c with fault throw. The scaling relationship fits both the coseismic and cumulative data well, suggesting that folding is accrued over time as faults accumulate throw. The scaling follows a power-law with exponent $\sim 0.50 \pm 0.04$ (standard error) suggesting more folding is accumulated in the earlier stages of faulting. This is consistent with the larger amounts of off-fault deformation measured around faults in their earlier stages of maturity (e.g. Dolan and Haravitch, 2014; Hatem et al., 2017; Perrin et al., 2021).

We define a resolvable wavelength for each fold as the maximum distance from the scarp that is well fit by the expression in equation 25 (Figure 65, top). In general, the folding wavelengths we resolve are smaller than 100 meters. For the coseismic data, the wavelengths we resolve are smaller than those visible from differential topography (Oskin et al., 2012), probably because of the higher sensitivity of the differential data. Resolvable wavelength weakly scales with fault throw suggesting that wavelength, like c, may increase with cumulative slip on the fault (Figure 65), bottom), though the data is very scattered. Folds at the Needles District consistently have lower resolvable wavelengths that folds in other locales. Two factors limit the extent folding may be characterized for at this site: the widely distributed secondary faulting in the footwall of the faults in the Needles District and the presence of vegetation in the unclassified lidar point clouds, which we resort to because the scarps are often miss-classified and removed in the ground-classified point cloud.

A mechanism for the creation of distributed folding

The folding we describe is, to first order, velocity-independent, as it is generated around faults that slip in very different regimes (triggered slip, steady-state creep, and seismogenic slip) without obvious differences at the scale we resolve with the lidar point clouds. To investigate the mechanism that generates distributed folding, we transform our displacements into strains, which requires taking the derivative of equation 25 with respect to distance from the fault:

$$\epsilon = \frac{c}{2\sqrt{x}} \tag{26}$$

This serves as a one-dimensional approximation of the shear strain associated with folding in the fault-perpendicular direction. This expression closely resembles the decay of stress in an elastic medium surrounding a crack tip in a linear elastic fracture mechanics framework ($\sigma(x) = \frac{K_c}{\sqrt{x}}$, where $K_c = \Delta\sigma\sqrt{L}$, where L is the fracture half-length and $\Delta\sigma$ is the difference between the far-field applied stress and the stress resolved on the crack walls). This suggests that folding represents a linear elastic response (strain) to the stress imposed on the medium by slip on the fault. Note that the decay of elastic stress away from a dislocation in an elastic half-space yields comparable solutions (Segall, 2010).

We can also use the folding strains described by equation 26 to make a prediction of the width of the yield zone (i.e. the location at which strain will fall below the elastic limit of rock). The extent of the yield zone x_{yield} is given by:

$$x_{yield} = \frac{c^2}{4\epsilon_{yield}^2} \tag{27}$$

where ϵ_{yield} is the elastic limit of rock at the surface, $3\text{x}10^{-3}$, estimated by Michel and Avouac (2006). Values of c for the coseismic folding range from 0.05 to 0.22 (Figure 64, bottom), which predicts a range in yield zone extent from 70 m to 1.3 km. For the cumulative folds, parameter c ranges from 0.06 to 3.2. This range results in yield zone extents from 100 meters to over 100 km (Figure 65, middle). Equation 27 predicts extents of yield much larger than the resolvable wavelengths we measure (Figure 65, top), which do not exceed 200 meters. This is unsurprising given the slope equivalent to the yielding strain is well below the resolution of the lidar point clouds. Beyond the resolution limitations, evidently, the predictions for the upper bound of this range are unrealistic. For example, physical limits to the extent of folding may include the spacing of faults or the width at the surface that scales with the down-dip extent of the rupture zone. Both of these have much smaller dimensions than 100 km. Nevertheless, our estimates suggest folding is responsible for widespread inelasticity in the bulk around faults ($>$ 100 m from the fault), incrementally

accumulating with subsequent slip events.

How do rocks accommodate folding strains? Insights from the Bishop Tuff

While the strain distributions we measure from our point cloud fits are well described by linear elastic fracture mechanics, their magnitudes exceed the elastic limit of rock by at least one order of magnitude, observed up to >100 meters and inferred up to kilometers from the fault. For example, ϵ at 1 m away from the fault is ~1 for c=1 and ~10^{-2} for c=0.1. The predicted strains for these values of c at 1 km from the fault are ~2x10^{-2} and ~2x10^{-3} respectively. These large strains must be accommodated within the rock mass by some inelastic deformation mechanism, which cannot be inferred from the remote measurements, requiring in-situ observations of the deformed rock mass.

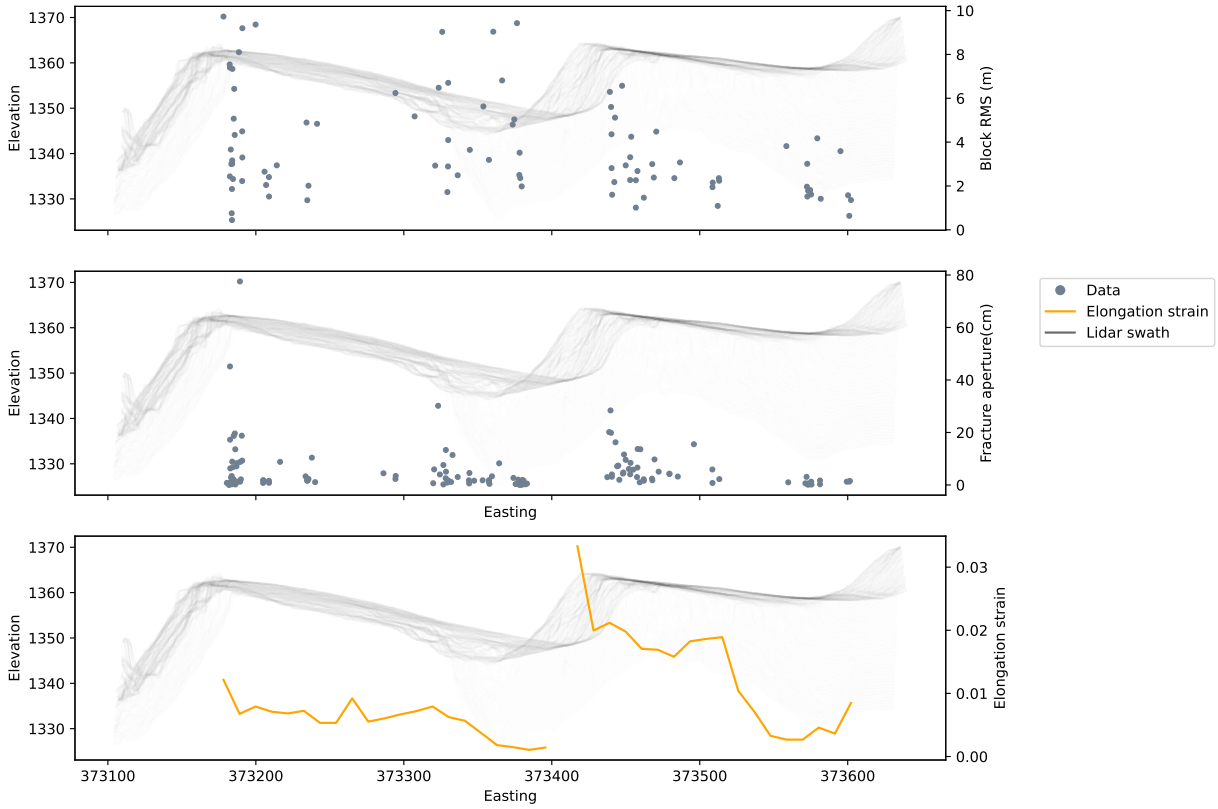

Figure 66: Data from field and lidar transect of the welded tuff surface at the Volcanic Tableland (CA). Top: Root mean square (RMS) of the longest axis and longest perpendicular axis to that one versus easting. The lines in the back represent the elevations of different lidar profiles within the swath the field data was collected in (see Figure 71). Middle: Fracture aperture versus easting. The fractures are generally more open on the footwalls of faults than the hanging walls. Fracture apertures have been reprojected to be fault-perpendicular. Bottom: One-dimensional elongation strain estimated as the ratio of median fracture aperture to median block RMS. Elongation strains are largest on the footwall of faults and decrease away from them to minimum values on the hanging wall.

To investigate what mechanism(s) accommodates inelastic folding, we collected field data in one of the sites where we measured folding remotely, the Volcanic Tableland in Bishop (CA). At the Volcanic Tableland, the Bishop Tuff can be divided into three sub-units: a capping welded tuff with a cooling texture with blocks bounded by mode I fractures, underlain by an unwelded tuff, underlain by a pyroclastic surge deposit. Neither the unwelded tuff or basal surge deposit exhibit observable rock fabric (Figure 70). These sub-units were determined in Ferrill et al. (2016), who described deformation within them qualitatively. Here, we combine his descriptions with field measurements to gain a quantitative understanding of how the bulk of the Bishop Tuff deforms in response to folding.

For the welded tuff, we measured fracture aperture and block size along a swath on the south-eastern end of the Tablelands (see methods and Figure 71). The block dimensions, captured by the root mean square (RMS) of the longest block axis and the perpendicular length, show a westwards increase that is independent of the block location with respect to the fault (Figure 66, top). This suggests that the block dimensions are a relict feature from cooling of the tuff and not affected by faulting. The fracture apertures are larger on the footwall of faults than the hanging wall (Figure 66, middle). This is consistent with the folding, which causes the footwall to be in extension and the hanging wall in compression, suggesting the fractures may be accommodating the off-fault strains we characterize from the lidar. We observed in the field that more open fractures often bounded larger blocks, consistent with fractures accommodating the off-fault folding while that intervening blocks remain rigid. To approximate the elongation strains accommodated by fracture, we take a moving median of the fracture aperture and the block RMS and calculate their ratio (Figure 66, bottom). The resulting elongation strains near the faults are on the order of 10^{-2}, consistent with the folding shear strains measured from the lidar point clouds.

Within the unwelded tuff, fractures are evident only in the regions immediately adjacent to faults. We collected a fracture transect perpendicular to a fault along a cliff exposure in this unit (see methods and Figure 72). Our transect shows a non-linear decay in fracture density with fault perpendicular distance (Figure 75). We interpret this observation to suggest that, in the absence of a pre-existing fabric, the rock deforms by creating and accommodating strain within a damage zone (e.g., Chester et al., 2005; Savage and Brodsky, 2011). White and Crider (2006) proposed that elastically generated folding becomes permanent by slip on joint planes and other fractures within the rock mass. Oskin et al. (2012) proposed slip on fractures as a potential mechanism to accommodate folding near the elastic limit of rock observed from differential lidar of the 2010 El Mayor Cucapah earthquake. The close correspondence between the elongation strains we measured in the field for the welded tuff and the shear strains measured from folding provide direct support for accommodation of off-fault folding via slip on pre-existing joints when available, and on new joints when needed (e.g. in the unwelded tuff).

We did not observe fractures in the basal surge deposit. We hypothesize that, within this sub-unit, deformation is accommodated microscopically via pore opening and closure. We observed some deformation bands next to a fault in an outcrop within this unit, consistent with our hypothesis of microscopically driven strain accommodation (Figure 76 in the appendix).

Evidently, our field observations are limited to a single locale and other lithologies and slip conditions may exhibit differences in how strain is accommodated. Nevertheless, across the three sub-units of the Bishop Tuff, the data suggest that pre-existing fabrics play a primary role in accommodating the folding strains within the rock mass.

Implications for the rheology of the shallow crust

Incremental folding produced during each event as the elastic response to slip on the fault must be transformed into permanent deformation, accommodated by fracture and other inelastic mechanisms, over some timescale. Immediately near the fault, this conversion is likely to be instantaneous, as folding strains exceed the elastic limit within a single event (e.g. c=0.1, the coseismic measured value for many folds in Figure 64, is equivalent to shear strains of 10^{-2} a meter away from the top of the fault scarp). Further away, the timing of this conversion cannot be resolved from our data, which is limited to the time of lidar point cloud collection, beyond the obvious constraint that the strains must be accommodated inelastically by the rock mass between the time it takes for the rupture to propagate and the next earthquake on the fault. Time is an essential component of characterizing rheology (the relationship between stress and strain rate). For example, in the absence of time constraints, plastic and viscous constitutive laws may be hard to distinguish.

The mechanisms accommodating the deformation within the rock mass observed at the Volcanic Tableland may provide clues to overcome the time limitations of the lidar data. The correspondence between the elongation strains accommodated by fracture and the folding strains measured from the lidar supports that strains above yield are responding to the applied stress linearly. The instantaneous elastic response (i.e. the folding shape) is very well preserved by the deformation in the rock mass. If residual stresses in the fractures result in additional, time-dependent deformation, this deformation is too small to distort the coseismic folding shape. The combination of these two facts suggests that the folding strains are accommodated by the rock mass coseismically and that the off-fault deformation we describe can be explained with time-independent elastoplasticity alone.

Figure 67 shows a simple mechanical model consistent with the folding we measured from the lidar data and the deformation we characterized in the Volcanic Tableland. Below the yield stress (σ_y in Figure 67) of the material, the rock mass deforms predominantly elastically, where fractures and other flaws can

accommodate some strain, but this strain is mechanically recoverable (i.e. anelastic deformation). Once the yield stress σ_y of the material is exceeded, new fractures will need to nucleate or pre-existing ones grow to accommodate the larger stress. In this elastoplastic regime, parts of the rock mass, like the rigid blocks in the Tableland, will continue to behave elastically. Over multiple earthquake cycles, as inelastic deformation is progressively added every time the yield stress is exceeded, the rock mass will continue to lose shear rigidity (G^*). The yield stress and ultimate strength (σ_u) of the material will also decrease over time. Eventually, if the ultimate strength of the rock mass is reached, the material will fail, for example through the creation of a thoroughgoing secondary fault.

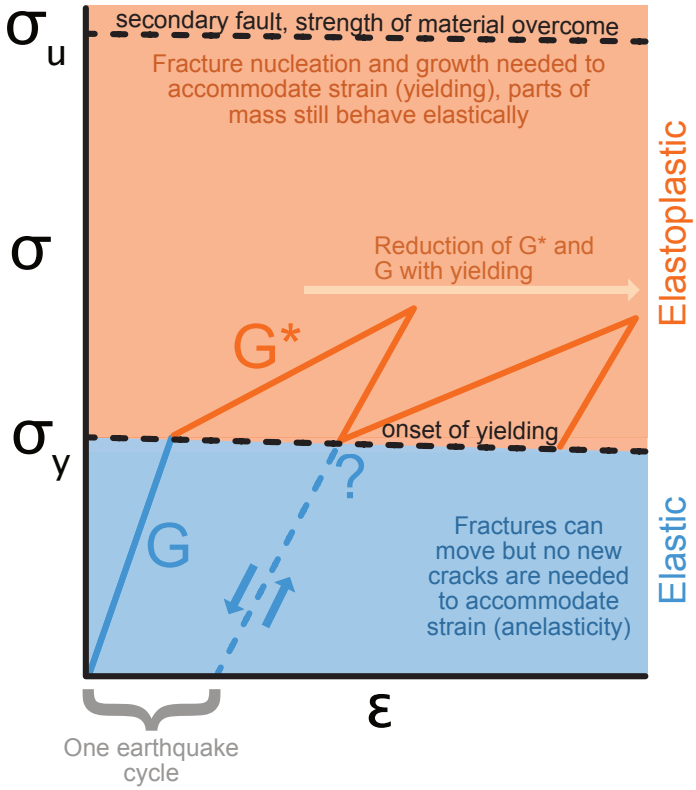

Figure 67: Cartoon illustrating the relationship between stress and strain that we interpret from our lidar and field observations. σ_y is the stress at the onset of yielding and σ_u is the ultimate strength, or the stress at which the strength of the material is completely overcome. Note that we use fracture as the yielding process in this cartoon but other inelastic deformation mechanisms, like pore opening and closure, can accommodate yielding in the rock mass as well.

To estimate how progressive off-fault deformation changes the shear rigidity of the rock mass, we derive a solution for the effective shear modulus G^* expected from the linear relationship between stress and strain we characterize (see methods section). We predict an effective shear modulus of 3-30 GPa, where the upper bound of this prediction overlaps with the typical shear moduli of relatively intact rock. The shear rigidity

reduction suggested by this range is consistent with the decrease in compliance measured geodetically and seismologically within fault damage zones (Fialko et al., 2002; Fialko, 2004; Cochran et al., 2009; Qiu et al., 2021; Xu et al., 2022; Xu et al., 2023). While G^* is not predicted to evolve with changing fault length, we expect it to decrease with additional damage, though we do not solve for this evolution. Therefore, our predicted value serves as an average effective shear modulus for a damaged rock mass affected by folding but below the ultimate strength of the material. This reduced rigidity will play an increasingly important role in the mechanics of the fault system by facilitating progressively more efficient strain localization in the compliant zone.

Conclusions

We measure long-wavelength folding adjacent to faults during the coseismic period and over geologic timescales. These observations reveal that folding extending hundreds of meters to kilometers from the fault accrues over multiple earthquake cycles, where pre-existing fabrics in the rock mass help accommodate the folding strains generated from incremental slip events. Our observations suggest that, once the yield stress is exceeded off-fault, deformation continues to scale linearly with stress, though the shear rigidity of the rock mass progressively decreases with the accrual of damage.

References

1. Antoine, S. L., Klinger, Y., Delorme, A., Wang, K., Bürgmann, R., & Gold, R. D. (2021). Diffuse deformation and surface faulting distribution from submetric image correlation along the 2019 Ridgecrest, California, ruptures. Bulletin of the Seismological Society of America, 111(5), 2275-2302.

2. Chester, J. S., Chester, F. M., & Kronenberg, A. K. (2005). Fracture surface energy of the Punchbowl fault, San Andreas system. Nature, 437(7055), 133-136.

3. Cochran, E. S., Li, Y. G., Shearer, P. M., Barbot, S., Fialko, Y., & Vidale, J. E. (2009). Seismic and geodetic evidence for extensive, long-lived fault damage zones. Geology, 37(4), 315-318.

4. Cowie, P. A., & Scholz, C. H. (1992). Displacement-length scaling relationship for faults: data synthesis and discussion. Journal of Structural Geology, 14(10), 1149-1156.

5. Dolan, J. F., & Haravitch, B. D. (2014). How well do surface slip measurements track slip at depth in large strike-slip earthquakes? The importance of fault structural maturity in controlling on-fault slip versus off-fault surface deformation. Earth and Planetary Science Letters, 388, 38-47.

6. Ferrill, D. A., Morris, A. P., McGinnis, R. N., Smart, K. J., Watson-Morris, M. J., & Wigginton, S. S. (2016). Observations on normal-fault scarp morphology and fault system evolution of the Bishop Tuff in the Volcanic Tableland, Owens Valley, California, USA. Lithosphere, 8(3), 238-253.

7. Fialko, Y., Sandwell, D., Agnew, D., Simons, M., Shearer, P., & Minster, B. (2002). Deformation on nearby faults induced by the 1999 Hector Mine earthquake. Science, 297(5588), 1858-1862.

8. Fialko, Y. (2004). Probing the mechanical properties of seismically active crust with space geodesy: Study of the coseismic deformation due to the 1992 Mw7. 3 Landers (southern California) earthquake. Journal of Geophysical Research: Solid Earth, 109(B3).

9. Furuya, M., Mueller, K., & Wahr, J. (2007). Active salt tectonics in the Needles District, Canyonlands (Utah) as detected by interferometric synthetic aperture radar and point target analysis: 1992–2002. Journal of Geophysical Research: Solid Earth, 112(B6).

10. Hatem, A. E., Cooke, M. L., & Toeneboehn, K. (2017). Strain localization and evolving kinematic efficiency of initiating strike-slip faults within wet kaolin experiments. Journal of Structural Geology, 101, 96-108.

11. Hudnut, K. W., Brooks, B. A., Scharer, K., Hernandez, J. L., Dawson, T. E., Oskin, M. E., ... & Sorhus, S. (2020). Airborne lidar and electro-optical imagery along surface ruptures of the 2019 Ridgecrest earthquake sequence, southern California. Seismological Research Letters, 91(4), 2096-2107.

12. Kravitz, K., Mueller, K., Bilham, R. G., & Walton, M. (2020). Active Steady-State Creep on A Nontectonic Normal Fault in Southeast Utah: Implications for Strain Release in a Rapidly Deforming Salt System. Geophysical Research Letters, 47(11), e2020GL087081.

13. Lienkaemper, J. J., Pezzopane, S. K., Clark, M. M., & Rymer, M. J. (1987). Fault fractures formed in association with the 1986 Chalfant Valley, California, earthquake sequence: preliminary report. Bulletin of the Seismological Society of America, 77(1), 297-305.

14. Michel, R., & Avouac, J. P. (2006). Coseismic surface deformation from air photos: The Kickapoo step over in the 1992 Landers rupture. Journal of Geophysical Research: Solid Earth, 111(B3).

15. Okubo, K., Bhat, H. S., Rougier, E., Marty, S., Schubnel, A., Lei, Z., ... & Klinger, Y. (2019). Dynamics, radiation, and overall energy budget of earthquake rupture with coseismic off-fault damage. Journal of Geophysical Research: Solid Earth, 124(11), 11771-11801.

16. Oskin, M. E., Arrowsmith, J. R., Corona, A. H., Elliott, A. J., Fletcher, J. M., Fielding, E. J., ... & Teran, O. J. (2012). Near-field deformation from the El Mayor–Cucapah earthquake revealed by differential LIDAR. Science, 335(6069), 702-705.

17. Personius, S. F., Crone, A. J., Machette, M. N., Mahan, S. A., & Lidke, D. J. (2009). Moderate rates of late Quaternary slip along the northwestern margin of the Basin and Range Province, Surprise Valley fault, northeastern California. Journal of Geophysical Research: Solid Earth, 114(B9).

18. Perrin, C., Waldhauser, F., & Scholz, C. H. (2021). The shear deformation zone and the smoothing of faults with displacement. Journal of Geophysical Research: Solid Earth, 126(5), e2020JB020447.

19. Pinter, N. (1995). Faulting on the volcanic tableland, Owens Valley, California. The Journal of Geology, 103(1), 73-83.

20. Qiu, H., Ben-Zion, Y., Catchings, R., Goldman, M. R., Allam, A. A., & Steidl, J. (2021). Seismic imaging of the Mw 7.1 Ridgecrest earthquake rupture zone from data recorded by dense linear arrays. Journal of Geophysical Research: Solid Earth, 126(7), e2021JB022043.

21. Savage, H. M., & Brodsky, E. E. (2011). Collateral damage: Evolution with displacement of fracture distribution and secondary fault strands in fault damage zones. Journal of Geophysical Research: Solid Earth, 116(B3).

22. Segall, P. (2010). Earthquake and volcano deformation. Princeton University Press.

23. White, I. R., & Crider, J. G. (2006). Extensional fault-propagation folds: Mechanical models and observations from the Modoc Plateau, northeastern California. Journal of Structural Geology, 28(7), 1352-1370.

24. Xu, X., Liu, D., & Lavier, L. (2023). Constraining fault damage zone properties from geodesy: A case study near the 2019 Ridgecrest earthquake sequence. Geophysical Research Letters, 50(5), e2022GL101692.

25. Xu, X., Liu, D., & Lavier, L. (2023). Constraining fault damage zone properties from geodesy: A case study near the 2019 Ridgecrest earthquake sequence. Geophysical Research Letters, 50(5), e2022GL101692.

Appendix

Geologic setting

Quantifying cumulative folding requires good exposures, high-resolution altimetry, and landscapes where the pre-faulted topography can be easily reconstructed. We consider three locations in the western United States that meet these criteria: the Volcanic Tableland, the Lake City fault zone in the Modoc Plateau, and the Needles District in Canyonlands National Park (Figure 68). We accompany these measurements of cumulative folding with coseismic folding measurements from the surface ruptures of the 2010 El Mayor Cucapah earthquake and the 2019 Ridgecrest earthquakes.

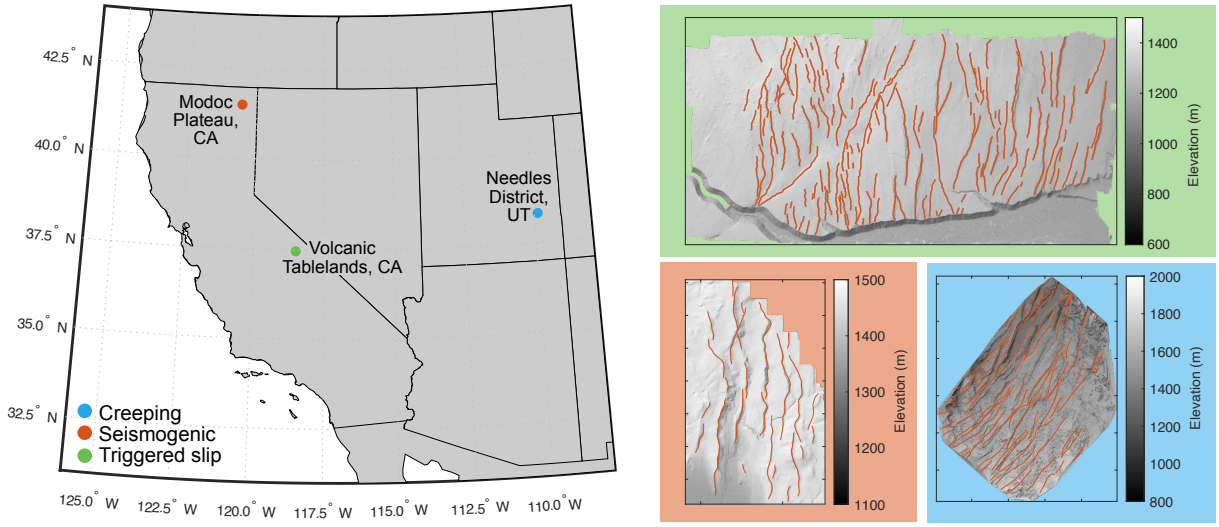

Figure 68: Locales where fault throw and folding geometry are measured in this study. The orange lines show the mapped faults and the lidar hillshades were generated using the data listed in table 6.

Volcanic Tableland (CA)

At the Volcanic Tableland, the Bishop Tuff forms a topographic plateau rising ∼50-120 meters over the northern Owens Valley, nested in the White Mountains Seismic Gap, between the White Mountains and the Sierra Nevada Mountains in Eastern California (Gilbert, 1938; Wilson and Hildreth, 1997). The Bishop Tuff formed 738±3 ky ago from the Long Valley Caldera eruption (Izett et al., 1988). Following deposition, the tuff layer at the Volcanic Tableland has undergone brittle deformation, resulting in the formation of north-south trending, steeply dipping normal faults (Bateman et al., 1965; Pinter, 1995; Dawers et al., 1993). Progressive deformation by these faults has resulted in hundreds of steeply-dipping scarps that cut the upper surface of the tuff and remain well-exposed due to little erosion of the footwall and negligible deposition along the hanging wall (Bateman et al., 1965). As a result, these faults have been the site of

several canonical fault-mechanics studies, e.g., establishing the evolution of on-fault slip with fault growth (Dawers et al., 1993) and understanding interactions within fault populations (Dawers and Anders, 1995; Ferrill et al., 2016).

The faults in the Volcanic Tableland act as an accommodation zone for extension associated with flexure of the Bishop Tuff, driven by motion on range-bounding faults of the White Mountains and the Eastern Sierra Nevada (Pinter, 1995). The faults in the Volcanic Tableland, which are too shallow to be seismogenic on their own, slip in response to earthquakes in these range-bounding faults. The most recent example of this behavior occurred during the 1986 Chalfant earthquake, where some of the faults in the Tableland experienced triggered normal slip from the strike-slip event (Lienkaemper et al., 1987; Pinter, 1995).

Needles District, Canyonlands National Park, UT

The Needles Fault District is nested in the Canyonlands National Park (UT), near the confluence of the Colorado and Green Rivers (Lewis and Campbell, 1965). The normal faults at this locale, which are arcuate in shape, steeply dipping, and have up to >100 m of throw are organized into a graben system that extends for ∼25 km along the river and is about 5 km wide east of it. The faults at the Needle District cut through a 460 meter thick plate of sandstone, which is underlain by ductile evaporites from the Paradox Formation (McGill and Stromquist, 1979). The flow of these evaporites toward the Colorado River drives steady-state creep on the faults in the upper unit (McGill and Stromquist, 1979; Kravitz et al., 2017). The Colorado River incised into the Paradox Formation at 0.5 Ma, the earliest possible onset of evaporite-driven creep (McGill and Stromquist, 1979). Creep rates on major faults are around 0.7±0.2 mm/yr (Kravitz et al., 2017). The distributed creep is around 2-3 mm/yr, distributed throughout the entire fault array with the largest values near the Colorado River (Furuya et al., 2007).

Lake City Fault Zone, Modoc Plateau, CA

The Lake City fault zone is part of an accommodation zone embedded on the footwall of the Surprise Valley Fault, a major fault bounding the western side of the geothermally active Surprise Valley in northern California (Egger et al., 2014). This area is part of the northwestern margin of the Basin and Range province (e.g. Egger and Miller, 2011). The normal faults in the Lake City fault zone cut through Late Miocene to Pliocene basalt flows and tuffaceous sediments exposed on the footwall of the Surprise Valley fault, placing a maximum age for initiation of the presently observed faulting at 4 Ma (Carmichael et al., 2006). These faults are seismogenic and have experienced events during the Holocene, with slip rates of ∼1-2 mm/yr (Personius et al., 2009).

Lidar data

To identify and extract the folding signal from the landscape, we rely on high-resolution lidar point clouds from five locations in western North America. The details of each dataset are included in Table 6.

Table 6: Location, point cloud density, and DOI for the lidar datasets considered in this study.

Location	Point cloud density	Reference
Surprise Valley, California	10.12 pts/m^s	`https://doi.org/10.5069/G9J10130`
Volcanic Tableland, California	15.48 pts/m^s	`https://doi.org/10.5069/G9RJ4GCH`
Needles District, Utah	10.47 pts/m^s	`https://doi.org/10.5069/G9X34VNQ`
Ridgecrest, California	33.13 pts/m^s	`https://doi.org/10.5069/G9W0942Z`
El Mayor-Cucapah, Mexico	9.12 pts/m^s	`https://doi.org/10.5069/G9TD9V7D`

Methods

Measuring fault throw and folding geometry from lidar point clouds

Where off-fault deformation is expressed as topographic uplift or subsidence (e.g. folding along normal faults) and the pre-faulted landscape is simple and can be easily reconstructed (e.g. tabular rock unit), high-resolution altimetry provides the opportunity to quantify off-fault deformation as it decays with distance away from a fault. To manipulate lidar point clouds and extract measurements we rely on open-source software lidR for R (Roussel et al., 2016).

Fault throw measurements

We mapped faults from the lidar DEMs listed in Table 6. Despite the presence of faults, we excluded the western half of the lidar point cloud for the Lake City fault zone in the Modoc Plateau, as the faulted basalt units are underlain by softer sediment in that region (MacDonald, 1966), resulting in mass wasting which distorts the fault scarps.

We discretized each mapped fault into 100 m spaced points, and extracted fault-perpendicular swaths of the point cloud centered on the fault at each increment. The lateral extent of the swaths ranges from 50 meters to 1 km, depending on the magnitude of fault throw, the fault scarp width, and the fault spacing. To assist with identification of the scarp end points and the subtle folding, the elevations in the point cloud were vertically exaggerated by a factor of 10. To fit the fault throw in each profile, we fit linear regressions through the hanging wall and the footwall using a least-squares approach. The resulting vertical separation where the lines connect is the fault throw.

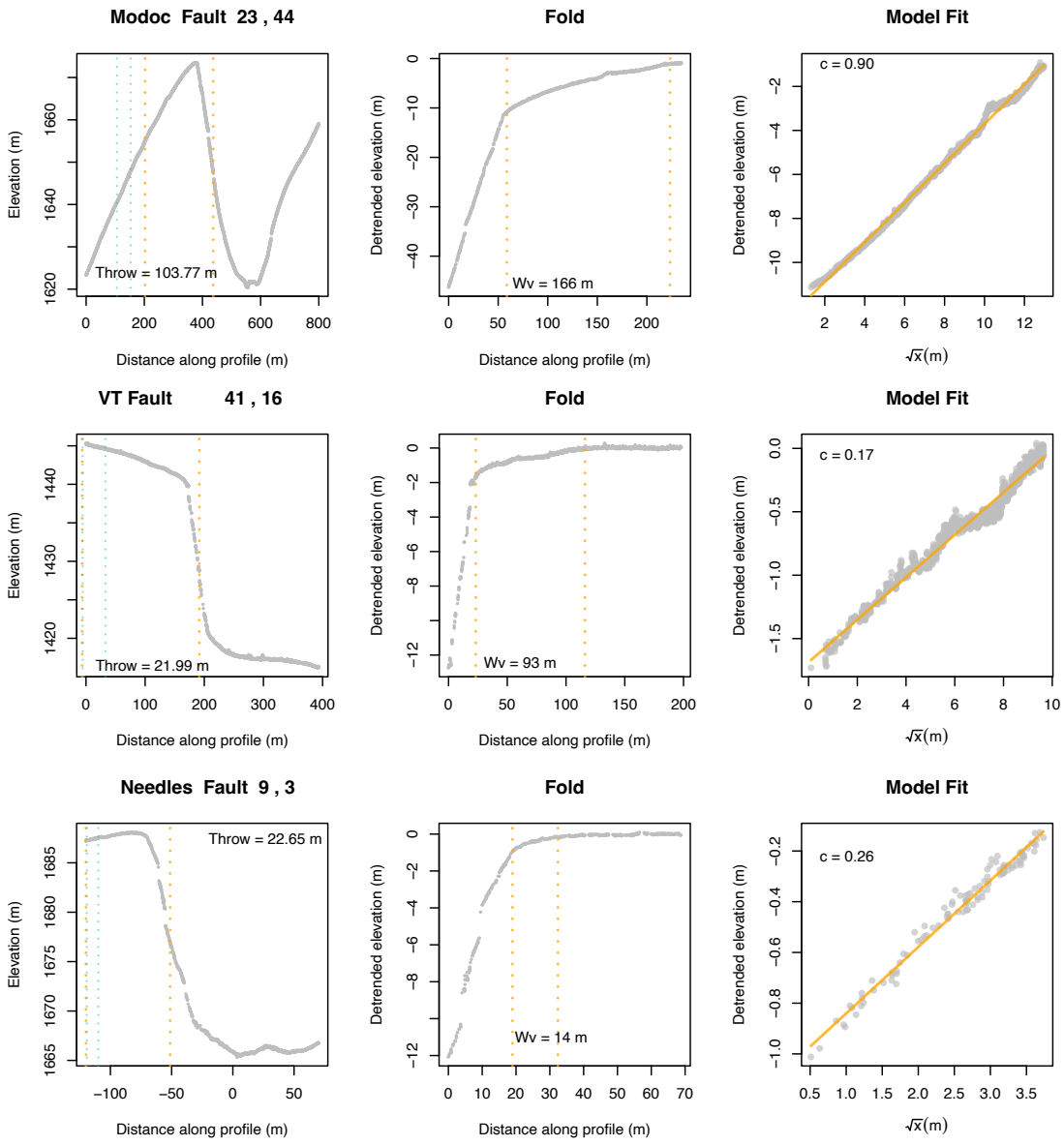

Figure 69: Point cloud profiles across faults and folds in the Modoc Plateau (top), the Volcanic Tableland (middle), and the Needles District (bottom). The first column of plots shows the faults cross-sections, with throw values annotated. The blue lines denote the section where regional slope was measured. The middle column corresponds to the section bound by the orange lines in the first column, which shows an inset of the footwall. The elevations have been detrended using the regional slope in the first column. The last column shows the folding measurement, where the x limits correspond to the section bound by the orange lines in the middle column. The x axis has been square rooted and the linear regression is used to fit the folding stretch value c, which is the slope of that line, shown on the top left of each plot.

Folding geometry measurements

We focus on folding on the footwall because the hanging wall of faults, especially those that have accumulated large displacements, host basins that obscure the folding signal. We started by measuring the regional slope away from the fault scarp, and detrended the elevations in the swath based on the measured slope. To fit equation 25 through the footwall elevations, we selected the section of the swath from the top of the fault scarp to the location where the folding appears to end through visual inspection. We then square rooted the x-axis of the clipped section (Figure 69) and fit a linear regression through the portion of the swath where elevations scale linearly with $\sqrt{x}$. The slope of the line fit yields the folding stretch factor c.

Effective shear modulus after multiple earthquake cycles

The stress field in the surrounding volume of a crack tip in a linear elastic medium is given by:

$$\sigma(x) \sim \frac{K}{\sqrt{2\pi r}} \tag{28}$$

Where r is the distance from the crack tip and K is the stress intensity factor given by:

$$K \sim \Delta\sigma\sqrt{\frac{L}{2}} \tag{29}$$

where $\Delta\sigma$ is the stress drop on the moving crack and L is the length of the crack from tip to tip.

The displacement distribution of a fold on the footwall of a fault is given by the distribution of elevations:

$$U(x) \sim c\sqrt{x} \tag{30}$$

where c is the folding stretch factor, and x is the distance from the fault in the fault-perpendicular direction. To turn equation 30 from a displacement into a strain, we take the derivative:

$$\epsilon(x) \sim \frac{c}{2\sqrt{x}} \tag{31}$$

Note the similarity between equations 28 and 31, which suggest the folding strain is the linear elastic response to the stress field around the rupturing fault. Note that x and r are equivalent in the fault-perpendicular direction. Equations 28 and 31 are related by the shear modulus. Combining equations 28, 31, and 29 yields:

$$\frac{\Delta\sigma\sqrt{\frac{L}{2}}}{\sqrt{2\pi r}} \sim G^* \frac{c}{2\sqrt{r}} \tag{32}$$

where G^* is the effective shear modulus that relates the incremental stress from a single slip event to the cumulative deformation folding signal accrued. Rearranging to solve for G^*:

$$G^* = \frac{2\Delta\sigma\sqrt{\frac{L}{2}}}{\sqrt{2\pi}c} \tag{33}$$

Equation 33 yields the effective shear modulus G^* at a finite fault length L. Parameters c and L are related by their dependence on fault throw. Parameter c scales with throw in a power-law relationship, $c = \beta\sqrt{T}$, where β is the intercept with values around 10^{-1} (Figure 64, bottom). Throw scales linearly with length, with slopes ranging from $10^{-5} - 10^{-3}$, for individual events (Hanks and Bakun, 2002) to cumulative displacement (Cowie and Scholz, 1992). Substituting the dependence of throw on length, using the scaling constant for a single event, into equation 33 eliminates the length-dependence, and equation 33 simplifies to:

$$G^* = \frac{\Delta\sigma}{3 \cdot 10^{-4}} \tag{34}$$

For every increment of slip, the stress drop is 1-10 MPa, so that G^* = 3-30 GPa.

Field measurements and unit descriptions

To investigate how the strain associated with the geodetic signal of folding is accommodated in the bulk, we collected field measurements at the Volcanic Tableland in Bishop, one of the locales we analyze lidar data for. The Bishop Tuff at the Volcanic Tableland can roughly be separated into three sub-units (Ferrill et al., 2016): capping the tuff is an indurated, welded tuff section that is a few meters thick, characterized by polygonal blocks from cooling during deposition, underlain by an unwelded tuff that is also several meters thick but lacks a pre-existing fabric, underlain by a pyroclastic surge deposit with also no apparent fabric.

To understand how strain is accommodated by the rock mass, we collected measurements of the fracture density, orientation, and aperture when possible for the welded and unwelded tuff units. For the welded tuff, we also collected measurements of block size, characterized as the root mean square (RMS) of the longest axis and the perpendicular length to consider the possibility of internal block deformation as a strain accommodation mechanism. The surge deposit does not have visible fractures, so we did not collect a transect but made some qualitative observations we report in the main body of this manuscript.

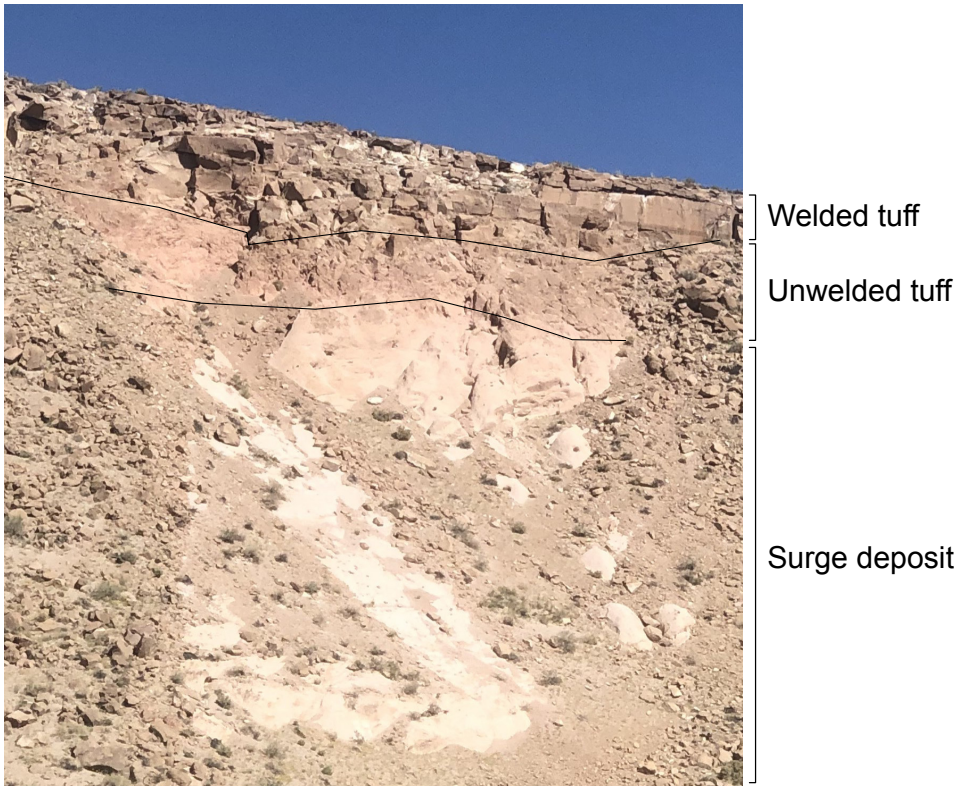

Figure 70: Cliff exposure of the Bishop Tuff at the Volcanic Tableland. The three main subunits of the Tuff can be clearly seen and are annotated on the right side of the image.

Welded tuff

The indurated top of the tuff sequence is well preserved throughout the Tableland, suggesting minor erosion since deposition (Bateman et al., 1965). At some locations, we observed remnant surfaces of the welded tuff that were up to 1.5 meters tall, suggesting that is the minimum amount of erosion experienced since the deposition of the tuff. We collected fracture and block measurements along a swath on the southeastern edge of the tuff (Figure 71). We selected this location because the fractures and blocks were not buried by sand, which is the case for most of the tuff's surface. For the fractures, we measured the aperture using a caliper or, for larger fractures, measuring tape. We also measured the fracture trend. We then reprojected the fracture apertures to the strike of the faults in the area of the transect, which is ∼195. For blocks, we measured the longest axis and then the longest dimension in the direction perpendicular to that axis. To assess whether internal block deformation is occurring, we calculate the root mean square (RMS) of each block as a proxy for shape. The measurements are shown in Figure 66 in the main text.

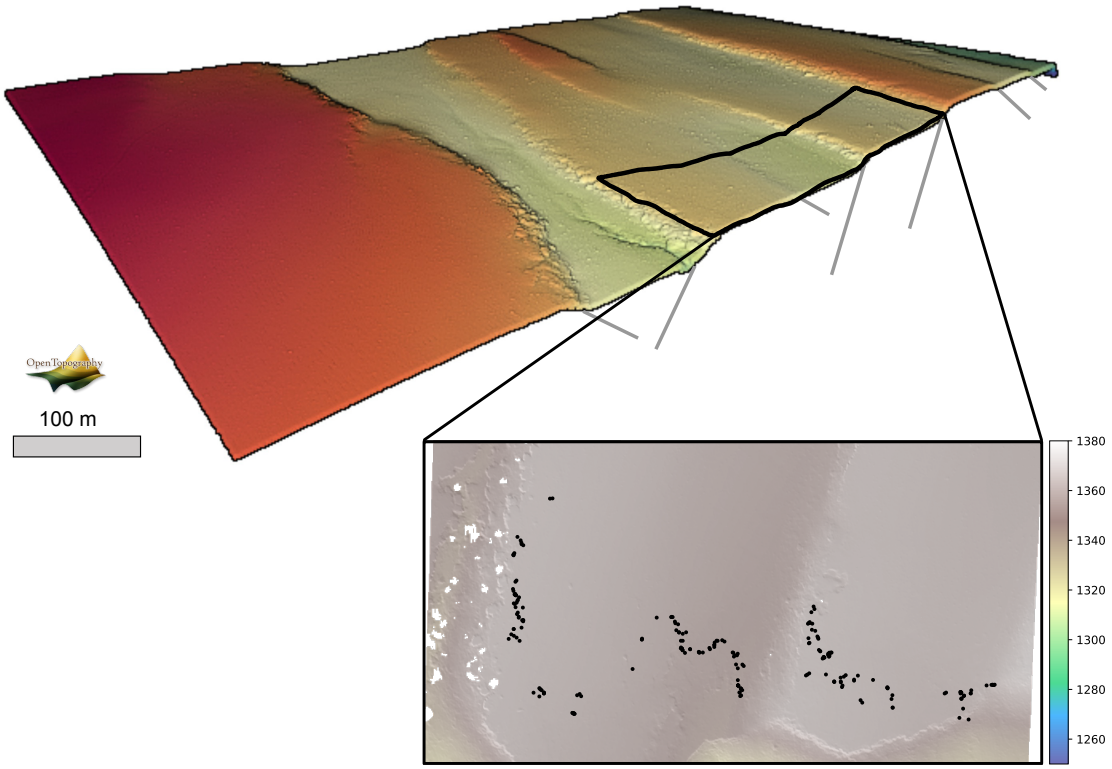

Figure 71: Swath where the field data was collected in the Volcanic Tableland. Top: 3D point cloud visualization of the swath area generated using the Open Topography browser visualization tool. Bottom: Lidar DEM of the swath area. The black scattered dots represent the locations where we measured fracture apertures or block RMS.

Unwelded tuff

The unwelded tuff unit lacks an observable cooling fabric, but fracturing occurs near the faults. We carried out a fracture count along a transect perpendicular to a fault in one of the cliff exposures on the central portion of the tuff (Figure 72). Note the fracture apertures were too narrow to be measured for this unit. The measurements are shown in Figure 75.

Pyroclastic surge deposit

The bottom sub-unit of the Bishop tuff is a pyroclastic surge deposit characterized by the absence of fractures or any rock fabric, so there were no features to measure at the mesoscopic scale. We observed deformation bands (Figure 76) near the fault, at the location highlighted with a black dot in Figure 72.

Figure 72: Location where we observed the unwelded tuff unit and underlying surge deposit (Chalk Bluff, Volcanic Tableland). The grey lines bound the surge deposit, the orange line represents a fault, and the orange arrow represents the location on the unwelded tuff unit where we collected a fracture transect (Figure 75). Note the absence of fractures away from the transect area and the fault. The black dot represents the location where we observed deformation bands in the pyroclastic surge deposit (Figure 76).

Strain transfer below the Bishop Tuff

The Bishop Tuff is underlain by older alluvial fans and lakebed deposits interbedded with thin air fall and ash flow deposits (Bateman, 1958; Wilson and Hildreth, 1997). The stratigraphic sequence of the deposits is partially exposed at the Eastern edge of the Volcanic Tableland. We mapped this exposure to examine how deformation behaves below the base of the tuff, with a focus on investigating whether the major faults throughout the tuff extend below it (Figure 73). Deformation within the underlying deposits is partitioned into multiple fault strands accommodating <5 meters of throw and many minor strands are restricted to some of the units within the deposits and accommodating only a few centimeters of throw. Only one of the major faults cutting the Bishop tuff (fault 2 in Figure 73), can be matched with a fault cutting these underlying deposits (fault c in Figure 73). Because deformation appears much more distributed below the Bishop Tuff, and faults cannot be directly correlated between the deposits and the tuff, we assert that the Bishop Tuff behaves as a distinct mechanical unit. This is consistent with the work of Lienkaemper et al. (1987) and Dawers et al. (2003), who postulated based on the shape of fault displacement profiles at the Tablelands that faults propagate downdip until they reach the end of the Bishop tuff and then continue to

propagate only along strike, so that faulting is confined to a discrete layer.

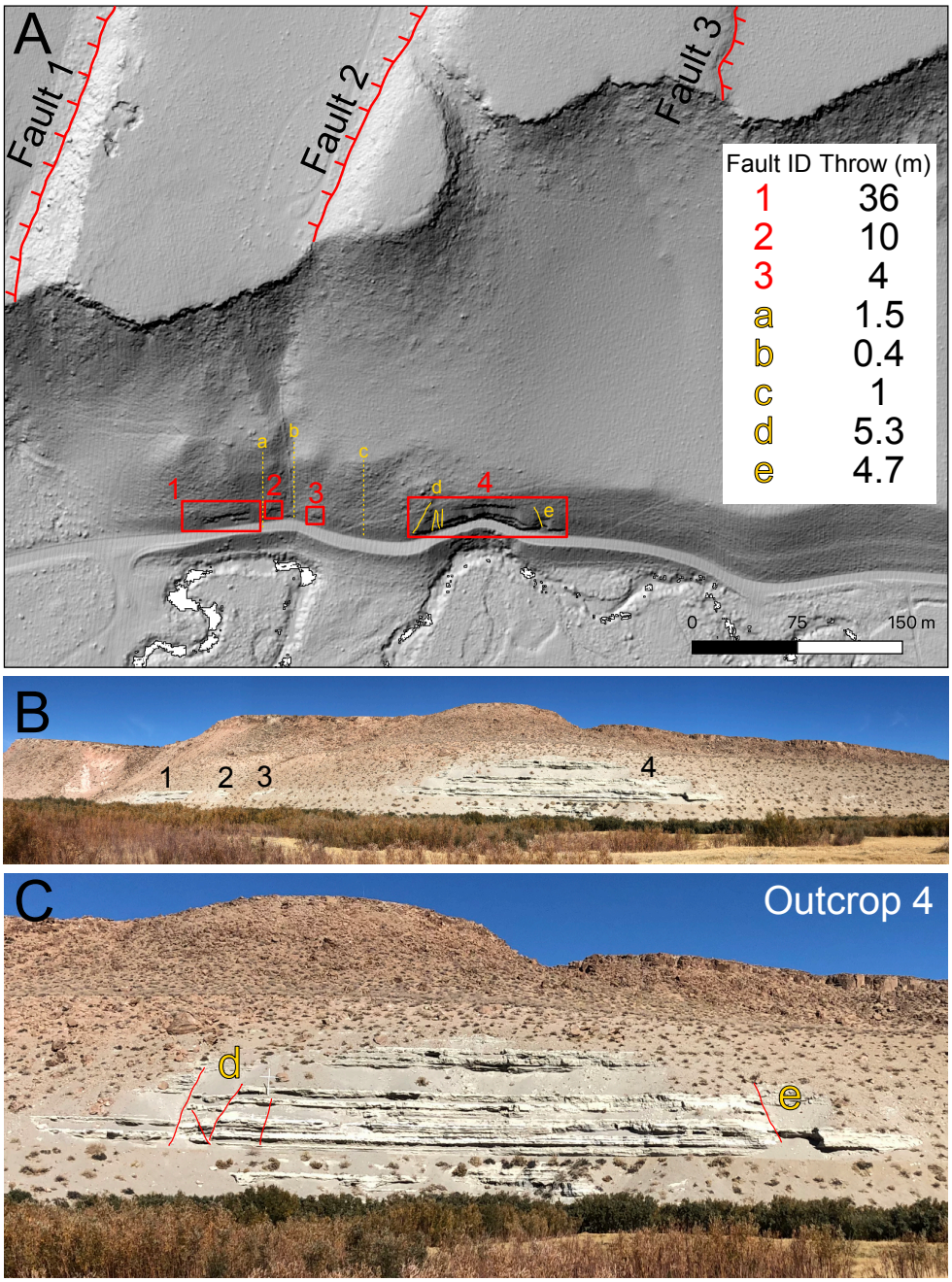

Figure 73: A: Lidar DEM of the Volcanic Tableland with main faults 1-3 cutting through the Bishop Tuff and minor faults a-e cutting the lakebed sediment underlying the tuff. B: Outcrops with exposure of the underlying lakebed sediments. C: Close-up view of fault zones d and e in outcrop 4 (B).

Appendix figures

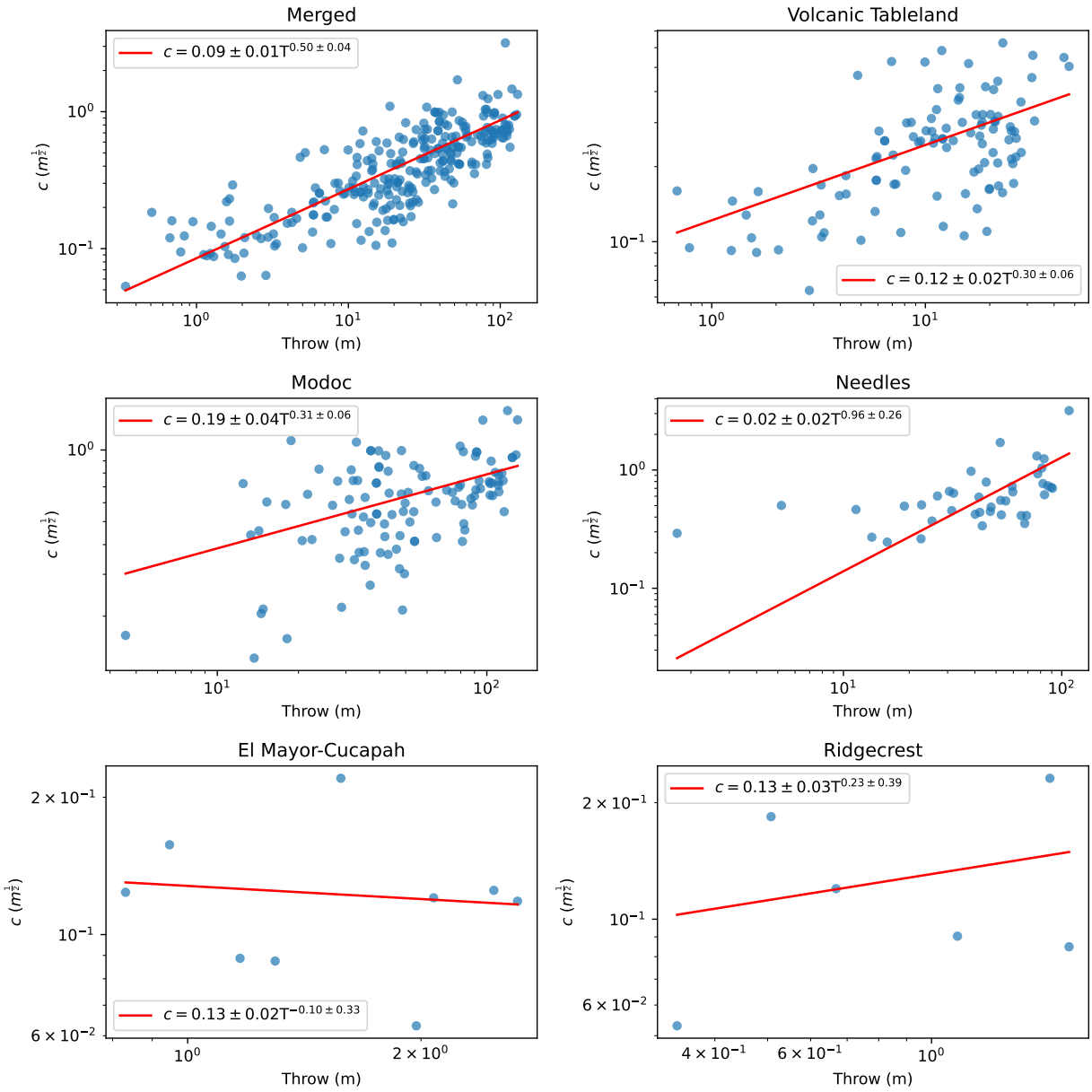

Figure 74: Scaling of c with fault throw for the different sites combined in Figure 64

.

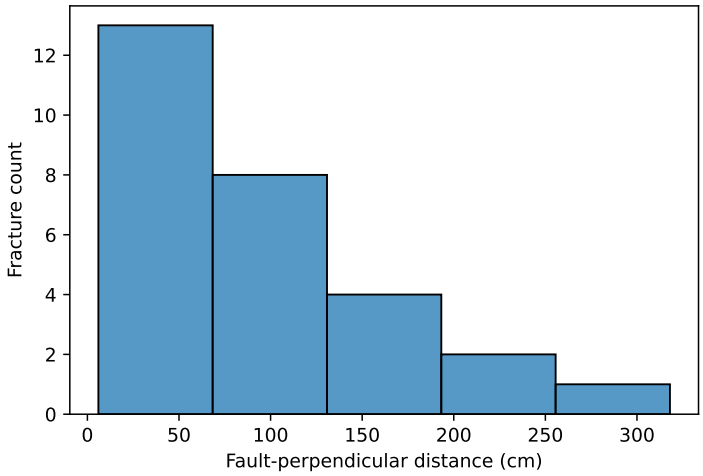

Figure 75: Distribution of fractures along a transect in the unwelded tuff unit. The fracture transect was collected along the orange arrow in Figure 72.

Figure 76: Deformation band in the surge deposit of the Volcanic Tableland. The red arrows point to the deformation band and a pen is shown for scale. The photograph was taken at the location marked by a black dot in Figure 72.

Supplementary references

1. Bateman, P. C., Pakiser, L. C., & Kane, M. F. (1965). Geology and tungsten mineralization of the Bishop district, California, with a section on gravity study of Owens Valley and a section on seismic profile (No. 470). US Govt. Print. Off.,.

2. Beanland, S., & Clark, M. M. (1993). Late Quaternary history of the Owens Valley fault zone, eastern California, and surface rupture associated with the 1872 earthquake. Geological Society of America, Abstracts with Programs;(United States), 25(CONF-9305259-).

3. Carmichael, I. S., Lange, R. A., Hall, C. M., & Renne, P. R. (2006). Faulted and tilted Pliocene olivine-tholeiite lavas near Alturas, NE California, and their bearing on the uplift of the Warner Range. Geological Society of America Bulletin, 118(9-10), 1196-1211.

4. Dawers, N. H., Anders, M. H., & Scholz, C. H. (1993). Growth of normal faults: Displacement-length scaling. Geology, 21(12), 1107-1110.

5. Dawers, N. H., & Anders, M. H. (1995). Displacement-length scaling and fault linkage. Journal of Structural Geology, 17(5), 607-614.

6. Egger, A. E., Glen, J. M., & McPhee, D. K. (2014). Structural controls on geothermal circulation in Surprise Valley, California: A re-evaluation of the Lake City fault zone. Bulletin, 126(3-4), 523-531.

7. Egger, A. E., & Miller, E. L. (2011). Evolution of the northwestern margin of the Basin and Range: The geology and extensional history of the Warner Range and environs, northeastern California. Geosphere, 7(3), 756-773.

8. Gilbert, C. M. (1938). Welded tuff in eastern California. Bulletin of the Geological Society of America, 49(121), 1829-1862.

9. Hanks, T. C., & Bakun, W. H. (2002). A bilinear source-scaling model for M-log A observations of continental earthquakes. Bulletin of the Seismological Society of America, 92(5), 1841-1846.

10. Izett, G. A., J. D. Obradovich, & H. H. Mehnert, The Bishopashbed (middle Pleistocene)and some-older (Plioceneand Pleistocene) chemically similar ash beds in California, Nevada, and Utah, U.S. Geol.Surv.Bull., 1675,37 pp., 1988.

11. Lewis, R. Q., Sr., & Campbell, R. H., 1965, Geology and uranium deposits of Elk Ridge and vicinity, San Juan County, Utah: U.S. Geological Survey Professional Paper 351,68 p.

12. MacDonald, G. A. (1966). Geology of the Cascade Range and Modoc Plateau. Geology of Northern California. Calif Div Mines Bull, 190, 65-95.

13. McGill, G. E., & Stromquist, A. W. (1979). The grabens of Canyonlands National Park, Utah: geometry, mechanics, and kinematics. Journal of Geophysical Research: Solid Earth, 84(B9), 4547-4563.

14. Rodriguez Padilla, A.M. (2020). Normal Fault Comparisons, Utah 2019. National Center for Airborne Laser Mapping (NCALM). Distributed by OpenTopography. https://doi.org/10.5069/G9X34VNQ.. Accessed: 2023-07-25

15. Roussel, J. R., Auty, D., Coops, N. C., Tompalski, P., Goodbody, T. R., Meador, A. S., ... & Achim, A. (2020). lidR: An R package for analysis of Airborne Laser Scanning (ALS) data. Remote Sensing of Environment, 251, 112061.

16. Surprise Valley, CA. Distributed by OpenTopography. https://doi.org/10.5069/G9J10130 . Accessed: 2023-07-25

17. Volcanic Tablelands in Bishop, California. Distributed by OpenTopography. https://doi.org/10.5069/G9RJ4GCH. Accessed: 2023-07-25

18. Wilson, C. J., & Hildreth, W. (1997). The Bishop Tuff: new insights from eruptive stratigraphy. The Journal of Geology, 105(4), 407-440.